UNIVERSITA' DEGLI STUDI DI SIENA
Dipartimento di Biotecnologie, Chimica e Farmacia

DOTTORATO DI RICERCA IN
Chemical and Pharmaceutical Science

37° Ciclo

COORDINATORE
Prof. Maurizio Taddei

Design, synthesis and transformation of new photoactive compounds for photocatalytic applications

SETTORE SCIENTIFICO DISCIPLINARE: CHIM-06

DOTTORANDA
Xheila Yzeiri
Università degli studi di Siena
CNR-ICCOM

Firmato digitalmente da
XHEILA YZEIRI
31/03/2025 21:08:20 +0200
powered by cheFirma!

TUTOR
Prof. Maurizio Taddei
Università degli studi di Siena

CO-TUTOR
Dr. Alessandro Mordini
Università degli studi di Firenze
CNR-ICCOM

ANNO ACCADEMICO: 2023/2024

Table of Contents

Abstract

In view of the current severe climate crisis and increasing resource scarcity, our society is in urgent need for new strategies to generate fuels, chemicals, and materials from renewable feedstocks. In the interest of future generations, actions need to be taken to develop more efficient transformations solely relying on renewable energy and without the emission of hazardous substances. In this context, photocatalysis as a direct sunlight-driven process has the potential to contribute to a sustainable economy that combines both synthesis and chemical recycling of various chemicals, materials, and fuels. Indeed, excited states generated by light enable thermodynamically uphill reactions, which forms the basis for solar energy storage into fuels. Furthermore, photocatalysis allows the development of novel reaction routes via excited-state reactivity that are inaccessible following ground-state catalytic pathways. Within this framework, this Ph.D thesis explore the application of photocatalytic prosses in the field of artificial photosynthesis and synthetic chemistry.

The main part of the research activity focused on Dye-Sensitized Photoelectrochemical Cells (DSPECs) for water splitting, a promising technology for converting solar energy into chemical energy. In this approach, sunlight is captured by a dye and used to promote the photo-oxidation of water (catalyzed by a water oxidation catalyst or WOC), producing *'solar' fuels* such as hydrogen (H_2). In this regard, we worked on the modeling, synthesis, and characterization of novel metal-free organic dyes. First, two families of donor-auxiliary acceptor-π-acceptor (D-A-π-A) sensitizers were designed: compounds **1a-c** with a 2,3-diphenylquinoxaline core, and compounds **PP2a-c** with a 2,3-diphenylpyrido[3,4-*b*]pyrazine core. These dyes were successfully synthesized and characterized spectroscopically and electrochemically. Furthermore, the ability of compounds **1a-c** to function as anodic sensitizers was evaluated through photo-electrochemical tests in a three-electrode cell, showing promising results, with compound **1a** demonstrating the highest photocurrent generation. Afterward, we turned our attention to alternative dye/catalyst photoanode-sensitization strategies, moving beyond conventional co-loading methods. Here, a novel metal-free sensitizer-catalyst covalent adduct (dyad) was designed, building on the structure of dye **1a** and modifying it to enable coordination with the Ru(bda) WOC. This led to the successful synthesis of dyad **D1A2**, whose obtainment was supported by a full spectro-electrochemical characterization.

In addition to this main subject, as a final part of this research work, we also explored the potential of near-ultraviolet and visible light irradiation as a powerful mean in synthetic chemistry. In particular, we investigated novel methodologies for N-functional groups migration on aromatic rings, facilitating the conversion of aryl azides into anilines with regioisomeric substitution patterns.

Chapter 1

Introduction

1.1 The World's energy status

As recently stated by Ognjen Š. Miljanić and Joseph A. Pratt in their book about energy and sustainability "since the very beginning of civilization, humans have used energy to power their daily activities. The history of humanity runs parallel with the history of its energy use: as our civilization and population grew, so did our need for energy".[1]

The processes involved in energy extraction, distribution, and consumption profoundly influence many aspects of global life, not only from an ecological and economic perspective but also in terms of social inequality.[2] A significant disparity exists in energy access, with approximately 10% of the population, concentrated in affluent nations, consuming nearly half of the World's total energy supply, while the poorest 25% use less than 3%. Although ensuring a sufficient energy supply is just one of the many challenges facing humanity, the availability of energy underpins almost every other pressing social and political issue of our time. From food production and clean water access to healthcare, environmental preservation, education, and even conflict, nearly all these problems are intricately linked to how energy is sourced, distributed, and utilized.[3]

With the advent of the modern era and the Industrial Revolution, global energy consumption has seen a dramatic rise, driven by population growth, industrialization, and increasing energy needs. This ascending trend has not stopped yet: in 2023, the global energy demand increased by 2% from 2022, reaching 620 EJ (17×10^4 terawatt hours), reflecting a widespread economic recovery from the impacts of the COVID-19 pandemic.[4]

Nowadays fossil fuels still provide almost 80% of the global primary energy supply, used in transportation, heating and electricity conversion. Fossil oil consumption averaged 101.1 million barrels a day in 2023, slightly above the pre-pandemic record of 101.0 million barrels a day. Coal consumption rose 1.4% to surpass 8.5 billion tonnes annually for the first time ever. For fossil gas, the annual growth rate in consumption has slowed from an average of 2.5% in 2017 to an average of 1.6% during 2021-2023. Modern renewables, such as hydropower, wind, solar energy and biofuels, represented 15% of total final energy consumption. In 2023, nearly half of the World's total final energy consumption was in the form of direct heat, followed by fuels (including liquid and gaseous fuels for transport), with a 29% share. The proportion of electricity (also used for heat and transport) in the global energy supply has been rising consistently – reaching 23% up from 19% in 2011 – with increasing dependence on electricity to meet demand across all sectors (Figure 1.1). The renewable share in electricity generation increased marginally from 29.4% in 2022 to 30.3% in 2023, although this mostly covered the increase in electricity demand rather than replacing fossil fuels.[5]

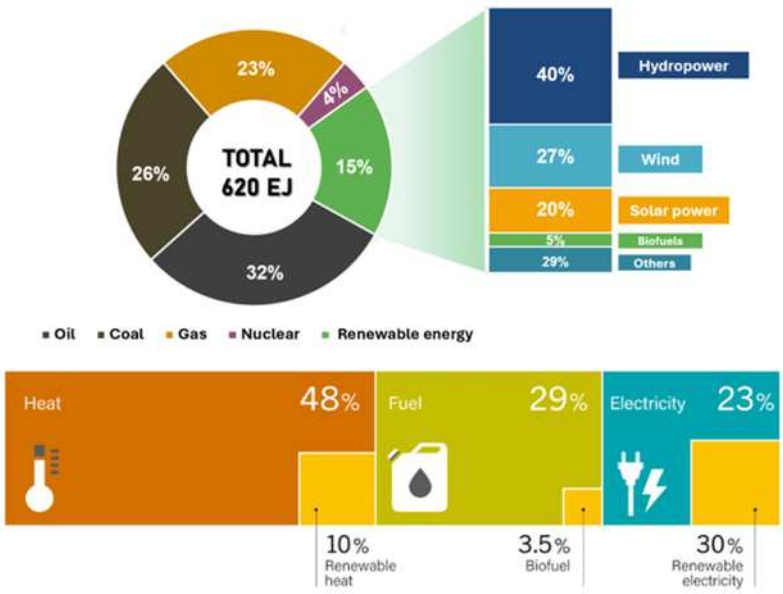

Figure 1.1 Total Final Energy Consumption and Share of Modern Renewables, by Energy Carrier, 2023 (bottom).[5]

Besides being a non-renewable source, fossil fuels are by far the largest contributor to global climate change, accounting for over 75% of global greenhouse gas emissions and nearly 90% of all carbon dioxide emissions, which is identified as the primary driver of climate change worldwide. So far, the global temperature increase compared with pre-industrial times (before 1850) has been near 1.2 °C, with 1.1 °C since 1900, and is projected to be at the 1.5 °C level within 15 to 20 years if emissions of greenhouse gases are not drastically reduced (Figure 1.2).[6]

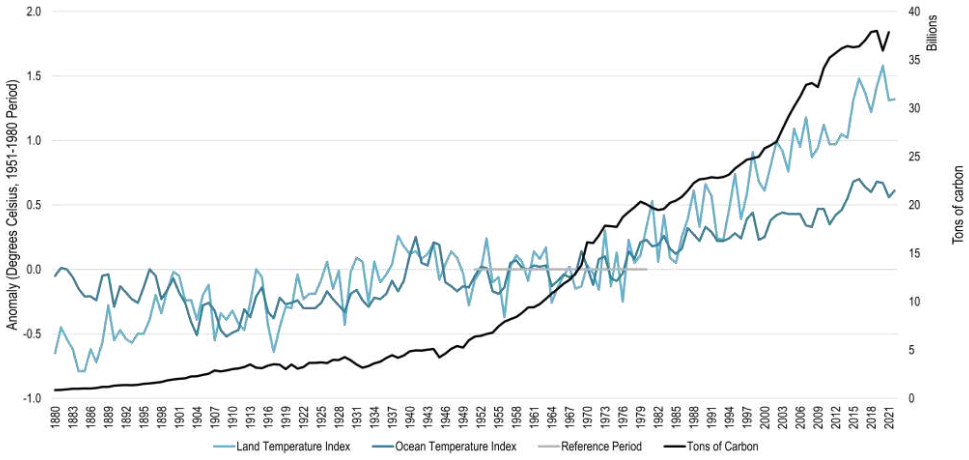

Figure 1.2 Average Global Temperature and Carbon Emissions from Fossil Fuel Burning, 1880-2021.[7]

In response to wide-ranging goals related to climate change and decarbonization, decision-makers have enacted new renewable energy policies. With the approval of the European Green Deal, in 2020, and RePowerEU, in 2022, the European Commission has launched a package of measures aimed at decarbonization and sustainable economic development with the goal of making the European Union climate neutral by 2050.

These initiatives focus mainly on accelerating the deployment of renewable energy sources like solar, wind, hydropower, and green hydrogen, while also enhancing energy efficiency and modernizing energy infrastructure. The aim is to reach at least 45% renewable energy by 2030, in order to reduce the EU's dependence on imported energy and move towards a more decentralized, locally-sourced energy supply. Driven by these policies, in 2023, renewable energy was the leading source of electricity in the EU, accounting for 44.7% of all electricity production generating 1.21 million Gigawatt-hours (GWh) - a 12.4% increase from 2022.[8]

Globally, the renewable power sector took a large step forward, deploying a record amount of new capacity and extending to new geographic areas. With 536 GW, a 54% increase over 2022, the globally installed renewable electricity generation capacity has now reached a new record of 4,034 GW. While the increases in renewable capacity in Europe, the United States and Brazil hit all-time highs, China's acceleration was extraordinary. In 2023, China commissioned as much solar photovoltaics (PV) as the entire world did in 2022, while its wind additions also grew by 66% year-on-year.[9]

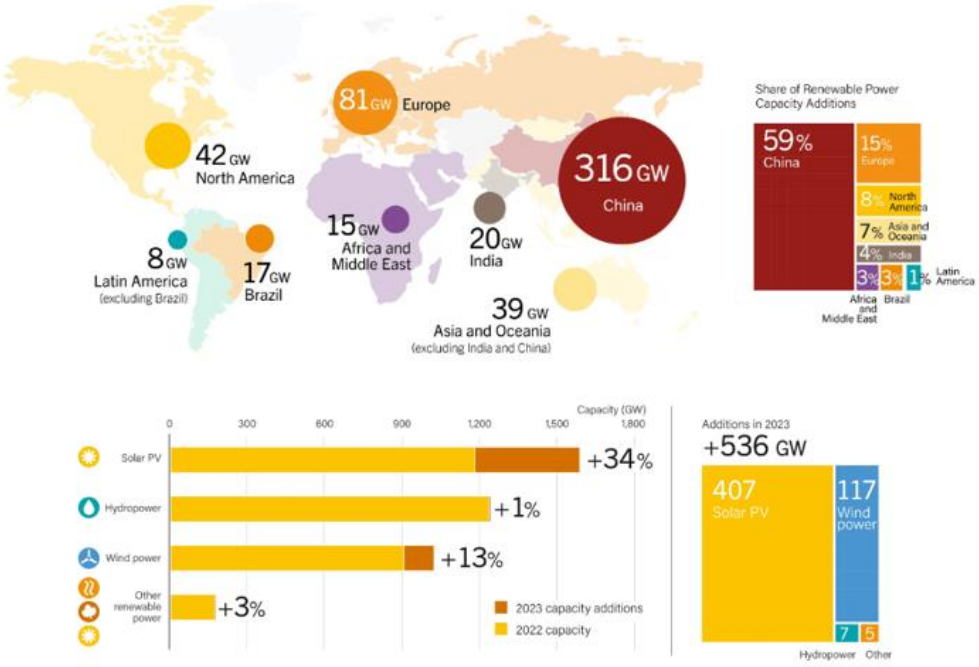

Figure 1.3 Renewable Power Capacity Additions, by Region/Country, 2023 (top); Renewable Power Total Installed Capacity and Additions, by Technology, 2023 (bottom). [5]

Solar installations rose by a record of 208 GW – from 199 GW in 2022 to 407 GW in 2023. Almost three-quarters of all renewable capacity built in 2023 was solar. Wind additions also increased by a sizable 51% in 2023, accounting for another quarter of renewable capacity additions in 2023. After two years of slower growth, 2023 saw a new record for wind capacity additions, beating the previous record set in 2020[10] (Figure 1.3).

1.2 Solar energy conversion

As seen above, nowadays the majority of new renewable energy installations across the World is related to solar energy. Indeed, solar energy is the most abundant permanent energy resource on earth. The sun emits energy at a rate of 3.8×10^{23} kW. Of this total, only a small fraction, approximately 1.8×10^{14} kW is intercepted by the earth, which is located about 150 million km away from the Sun. About 60% of this amount, ca. 1.08×10^{14} kW, reaches the Earth's surface. The rest is reflected back into space and absorbed by the atmosphere. Even if only 0.1% of the energy hitting the Earth's surface could be converted with a power conversion efficiency of only 10%, it would be four times the world's total generating capacity of about 3000 GW. Looking at it another way, the total annual solar radiation falling on the Earth is more than 7500 times the world's total annual primary energy consumption of 620 EJ.[11] Solar energy has then tremendous potential as a clean, abundant, widely distributed and affordable energy source, but it has some drawbacks that limit its exploitation: it is diffuse (ca. 170 W m^{-2}) and intermittent, so it must be concentrated and converted into more useful forms of energy, such as electricity or fuels, and then stored and distributed.[12]

In the last two decades, a large amount of work has been devoted to increasing the efficiency of existing technologies able to convert solar energy into electric current (see paragraph 1.2.1), as well as to developing new ones. On the other hand, electricity accounts only for a minor portion of the global energy needs, so the development of new technologies for the production of fuels in a renewable and clean manner is becoming mandatory for the imminent energy transition. Direct production of fuels from sunlight appears to be one of the most promising technologies in this field, and it will be further discussed in paragraph 1.3.

1.2.1 Electricity from the Sun: photovoltaics

Sunlight can be converted into electricity either indirectly through concentrated solar power (CSP) or directly through photovoltaics (PV). CSP works by concentrating sunlight with optical systems like parabolic collectors and solar towers, producing high-temperature fluids that drive conventional turbines for large-scale electricity generation. Although CSP can offer cost-effective electricity, it has a major drawback: it is only economically feasible in the sunbelt region, a geographic area located between the 35th northern and southern latitudes. This rules out the vast majority of the wealthiest countries, an obvious obstacle for stimulating wide market diffusion.[13]

Photovoltaic devices, which directly convert light into electricity, are to date the most widely used solar energy technology not only because they are relatively cheap, but also thanks to their simplicity of installation and use. Even though the fundamental principles behind photovoltaic technology were already known since the 19th century, after the discovery of photovoltaic effect by Alexandre Edmond Becquerel,[14] the first practical photovoltaic device, also known as solar cell, was publicly demonstrated in the mid-50's at Bell Laboratories.[15] Since then, PV technology has advanced significantly, especially over the past 30 years, with notable improvements in device performance and a broadening range of applications. This growing interest in photovoltaics has been accompanied by continuous technological progress, resulting in higher efficiencies and sharply reduced production costs, which has fuelled the rapid expansion of the photovoltaic industry.[16]

Nowadays, solar cells are usually classified according to consecutive technology generations. Based on the nature and physical properties of the materials employed for their fabrication, three main classes of solar cells can be identified:

- Silicon-based solar technology (First generation);
- Thin-film PV cells (Second generation);
- Emerging (organic and hybrid) photovoltaics (Third generation).

1.2.1.1 First generation: silicon-based solar cells

Silicon-based solar cells historically represent the first class of solar cells ever developed. These devices are based on p-n junctions consisting of two contacting silicon semiconductor layers with opposite doping. This wafer of approximately 200-300 μm thickness, is created by doping the growing crystals of silicon with 0.1% of atoms of Group III (B or Al for the positive layer) and Group V (P or As for the negative layer). The working mechanism of this kind of cells is shown in Figure 1.4: in the dark, at the interface, the electrons flow from the negative region to the positive one, generating an in-built electric field and creating the so-called space-charge region (Figure 1.4a). When light hits the device at a proper angle of impact, electrons in the *p*-type region are promoted to the conduction band (CB), leaving holes in the valence band (VB). The electron-hole pairs diffuse toward the space-charge region; once there, electrons are taken across the junction by action of the built-in potential created at the interface (V_{bi}, Figure 1.4, bottom)), leaving holes behind (charge separation). Once in the n-region, the electrons then diffuse towards the contact and enter the external circuit. The cycle is over when such electrons re-enter the device and fill the holes at the *p*-side. The same, but opposite, process happens for holes generated on the *n*-side.[17]

The semiconductor used can be mono- or polycrystalline silicon. Monocrystalline solar cells are made using a single crystal of silicon (Si), produced with high accuracy by the Czochralski process.[18] Although monocrystalline solar modules are more efficient, reaching a record solar-to-power efficiency of 27.3%[19], they are also more expensive because of the higher production costs of the semiconducting material and the complicated production procedures; for this reason, modules based on polycrystalline silicon are the most applied in practice (record efficiency: 24.4%).[19]

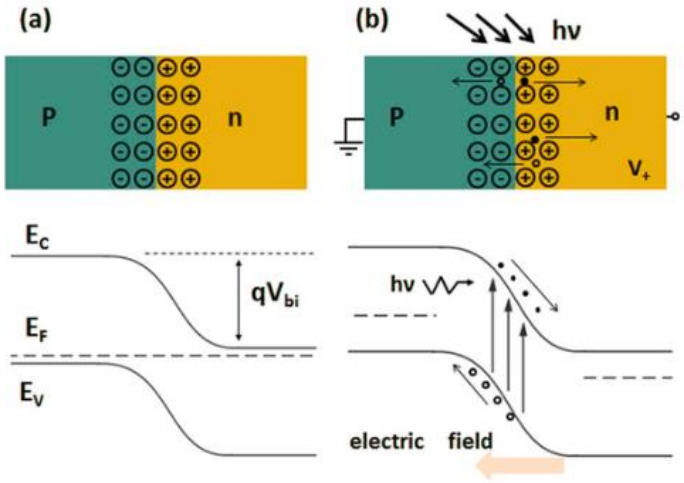

Figure 1.4 Diagram of a p-n junction (a) at the equilibrium and (b) under illumination.[20]

Nowadays, approximately 95% of the total market share of solar cells comes from crystalline silicon materials. The popularity of these devices is based not only on their long lifetime, good efficiency and low installation costs, but also on the fact that the key materials used are abundant, nontoxic and easy to recycle at end-of-life of the cell. Despite the enormous benefits related to the use of this technology, silicon-based solar cells still face several challenges. These include a complex manufacturing process, as well as difficulty in seamless integration into buildings and urban environments due to their thickness, limited flexibility, and less aesthetically pleasing appearance.[21]

1.2.1.2 Second generation: thin film technology

Thin-film solar cells are made by coating thin layers of photovoltaic materials onto a glass, plastic, or metal substrate. These devices are significantly thinner than first-generation crystalline silicon cells, with thicknesses ranging from a few hundred nanometers to several micrometers. Despite their differences in structure, thin-film cells still operate on the principle of a p-n junction, like traditional silicon-based solar cells. Typically, cadmium sulfide (CdS) serves as the *n*-type layer, while various photovoltaic materials are used as the *p*-type, or light-absorbing, side. Depending

on the specific semiconductors paired with CdS, thin-film solar panels are categorized into five distinct types:

i. *Amorphous Silicon (a-Si)*[22] is the most used thin-film solar technology. It stands out for being more environmentally friendly and durable compared to alternatives like CdTe and CIGS (see below). Additionally, it uses significantly less silicon compared to crystalline modules, making its production more economical than conventional silicon-based cells. However, a-Si cells are less efficient, with a peak efficiency of around 14%, [23] which makes them best suited for low-power applications such as consumer electronics.

ii. *Cadmium telluride (CdTe)*[24]*:* due to the band-gap of of 1.45 eV, that fits very well with the energy of solar radiation, CdTe film reached efficiencies comparable with crystalline-Si (22.6% for lab cells,[25] 19% for modules[26]). Despite the competitive efficiencies, CdTe films unfortunately present other significant drawbacks: cadmium is a relatively toxic element, and tellurium supplies are limited.

iii. *Copper indium gallium selenide (CIGS)*[27] have an exceptionally high absorption coefficient, allowing them to be much thinner than other semiconductor materials while maintaining competitive costs and solid performance. Lab-scale CIGS cells have achieved efficiencies of 23.6%,[28] with commercial modules reaching over 19%.[29] However, like CdTe technology, a major downside is the use of toxic and rare elements, such as indium and gallium, which raises environmental concerns due to their scarcity and potential ecological impact.

iv. *Copper zinc tin sulfide (CZTSSe)*[30]*:* this material, also known as kesterite, is an attractive alternative to CIGS since it is composed of less toxic, earth-abundant and low-cost elements. Despite that, the current relatively low efficiencies (13.8%[31]) still prevent a commercial application of this technology.

v. *Gallium Arsenide (GaAs)*[32]*:* the most expensive among thin-film technologies, GaAs holds a world record 27.6%[33] efficiency for all single-junction solar cells. Due to their cost and the scarcity of gallium reserves, these devices are primarily used for technologically advanced applications (e.g. on spacecrafts) or for versatile, mass-scale instalments of PV energy in unusual environments.

Even if flexibility, low weight and attractive look of this technology have led to innovative design and implementation of photovoltaics in buildings (BIPV - building-integrated photovoltaics),[34] as well as in flexible and portable device, the global market diffusion of thin-film cells never reached more than 20% and has declined in recent years.

1.2.1.3 Third generation: emerging photovoltaics

Silicon-based and thin-film solar cells described in the previous paragraphs, are bound by the Shockley-Queisser limit, a thermodynamic principle that establishes the maximum theoretical efficiency for single-junction solar cells. Semiconductors can absorb only photons with energy equal or higher in respect to their own band gap (E_g), so electrons excited by photons with higher energy then relax to the band edges, releasing surplus energy as heat (thermalization loss). For this reason, this limit depends on the proper band gap energy of each photovoltaic material inside the cell and can vary from 31% to 41%.[35]

In contrast, emerging photovoltaic technologies represent a new generation of solar cells which are potentially able to overcome the Shockley-Queisser limit, achieving higher efficiencies and possibly reducing costs. One approach to overcome this limit is through the development of multi-junction cells, which incorporate layers of different photoactive materials. By combining materials with varying band gaps, these cells can absorb a broader range of the solar spectrum.[36] Notably, a four-junction cell made from GaAs and In-based semiconductors has achieved remarkable results, reaching a record solar-to-power conversion efficiency of 47.6%[37] under a photovoltaic concentrator system. However, the high production costs of such cells currently hinder widespread practical application.

Besides multijunction cells, the last two decades hosted the rise of alternative PV cells based on molecular organic systems and hybrid organic-inorganic systems, exploiting different mechanisms to convert solar energy in electric current. Dye Sensitized Solar Cells (DSSC) [38] and Perovskite Solar Cells (PSC) [39] represent the very last frontier in photovoltaic technology.

Dye-sensitized solar cells technology was first reported in 1991 in the seminal paper by Michael Grätzel and Brian O'Regan. [40] The two chemists first introduced a completely new working mechanism, different form the other photovoltaic technologies and inspired, instead, to the natural photosynthesis. In contrast with PVs described so far, where the semiconductor layer acts as both photoreceptor and charge transfer medium, in a so-called "Grätzel's cell" the semiconductor is linked with a fully organic or hybrid metal-organic sensitizer that can absorb photons in the visible region of the solar spectrum and transfer electrons to the it. The basic components of a DSSC are the dye-sensitized semiconductor electrode (or photoanode), the redox mediator (RM) and the counter electrode (or cathode) The photoanode is composed by a conducting glass sheet, like tin oxide doped with fluorine (FTO) or indium-tin oxide (ITO), upon which a few μm thick layer of

a nanocrystalline, wide band gap semiconductor (typically TiO_2) is deposed. The electrode is sensitized towards the harvesting of visible light by adsorption of a monolayer of dye molecules on its surface.

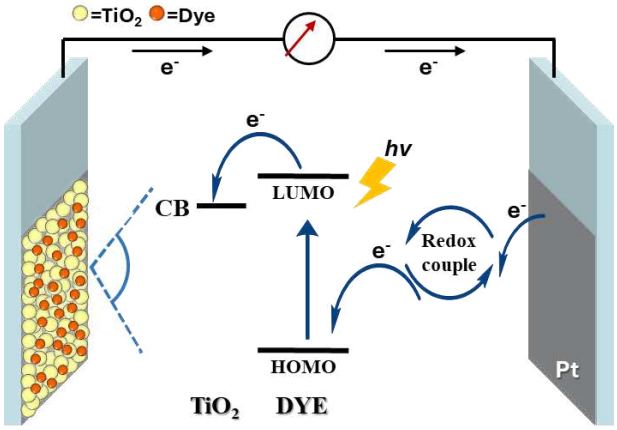

Figure 1.5 Schematic representation of the working mechanism of a DSSC.

The generation of photocurrents in a DSSC occurs through the processes shown in Figure 1.5. When light is absorbed by the dye, an electron is excited to a higher energy level as a result of a transition between an occupied and an unoccupied frontier molecular orbital (FMO). The excited dye "injects" an electron into the conduction band of TiO_2. The resulting oxidized dye is subsequently reduced back to its original neutral state through electron donation from the redox mediator. The injected electron moves through the TiO_2 nanoparticles to arrive at the FTO and then through the external circuit to the counter-electrode; here, the reduction of the redox shuttle occurs. Thus, the cycle is over with production of electric current and without any permanent chemical modification.

DSSC technology offer several exciting advantages over traditional first- and second-generation technologies. One of the most notable benefits is their potential for integration into building structures, including applications in windows and facades.[41] This not only enhances aesthetic appeal but also allows for the effective utilization of otherwise wasted surface area for energy generation. Additionally, the manufacturing processes for DSSC have the potential to be more cost-effective than traditional photovoltaic technologies, which could substantially reduce production costs and facilitate wider adoption. Performance is another strong suit; this technology can operate effectively under non-standard illumination conditions and varying temperatures, making them versatile for diverse environments. Moreover, DSSCs have lower requirements in terms of quantity and quality of raw materials, which could reduce resource depletion and environmental impact compared to conventional solar technologies.[42]

Despite these advantages, the challenge of achieving efficiencies on par with silicon-based devices remains a significant hurdle. The current lower efficiency rates (ca. 15% [43]) limit their commercial viability, preventing them from gaining a foothold in the competitive renewable energy market.

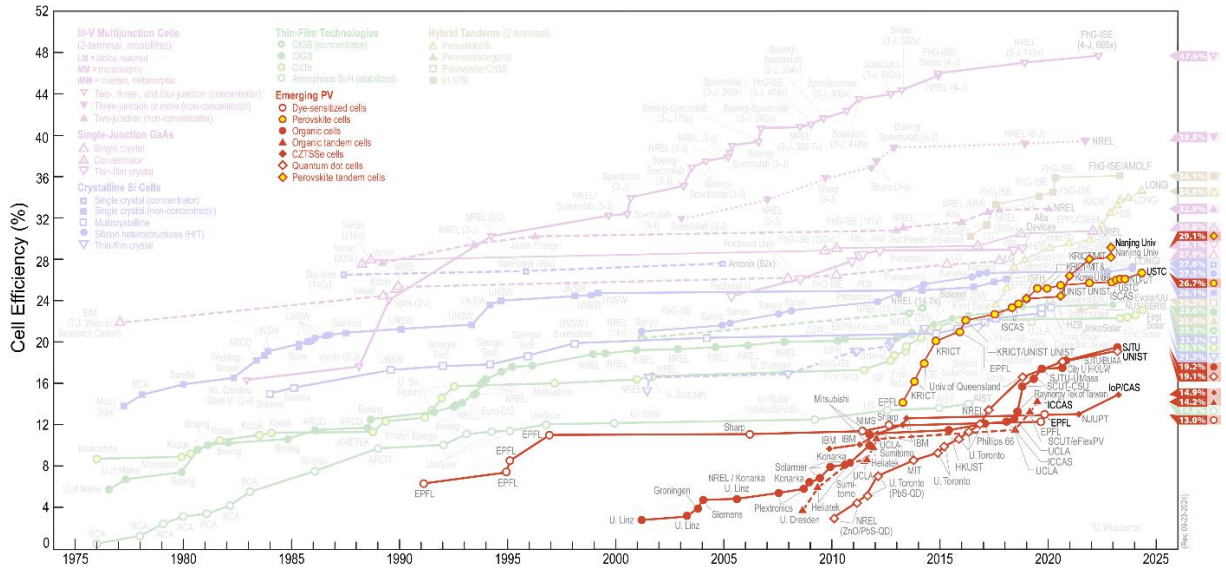

Figure 1.6 Evolution of emerging photovoltaic technology.

More recently, Perovskite solar cells (PSCs) have emerged as a leading candidate for next-generation solar technology, addressing critical energy and environmental challenges. As illustrated in Figure 1.6, their efficiency has impressively surged from 3.8% in 2009 to 26.7% in 2024,[19] showcasing exceedingly rapid advancements in the field. Initially developed as a variation of traditional DSSCs,[44] PSCs utilize mixed organic-inorganic metal halide perovskites—such as methylammonium lead iodide ($MAPbI_3$) and formamidinium lead iodide ($FAPbI_3$)—as light-harvesting materials, which are sandwiched between hole- and electron-conducting layers.

This technology is attractive due to its cost-effectiveness and the relative ease of synthesizing and assembling perovskite materials. However, despite these advantages, the commercialization of perovskite-based solar cells is still hindered by several challenges. The high solubility in water of these materials, while beneficial for device fabrication, makes them sensitive to moisture. Additionally, their crystallinity can deteriorate at the elevated temperatures experienced in solar panels under intense irradiation, leading to a decline in efficiency. Furthermore, the dissolution of perovskite materials generates lead iodide (PbI_2), a carcinogenic compound, raising concerns about environmental safety. Although PSCs have achieved remarkable efficiencies compared to DSSCs, positioning them as the most advanced third-generation photovoltaic technology, doubts about their scalability remain. These concerns primarily arise from their limited stability, challenges in processing, and the presence of toxic materials such Pb.[45] On the other hand, DSSCs continue to present promising opportunities, especially in the rapidly growing area of indoor photovoltaics,

where they can effectively power small electronic devices for Internet of Things (IoT) applications.[46,47]

1.3 Fuels from the Sun

As can be deducted by the previous discussion, in recent decades, solar energy research has predominantly focused on the direct conversion of sunlight into electricity. However, this emphasis overlooks a crucial reality: electricity fulfils only a fraction of our global energy needs. Currently, more than 60% of energy consumption is tied to fuels used in transportation, heating and as raw materials for the production of chemical intermediates. In the field of transportation, despite remarkable advancements in electric vehicle technology, these innovations are not yet capable of fully replacing traditional fossil fuel-fed internal combustion engines, especially for large transportation or industrial vehicles.[48] Therefore, electricity alone cannot achieve a comprehensive transition away from fossil fuels on a large scale. This limitation stems from the significantly lower energy density of batteries compared to chemical fuels, both in terms of weight and volume. Accordingly, it is critically important to develop new technologies to access the production of fuels in a renewable and clean manner to phase out fossil sources.[49] In one approach that meets the requirements of both storage and transportation, solar energy is captured and stored directly in the chemical bonds of a material or 'fuel', and then used when needed. These chemical fuels, in which energy from the sun has deliberately been stored, are called *solar fuels*. Solar fuels can be produced from solar energy by both indirect and direct pathways. Examples of indirect pathways include conversion of biomass to biogas, as well as hydrogen production by electrolysis of water using electricity from photovoltaics. Direct pathways produce the fuel directly in an integrated system, without intermediate energy carriers. Among them, artificial photosynthesis (AP) represents the main approach for the direct conversion of solar energy into chemical fuels[50] and will be discussed in detail in the next paragraphs.

1.3.1 Natural photosynthesis

For billions of years, green plants, algae and photosynthetic bacteria have continuously achieved what the scientific community seeks to replicate. Through the intricate process of photosynthesis, these organisms capture sunlight and convert it into the chemical energy stored in organic molecules, which serve as the fundamental building blocks of all living things, as well as the origin of fossil fuels like oil, gas, and coal. These fossil fuels, formed from ancient photosynthetic activity, now provide most of the energy we rely on to power our technologies, heat our

homes, and manufacture the diverse array of materials that sustains our daily lives.[51] The effectiveness of photosynthesis as an energy-generating and -storing system lies in its use of abundant resources: sunlight, water, and carbon dioxide. Central to this process is the splitting of water molecules by sunlight, resulting in oxygen and hydrogen equivalents. The released oxygen enriches our atmosphere, enabling respiration in living organisms and combustion in our technologies. Meanwhile, the hydrogen equivalents are utilized to convert carbon dioxide into sugars and various organic compounds. When we burn fossil fuels, biomass, or other biofuels, we essentially reverse the process of photosynthesis by combining the stored hydrogen in these organic molecules with atmospheric oxygen, producing water, CO_2, and releasing energy. A similar energy release occurs when we metabolize food through respiration, where our bodies convert oxygen and hydrogen into metabolic energy. Thus, in the biological realm, photosynthesis splits water to produce oxygen and hydrogen, while respiration combines them in a highly efficient manner to generate energy. From an energetic perspective, the synthesis of organic molecules represents a method of storing hydrogen, effectively capturing solar energy in the form of chemical bonds (Figure 1.7).[52]

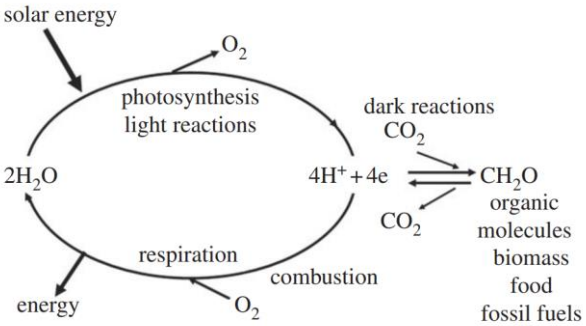

Figure 1.7 A diagrammatic representation of energy flow in biology.[52]

Photosynthesis occurs through the cooperation of photosystem-II, and photosystem-I. Each of these photosystems contains a reaction centre where the main photosynthetic pigment (chlorophyll-*a*) and the accessory pigments (chlorophyll-*b* and carotenoids) are located, the so-called antenna system. The role of the pigments is to absorb light energy, initiating the process to convert it into chemical energy. About 250-400 chlorophyll-*a* molecules constitute a single photosystem. The two different photosystems contain different forms of chlorophyll-*a* in their reaction centres. In photosystem-I, chlorophyll–*a* with maximum absorption at 700 nm (P_{700}) and in photosystem-II, chlorophyll–*b* with peak absorption at 680 nm (P_{680}), act as reaction centres. (P stands for pigment).[53] The whole solar energy conversion system constitutes a so-called "Z-Scheme" (Figure 1.8). In principle, the light absorber (P_{680}) in photosystem-II is excited by photons, creating electron-hole pairs. The excited electron is then transferred to photosystem-I through an electron transfer chain. In photosystem-I, the electron is further excited to a higher energy level by P_{700} and used

for the reduction of $NADP^+$ to NADPH mediated by a specific enzyme called ferredoxin-$NADP^+$ reductase (FNR).

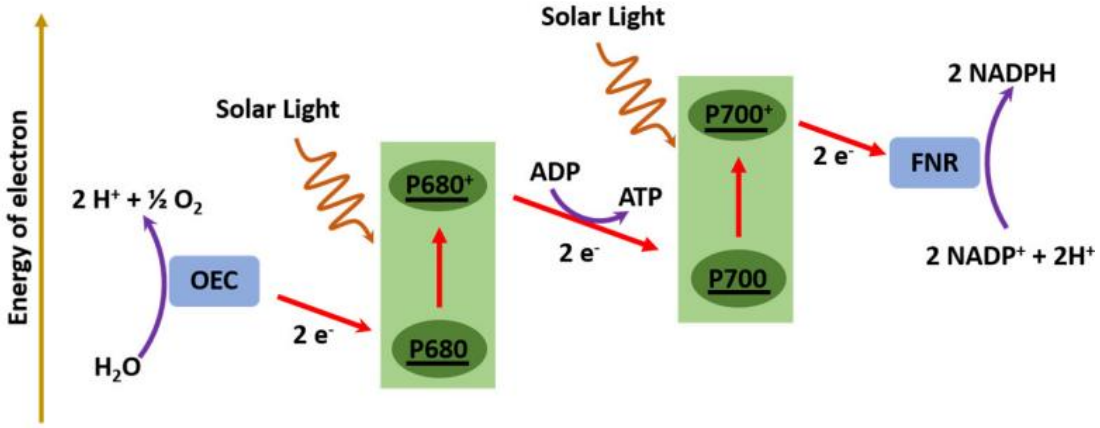

Figure 1.8 Simplified Z-scheme diagram of the natural photosynthesis.[54]

Subsequently, NADPH is used for CO_2 fixation in the Calvin cycle (*i. e.* "dark" cycle, since it does not require light to proceed) to produce carbohydrates and store energy. To accomplish the whole photosynthetic process, the oxidized P_{680}^+ extracts electrons and protons from water by the water oxidation process, which is catalyzed by the oxygen-evolving complex (OEC) in photosystem-II. In other words, the water oxidation reaction (WOR) plays a pivotal role as an electron and proton source in the whole natural photosynthetic machinery.[55]

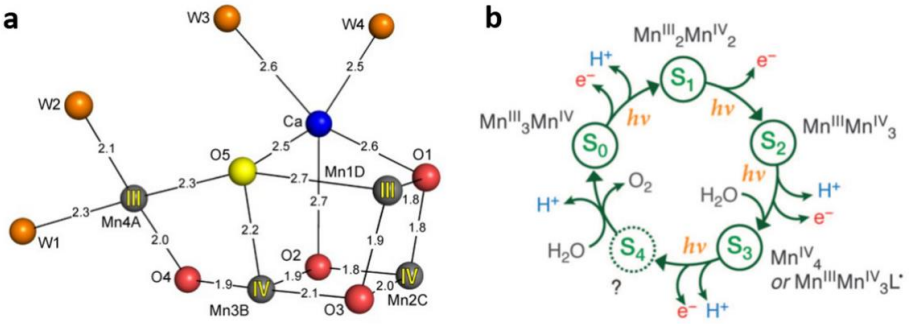

Figure 1.9 a) The structure of OEC in photosystem-*II, adapted from reference 56. Copyright 2015 Nature Publishing Group. b) The catalytic cycle of water oxidation on OEC in* photosystem-*II, adapted from reference 57.*

The catalytically active site for water oxidation in natural OEC has been revealed to consist of a Mn_4CaO_5 cluster (Figure 1.9a), assisted by several protein residues acting as electron and proton shuttles. The Mn_4CaO_5 cluster has a cubane-like structure with three manganese atoms and one calcium atom connected by oxygen atoms. Another manganese atom is situated outside of the cluster and is known as the dangling manganese. The catalytic mechanism of water oxidation in the OEC has been thoroughly studied during the past years but is not yet fully elucidated. It is widely accepted that five redox intermediates (named "S-states") featuring different Mn valence

states are involved in the catalytic cycle (Figure 1.9b). The O-O bond formation has been proposed to take place in the S_4 state, yet the reaction mechanism is still controversial.

1.3.2 Artificial photosynthesis

The idea of using the basic science underlying photosynthesis to obtain solar fuels was already discussed over 100 years ago by an Italian scientist, Giacomo Ciamician, in a famous paper entitled "*The photochemistry of the future*", in which he stated: "Photochemistry will artificially put solar energy to practical uses. To do this, it would be sufficient to be able to imitate the assimilating processes of plants".[58] To mimic the natural photosynthesis process, scientists have developed artificial photosynthesis systems to convert solar energy into chemical energy with man-made materials.[59] Although several different strategies have been investigated for artificial photosynthesis, most commonly the main functional unit is composed of a light harvester, charge separator, and catalysts for oxidation/reduction reactions.

Different types of fuels and high value-added chemicals can be accessed with artificial photosynthesis by driving the corresponding redox reactions,[60] such as hydrogen gas from water splitting,[61] carbon-based organic feedstocks form CO_2 reduction,[62] ammonia production from nitrogen fixation,[63] epoxide production from hydrocarbon oxygenation,[64] and hydrogen peroxide production from oxygen reduction[65] Among all, the water splitting reaction to produce hydrogen fuel is the most investigated reaction in artificial photosynthesis.[66] Notably, due to its remarkable features such as high specific energy, low carbon footprint, and its potential for direct conversion to electricity in fuel cells, hydrogen has emerged as a promising sustainable energy vector to replace fossil fuels.

The water oxidation reaction (equation 1) represents the key step of water splitting reaction (equation 2). However, it is also the bottleneck for the successful development of efficient photocatalytic systems, because it requires a high thermodynamic potential ($\Delta G \approx 237$ kJ mol^{-1} and $E^0 \approx 1.23$ V) and a high overpotential to overcome the kinetic barrier involved in the transfer of $4H^+$ and $4e^-$.[67]

$$2H_2O \rightarrow O_2 + 4H^+ + 4e^- \qquad E^0 \text{ (pH 7)} = +0.82 \text{ V } \textit{vs} \text{ NHE} \qquad (1.1)$$

$$H_2O \rightarrow H_2 + \tfrac{1}{2}O_2 \qquad \Delta G = 1.23 \text{ eV (237 kJ mol}^{-1}\text{)} \qquad (1.2)$$

Therefore, to improve water oxidation efficiency, water oxidation catalysts with lower overpotentials, *i.e.* lower activation energies, are highly demanded.

The photolysis of water was first demonstrated by the pioneering work of Honda and Fujishima in 1972.[68] Since then, tremendous efforts have been made for the development of new technologies for efficient sun-driven water splitting. To date, three different approaches can be

envisaged (Figure 1.10): photovoltaic-electrochemical (PV-EC) systems,[69] photocatalytic (PC) systems,[70] and photoelectrochemical (PEC) systems.[69] While the first of these technologies has been already used in industrialization pilot projects, PC- and PEC-systems are still in the research stage of rapid development.

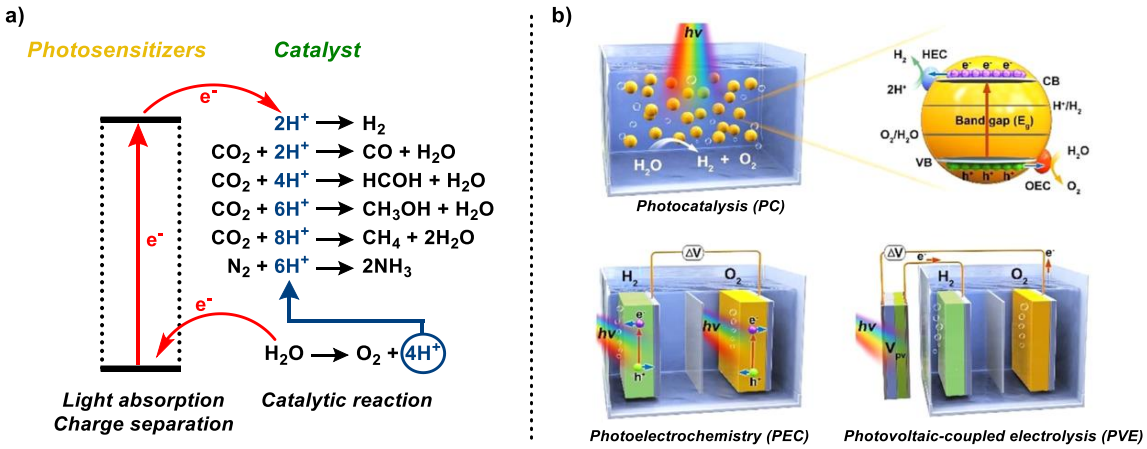

Figure 1.10 a) General concept of artificial photosynthesis;[71] b) Schematic diagrams of commonly studied Photosynthetic systems.[72]

1.3.2.1 Photovoltaic-electrochemical (PV-EC) systems

Photovoltaic–electrochemical (PV–EC) systems seamlessly combine two well-established technologies, such as photovoltaic devices and electrolysers (Figure 1.10, bottom right). In these systems, PV modules absorb photons and generate electron carriers, which are transported to the electrolyser electrodes through an external wire, providing all the electrical energy for the redox chemical reactions occurring at the anode and the cathode. The separation of the light absorption part from the electrochemical reaction offers several advantages: (1) two components, *i.e.*, solar cell and electrolyser, can be investigated and developed separately; (2) light absorber can be protected from the damage of the electrochemical process, conferring excellent stability to these devices in comparison with the photoelectrodes in the PEC system (*see below*). More significantly, PV–EC systems can achieve a high energy conversion efficiency[73–75]. To date, PV–EC systems have reached a remarkable solar to hydrogen (STH) efficiency of over 30% by using one InGaP/GaAs/GaInNAsSb triple-junction solar cell and two polymer electrolyte membrane electrolysers in series.[76]

The development of PV-EC devices for H_2 production from H_2O based on the available technologies represents currently the best possible approach and the solution closer to practical application. However, given their high cost and the huge demand that would follow large scale deployment of

PV-EC systems, the replacement of noble metal-based electrocatalysts must be addressed in order to make this technology really fit for market application.

1.3.2.2 Photocatalytic (PC) systems

The heart of photocatalytic water splitting is the semiconductor (SC). When a semiconductor absorbs photons with higher energies than its band gap energy, electrons in the VB are excited to the CB. As a result, excited electrons and holes are generated in the conduction and valence bands, respectively. The charge separation (e^- in the CB and h^+ in the VB) is then followed by the charge migration from the bulk to the surface where the real water splitting reaction can take place (Figure 1.11a).

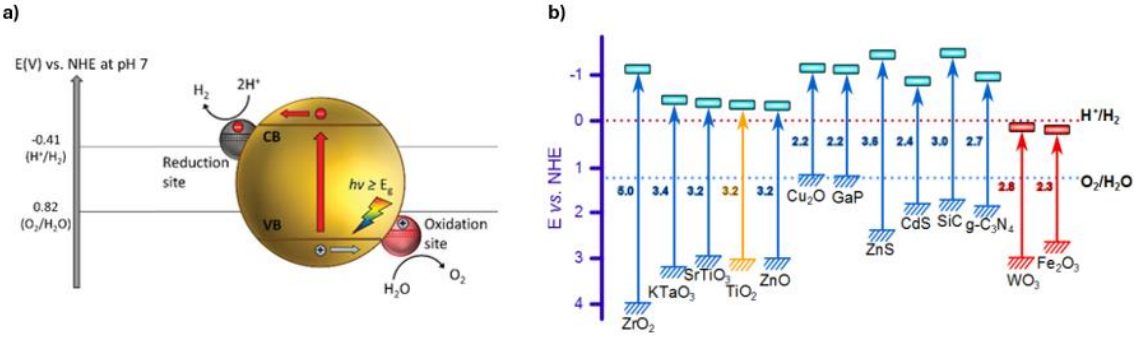

Figure 1.11 a) Schematic illustration of the overall water-splitting reaction on a semiconductor surface;[77] b) Band gap energies and band position of several semiconductors in relation with the redox potentials of water splitting. The position of the CB and VB edges are presented relative to the NHE at pH = 0.[78]

The photogenerated carriers can drive reduction and oxidation reactions if the charge transfers to the reactants are thermodynamically favorable. To achieve photocatalytic water splitting using a single photocatalyst, the band gap of the semiconductor must straddle the reduction and oxidation potentials of water, which are +0.0 and +1.23 V *vs.* normal hydrogen electrode (NHE), respectively, when the reactant solution is at pH 0.[79] Under these conditions the theoretical minimal band gap for water splitting is 1.23 eV, which corresponds to a wavelength of about 1010 nm. Thus, theoretically 70% of solar photons could be employed for water splitting reaction, but in practice, this value rises to 2.0– 2.4 eV, due to kinetic overpotentials and energy losses during the process.[80] In the last decades, thousands of different semiconductors have been tested as photocatalysts for water splitting. Among them, over 130, including oxides, sulfides, nitrides, and hydroxides, have been shown to be able to split water.[81] In terms of quantum efficiency (QE) (defined as the number of photons actually utilized for the target reaction divided by the number of incident photons) the record holder is a $NiO/NaTaO_3$ junction , with a QE of 56%.[82]As can be seen from Figure 1.11b, some semiconductors, such as Fe_2O_3 (E_g = 2.2 eV) and Cu_2O (E_g = 2.2 eV), have sufficiently small

bandgaps, which allow a broader light absorption in the visible region, but their CB and VB are not in the correct position to drive the overall water- splitting process alone. Indeed, the CB of Cu_2O is in the correct position to guide the proton reduction reaction, but its VB is not positive enough to favor the oxidation of water. On the other hand, Fe_2O_3 has a VB positive enough to perform the oxidation of water, but a CB which is not negative enough. Consequently, these materials can only be used for one of the half- reactions: photo- driven water oxidation or hydrogen evolution. In an alternative approach to the single photocatalyst system, it is possible to connect these two SC with a redox couple (IO_3^-/I^-, Fe^{2+}/Fe^{3+}, etc.) to obtain a tandem configuration, quite similar to the Z-scheme of the photosystem-I and photosystem-II (Figure 1.12). However, in this case, the energy of two photons is required to generate the electron/hole couple on both SCs, thus the efficiency of the charge separation reaction drops to 50%.[83]

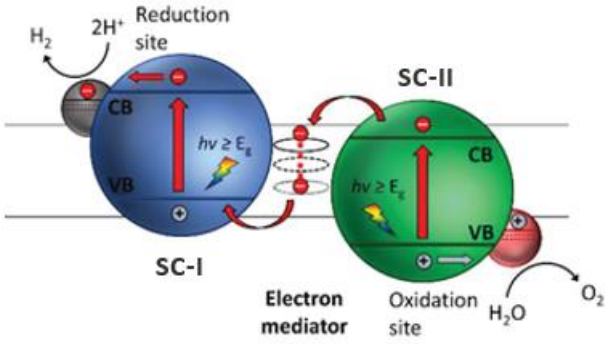

Figure 1.12 A Z-scheme tandem configuration composed of two SCs connected through a redox couple.[84]

Among all tested SCs for water splitting, either alone or combined with other materials, TiO_2 is still considered the most promising material for hydrogen generation because it is photostable, environmentally friendly, cheap, and readily available. Despite that, still several drawbacks are associated with the use of TiO_2:

- TiO_2 has a large overpotential as water splitting catalyst, thus reaction on pure TiO_2 proceeds very slowly and with low yields.[85]
- Rapid electron/hole recombination takes place on TiO_2: studies found that 90% of the photogenerated charges are bound to recombine.[86]
- Thermal back reaction between H_2 and O_2 to give H_2O is highly favoured.[87]
- TiO_2 is unable of absorbing visible light, only UV can be used so that only a narrow part of the solar spectrum can be harvested (UV covers 4-5% of the solar spectrum, while visible photons, $400\ nm < \lambda < 700\ nm$, compose approx. 50% of it).[88]

Many modifications have been developed to enhance TiO_2 activity and solve or limit its drawbacks.[89] These include: the loading of nanoparticulate cocatalysts that significantly lower the reaction overpotential, suppress the recombination of e^- and h^+ and increase activity (Pt and Rh are

the most used for reduction and oxidation reaction, respectively);[90–92] and surface sensitization with small bandgap semiconductors,[93,94] noble metal nanoparticles[95,96] and dyes.[97–100]

1.3.2.3 Photoelectrochemical (PEC) systems

Photoelectrochemical (PEC) cells represent an alternative approach to mimic the first step of natural photosynthesis, namely solar-driven water splitting.[101] PEC cells convert solar energy into storable chemical energy through PEC processes that combine light harvesting and water electrolysis in a single device. In addition to chemical energy, electricity is produced simultaneously. A typical PEC cell for water splitting consists of two electrodes, an anode and a cathode, connected through an external circuit and immersed in two different half-cells filled with an aqueous medium. To collect solar radiation, the anode and cathode are made by *n*- or *p*- type SC, respectively, and are called photoelectrodes.[102] Depending on the type of photoactive electrode(s) used, a photoelectrochemical (PEC) cell can be configured in three main classes: PECs with a photoanode (PA) and a passive cathode, PECs with a photocathode (PC) and a passive anode, or PECs with a photoanode and a photocathode (Figure 1.13). The last configuration, known as a tandem PEC, is the most promising because it enables the collection of a broader range of the solar spectrum, closely resembling the process of natural photosynthesis.[103]

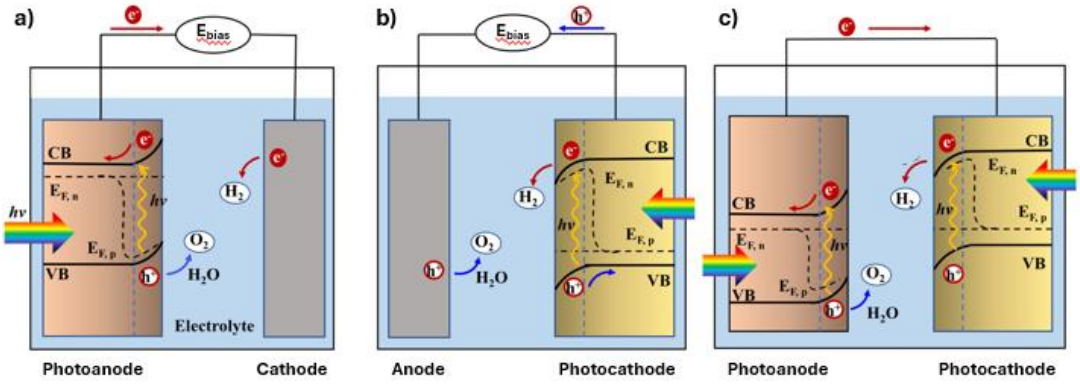

Figure 1.13 Configurations of PEC for water splitting and operating principle under illumination. a) PEC with photoanode and a passive cathode; b) PEC with a photocathode and a passive anode; c) tandem PEC with a photoanode and a photocathode. [104]

Among multiple device architectures, a remarkably simple approach was reported by Honda and Fujishima in 1972, which demonstrated the feasibility of PECs for water splitting under ultraviolet (UV) irradiation. This device employed a *n*-type TiO_2 (anatase, E_g = 3.2 eV, λ_{abs} < 390 nm) photoanode coupled with a platinum (Pt) cathode, and was able to drive water splitting by means of the fundamental mechanism of operation shown in Figure 1.14.

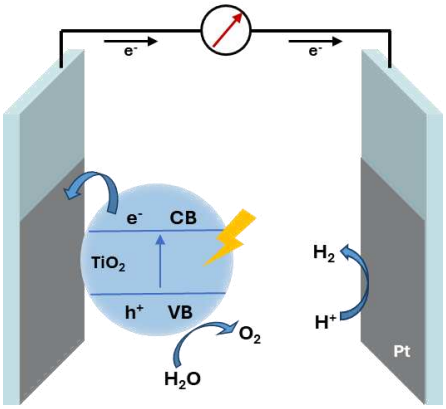

Figure 1.14 Honda-Fujishima photoelectrochemical cell with TiO_2 as photoanode.

Water splitting into H_2 and O_2 occurred in acidic solution with a small applied bias following UV excitation of TiO_2 and charge separation. The photogenerated holes (h^+) in the VB of TiO_2 nanoparticles oxidize water at the surface. Meanwhile, free conduction-band electrons migrated to the cathode for H^+ reduction to H_2. Even if this device achieved a low efficiency, it laid the basis for future developments and studies in this direction. Since then, significant progress has been made on developing new photoelectrode materials and improving the solar water splitting performances. Some examples of tandem PECs for water splitting made by pure SCs have also been reported. The most used SCs in these types of PECs are metal oxides and oxynitrides for the photoanode, like WO_3, Fe_2O_3, TaON, $LaTiO_2N$ and *p*- type chalcogenides and metal oxides for the photocathode, like CdTe, $CuIn_{1-x}Ga_xSe_2$, *p*- Cu_2O_4. However, their efficiency is still below the threshold for commercial application.[105–112]

As already discussed for PC systems, one dilemma commonly occurring in the research of SC photocatalysts or photoelectrodes is that it is intrinsically difficult to develop an oxide SC that possesses both a sufficiently narrow band gap to absorb visible light and suitable energy levels to drive both WS catalytic reactions simultaneously, thus resulting in either poor absorption characteristic or use of additional undesirable external bias. Moreover, it is also intrinsically difficult to fine tune the band levels of these inorganic materials.[113] An innovative approach for PEC cells, that addresses these problems, involves a hybrid design where semiconductor materials with large band gaps are sensitized with dyes and paired with a water oxidation catalyst (WOC) and/or a hydrogen evolution catalyst (HEC). The addition of dyes enhances the film light-harvesting capability, while catalysts accelerate the water-splitting reactions. This approach defines dye-sensitized photoelectrochemical cells (DSPECs).[114]

1.4 Dye-sensitized photoelectrochemical cells (DSPECs)

1.4.1 From DSSCs to DSPECs

The concept of a DSPEC has evolved from the dye-sensitized solar cell (DSSC), and as can be seen from the schematic representations shown in Figure 1.15, the fundamental structure of a DS-PEC is closely related to that of a DSSC. Indeed, the electron transfer processes listed below are analogous in the two devices:[115]

(1) Upon absorption of visible light, the sensitizer undergoes a photoexcitation process, promoting an electron from its highest occupied molecular orbital (HOMO) to the lowest unoccupied molecular orbital (LUMO).

(2) The excited dye "injects" an electron into the CB of TiO_2.

(3) The injected electrons migrate through the bulk of nanocrystalline TiO_2 film, FTO conducting layer and external wires to the counter electrode, producing current.

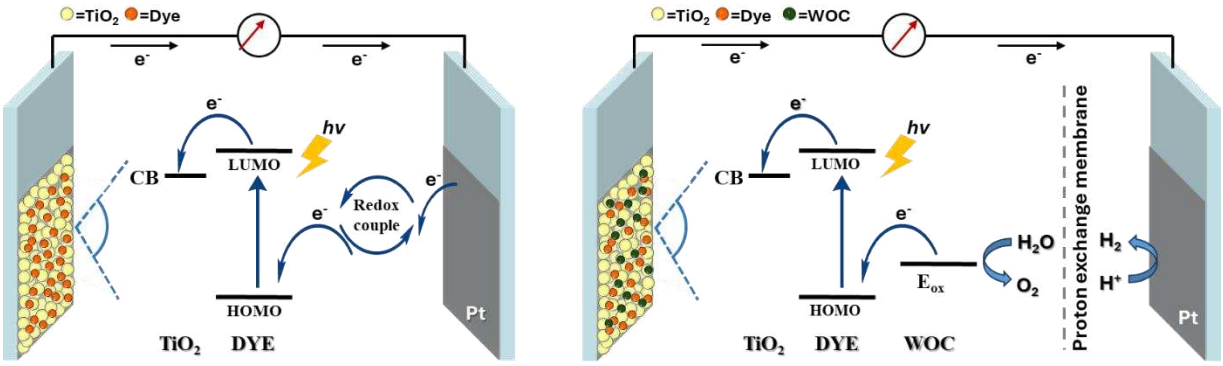

Figure 1.15 The architecture of n-type DSSCs (left) and n-type DSPECs (right).

The main differences between the two PEC devices are related to the regeneration of the dyes attached on TiO_2 film.[116] As previously discussed, in DSSCs the oxidized dye is regenerated by the redox mediator (RM) in the electrolyte. The oxidized form of the redox mediator diffuses to the counter electrode where it receives electrons to close the whole circuit. In DSPECs based on *n*-type semiconductors, water oxidation catalysts (WOCs) are coupled to the dye molecules to regenerate the ground state dye instead of using redox mediators in electrolytes.[117] Subsequently, water molecules are oxidized to oxygen by the catalyst at photoanodes. The photogenerated electrons that transfer to the counter electrode are used to generate hydrogen to complete overall water splitting. DSPECs based on *p*-type semiconductors are also developed.[118,119] Compared to *p*-type DSSCs, hydrogen evolving catalysts (HECs) are used as electron acceptors to regenerate dye molecules in DSPECs rather than redox mediators in electrolyte, and then water reducing reaction

occurs at the site of HECs. On the other side, water molecules are oxidized to form oxygen at the anode.

Compared to DSSCs, DSPECs show a lower quantum yield of the process, typically 1-2%. In DSSCs, photogenerated electrons can inject into the TiO_2 CB on a sub-picosecond timescale with a high quantum yield. Then the oxidized dye can be regenerated by the redox mediator on the nanosecond timescale, which is faster than back electron transfer from TiO_2 to the oxidized dye or redox mediator in the electrolyte (micro- to milliseconds). In DSPECs, the process of catalytic water oxidation typically takes place on the millisecond timescale because of the weak driving force for the reaction. As already mentioned, water oxidation is a four-electron, multiatomic, thermodynamic energy-demanding, and kinetically hampered process with a high activation barrier. Therefore, the catalytic site needs time to accumulate four holes to oxidize water, while the charge recombination reactions occur on a sub-millisecond time scale. [105,117]

1.4.2 Working mechanism of tandem DS-PEC

Among all possible configurations, tandem DSPECs, [120] constructed with both a PA and a PC, represents the most attractive cell-type, since it is the closest to natural photosynthesis and can absorb two photons and thus transfer two electrons at one time.

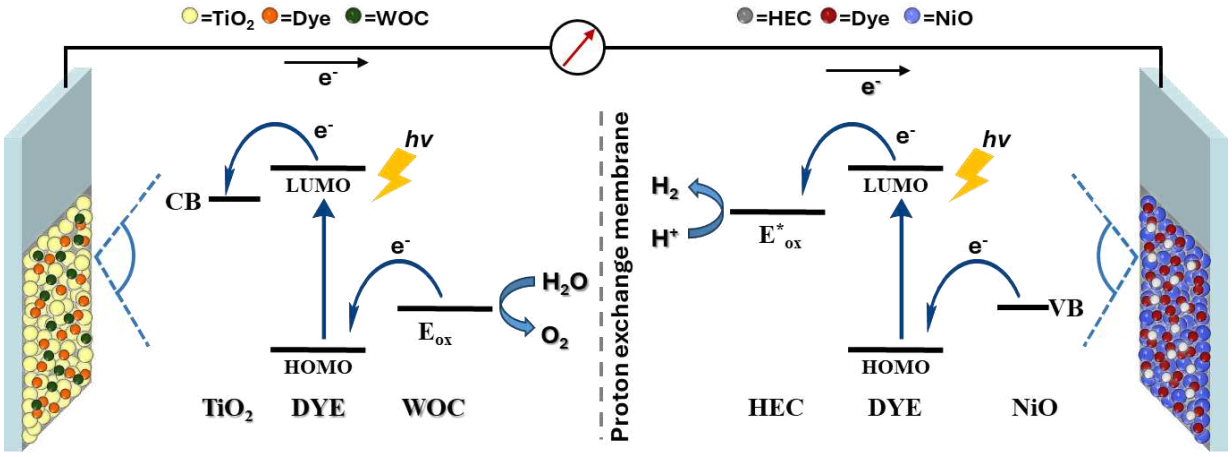

Figure 1.16 The schematic diagram of tandem DSPECs.

Moreover, compared to single-photoelectrode-based DSPECs which usually cannot provide sufficient photogenerated potential for water splitting and need the assistance of an external electrical bias, tandem DS-PEC can perform unassisted water splitting process. Furthermore, the two different photoelectrodes can maximize solar energy utilization due to their complementary absorption spectra, thus improving the theoretical maximum energy conversion efficiency of the whole system. [121,122] The schematic representation of a tandem DSPEC is shown in Figure 1.16.

Concerning the working mechanism, in a tandem cell the electron transfer processes of each half-cell occur simultaneously. On the photoanode side, excitation of the dye occurs when the incident photon possesses energy (hv) that surpasses the optical band gap of photosensitizer (PS), resulting in the formation of the excited state of PS (PS^*). Then, the photo-generated electrons are injected into the bottom of CB of *n*-SC in one cycle and are transported to the counter electrode through an external circuit to accomplish the reduction of protons and the production of H_2. The resulting oxidized PS species (PS^+) is reduced by WOC that donates an electron to regenerate a neutral PS in one cycle, raising its oxidation state (WOC^{1st+}). Four cycles of forward electron transfer lead to a fully oxidized WOC that can drive water oxidation reaction.[103,123] Meanwhile, at the photocathode photons with sufficient energy induce the formation of PS*. Then, two charge transfer processes, depending on the dye species, have been proposed:

(i) The reduction of HEC is preceded by a thermodynamic hole injection from PS* into p-SC (reductive quenching): a hole from PS* injects into the top of VB of *p*-SC, forming the reduced state of PS (PS^-) and then initiating the first reduction of HEC (HEC^{1st-}). Then PS^- transfers one electron to HEC, regenerating one PS per cycle.

(ii) HEC directly accepts electrons from PS* and hole injection then occurs between PS^+ and *p*-SC (oxidative quenching): one electron from PS^* directly moves to HEC to form HEC^{1st-}, then one electron travels from the *p*-type's top of VB to PS^+, regenerating one PS per cycle.

Nevertheless, proton reduction driven by the fully reduced HEC is finally achieved after two cycles of forward electron transfer processes.[124]

For all the types of DSPECs described above, five basic elements are required to construct an assembled device, including semiconductor, photosensitizer, water oxidation catalyst and/or hydrogen evolution catalyst, counter electrodes, and electrolytes. Every individual component has a unique function and adds to the overall performance of the device, which will be explained thoroughly in the next sections.

1.4.3 Component materials

1.4.3.1 Semiconductors (SC)

In the construction of a DSPEC device, a proper SC should be stable when irradiated under long-term illumination and immersed in electrolytes over a wide pH range. Meanwhile, as discussed above, the potential of CB/ VB should be suitable for photoinduced electron/hole injection from the exited photosensitizer. In addition, the surface roughness and area of SC are also im-

portant, which mainly affects the number of absorbed dyes on its surface. Therefore, porous nanocrystalline SC films with remarkable surface areas are widely used as substrates for DSPECs.[124,125] In PA-DSPEC, many *n*-type SCs have been exploited, such as TiO_2,[126–128] SnO_2, [129] and WO_3.[130] Among them, TiO_2 is once again the most extensively studied material due to its superior stability in aqueous solutions, facile synthesis and low toxicity.[131] In PC-DSPEC, the ability to quench holes on the sensitizer is an important property for a suitable SC candidate. The most common *p*-SC used for PC-DSPEC cathodes is NiO.[117] NiO is a mixed-valence SC consisting of Ni^{2+} and Ni^{3+} states. It has a quite wide bandgap (about 3.6-4 eV); thus it cannot compete with the dye for light absorption. It has good thermal and chemical stability, and it is easily synthesized in the form of nano particles at reasonably low temperatures. The potential of the NiO VB is 0.47 V *vs*. NHE at pH 7, which makes it a good electron donor for many sensitizers. Unfortunately, a critical drawback for NiO is its low carrier mobility, which leads to fast charge recombination. According to recent studies, the hole diffusion coefficient of NiO is approximately 10^{-8} to 10^{-7} cm^2 /s, which is at least a hundred times lower than the electron diffusion coefficient of TiO_2.[117] Therefore, several research groups have attempted exploring viable alternatives, reporting on the use of $CuGaO_2$,[132–134] $CuAlO_2$,[135,136] and *p*-Si[137,138] as *p*-SC, respectively.

1.4.3.2 Photosensitizer (PS)

The sensitization of the surface plays a central role since, as it emerges from the previous discussion, the dye is involved in some of the most crucial steps of the working mechanism of DSPEC, namely light harvesting and charge separation. In general, the following properties are of great importance to identify a high-performance PS in DSPECs:

1. Broad light absorption covering most of the visible light spectrum and even extending into the near-infrared (near-IR) region, and high molar extinction coefficients that can guarantee sufficient light-harvesting ability even at low dye loading conditions.
2. Appropriate LUMO level matched to the CB of *n*-type SCs (in the PA) or the reduction potential of HERs (in the PC) to ensure sufficient thermodynamic driving force for electron transfer.
3. Appropriate HOMO level matched to the VB of p-type SCs (In the PC) or the oxidation potential of WOCs (in the PA) to ensure fast hole transport.
4. High photophysical, photochemical, and electrochemical stability to avoid unwanted degradation in multiple working cycles.
5. Favorable spatial configuration to prevent intermolecular aggregation and reduce energy loss due to self-quenching.

6. Proper aqueous solution adaptability to ensure favorable reaction processes.
7. Strong and permanent linkage to the semiconductor, obtained thanks to one, or more, anchoring groups, which should also be able to promote charge injections, minimizing interfacial charge-transfer resistance.

For what concern the last point, a variety of anchoring groups have been developed, including catecholates (**a**),[139] carboxylates (**b**,**c**),[140,141] phosphonates (**d**),[126,142,143] silatranes (**e**,**f**),[125] hydroxamates (**g**)[144,145] and pyridynes (**h**)[146] (Figure 1.17).

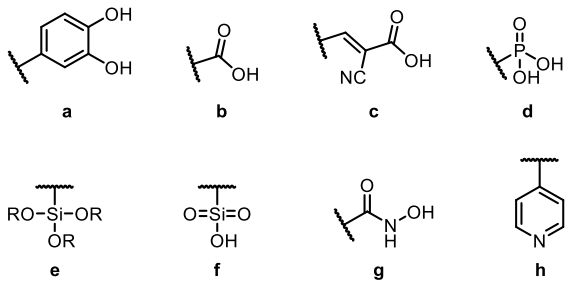

Figure 1.17 E*xamples of anchoring and/or acceptor groups of PS for DSPEC.*

Among them, carboxylic and cyanoacrylic acid are the most used anchoring groups for organic dyes, mainly due to their relatively easy synthesis and rapid electron injection rate. In particular, cyanoacrylic acid conjugates the electron-withdrawing properties of the cyano group with the binding properties of the carboxylic moiety which is responsible for anchoring the dye to TiO_2 thanks to formation of a titanate ester linkage. However, their stability in acidic aqueous solutions (pH < 4) is only moderate, and at elevated pH levels, hydrolysis takes place quickly, resulting in dye desorption. On the other hand, due to their ability to resist oxidation and maintain stability in acidic, neutral, and basic conditions, phosphonic and hydroxamic acids exhibit a promising potential for application.[146] In recent years, pyridyl group has become a rising alternative due to its water- and alkali-resistance property. In this case, the bond formed between a pyridyl anchoring group and TiO_2 is typically a coordination bond. This interaction is favored due to the strong electron-donating ability of the pyridyl nitrogen and the high affinity of titanium for such ligands, creating a stable N-Ti bond. In 2017, Ozawa *et al.*[147] reported the first Ru-based photosensitizer with pyridyl anchor groups, which gave better performance than the photosensitizers with carboxyl and phosphate groups in the H_2 evolution experiment.

Besides their anchoring groups, DSPEC sensitizers can be classified into several categories, based on their structure or their relevant photo- and electrochemical properties. In terms of structure, the two most common categories are metal coordination complexes and fully organic dyes, whose main features are described below.

Metal coordination complexes

Historically, transition metal-based complexes have been the first class of sensitizers ever employed in DSPEC. Especially, ruthenium (II) *tris*-bipyridine complexes (the parent compound being $[Ru(bpy)_3]^{2+}$) have been extensively investigated over the last decade as light absorbers due to their long-lived excited state lifetimes (ca. 600 ns), high absorptivity in the visible region with $\lambda >$ 450 nm, owing to the metal-to-ligand charge transfer (MLCT) process, and a high ground-state oxidation potential (ca. 1.26 V vs NHE). Furthermore, MLCT states can be altered systematically by modifying the substitution pattern of the polypyridyl ligand. The wide possibilities to tune the MLCT energy has led to the preparation of many different compounds that have been investigated for semiconductor sensitization.[147,148]

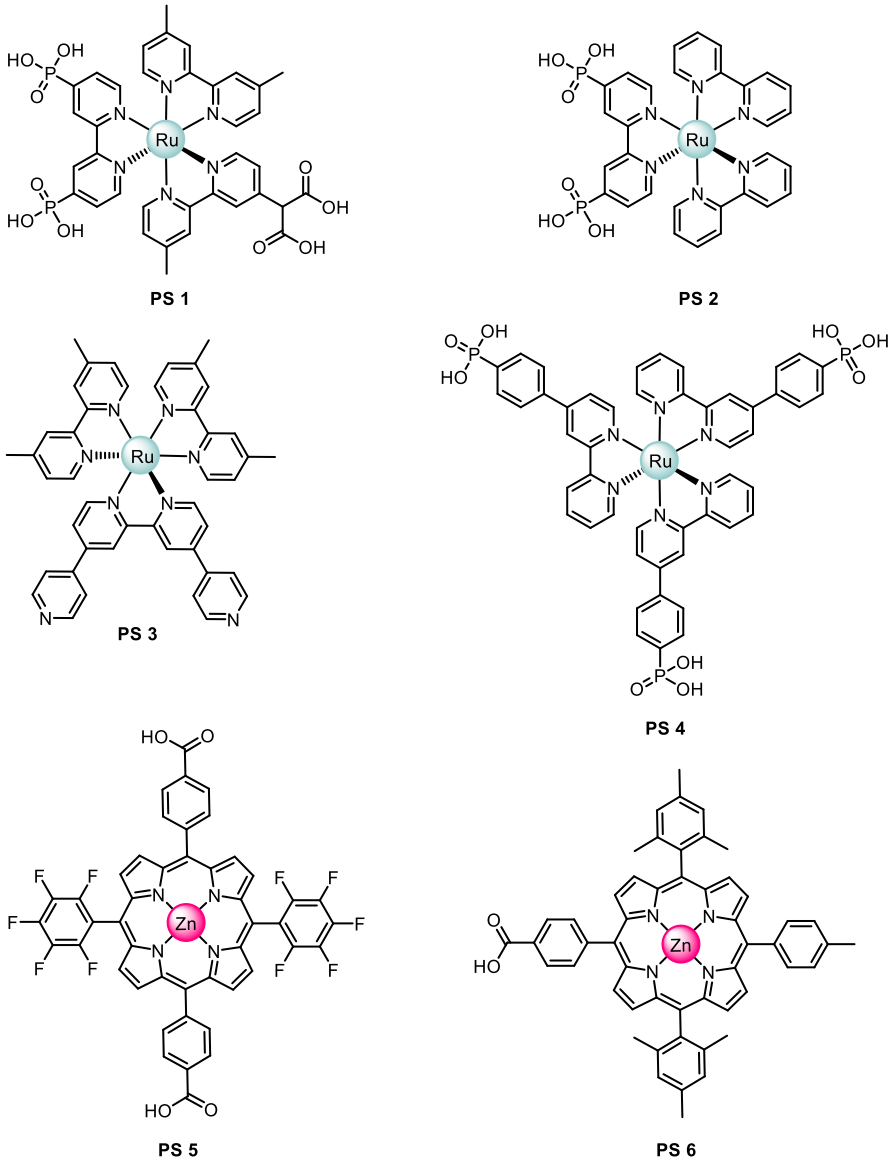

Figure 1.18 Examples of Ru- and Zn- based photosensitizers reported in literature.

The first example of a ruthenium-polypyridine complex (**PS1,** Figure 1.18) was published by Mallouk et al. in 2009.[149] This sensitizer is characterized by two phosphonic anchoring groups for

the SC and a malonic acid group for binding hydrated iridium oxide nanoparticles (that acted as WOC in that system). Since then, these classes of compounds have dominated early DS-PEC investigations (see, for example, **PS2-PS4** in Figure 1.18),[150–152]. However, the high cost of ruthenium and the instability of its related complexes in oxygen rich environments for water oxidation poses serious limits to it possible larger scale employment.[153]

Alternatively, a few examples have been reported in the literature in which organometallic dyes made with abundant metals, such as zinc porphyrins, were applied as sensitizers for either the photoanode or photocathode (**PS5**[140] and **PS6**[154], respectively). Zinc porphyrins show very intense absorption bands in the visible region of the solar spectrum and give efficient electron injection in the conduction band of TiO_2. Despite remarkable activities, this class of compounds often requires a complex synthetic pathway, characterized by difficult purification and low yields, hampering their practical use.

Metal-free organic dyes

Presently, there is increasing scientific attention concerning the development of metal-free dyes for utilization in DSPECs. These compounds have attracted much interest as potential alternatives to metal-based sensitizers thanks to their lower production costs and absence of critical or precious metals. Furthermore, their molar extinction coefficients are usually higher and their photophysical and electrochemical properties can be easily tuned by fine optimization of the structure. Despite these advantages, when compared to DSSCs, where the use of metal-free organic sensitizer has been the subject of countless studies,[155] the use of metal-free dyes in DS-PECs has remained less developed.[114] To date, three classes of organic sensitizers have been reported in DS-PEC: metal-free porphyrins, perylene derivatives, and donor–acceptor (or push-pull) D-π-A molecules.

Metal-free porphyrins are characterized by a strong Soret band absorption in the blue region of the visible spectrum and weaker Q bands at longer wavelengths. This allows them to efficiently overlap with visible solar radiation. Additionally, their conjugated macrocylcic structure provides good photochemical and electrochemical stability. Furthermore, their redox properties can be adjusted through synthetic modification of the periphery, making them ideal candidates for DSPECs. However, porphyrin-sensitized photoanodes exhibit lower photocurrents compared to their ruthenium-complex counterparts, mainly due to a lower injection rate. Nonetheless, their ability to utilize red photons for water splitting has heightened interest in this category of dyes and several groups have investigated their use mainly for photoanode sensitization (**PS7**[156] and **PS8**[157]**,** Figure 1.19).

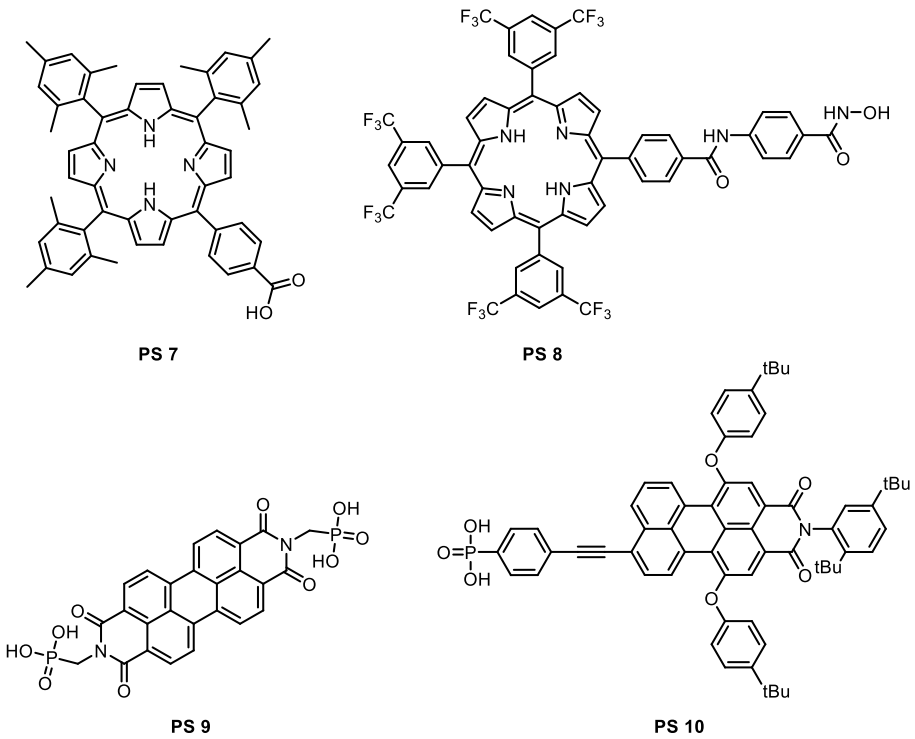

Figure 1.19 Examples of porphyrins and perylene dyes reported in literature.

Perylene dyes are known for their strong absorption in the visible region, high molar extinction coefficients and relatively easy modification. Twelve positions are available for functionalization in perylene cores, giving rise to a potentially very large number of derivatives. Among them, extensive studies have been devoted to the synthesis and development of perylene imide derivatives,[158] including perylene diimides (PDI) and perylene monoimides (PMI), for DSPEC application. PDIs exhibit superior thermal and oxidative stability in water and air,[159] while PMIs exhibit a stronger reducing ability than PDIs, so they have been reported to have more success for electron injection into TiO_2.[160] In these compounds, the nitrogen atom can be easily modified to insert anchor groups (**PS9**[161], Figure 1.19) or to increase the steric hindrance (**PS10** [162], Figure 1.18) of the molecules, since these compounds suffer from strong π-π stacking aggregation. This functionalization is also important to obtain a long-lived charge separation state to avoid the back electron transfer from the SC.

Currently, several reports dealing with the use of organic sensitizers for DS-PEC describe the application of electron push-pull dyes, which contain electron-donating and withdrawing moieties that form dipolar molecules: the so-called donor (D)–acceptor (A) dyes. Such approach relies on the use of building blocks that have little or no visible light absorption themselves, but when combined can generate broadly absorbing dyes due to intramolecular charge transfer (ICT) [155] events, in which a significant transfer of electron density is observed upon the transition between ground- and excited state. Usually, a conjugated π-bridge is inserted between donor and acceptor fragments

to generate D-π-A systems, allowing to increase or decrease the conjugation lengths and thus to adjust the optical energy gaps. As mentioned above, in a D-π-A dye, light absorption is usually due to an intramolecular charge transfer process (ICT) from the donor unit, where the HOMO is mostly localized, to the acceptor group, where the LUMO is usually located. Subsequently, electrons are injected from the LUMO of the dye to the conduction band of TiO_2, where the acceptor, which has also the role of anchoring group, is directly bound. The conjugated spacer (π) ensures the electron flow and, at the same time, separates the donor part from the acceptor one and, consequently, from the TiO_2 surface, reducing losses due to charge recombination. Furthermore, the insertion of a conjugated spacer (π) can reduce the energy difference between the HOMO and LUMO levels, also called optical bandgap, shifting the absorption band towards longer wavelengths and making the transition more intense. However, the narrowed band gap is likely to lead to a higher HOMO and lower LUMO level, which will weaken the oxidation and reduction capabilities of the dyes. Balancing those opposing requirements represents the major challenge of design strategies for efficient DSPEC sensitizers.

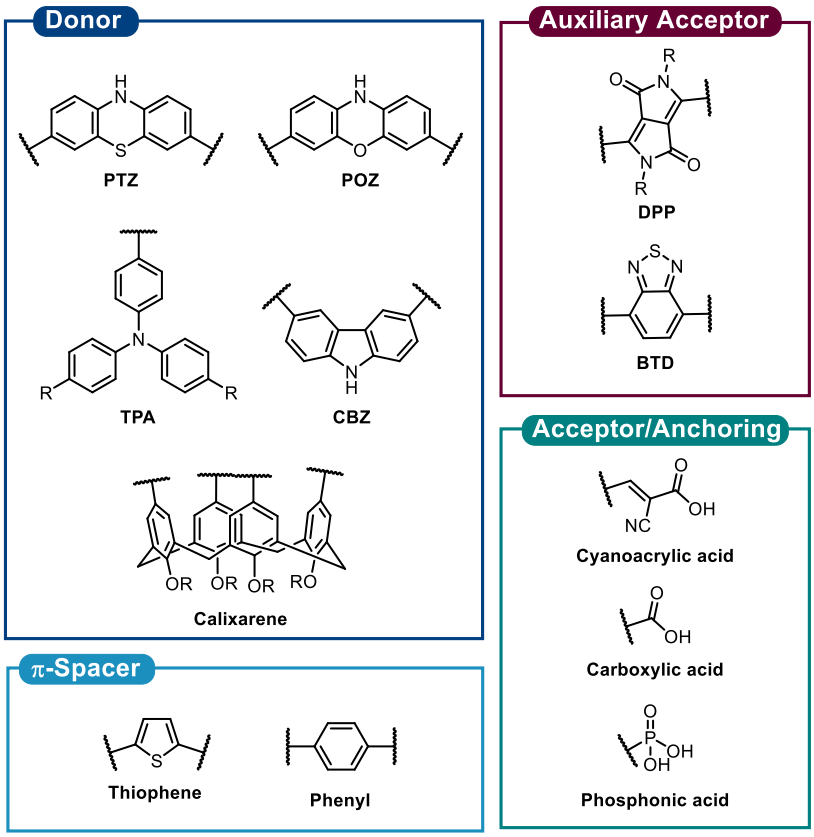

Figure 1.20 Examples of donor groups (D), π-spacer *and acceptors (A) moieties in organic D-π-A sensitizers.*

Up until now, D-π-A dyes have been widely investigated in DSSCs, and the results of these studies have represented the starting points for the design of PS for DSPECs, that strongly depends on the kind of electrode they will be applied to. In the photoanode case, the acceptor group is the closest

part to the SC and brings the anchor functionality. It should help the charge separation that takes place after the solar-driven excitation, injecting the electrons into the SC. At the same time, the donor group facilitates the electron transfer to the acceptor, stabilizing the generated hole. Hence, the donor moiety should be the most peripheral part and interact with the aqueous medium. The opposite discussion applies to D-π-A dyes designed for photocathodes.

Regarding the donor group, variations of several electron-donating moieties have been investigated as promising candidates, including phenothiazine (PTZ),[163] phenoxazine (POZ),[164] carbazole (CBZ),[164,165] and stereoscopic cone-shaped calixarene[166] (Figure 1.20).

However, triphenylamine (TPA) with various substituents in the terminal 4 and 4' positions, has been the most widely used unit because of its strong electron-donating ability coupled with good hole transport properties.[167–169] Additionally, due to its non-planar structure, TPA effectively inhibits aggregation. For the π-spacer, thiophene and benzene have been widely used and extensively studied. [117] Furthermore, introduction of auxiliary acceptors such as diketopyrrolopyrrole (DPP)[170] and benzothiadiazole (BTD)[171] in the conjugated scaffold has been explored, leading to a more complex D-A-π-A framework. In such structure, the additional acceptor unit acts as an electron trap to separate charges and facilitate migration to the final acceptor; moreover, it enhances long term stability thanks to a general lowering of molecular energy levels, while the downshift of the LUMO energy level also means a more intense light absorption in the near-IR region of the spectrum. In terms of electron acceptors, carboxylic acid, cyanoacrylic acid and phosphonic acid with strong electron withdrawing effects are the most common anchoring groups, as mentioned above.[172]

1.4.3.3 Water oxidation catalyst (WOC)

As discussed previously, the presence of both anodic and cathodic overpotentials further slows down the water splitting process. Hence, in PA-DSPEC, the catalyst is necessary to lower the water oxidation energy barrier and speed up the reaction. In order to have efficient charge transfer, the WOC must have an oxidation potential less positive than the ground-state oxidation potential of the dye to ensure the regeneration of the oxidized photosensitizer. Two different classes of water oxidation catalysts have been reported to date: metal oxide nanoparticles and molecular catalysts. For what concerns the first class, several reports have been focused on iridium oxide or cobalt oxide.[149,161,173] However, despite the higher stability shown by this type of WOCs, they suffer from slow electron transfer kinetics between the oxidized PS and the WOC, causing fast kinetics of back electron transfer which reduces the efficiency of the device. To overcome these problems, different approaches have been investigated such as the possibility of adding a thin layer

of TiO_2 over the dye-sensitized SC and /or establish a basic environment near the electrode, since the free protons generated by the water oxidation combine with the electrons in the SC causing a drastic drop in the efficiency. Furthermore, low overpotential metal oxides, like $NiFeO_x$[174] or $CoFeO_x$,[175] have been tested aiming to speed up the kinetics of the charge transfer between oxidized dye and WOC.

On the other hand, molecular catalysts, despite having an inferior durability, show several advantages such as:(i) known molecular structures with clearly identified catalytic active sites; (ii) possibility of fine tuning of both steric configuration and electronic structure by adjustment of the specific coordination environment through ligand design and (iii) high product selectivity. In general, molecular WOCs are redox-active transition-metal-based complexes (typically Ru, Ir and Mn) [71] with unsaturated first coordination spheres, which function as active sites for the substrate water molecule.[176] To catalyse water oxidation, a catalyst must allow the accumulation of multiple charges to form a high-valent metal–oxo intermediate. As can be seen from Figure 1.21, the catalytic cycle starts with the binding to the catalytic active site of a substrate H_2O molecule.

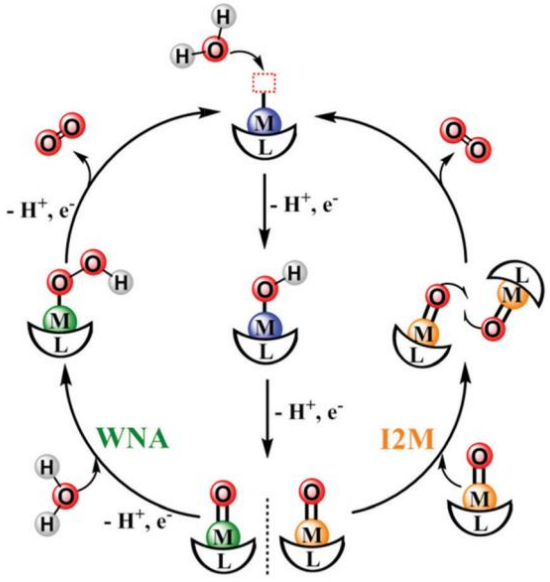

Figure 1.21 Schematic representation of the water nucleophilic attack (WNA) and the interaction between two M–O intermediate (I2M) pathways to form O–O bonds catalysed by molecular catalysts.[71]

After two consecutive proton-coupled electron transfer (PCET) steps, the WOC generates a high-valent M=O intermediate, which is essential for the next crucial O–O bond formation step. Depending on the nature of this M=O intermediate, two pathways for O–O bond formation have been proposed: (i) water nucleophilic attack (WNA) and (ii) interaction of two M–O units (I2M). In the WNA pathway, a second H_2O molecule attacks the electrophilic O on the M=O intermediate, resulting in a two-electron reduction of the metal center and O–O bond formation on a metal hydroperoxide intermediate (M–OOH). Next, O_2 evolution occurs after further oxidation of the M–

OOH. On the other hand, the I2M pathway relies on the possible higher electron spin and radical character of O on the M=O intermediate. In this context, the O–O bond forms *via* coupling of two radical-like species, leading to an M–O–O–M species, which can release O_2 upon further oxidization.[115,177,178]

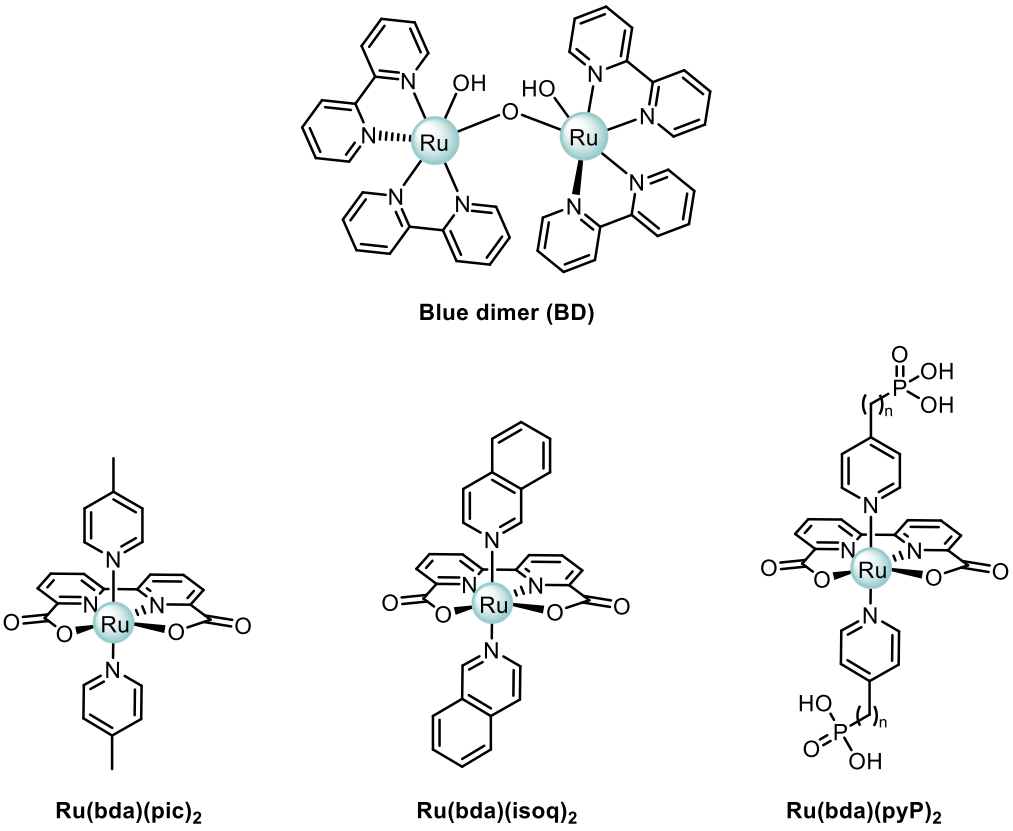

Figure 1.22 Structures of common Ru-based WOCs used in DSPECs.

Since 1982, when Meyer and co-workers reported the first molecular WOC, the so called 'blue dimer'(BD)[179] (Figure 1.22), Ru-Based molecular catalysts have been the most intensively studied. The first systems able to reach an electron transfer rate comparable to that of photosystem II were [Ru(bda)(X_2)] (H_2bda=2,2′-bipyridine-6,6′-dicarboxylic acid, X = 4-picoline or isoquinoline) complexes designed by L. Sun and coworkers.[180] These complexes showed a turnover number (TON) of 2000 and a turnover frequency (TOF) of 41 s^{-1} in homogeneous oxygen evolution reactions from water using Ce^{4+} as a sacrificial oxidant. This dramatic improvement compared to BD, that only achieved a TON of 13 and TOF of 0.0042 s^{-1} under similar conditions, is attributed to the introduction of carboxylate groups into the ligands and the special steric configuration, which provides an open site for the substrate water molecule and allows 7-coordination at this catalytic site.[181,182] However, since these WOCs are devoid of anchoring groups, for their use in DS-PEC they had to be necessarily dissolved in the electrolyte medium. This configuration drastically reduces the efficiency of the photosystem, since the charge transfer rate is governed by the diffusion

of the WOC near the electrode, which can also cause charge recombination reactions between the WOC and the SC. For these reasons, a more efficient configuration contemplates a WOC immobilized on the SC surface. The typical approach relies on the functionalization of the WOC by adding a suitable anchoring group on to one or more of the ligands. In most cases, the functionalization is made on the axial ligand by adding a spacer constituted by an alkyl chain carrying the proper anchoring group at one extremity. The longer the chain, the higher the conformational flexibility of the spacer. This notable feature increases the opportunity for two WOCs to meet and form the above-mentioned dioxo bridge necessary in the I2M pathway. Moreover, longer alkyl chains can reduce the back electron transfer since they increase the spatial distance between the catalytic site and SC surface.[183]

In the development of molecular WOCs, Ir-based complexes constitute another type of classic catalysts.[184] In 2008, the Bernhard group pioneered this area by introducing a series of iridium complexes. These complexes, exemplified by **WOC1** [185] in Figure 1.23, feature two substituted 2-phenylpyridine ligands and two water ligands. They demonstrated the ability to catalyze water oxidation with a remarkable turnover number (TON) of 2760 using Ce^{4+} as the terminal oxidant. This breakthrough spurred the development of numerous iridium-based molecular WOCs. A second major family of iridium WOCs, extensively studied, includes Ir complexes with cyclopentadienyl (Cp) or pentamethylcyclopentadienyl (Cp*) ligands. These complexes, exemplified by **WOC2**[186] in Figure 1.23, were reported by Crabtree, Brudvig, and co-workers. [186,187] This type of Ir-based catalyst offers faster catalytic rates compared to those developed by Bernhard's group. However, the enhanced speed comes at the cost of reduced stability, as these half-sandwich complexes are less robust.

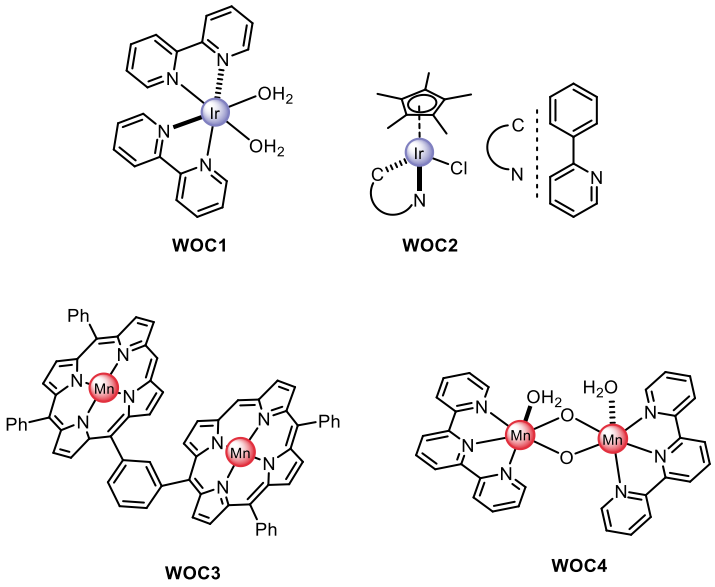

Figure 1.23 Representative structures of Ir- and Mn-based WOCs.

Manganese-based complexes have been also considered promising candidates for WOCs because manganese is the third-most-abundant transition metal on earth, is a low-cost material, and, as seen before, is present in the form of a Mn_4CaO_5 cluster in the oxygen-evolving complex (OEC) in photosystem-II. Moreover, manganese has a rich redox chemistry and can bear multiple charges to generate reactive high-valent intermediates for water oxidation. **WOC3**[188] and **WOC4**[189] are reported in Figure 1.23 as examples of this class of WOCs.

1.4.3.4 Hydrogen evolution catalyst (HEC)

The kinetics for the reduction reaction of protons to molecular hydrogen can be accelerated by using an appropriate catalyst on the photocathode side. In order to have an efficient regeneration of the dye, a HEC must have a reduction potential less negative than the excited state oxidation potential of the dye. If this step is not efficient, a charge recombination between the reduced photosensitizer and the holes in the *p*-type SC would be observed. A general catalytic mechanism for hydrogen evolution is shown in Figure 1.24. The active metal center undergoes a series of electron and proton transfers to generate a reactive metal-hydride intermediate, which can react in two possible ways to evolve hydrogen. In the left cycle, the metal-hydride reacts with another metal-hydride to generate H_2 via reductive elimination. Alternatively, in the right cycle, the metal-hydride is further reduced and protonated to form H_2. [190–192] Based on this working mechanism, to obtain high activity for hydrogen evolution, a metal complex should have wide open coordination sites for binding the substrate and an appropriate electronic structure for generating and stabilizing a reactive metal-hydride intermediate.

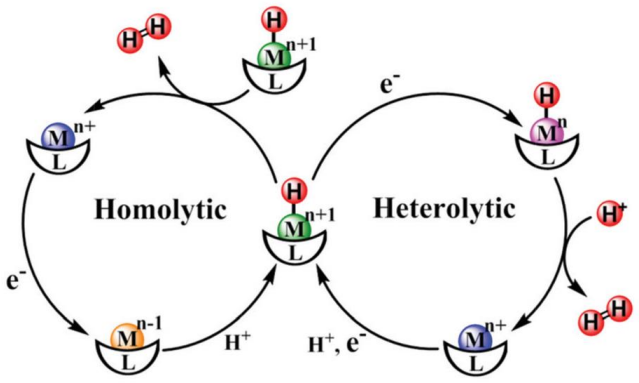

Figure 1.24 Proposed mechanistic pathways for H_2 evolution by a metallic catalytic center.[71]

As well as for the WOCs, several metal-based (typically Rh,[193] Fe,[194] and Ni[195]) molecular HECs have been reported to date. Some examples are shown in Figure 1.25.

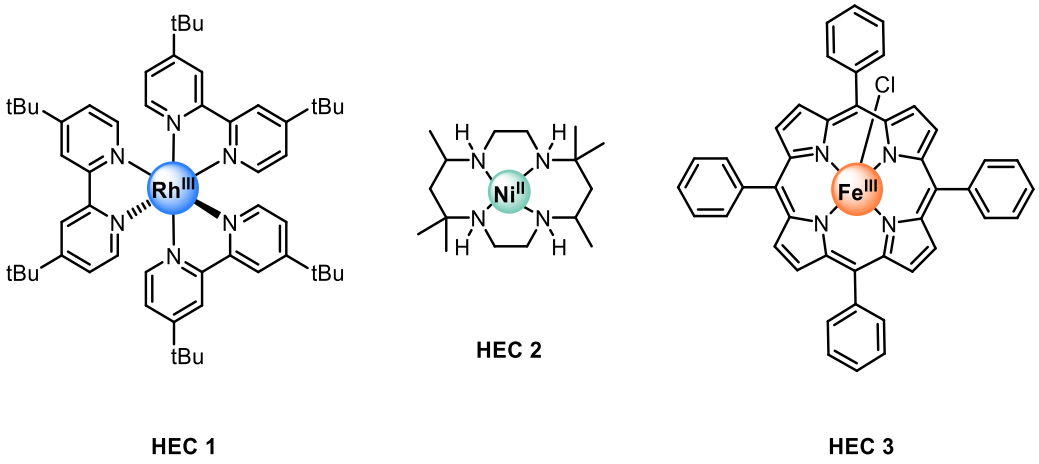

Figure 1.25 Representative structures of HECs.

1.4.3.5 Counter electrode

In PA-DSPEC and PC-DSPEC systems, the counter electrode is not photoactive but plays a vital role in facilitating electron transfer to and from external circuits, as well as catalyzing the respective half-reactions (hydrogen evolution reaction for PA-DSPEC and water oxidation reaction for PC-DSPEC). This function complements that of the photoactive working electrode. Platinum (Pt) electrodes have been commonly employed as counter electrodes in DSPECs due to their excellent electrical conductivity, high chemical stability in aqueous environments, and remarkable electrocatalytic efficiency for both half reactions. However, Pt is a rare and high-cost metal which pose challenges for large-scale applications.[196] Alternatives such as graphite electrodes and cobalt sulfide have been explored in DSSCs, prompting further research into effective Pt-free counter electrodes for DSPECs.[197,198] Graphite electrodes, for instance, are more affordable and easier to manufacture in larger sizes compared to platinum, making them suitable for high-current applications and less critical reactions, though their stability is not on par with that of platinum electrodes.

1.4.3.6 Electrolyte

The aqueous electrolyte solution represents the medium where the two photoelectrodes are immersed, so the relevant parameters of an electrolyte, such as solute species, pH, and ionic strength, strongly influence the overall performance of DSPECs. Since the electrolyte should enable efficient proton transfer between the anode and cathode, inorganic salts are used as solute species.[139] Among all the electrolyte parameters, the effect of pH on the photocurrent of DSPECs has been noticed and investigated in many reports but no linear relationship between pH and photocurrent density is observed.[199] From a thermodynamic perspective, an acidic pH promotes the HER but

inhibits the WOR. In contrast, a basic pH has the opposite effect. While a basic pH might appear advantageous, given the greater challenge posed by the WOR, it introduces significant stability issues, as dyes and WOCs are prone to decomposition under these conditions. As a result, a neutral or slightly acidic pH is normally preferred. At present, three frequently employed inorganic electrolytes are utilized in DSPECs, which comprise phosphate buffer solution (PBS),[200] sodium sulfate (Na_2SO_4),[201] and acetate buffer solution (ABS).[202]

1.4.4 Characterization methods and performance metrics

1.4.4.1 Photocurrent measurements

In the development process of photoelectrodes capable of splitting water efficiently under solar irradiation, performances need to be properly evaluated and compared to achieve improved results. To evaluate the performance of a DSPEC photoelectrode, the most common practice is to measure the photocurrent density in a three-electrode configuration cell under 1 sun AM1.5 G illumination (100 mW cm^{-2}) since the photocurrent should be proportional to the hydrogen or oxygen production rate. The basic experimental setup for photocurrent measurements consists of a photoelectrochemical cell with three-electrodes configuration immersed in a water-based electrolyte, a light source (*i.e.* a solar simulator) and a potentiostat as shown in Figure 1.26a.[203] To optimize the device, the photoanode and photocathode are typically studied separately using a simple platinum wire as the counter electrode (CE). The working electrode (WE) is represented by the investigated photoelectrode, (e.g., dye/catalyst-sensitized TiO_2 film), which is deposited on a conductive substrate as the back contact (typically, transparent conductive oxides, such as fluorine-doped tin oxide (FTO) and indium tin oxide (ITO)). Meanwhile the reference electrode (RE) is typically an Ag/AgCl electrode or saturated calomel electrode (SCEs). This set-up requires a supply of electric current (bias) to increase the electron injection into the SC. Normally, two different type of photocurrent measurement are carried out: linear sweep voltammetry (LSV) and chronoamperometry (CA). LSV measurements involve recording the photocurrent density (J, $\mu A/cm^2$) of the working electrode under both dark and illuminated conditions, while the potential (V) between the working electrode and the reference electrode is linearly swept with a constant scan-rate. The recorded photocurrent is tipically normalized by the projected geometric surface area of the sample that is illuminated and exposed to the electrolyte to calculate the photocurrent density value. LSV is measured under dark and light conditions, in order to verify the photoactivity of the system. Under dark conditions the recorded photocurrent must be almost zero, meanwhile a clear signal must be seen under illumination mode. By comparing their current densities under dark and light conditions

in the LSV plot (*J-V* curve, Figure 1.26b) it is possible to determine the potential where the light/dark ratio is greatest; this value represents the optimal bias potential of the system and is then set in the CA experiment.

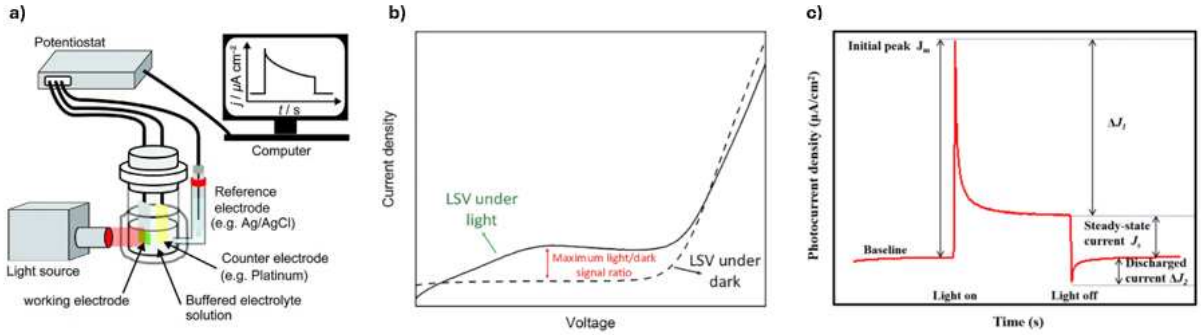

Figure 1.26 a) The experimental setup for PEC photocurrent measurement;[203] b) LSV curves of a DS-PEC;[114] c) CA curve of a DS-PEC. J_1 is the difference between the stable photocurrent and the dark current.[204]

During CA experiments the photocurrent response of the WE at a fixed applied potential is recorded over time, obtaining the corresponding *J-t* curve shown in Figure 1.26c. Typically, the *J-t* curve exhibits a spike-like shape. In the dark, a photocurrent baseline, which is likely to be influenced by electrode components, electrolyte species and applied bias, is observed. When illumination is started, a drastic initial photocurrent peak J_m appears, resulting from the rapid electron injection/transfer at the moment of irradiation. A rapid decaying peak follows, going into a steady state current density J_s. The difference between J_m and J_s (ΔJ_1) is often referred to as the recombination current, which results from rapid charge recombination competing with hole transfer to the electrolyte. When the light is cut off, a discharge current (ΔJ_2) occurs, and its magnitude is related to the recombination resistance of the photoelectrode. Long term CA measurements under light illumination allow to evaluate the stability of the device under working conditions. [205]

1.4.4.2 Gas evolution measurements and efficiency parameters

Verifying and quantitating production of the desired O_2 and H_2 products in a DSPEC for water splitting represents another important aspect for characterizing a given system. While the observation of sustained photocurrent implies catalytic activity, artificial photocurrent can arise from oxidative decomposition of the chromophore or other non-productive surface reactions. Therefore, it is usually helpful to identify and quantify the desired reaction products, which should be collected, with a stoichiometry of 1:2.[206] For hydrogen quantification, gas chromatography with thermal conductivity detector (TCD-GC) represents the standard approach. A typical TCD-GC set-up includes a GC, equipped with a detector that senses changes in the thermal conductivity of the column effluent, and compares it to a reference flow of Argon as carrier gas in order to detect

H_2.[207] On the other hand, quantitating the production of O_2 presents a greater challenge, especially because of interference from atmospheric oxygen. A possible approach to achieve an unambiguous determination of O_2 from water involves the use of water isotopically labeled with ^{18}O combined with mass spectrometry. Electrochemistry offers two other methods for detecting and quantitating O_2 that are especially pertinent to the study of DSPEC water splitting systems; namely the use of a Clark electrode[208] or a dual working electrode method (referred to as the collector-generator method).[209] In recent reports, the latter method has been extensively employed, wherein an unchanged FTO electrode (collector) is positioned nearby the working electrode (generator) and subjected to a suitable potential for the detection and reduction of O_2 diffusion originating from the working electrode. With the detected amount of evolved gas and the photocurrent through the photoelectrode, the faradaic efficiency (FE) (equation 3) can be calculated and considered as an indicator of the device's performance in terms of reaction selectivity.[54]

$$FE\ (\eta_f) = \frac{z \times n \times F}{i \times t} \times 100\% \qquad (1.3)$$

Where z is the number of electrons (2 for the hydrogen evolution reaction or 4 for water oxidation reaction), n is the molar amount of detected gas, F is the Faraday coefficient, i is the recorded photocurrent and t is the test time.

An additional parameter to determine the efficiency of a DSPEC is the solar-to-hydrogen efficiency (STH). This value is the efficiency of the photosystem in terms of incoming solar energy power converted into output power related to the produced hydrogen (equation 4).[210]

$$STH = \frac{J_{sc}\ (mA\ cm^{-2}) \times 1.229\ (V) \times \eta_f}{P_{total}(\text{mW}\ cm^{-2})} \qquad (1.4)$$

Where Jsc is the short-circuit photocurrent density, η_f is the faradic efficiency and P_{total} is the the energy of incident sunlight. In many cases, an external bias is provided for a working DSPEC in the actual experiment. In this case, the applied bias photon-to-current efficiency (ABPE) is defined as an analogue to the STH efficiency with no bias. ABPE can be calculated by using equation 5.[211]

$$\text{ABPE} = \frac{J_{sc}\ (mA\ cm^{-2}) \times (1.229 - |V_{app}|)(V) \times \eta_f}{P_{total}(\text{mW}\ cm^{-2})} \qquad (1.5)$$

1.5 References

(1) O. S. Miljanić; J. A. Pratt. *Introduction to Energy and Sustainability*, 1st ed.; Wiley-VCH GmbH, 2022.

(2) Armaroli, N.; Balzani, V. The Future of Energy Supply: Challenges and Opportunities. *Angew. Chem. Int. Ed.* **2007**, *46* (1–2), 52–66. https://doi.org/10.1002/anie.200602373.

(3) Armaroli, N.; Balzani, V. The Hydrogen Issue. *ChemSusChem* **2011**, *4* (1), 21–36. https://doi.org/10.1002/cssc.201000182.

(4) BP. *Energy Outlook 2024 Edition*; 2024.

(5) REN21. *Renewables 2024 Global Status Report*; 2024.

(6) Intergovernmental Panel on Climate Change (IPCC). *Emissions Trends and Drivers 2024 Edition*; 2024.

(7) Rodrigue, J.-P. *The Geography of Transport Systems*; Routledge, 2024. https://doi.org/10.4324/9781003343196.

(8) International Renewable Energy Agency (IRENA). *Renewable Energy and Jobs: Annual Review 2024*; 2024.

(9) International Renewable Energy Agency (IRENA). *Solar PV Supply Chains-Technical and ESG Standards for Market Integration*; 2024.

(10) Global Wind Report 2024. *Global Wind Energy Council*; 2024.

(11) Schneider, E. A.; Deinert, M. R.; Cady, K. B. Cost Analysis of the US Spent Nuclear Fuel Reprocessing Facility. *Energy Econ.* **2009**, *31* (5), 627–634. https://doi.org/10.1016/j.eneco.2008.12.011.

(12) Service, R. F. Is It Time to Shoot for the Sun? *Science (1979)* **2005**, *309* (5734), 548–551. https://doi.org/10.1126/science.309.5734.548.

(13) Tamaura, Y.; Shigeta, S.; Meng, Q.-L.; Aiba, T.; Kikura, H. Cross Linear Solar Concentration System for CSP and CPV. *Energy Procedia* **2014**, *49*, 249–256. https://doi.org/10.1016/j.egypro.2014.03.027.

(14) A. E. Becquerel. Memoire Sur Les Effects d'Electriques Produits Sous l'Influence Des Rayons Solaires. *C. R. Acad. Sci. Paris* **1839**, *9*, 561–567.

(15) Bell Laboratories Record, 1954.

(16) Marques Lameirinhas, R. A.; Torres, J. P. N.; de Melo Cunha, J. P. A Photovoltaic Technology Review: History, Fundamentals and Applications. *Energies (Basel)* **2022**, *15* (5), 1823. https://doi.org/10.3390/en15051823.

(17) Wenham, S. R.; Green, M. A. Silicon Solar Cells. *Prog. Photovolt.: Res. Appl.* **1996**, *4* (1), 3–33. https://doi.org/10.1002/(SICI)1099-159X(199601/02)4:1<3::AID-PIP117>3.0.CO;2-S.

(18) Rathore, N.; Panwar, N. L.; Yettou, F.; Gama, A. A Comprehensive Review of Different Types of Solar Photovoltaic Cells and Their Applications. *Int. J. Ambient Energy* **2021**, *42* (10), 1200–1217. https://doi.org/10.1080/01430750.2019.1592774.

(19) Green, M. A.; Dunlop, E. D.; Yoshita, M.; Kopidakis, N.; Bothe, K.; Siefer, G.; Hinken, D.; Rauer, M.; Hohl-Ebinger, J.; Hao, X. Solar Cell Efficiency Tables (Version 64). *Prog. Photovolt: Res Appl.* **2024**, *32* (7), 425–441. https://doi.org/10.1002/pip.3831.

(20) Machín, A.; Márquez, F. Advancements in Photovoltaic Cell Materials: Silicon, Organic, and Perovskite Solar Cells. *Materials* **2024**, *17* (5), 1165. https://doi.org/10.3390/ma17051165.

(21) Di Sabatino, M.; Hendawi, R.; Garcia, A. S. Silicon Solar Cells: Trends, Manufacturing Challenges, and AI Perspectives. *Crystals (Basel)* **2024**, *14* (2), 167. https://doi.org/10.3390/cryst14020167.

(22) Sreejith, S.; Ajayan, J.; Kollem, S.; Sivasankari, B. A Comprehensive Review on Thin Film Amorphous Silicon Solar Cells. *Silicon* **2022**, *14* (14), 8277–8293. https://doi.org/10.1007/s12633-021-01644-w.

(23) Ghahremani, A.; Fathy, A. E. High Efficiency Thin-film Amorphous Silicon Solar Cells. *Energy sci. eng.* **2016**, *4* (5), 334–343. https://doi.org/10.1002/ese3.131.

(24) Zghaibeh, M.; Okonkwo, P. C.; Emori, W.; Ahmed, T.; Mohamed, A. M. A.; Aliyu, M.; Ogunleye, G. J. CdTe Solar Cells Fabrication and Examination Techniques: A Focused Review. *Int. J. Green Energy* **2023**, *20* (5), 555–570. https://doi.org/10.1080/15435075.2022.2126943.

(25) First Solar Press Release. *First Solar Achieves Yet Another Cell Conversion Efficiency World Record*; 2016.

(26) First Solar Inc. *First Solar Series 6- Advanced Thin Film Solar Technology*; 2021.

(27) Salhi, B. The Photovoltaic Cell Based on CIGS: Principles and Technologies. *Materials* **2022**, *15* (5), 1908. https://doi.org/10.3390/ma15051908.

(28) Keller, J.; Kiselman, K.; Donzel-Gargand, O.; Martin, N. M.; Babucci, M.; Lundberg, O.; Wallin, E.; Stolt, L.; Edoff, M. High-Concentration Silver Alloying and Steep Back-Contact Gallium Grading Enabling Copper Indium Gallium Selenide Solar Cell with 23.6% Efficiency. *Nat. Energy* **2024**, *9* (4), 467–478. https://doi.org/10.1038/s41560-024-01472-3.

(29) Bheemreddy, V.; Bill Liu, J. J.; Wills, A.; Murcia, C. P. Life Prediction Model Development for Flexible Photovoltaic Modules Using Accelerated Damp Heat Testing. In *2018 IEEE 7th World Conference on Photovoltaic Energy Conversion (WCPEC) (A Joint Conference of 45th IEEE PVSC, 28th PVSEC & 34th EU PVSEC)*; IEEE, 2018; pp 1249–1251. https://doi.org/10.1109/PVSC.2018.8547610.

(30) Li, Y.; Wei, H.; Cui, C.; Wang, X.; Shao, Z.; Pang, S.; Cui, G. CZTSSe Solar Cells: Insights into Interface Engineering. *J. Phys. Chem. A* **2023**, *11* (10), 4836–4849. https://doi.org/10.1039/D2TA09561K.

(31) Zhou, J.; Xu, X.; Wu, H.; Wang, J.; Lou, L.; Yin, K.; Gong, Y.; Shi, J.; Luo, Y.; Li, D.; Xin, H.; Meng, Q. Control of the Phase Evolution of Kesterite by Tuning of the Selenium Partial Pressure for Solar Cells with 13.8% Certified Efficiency. *Nat. Energy* **2023**, *8* (5), 526–535. https://doi.org/10.1038/s41560-023-01251-6.

(32) Papež, N.; Dallaev, R.; Ţălu, Ş.; Kaštyl, J. Overview of the Current State of Gallium Arsenide-Based Solar Cells. *Materials* **2021**, *14* (11), 3075. https://doi.org/10.3390/ma14113075.

(33) Kayes, B. M.; Nie, H.; Twist, R.; Spruytte, S. G.; Reinhardt, F.; Kizilyalli, I. C.; Higashi, G. S. 27.6% Conversion Efficiency, a New Record for Single-Junction Solar Cells under 1 Sun Illumination. In *2011 37th IEEE Photovoltaic Specialists Conference*; IEEE, 2011; pp 000004–000008. https://doi.org/10.1109/PVSC.2011.6185831.

(34) Dai, Y.; Bai, Y. Performance Improvement for Building Integrated Photovoltaics in Practice: A Review. *Energies (Basel)* **2020**, *14* (1), 178. https://doi.org/10.3390/en14010178.

(35) Shockley, W.; Queisser, H. J. Detailed Balance Limit of Efficiency of *p-n* Junction Solar Cells. *J. Appl. Phys.* **1961**, *32* (3), 510–519. https://doi.org/10.1063/1.1736034.

(36) Baiju, A.; Yarema, M. Status and Challenges of Multi-Junction Solar Cell Technology. *Front. energy res.* **2022**, *10*. https://doi.org/10.3389/fenrg.2022.971918.

(37) Dimroth, F.; Tibbits, T. N. D.; Niemeyer, M.; Predan, F.; Beutel, P.; Karcher, C.; Oliva, E.; Siefer, G.; Lackner, D.; Fus-Kailuweit, P.; Bett, A. W.; Krause, R.; Drazek, C.; Guiot, E.; Wasselin, J.; Tauzin, A.; Signamarcheix, T. Four-Junction Wafer-Bonded Concentrator Solar Cells. *IEEE J. Photovolt.* **2016**, *6* (1), 343–349. https://doi.org/10.1109/JPHOTOV.2015.2501729.

(38) Hagfeldt, A.; Boschloo, G.; Sun, L.; Kloo, L.; Pettersson, H. Dye-Sensitized Solar Cells. *Chem Rev* **2010**, *110* (11), 6595–6663. https://doi.org/10.1021/cr900356p.

(39) Chen, P.; Xiao, Y.; Li, S.; Jia, X.; Luo, D.; Zhang, W.; Snaith, H. J.; Gong, Q.; Zhu, R. The Promise and Challenges of Inverted Perovskite Solar Cells. *Chem. Rev.* **2024**, *124* (19), 10623–10700. https://doi.org/10.1021/acs.chemrev.4c00073.

(40) O'Regan, B.; Grätzel, M. A Low-Cost, High-Efficiency Solar Cell Based on Dye-Sensitized Colloidal TiO2 Films. *Nature* **1991**, *353* (6346), 737–740. https://doi.org/10.1038/353737a0.

(41) Mirabi, E.; Akrami Abarghuie, F.; Arazi, R. Integration of Buildings with Third-Generation Photovoltaic Solar Cells: A Review. *Clean Energy* **2021**, *5* (3), 505–526. https://doi.org/10.1093/ce/zkab031.

(42) Ho-Baillie, A. W. Y.; Bremner, S.; Brenner, C.; Cairns, I. H.; Granados-Caro, L.; Conibeer, G.; Curry, J.; Ekins-Daukes, N.; Griffin, D.; Leung, T. L.; Mahmud, M. A.; McKenzie, D.; Peracchi, S.; Shrestha, S.; Wilt, D. Emerging Photovoltaics for Onboard Space Applications. *Nat. Rev. Mater.* **2024**, *9*, 759–761. https://doi.org/10.1038/s41578-024-00723-9.

(43) Ren, Y.; Zhang, D.; Suo, J.; Cao, Y.; Eickemeyer, F. T.; Vlachopoulos, N.; Zakeeruddin, S. M.; Hagfeldt, A.; Grätzel, M. Hydroxamic Acid Pre-Adsorption Raises the Efficiency of Cosensitized Solar Cells. *Nature* **2023**, *613* (7942), 60–65. https://doi.org/10.1038/s41586-022-05460-z.

(44) Kojima, A.; Teshima, K.; Shirai, Y.; Miyasaka, T. Organometal Halide Perovskites as Visible-Light Sensitizers for Photovoltaic Cells. *J. Am. Chem. Soc.* **2009**, *131* (17), 6050–6051. https://doi.org/10.1021/ja809598r.

(45) Pastuszak, J.; Węgierek, P. Photovoltaic Cell Generations and Current Research Directions for Their Development. *Materials* **2022**, *15* (16), 5542. https://doi.org/10.3390/ma15165542.

(46) Biswas, S.; Lee, Y.; Choi, H.; Lee, H. W.; Kim, H. Progress in Organic Photovoltaics for Indoor Application. *RSC Adv.* **2023**, *13* (45), 32000–32022. https://doi.org/10.1039/D3RA02599C.

(47) D'Amico, F.; de Jong, B.; Bartolini, M.; Franchi, D.; Dessì, A.; Zani, L.; Yzeiri, X.; Gatto, E.; Santucci, A.; Di Carlo, A.; Reginato, G.; Cinà, L.; Vesce, L. Recent Advances in Organic Dyes for Application in Dye-Sensitized Solar Cells under Indoor Lighting Conditions. *Materials* **2023**, *16* (23), 7338. https://doi.org/10.3390/ma16237338.

(48) Reddy, V. J.; Hariram, N. P.; Maity, R.; Ghazali, M. F.; Kumarasamy, S. Sustainable Vehicles for Decarbonizing the Transport Sector: A Comparison of Biofuel, Electric, Fuel Cell and Solar-Powered Vehicles. *World Electr. Veh. J.* **2024**, *15* (3), 93. https://doi.org/10.3390/wevj15030093.

(49) MIT. *The Future of Solar Energy-An Interdisciplinary MIT Study*; 2015.

(50) Kathpalia, R.; Kamra Verma, A. Artificial Photosynthesis as an Alternative Source of Renewable Energy: Potential and Limitations; 2023. https://doi.org/10.5772/intechopen.111501.

(51) Wang, Y.; Suzuki, H.; Xie, J.; Tomita, O.; Martin, D. J.; Higashi, M.; Kong, D.; Abe, R.; Tang, J. Mimicking Natural Photosynthesis: Solar to Renewable H_2 Fuel Synthesis by Z-Scheme Water Splitting Systems. *Chem. Rev.* **2018**, *118* (10), 5201–5241. https://doi.org/10.1021/acs.chemrev.7b00286.

(52) Barber, J.; Tran, P. D. From Natural to Artificial Photosynthesis. *J. R. Soc. Interface* **2013**, *10* (81), 20120984. https://doi.org/10.1098/rsif.2012.0984.

(53) Barber, J. Photosynthetic Energy Conversion: Natural and Artificial. *Chem. Soc. Rev.* **2009**, *38* (1), 185–196. https://doi.org/10.1039/B802262N.

(54) Zhang, S.; Ye, H.; Hua, J.; Tian, H. Recent Advances in Dye-Sensitized Photoelectrochemical Cells for Water Splitting. *EnergyChem* **2019**, *1* (3), 100015. https://doi.org/10.1016/j.enchem.2019.100015.

(55) Whang, D. R.; Apaydin, D. H. Artificial Photosynthesis: Learning from Nature. *ChemPhotoChem* **2018**, *2* (3), 148–160. https://doi.org/10.1002/cptc.201700163.

(56) Suga, M.; Akita, F.; Hirata, K.; Ueno, G.; Murakami, H.; Nakajima, Y.; Shimizu, T.; Yamashita, K.; Yamamoto, M.; Ago, H.; Shen, J.-R. Native Structure of Photosystem II at 1.95 Å Resolution Viewed by Femtosecond X-Ray Pulses. *Nature* **2015**, *517* (7532), 99–103. https://doi.org/10.1038/nature13991.

(57) Cox, N.; Retegan, M.; Neese, F.; Pantazis, D. A.; Boussac, A.; Lubitz, W. Electronic Structure of the Oxygen-Evolving Complex in Photosystem II Prior to O-O Bond Formation. *Science (1979)* **2014**, *345* (6198), 804–808. https://doi.org/10.1126/science.1254910.

(58) Ciamician, G. The Photochemistry of the Future. *Science (1979)* **1912**, *36* (926), 385–394. https://doi.org/10.1126/science.36.926.385.

(59) El-Khouly, M. E.; El-Mohsnawy, E.; Fukuzumi, S. Solar Energy Conversion: From Natural to Artificial Photosynthesis. *J. Photochem. Photobiol. C* **2017**, *31*, 36–83. https://doi.org/10.1016/j.jphotochemrev.2017.02.001.

(60) Falciani, G.; Chiavazzo, E. An Overview on Modelling Approaches for Photochemical and Photoelectrochemical Solar Fuels Processes and Technologies. *Energy Convers. Manag.* **2023**, *292*, 117366. https://doi.org/10.1016/j.enconman.2023.117366.

(61) Zhao, Y.; Niu, Z.; Zhao, J.; Xue, L.; Fu, X.; Long, J. Recent Advancements in Photoelectrochemical Water Splitting for Hydrogen Production. *Electrochem. Energy Rev.* **2023**, *6* (1), 14. https://doi.org/10.1007/s41918-022-00153-7.

(62) Putri, L. K.; Ng, B.; Ong, W.; Chai, S.; Mohamed, A. R. Toward Excellence in Photocathode Engineering for Photoelectrochemical CO_2 Reduction: Design Rationales and Current Progress. *Adv. Energy Mater.* **2022**, *12* (41). https://doi.org/10.1002/aenm.202201093.

(63) Foster, S. L.; Bakovic, S. I. P.; Duda, R. D.; Maheshwari, S.; Milton, R. D.; Minteer, S. D.; Janik, M. J.; Renner, J. N.; Greenlee, L. F. Catalysts for Nitrogen Reduction to Ammonia. *Nat. Catal.* **2018**, *1* (7), 490–500. https://doi.org/10.1038/s41929-018-0092-7.

(64) Inoue, H.; Shimada, T.; Kou, Y.; Nabetani, Y.; Masui, D.; Takagi, S.; Tachibana, H. The Water Oxidation Bottleneck in Artificial Photosynthesis: How Can We Get Through It? An Alternative Route Involving a Two-Electron Process. *ChemSusChem* **2011**, *4* (2), 173–179. https://doi.org/10.1002/cssc.201000385.

(65) Fukuzumi, S.; Lee, Y.; Nam, W. Solar-Driven Production of Hydrogen Peroxide from Water and Dioxygen. *Chem. Eur. J.* **2018**, *24* (20), 5016–5031. https://doi.org/10.1002/chem.201704512.

(66) Su, J.; Vayssieres, L. A Place in the Sun for Artificial Photosynthesis? *ACS Energy Lett.* **2016**, *1* (1), 121–135. https://doi.org/10.1021/acsenergylett.6b00059.

(67) Kudo, A.; Miseki, Y. Heterogeneous Photocatalyst Materials for Water Splitting. *Chem. Soc. Rev.* **2009**, *38* (1), 253–278. https://doi.org/10.1039/B800489G.

(68) FUJISHIMA, A.; HONDA, K. Electrochemical Photolysis of Water at a Semiconductor Electrode. *Nature* **1972**, *238* (5358), 37–38. https://doi.org/10.1038/238037a0.

(69) Gopinath, M.; Marimuthu, R. A Review on Solar Energy-Based Indirect Water-Splitting Methods for Hydrogen Generation. *Int. J. Hydrogen Energy* **2022**, *47* (89), 37742–37759. https://doi.org/10.1016/j.ijhydene.2022.08.297.

(70) Cecconi, B.; Manfredi, N.; Montini, T.; Fornasiero, P.; Abbotto, A. Dye-Sensitized Solar Hydrogen Production: The Emerging Role of Metal-Free Organic Sensitizers. *Eur. J. Org. Chem.* **2016**, *2016* (31), 5194–5215. https://doi.org/10.1002/ejoc.201600653.

(71) Zhang, B.; Sun, L. Artificial Photosynthesis: Opportunities and Challenges of Molecular Catalysts. *Chem. Soc. Rev.* **2019**, *48* (7), 2216–2264. https://doi.org/10.1039/C8CS00897C.

(72) Bian, H.; Li, D.; Yan, J.; Liu, S. (Frank). Perovskite – A Wonder Catalyst for Solar Hydrogen Production. *J. Energy Chem.* **2021**, *57*, 325–340. https://doi.org/10.1016/j.jechem.2020.08.057.

(73) Gurudayal, G.; Bullock, J.; Srankó, D. F.; Towle, C. M.; Lum, Y.; Hettick, M.; Scott, M. C.; Javey, A.; Ager, J. Efficient Solar-Driven Electrochemical CO_2 Reduction to Hydrocarbons and Oxygenates. *Energy Environ. Sci.* **2017**, *10* (10), 2222–2230. https://doi.org/10.1039/C7EE01764B.

(74) Cheng, W.-H.; Richter, M. H.; Sullivan, I.; Larson, D. M.; Xiang, C.; Brunschwig, B. S.; Atwater, H. A. CO_2 Reduction to CO with 19% Efficiency in a Solar-Driven Gas Diffusion Electrode Flow Cell under Outdoor Solar Illumination. *ACS Energy Lett.* **2020**, *5* (2), 470–476. https://doi.org/10.1021/acsenergylett.9b02576.

(75) Luo, J.; Im, J.-H.; Mayer, M. T.; Schreier, M.; Nazeeruddin, M. K.; Park, N.-G.; Tilley, S. D.; Fan, H. J.; Grätzel, M. Water Photolysis at 12.3% Efficiency via Perovskite Photovoltaics and Earth-Abundant Catalysts. *Science (1979)* **2014**, *345* (6204), 1593–1596. https://doi.org/10.1126/science.1258307.

(76) Jia, J.; Seitz, L. C.; Benck, J. D.; Huo, Y.; Chen, Y.; Ng, J. W. D.; Bilir, T.; Harris, J. S.; Jaramillo, T. F. Solar Water Splitting by Photovoltaic-Electrolysis with a Solar-to-Hydrogen Efficiency over 30%. *Nat. Commun* **2016**, *7* (1), 13237. https://doi.org/10.1038/ncomms13237.

(77) Pervaiz, E.; Ali, M.; Abbasi, M. A.; Noor, T.; Said, Z.; Alawadhi, H. Unfolding Essence of Nanoscience for Improved Water Splitting Hydrogen Generation in the Light of Newly Emergent Nanocatalysts. *Int. J. Hydrog. Energy* **2022**, *47* (63), 26915–26955. https://doi.org/10.1016/j.ijhydene.2022.06.060.

(78) Samal, A.; Das, N. Mini-Review on Remediation of Plastic Pollution through Photoreforming: Progress, Possibilities, and Challenges. *ESPR* **2023**, *30* (35), 83138–83152. https://doi.org/10.1007/s11356-023-28253-x.

(79) Navarro Yerga, R. M.; Álvarez Galván, M. C.; del Valle, F.; Villoria de la Mano, J. A.; Fierro, J. L. G. Water Splitting on Semiconductor Catalysts under Visible-Light Irradiation. *ChemSusChem* **2009**, *2* (6), 471–485. https://doi.org/10.1002/cssc.200900018.

(80) Bolton, J. R. Solar Photoproduction of Hydrogen: A Review. *Solar Energy* **1996**, *57* (1), 37–50. https://doi.org/10.1016/0038-092X(96)00032-1.

(81) Osterloh, F. E. Inorganic Materials as Catalysts for Photochemical Splitting of Water. *Chem. Mater.* **2008**, *20* (1), 35–54. https://doi.org/10.1021/cm7024203.

(82) Kato, H.; Asakura, K.; Kudo, A. Highly Efficient Water Splitting into H_2 and O_2 over Lanthanum-Doped $NaTaO_3$ Photocatalysts with High Crystallinity and Surface Nanostructure. *J. Am. Chem. Soc.* **2003**, *125* (10), 3082–3089. https://doi.org/10.1021/ja027751g.

(83) Abe, R.; Sayama, K.; Domen, K.; Arakawa, H. A New Type of Water Splitting System Composed of Two Different TiO2 Photocatalysts (Anatase, Rutile) and a IO3−/I− Shuttle Redox Mediator. *Chem. Phys. Lett.* **2001**, *344* (3–4), 339–344. https://doi.org/10.1016/S0009-2614(01)00790-4.

(84) Ishaq, T.; Ehsan, Z.; Qayyum, A.; Abbas, Y.; Irfan, A.; Al-Hussain, S. A.; Irshad, M. A.; Zaki, M. E. A. Recent Strategies to Improve the Photocatalytic Efficiency of TiO2 for Enhanced Water Splitting to Produce Hydrogen. *Catalysts* **2024**, *14* (10), 674. https://doi.org/10.3390/catal14100674.

(85) Linsebigler, A. L.; Lu, G.; Yates, J. T. Photocatalysis on TiO2 Surfaces: Principles, Mechanisms, and Selected Results. *Chem. Rev.* **1995**, *95* (3), 735–758. https://doi.org/10.1021/cr00035a013.

(86) Philip Colombo, D.; Roussel, K. A.; Saeh, J.; Skinner, D. E.; Cavaleri, J. J.; Bowman, R. M. Femtosecond Study of the Intensity Dependence of Electron-Hole Dynamics in TiO2 Nanoclusters. *Chem. Phys. Lett.* **1995**, *232* (3), 207–214. https://doi.org/10.1016/0009-2614(94)01343-T.

(87) Wang, Q.; Domen, K. Particulate Photocatalysts for Light-Driven Water Splitting: Mechanisms, Challenges, and Design Strategies. *Chem. Rev.* **2020**, *120* (2), 919–985. https://doi.org/10.1021/acs.chemrev.9b00201.

(88) Yamaguti, K.; Sato, S. Photolysis of Water over Metallized Powdered Titanium Dioxide. *J. Chem. Soc., Faraday Trans. 1* **1985**, *81* (5), 1237. https://doi.org/10.1039/f19858101237.

(89) Christoforidis, K. C.; Fornasiero, P. Photocatalytic Hydrogen Production: A Rift into the Future Energy Supply. *ChemCatChem* **2017**, *9* (9), 1523–1544. https://doi.org/10.1002/cctc.201601659.

(90) Zani, L.; Melchionna, M.; Montini, T.; Fornasiero, P. Design of Dye-Sensitized TiO_2 Materials for Photocatalytic Hydrogen Production: Light and Shadow. *J. Phys. Energy* **2021**, *3* (3), 031001. https://doi.org/10.1088/2515-7655/abe04b.

(91) Fajrina, N.; Tahir, M. A Critical Review in Strategies to Improve Photocatalytic Water Splitting towards Hydrogen Production. *Int. J. Hydrogen Energy* **2019**, *44* (2), 540–577. https://doi.org/10.1016/j.ijhydene.2018.10.200.

(92) Willkomm, J.; Orchard, K. L.; Reynal, A.; Pastor, E.; Durrant, J. R.; Reisner, E. Dye-Sensitised Semiconductors Modified with Molecular Catalysts for Light-Driven H_2 Production. *Chem. Soc. Rev.* **2016**, *45* (1), 9–23. https://doi.org/10.1039/C5CS00733J.

(93) Xu, J.; Wang, W.; Sun, S.; Wang, L. Enhancing Visible-Light-Induced Photocatalytic Activity by Coupling with Wide-Band-Gap Semiconductor: A Case Study on Bi2WO6/TiO2. *Appl. Catal. B: Environmental* **2012**, *111–112*, 126–132. https://doi.org/10.1016/j.apcatb.2011.09.025.

(94) Arora, I.; Chawla, H.; Chandra, A.; Sagadevan, S.; Garg, S. Advances in the Strategies for Enhancing the Photocatalytic Activity of TiO2: Conversion from UV-Light Active to Visible-Light Active Photocatalyst. *Inorg. Chem. Commun.* **2022**, *143*, 109700. https://doi.org/10.1016/j.inoche.2022.109700.

(95) Jin, R.; Cao, Y.; Mirkin, C. A.; Kelly, K. L.; Schatz, G. C.; Zheng, J. G. Photoinduced Conversion of Silver Nanospheres to Nanoprisms. *Science (1979)* **2001**, *294* (5548), 1901–1903. https://doi.org/10.1126/science.1066541.

(96) Kowalska, E.; Abe, R.; Ohtani, B. Visible Light-Induced Photocatalytic Reaction of Gold-Modified Titanium(Iv) Oxide Particles: Action Spectrum Analysis. *Chem. Commun.* **2009**, No. 2, 241–243. https://doi.org/10.1039/B815679D.

(97) Xiao, B.; Wang, X.; Huang, H.; Zhu, M.; Yang, P.; Wang, Y.; Du, Y. Improved Superiority by Covalently Binding Dye to Graphene for Hydrogen Evolution from Water under Visible-Light Irradiation. *J. Phys. Chem. C* **2013**, *117* (41), 21303–21311. https://doi.org/10.1021/jp405497j.

(98) Reginato, G.; Zani, L.; Calamante, M.; Mordini, A.; Dessì, A. Dye-Sensitized Heterogeneous Photocatalysts for Green Redox Reactions. *Eur. J. Inorg. Chem.* **2020**, *2020* (11–12), 899–917. https://doi.org/10.1002/ejic.201901174.

(99) Bartolini, M.; Gombac, V.; Sinicropi, A.; Reginato, G.; Dessì, A.; Mordini, A.; Filippi, J.; Montini, T.; Calamante, M.; Fornasiero, P.; Zani, L. Tuning the Properties of Benzothiadiazole Dyes for Efficient Visible Light-Driven Photocatalytic H_2 Production under Different Conditions. *ACS Appl. Energy Mater.* **2020**, *3* (9), 8912–8928. https://doi.org/10.1021/acsaem.0c01391.

(100) Gonuguntla, S.; Kamesh, R.; Pal, U.; Chatterjee, D. Dye Sensitization of TiO2 Relevant to Photocatalytic Hydrogen Generation: Current Research Trends and Prospects. *J. Photochem. Photobiol. C* **2023**, *57*, 100621. https://doi.org/10.1016/j.jphotochemrev.2023.100621.

(101) Grätzel, M. Photoelectrochemical Cells. *Nature* **2001**, *414* (6861), 338–344. https://doi.org/10.1038/35104607.

(102) Niu, F.; Wang, D.; Li, F.; Liu, Y.; Shen, S.; Meyer, T. J. Hybrid Photoelectrochemical Water Splitting Systems: From Interface Design to System Assembly. *Adv. Energy Mater.* **2020**, *10* (11). https://doi.org/10.1002/aenm.201900399.

(103) Swierk, J. R.; Mallouk, T. E. Design and Development of Photoanodes for Water-Splitting Dye-Sensitized Photoelectrochemical Cells. *Chem. Soc. Rev.* **2013**, *42* (6), 2357–2387. https://doi.org/10.1039/C2CS35246J.

(104) Cheng, C.; Zhang, W.; Chen, X.; Peng, S.; Li, Y. Strategies for Improving Photoelectrochemical Water Splitting Performance of Si-based Electrodes. *Energy Sci. Eng.* **2022**, *10* (4), 1526–1543. https://doi.org/10.1002/ese3.1087.

(105) Collomb, M.-N.; Morales, D. V.; Astudillo, C. N.; Dautreppe, B.; Fortage, J. Hybrid Photoanodes for Water Oxidation Combining a Molecular Photosensitizer with a Metal Oxide Oxygen-Evolving Catalyst. *Sustain. Energy Fuels* **2020**, *4* (1), 31–49. https://doi.org/10.1039/C9SE00597H.

(106) Swierk, J. R.; Mallouk, T. E. Design and Development of Photoanodes for Water-Splitting Dye-Sensitized Photoelectrochemical Cells. *Chem. Soc. Rev.* **2013**, *42* (6), 2357–2387. https://doi.org/10.1039/C2CS35246J.

(107) Kasahara, A.; Nukumizu, K.; Takata, T.; Kondo, J. N.; Hara, M.; Kobayashi, H.; Domen, K. $LaTiO_2N$ as a Visible-Light (≤600 Nm)-Driven Photocatalyst (2). *J. Phys. Chem. B* **2003**, *107* (3), 791–797. https://doi.org/10.1021/jp026767q.

(108) Ohashi, K.; Uosaki, K.; Bockris, J. O. Cathodes For Photodriven Hydrogen Generators: Znte and Cdte. *Int. J. Energy Res.* **1977**, *1* (1), 25–30. https://doi.org/10.1002/er.4440010104.

(109) Sherman, B. D.; McMillan, N. K.; Willinger, D.; Leem, G. Sustainable Hydrogen Production from Water Using Tandem Dye-Sensitized Photoelectrochemical Cells. *Nano Converg.* **2021**, *8* (1), 7. https://doi.org/10.1186/s40580-021-00257-8.

(110) Yokoyama, D.; Minegishi, T.; Maeda, K.; Katayama, M.; Kubota, J.; Yamada, A.; Konagai, M.; Domen, K. Photoelectrochemical Water Splitting Using a Cu(In,Ga)Se2 Thin Film. *Electrochem. commun.* **2010**, *12* (6), 851–853. https://doi.org/10.1016/j.elecom.2010.04.004.

(111) Ohashi, K.; Uosaki, K.; Bockris, J. O. Cathodes For Photodriven Hydrogen Generators: Znte and Cdte. *Int J Energy Res* **1977**, *1* (1), 25–30. https://doi.org/10.1002/er.4440010104.

(112) Kasahara, A.; Nukumizu, K.; Takata, T.; Kondo, J. N.; Hara, M.; Kobayashi, H.; Domen, K. $LaTiO_2N$ as a Visible-Light (≤600 Nm)-Driven Photocatalyst (2). *J Phys Chem B* **2003**, *107* (3), 791–797. https://doi.org/10.1021/jp026767q.

(113) Yu, Z.; Li, F.; Sun, L. Recent Advances in Dye-Sensitized Photoelectrochemical Cells for Solar Hydrogen Production Based on Molecular Components. *Energy Environ. Sci.* **2015**, *8* (3), 760–775. https://doi.org/10.1039/C4EE03565H.

(114) Decavoli, C.; Boldrini, C. L.; Manfredi, N.; Abbotto, A. Molecular Organic Sensitizers for Photoelectrochemical Water Splitting. *Eur. J. Inorg. Chem.* **2020**, *2020* (11–12), 978–999. https://doi.org/10.1002/ejic.202000026.

(115) Concepcion, J. J.; Jurss, J. W.; Brennaman, M. K.; Hoertz, P. G.; Patrocinio, A. O. T.; Murakami Iha, N. Y.; Templeton, J. L.; Meyer, T. J. Making Oxygen with Ruthenium Complexes. *Acc. Chem. Res.* **2009**, *42* (12), 1954–1965. https://doi.org/10.1021/ar9001526.

(116) Song, W.; Chen, Z.; Glasson, C. R. K.; Hanson, K.; Luo, H.; Norris, M. R.; Ashford, D. L.; Concepcion, J. J.; Brennaman, M. K.; Meyer, T. J. Interfacial Dynamics and Solar Fuel Formation in Dye-Sensitized Photoelectrosynthesis Cells. *ChemPhysChem* **2012**, *13* (12), 2882–2890. https://doi.org/10.1002/cphc.201200100.

(117) Xu, P.; McCool, N. S.; Mallouk, T. E. Water Splitting Dye-Sensitized Solar Cells. *Nano Today* **2017**, *14*, 42–58. https://doi.org/10.1016/j.nantod.2017.04.009.

(118) Li, L.; Duan, L.; Wen, F.; Li, C.; Wang, M.; Hagfeldt, A.; Sun, L. Visible Light Driven Hydrogen Production from a Photo-Active Cathode Based on a Molecular Catalyst and Organic Dye-Sensitized p-Type Nanostructured NiO. *Chem. Commun.* **2012**, *48* (7), 988–990. https://doi.org/10.1039/C2CC16101J.

(119) Antila, L. J.; Ghamgosar, P.; Maji, S.; Tian, H.; Ott, S.; Hammarström, L. Dynamics and Photochemical H_2 Evolution of Dye–NiO Photocathodes with a Biomimetic FeFe-Catalyst. *ACS Energy Lett.* **2016**, *1* (6), 1106–1111. https://doi.org/10.1021/acsenergylett.6b00506.

(120) Brennaman, M. K.; Dillon, R. J.; Alibabaei, L.; Gish, M. K.; Dares, C. J.; Ashford, D. L.; House, R. L.; Meyer, G. J.; Papanikolas, J. M.; Meyer, T. J. Finding the Way to Solar Fuels with Dye-Sensitized Photoelectrosynthesis Cells. *J. Am. Chem. Soc.* **2016**, *138* (40), 13085–13102. https://doi.org/10.1021/jacs.6b06466.

(121) Sherman, B. D.; Sheridan, M. V.; Wee, K.-R.; Marquard, S. L.; Wang, D.; Alibabaei, L.; Ashford, D. L.; Meyer, T. J. A Dye-Sensitized Photoelectrochemical Tandem Cell for Light Driven Hydrogen Production from Water. *J. Am. Chem. Soc.* **2016**, *138* (51), 16745–16753. https://doi.org/10.1021/jacs.6b10699.

(122) Zhang, S.; Ye, H.; Ding, H.; Yu, F.; Hua, J. Photo-Driven Water Splitting Photoelectrochemical Cells by Tandem Organic Dye Sensitized Solar Cells with I−/I3− as Redox Mediator. *Sci. China Chem.* **2020**, *63* (2), 228–236. https://doi.org/10.1007/s11426-019-9596-7.

(123) McDaniel, N. D.; Bernhard, S. Solar Fuels: Thermodynamics, Candidates, Tactics, and Figures of Merit. *Dalton Trans.* **2010**, *39* (42), 10021. https://doi.org/10.1039/c0dt00454e.

(124) Gatty, M. G.; Pullen, S.; Sheibani, E.; Tian, H.; Ott, S.; Hammarström, L. Direct Evidence of Catalyst Reduction on Dye and Catalyst Co-Sensitized NiO Photocathodes by Mid-Infrared Transient Absorption Spectroscopy. *Chem. Sci.* **2018**, *9* (22), 4983–4991. https://doi.org/10.1039/C8SC00990B.

(125) Gao, Y.; Ding, X.; Liu, J.; Wang, L.; Lu, Z.; Li, L.; Sun, L. Visible Light Driven Water Splitting in a Molecular Device with Unprecedentedly High Photocurrent Density. *J. Am. Chem. Soc.* **2013**, *135* (11), 4219–4222. https://doi.org/10.1021/ja400402d.

(126) Ding, X.; Gao, Y.; Zhang, L.; Yu, Z.; Liu, J.; Sun, L. Visible Light-Driven Water Splitting in Photoelectrochemical Cells with Supramolecular Catalysts on Photoanodes. *ACS Catal* **2014**, *4* (7), 2347–2350. https://doi.org/10.1021/cs500518k.

(127) Ding, X.; Gao, Y.; Fan, T.; Ji, Y.; Zhang, L.; Yu, Z.; Ahlquist, M. S. G.; Sun, L. Silicon Compound Decorated Photoanode for Performance Enhanced Visible Light Driven Water Splitting. *Electrochim. Acta* **2016**, *215*, 682–688. https://doi.org/10.1016/j.electacta.2016.08.152.

(128) Zhang, H.; Chen, G.; Bahnemann, D. W. Photoelectrocatalytic Materials for Environmental Applications. *J. Mater. Chem.* **2009**, *19* (29), 5089. https://doi.org/10.1039/b821991e.

(129) Nayak, A.; Knauf, R. R.; Hanson, K.; Alibabaei, L.; Concepcion, J. J.; Ashford, D. L.; Dempsey, J. L.; Meyer, T. J. Synthesis and Photophysical Characterization of Porphyrin and Porphyrin–Ru(Ii) Polypyridyl Chromophore–Catalyst Assemblies on Mesoporous Metal Oxides. *Chem. Sci.* **2014**, *5* (8), 3115. https://doi.org/10.1039/c4sc00875h.

(130) Ronconi, F.; Syrgiannis, Z.; Bonasera, A.; Prato, M.; Argazzi, R.; Caramori, S.; Cristino, V.; Bignozzi, C. A. Modification of Nanocrystalline WO_3 with a Dicationic Perylene Bisimide: Applications to Molecular Level Solar Water Splitting. *J. Am. Chem. Soc.* **2015**, *137* (14), 4630–4633. https://doi.org/10.1021/jacs.5b01519.

(131) Ni, M.; Leung, M. K. H.; Leung, D. Y. C.; Sumathy, K. A Review and Recent Developments in Photocatalytic Water-Splitting Using TiO2 for Hydrogen Production. *Renew. Sustain. Energy Rev.* **2007**, *11* (3), 401–425. https://doi.org/10.1016/j.rser.2005.01.009.

(132) Xu, Z.; Xiong, D.; Wang, H.; Zhang, W.; Zeng, X.; Ming, L.; Chen, W.; Xu, X.; Cui, J.; Wang, M.; Powar, S.; Bach, U.; Cheng, Y.-B. Remarkable Photocurrent of P-Type Dye-Sensitized Solar Cell Achieved by Size Controlled $CuGaO_2$ Nanoplates. *J. Mater. Chem. A* **2014**, *2* (9), 2968–2976. https://doi.org/10.1039/C3TA14072E.

(133) Renaud, A.; Chavillon, B.; Le Pleux, L.; Pellegrin, Y.; Blart, E.; Boujtita, M.; Pauporté, T.; Cario, L.; Jobic, S.; Odobel, F. CuGaO2: A Promising Alternative for NiO in p-Type Dye Solar Cells. *J. Mater. Chem.* **2012**, *22* (29), 14353. https://doi.org/10.1039/c2jm31908j.

(134) Yu, M.; Natu, G.; Ji, Z.; Wu, Y. P-Type Dye-Sensitized Solar Cells Based on Delafossite $CuGaO_2$ Nanoplates with Saturation Photovoltages Exceeding 460 MV. *J. Phys. Chem. Lett.* **2012**, *3* (9), 1074–1078. https://doi.org/10.1021/jz3003603.

(135) Nattestad, A. Dye-Sensitized CuAlO₂ Photocathodes for Tandem Solar Cell Applications. *J. Photonics Energy* **2011**, *1* (1), 011103. https://doi.org/10.1117/1.3528236.

(136) KORICHE, N.; BOUGUELIA, A.; AIDER, A.; TRARI, M. Photocatalytic Hydrogen Evolution over Delafossite. *Int. J. Hydrogen Energy* **2005**, *30* (7), 693–699. https://doi.org/10.1016/j.ijhydene.2004.06.011.

(137) Leung, J. J.; Warnan, J.; Nam, D. H.; Zhang, J. Z.; Willkomm, J.; Reisner, E. Photoelectrocatalytic H_2 Evolution in Water with Molecular Catalysts Immobilised on p-Si via a Stabilising Mesoporous TiO_2 Interlayer. *Chem. Sci.* **2017**, *8* (7), 5172–5180. https://doi.org/10.1039/C7SC01277B.

(138) Ji, L.; McDaniel, M. D.; Wang, S.; Posadas, A. B.; Li, X.; Huang, H.; Lee, J. C.; Demkov, A. A.; Bard, A. J.; Ekerdt, J. G.; Yu, E. T. A Silicon-Based Photocathode for Water Reduction with an Epitaxial SrTiO3 Protection Layer and a Nanostructured Catalyst. *Nat. Nanotechnol.* **2015**, *10* (1), 84–90. https://doi.org/10.1038/nnano.2014.277.

(139) Ding, X.; Zhang, L.; Wang, Y.; Liu, A.; Gao, Y. Design of Photoanode-Based Dye-Sensitized Photoelectrochemical Cells Assembling with Transition Metal Complexes for Visible Light-Induced Water Splitting. *Coord. Chem. Rev.* **2018**, *357*, 130–143. https://doi.org/10.1016/j.ccr.2017.10.020.

(140) Moore, G. F.; Blakemore, J. D.; Milot, R. L.; Hull, J. F.; Song, H.; Cai, L.; Schmuttenmaer, C. A.; Crabtree, R. H.; Brudvig, G. W. A Visible Light Water-Splitting Cell with a Photoanode Formed by Codeposition of a High-Potential Porphyrin and an Iridium Water-Oxidation Catalyst. *Energy Environ. Sci.* **2011**, *4* (7), 2389. https://doi.org/10.1039/c1ee01037a.

(141) Li, F.; Fan, K.; Xu, B.; Gabrielsson, E.; Daniel, Q.; Li, L.; Sun, L. Organic Dye-Sensitized Tandem Photoelectrochemical Cell for Light Driven Total Water Splitting. *J. Am. Chem. Soc.* **2015**, *137* (28), 9153–9159. https://doi.org/10.1021/jacs.5b04856.

(142) Zhang, L.; Gao, Y.; Ding, X.; Yu, Z.; Sun, L. High-Performance Photoelectrochemical Cells Based on a Binuclear Ruthenium Catalyst for Visible-Light-Driven Water Oxidation. *ChemSusChem* **2014**, *7* (10), 2801–2804. https://doi.org/10.1002/cssc.201402561.

(143) Ding, X.; Gao, Y.; Zhang, L.; Yu, Z.; Liu, J.; Sun, L. Visible Light-Driven Water Splitting in Photoelectrochemical Cells with Supramolecular Catalysts on Photoanodes. *ACS Catal* **2014**, *4* (7), 2347–2350. https://doi.org/10.1021/cs500518k.

(144) Fan, K.; Li, F.; Wang, L.; Daniel, Q.; Gabrielsson, E.; Sun, L. Pt-Free Tandem Molecular Photoelectrochemical Cells for Water Splitting Driven by Visible Light. *Phys. Chem. Chem. Phys.* **2014**, *16* (46), 25234–25240. https://doi.org/10.1039/C4CP04489D.

(145) Martini, L. A.; Moore, G. F.; Milot, R. L.; Cai, L. Z.; Sheehan, S. W.; Schmuttenmaer, C. A.; Brudvig, G. W.; Crabtree, R. H. Modular Assembly of High-Potential Zinc Porphyrin Photosensitizers Attached to TiO_2 with a Series of Anchoring Groups. *J. Phys. Chem. C* **2013**, *117* (28), 14526–14533. https://doi.org/10.1021/jp4053456.

(146) Yan, X.; Sakai, K.; Ozawa, H. Highly Efficient and Stable Molecular-Based TiO_2 Photoanodes for Photoelectrochemical Water Splitting Achieved by Pyridyl Anchoring Technique. *ACS Catal* **2023**, *13* (20), 13456–13465. https://doi.org/10.1021/acscatal.3c03136.

(147) Takijiri, K.; Morita, K.; Nakazono, T.; Sakai, K.; Ozawa, H. Highly Stable Chemisorption of Dyes with Pyridyl Anchors over TiO_2 : Application in Dye-Sensitized Photoelectrochemical Water Reduction in Aqueous Media. *Chem. comm.* **2017**, *53* (21), 3042–3045. https://doi.org/10.1039/C6CC10321A.

(148) Caspar, J. V.; Meyer, T. J. Photochemistry of MLCT Excited States. Effect of Nonchromophoric Ligand Variations on Photophysical Properties in the Series Cis-Ru(Bpy)2L22+. *Inorg. Chem.* **1983**, *22* (17), 2444–2453. https://doi.org/10.1021/ic00159a021.

(149) Youngblood, W. J.; Lee, S.-H. A.; Kobayashi, Y.; Hernandez-Pagan, E. A.; Hoertz, P. G.; Moore, T. A.; Moore, A. L.; Gust, D.; Mallouk, T. E. Photoassisted Overall Water Splitting in a Visible Light-Absorbing Dye-Sensitized Photoelectrochemical Cell. *J. Am. Chem. Soc.* **2009**, *131* (3), 926–927. https://doi.org/10.1021/ja809108y.

(150) Sheridan, M. V.; Wang, Y.; Wang, D.; Troian-Gautier, L.; Dares, C. J.; Sherman, B. D.; Meyer, T. J. Light-Driven Water Splitting Mediated by Photogenerated Bromine. *Angew. Chem. Int. Ed.* **2018**, *130* (13), 3507–3511. https://doi.org/10.1002/ange.201708879.

(151) Gross, M. A.; Creissen, C. E.; Orchard, K. L.; Reisner, E. Photoelectrochemical Hydrogen Production in Water Using a Layer-by-Layer Assembly of a Ru Dye and Ni Catalyst on NiO. *Chem. Sci.* **2016**, *7* (8), 5537–5546. https://doi.org/10.1039/C6SC00715E.

(152) Ji, Z.; He, M.; Huang, Z.; Ozkan, U.; Wu, Y. Photostable P-Type Dye-Sensitized Photoelectrochemical Cells for Water Reduction. *J. Am. Chem. Soc.* **2013**, *135* (32), 11696–11699. https://doi.org/10.1021/ja404525e.

(153) Gao, Y.; Ding, X.; Liu, J.; Wang, L.; Lu, Z.; Li, L.; Sun, L. Visible Light Driven Water Splitting in a Molecular Device with Unprecedentedly High Photocurrent Density. *J Am Chem Soc* **2013**, *135* (11), 4219–4222. https://doi.org/10.1021/ja400402d.

(154) Kou, Y.; Nakatani, S.; Sunagawa, G.; Tachikawa, Y.; Masui, D.; Shimada, T.; Takagi, S.; Tryk, D. A.; Nabetani, Y.; Tachibana, H.; Inoue, H. Visible Light-Induced Reduction of Carbon Dioxide Sensitized by a Porphyrin–Rhenium Dyad Metal Complex on p-Type Semiconducting NiO as the Reduction Terminal End of an Artificial Photosynthetic System. *J. Catal.* **2014**, *310*, 57–66. https://doi.org/10.1016/j.jcat.2013.03.025.

(155) Muñoz-García, A. B.; Benesperi, I.; Boschloo, G.; Concepcion, J. J.; Delcamp, J. H.; Gibson, E. A.; Meyer, G. J.; Pavone, M.; Pettersson, H.; Hagfeldt, A.; Freitag, M. Dye-Sensitized Solar Cells Strike Back. *Chem. Soc. Rev.* **2021**, *50* (22), 12450–12550. https://doi.org/10.1039/D0CS01336F.

(156) Swierk, J. R.; Méndez-Hernández, D. D.; McCool, N. S.; Liddell, P.; Terazono, Y.; Pahk, I.; Tomlin, J. J.; Oster, N. V.; Moore, T. A.; Moore, A. L.; Gust, D.; Mallouk, T. E. Metal-Free Organic Sensitizers for Use in Water-Splitting Dye-Sensitized Photoelectrochemical Cells. *PNAS* **2015**, *112* (6), 1681–1686. https://doi.org/10.1073/pnas.1414901112.

(157) Materna, K. L.; Jiang, J.; Regan, K. P.; Schmuttenmaer, C. A.; Crabtree, R. H.; Brudvig, G. W. Optimization of Photoanodes for Photocatalytic Water Oxidation by Combining a Heterogenized Iridium Water-Oxidation Catalyst with a High-Potential Porphyrin Photosensitizer. *ChemSusChem* **2017**, *10* (22), 4526–4534. https://doi.org/10.1002/CSSC.201701693.

(158) Li, C.; Wonneberger, H. Perylene Imides for Organic Photovoltaics: Yesterday, Today, and Tomorrow. *Adv. Mater.* **2012**, *24* (5), 613–636. https://doi.org/10.1002/adma.201104447.

(159) Pasaogullari, N.; Icil, H.; Demuth, M. Symmetrical and Unsymmetrical Perylene Diimides: Their Synthesis, Photophysical and Electrochemical Properties. *Dyes Pigm.* **2006**, *69* (3), 118–127. https://doi.org/10.1016/j.dyepig.2005.03.001.

(160) Raavi, S. S. K.; Docampo, P.; Wehrenfennig, C.; Alcocer, M. J. P.; Sadoughi, G.; Herz, L. M.; Snaith, H. J.; Petrozza, A. Impact of Molecular Charge-Transfer States on Photocurrent Generation in Solid State Dye-Sensitized Solar Cells Employing Low-Band-Gap Dyes. *J. Phys. Chem. C* **2014**, *118* (30), 16825–16830. https://doi.org/10.1021/jp5000667.

(161) Kirner, J. T.; Stracke, J. J.; Gregg, B. A.; Finke, R. G. Visible-Light-Assisted Photoelectrochemical Water Oxidation by Thin Films of a Phosphonate-Functionalized Perylene Diimide Plus CoO_x Cocatalyst. *ACS Appl. Mater. Interfaces* **2014**, *6* (16), 13367–13377. https://doi.org/10.1021/am405598w.

(162) Creissen, C. E.; Warnan, J.; Antón-García, D.; Farré, Y.; Odobel, F.; Reisner, E. Inverse Opal $CuCrO_2$ Photocathodes for H_2 Production Using Organic Dyes and a Molecular Ni Catalyst. *ACS Catal.* **2019**, *9* (10), 9530–9538. https://doi.org/10.1021/acscatal.9b02984.

(163) Decavoli, C.; Boldrini, C. L.; Faroldi, F.; Baldini, L.; Sansone, F.; Ranaudo, A.; Greco, C.; Cosentino, U.; Moro, G.; Manfredi, N.; Abbotto, A. Calix[4]Arene-Based Sensitizers for Host-Guest Supramolecular Dyads for Solar Energy Conversion in Photoelectrochemical Cells. *Eur. J. Org. Chem.* **2022**, *2022* (34), e202200649. https://doi.org/10.1002/ejoc.202200649.

(164) Manfredi, N.; Boldrini, C. L.; Abbotto, A. Organic Sensitizers for Photoanode Water Splitting in Dye-Sensitized Photoelectrochemical Cells. *ChemElectroChem* **2018**, *5* (17), 2395–2402. https://doi.org/10.1002/CELC.201800592.

(165) Decavoli, C.; Boldrini, C. L.; Trifiletti, V.; Luong, S.; Fenwick, O.; Manfredi, N.; Abbotto, A. Dye–Catalyst Dyads for Photoelectrochemical Water Oxidation Based on Metal-Free Sensitizers. *RSC Adv.* **2021**, *11* (10), 5311–5319. https://doi.org/10.1039/D0RA10971A.

(166) Luo, T.; Li, X. A.; Bai, C. J.; Lv, C. Y.; Huang, J. F.; Liu, J. M. Bias-Free Photoelectrochemical Water Splitting Cells Constructed by Calixarene Dyes and Molecular Ru Catalysts via Pyridyl Anchoring Groups. *ACS Appl. Energy Mater.* **2021**, *4* (12), 14671–14680. https://doi.org/https://doi.org/10.1021/ACSAEM.1C03301.

(167) Zhu, Y.; Wang, D.; Ni, W.; Gurzadyan, G. G.; Sun, L.; Meyer, T. J.; Li, F. Water Oxidation by a Noble Metal-Free Photoanode Modified with an Organic Dye and a Molecular Cobalt Catalyst. *J. Phys. Chem. A* **2022**, *10* (16), 9121–9128. https://doi.org/10.1039/D2TA00573E.

(168) Wee, K. R.; Sherman, B. D.; Brennaman, M. K.; Sheridan, M. V.; Nayak, A.; Alibabaei, L.; Meyer, T. J. An Aqueous, Organic Dye Derivatized SnO2/TiO2 Core/Shell Photoanode. *J. Phys. Chem. A* **2016**, *4* (8), 2969–2975. https://doi.org/10.1039/c5ta06678f.

(169) Alibabaei, L.; Dillon, R. J.; Reilly, C. E.; Brennaman, M. K.; Wee, K. R.; Marquard, S. L.; Papanikolas, J. M.; Meyer, T. J. Chromophore-Catalyst Assembly for Water Oxidation Prepared by Atomic Layer Deposition. *ACS Appl. Mater. Interfaces* **2017**, *9* (44), 39018–39026. https://doi.org/https://doi.org/10.1021/ACSAMI.7B11905.

(170) Sokol, K. P.; Robinson, W. E.; Warnan, J.; Kornienko, N.; Nowaczyk, M. M.; Ruff, A.; Zhang, J. Z.; Reisner, E. Bias-Free Photoelectrochemical Water Splitting with Photosystem II on a Dye-Sensitized Photoanode Wired to Hydrogenase. *Nat. Energy* **2018**, *3* (11), 944–951. https://doi.org/10.1038/s41560-018-0232-y.

(171) Eom, Y. K.; Nhon, L.; Leem, G.; Sherman, B. D.; Wang, D.; Troian-Gautier, L.; Kim, S.; Kim, J.; Meyer, T. J.; Reynolds, J. R.; Schanze, K. S. Visible-Light-Driven Photocatalytic Water Oxidation by a π-Conjugated Donor-Acceptor-Donor Chromophore/Catalyst Assembly. *ACS Energy Lett.* **2018**, *3* (9), 2114–2119. https://doi.org/https://doi.org/10.1021/ACSENERGYLETT.8B0102.

(172) He, G. S.; Tan, L. S.; Zheng, Q.; Prasad, P. N. Multiphoton Absorbing Materials: Molecular Designs, Characterizations, and Applications. *Chem. Rev.* **2008**, *108* (4), 1245–1330. https://doi.org/https://doi.org/10.1021/CR050054X.

(173) Kirner, J. T.; Finke, R. G. Sensitization of Nanocrystalline Metal Oxides with a Phosphonate-Functionalized Perylene Diimide for Photoelectrochemical Water Oxidation with a CoOx Catalyst. *ACS Appl. Mater. Interfaces* **2017**, *9* (33), 27625–27637. https://doi.org/10.1021/ACSAMI.7B05874/ASSET/IMAGES/LARGE/AM-2017-05874V_0008.JPEG.

(174) Seenivasan, S.; Adhikari, S.; Kim, D. H. Surface Restructuring of Hematite Photoanodes through Ultrathin NiFeOx Catalyst: Amplified Charge Collection for Solar Water Splitting and Pollutant Degradation. *J. Chem. Eng.* **2021**, *422*, 130137. https://doi.org/10.1016/J.CEJ.2021.130137.

(175) Gao, L.; Guo, C.; Sun, X.; Sun, X.; Yang, H.; Xie, J.; Ma, X.; Zhao, M.; Zhu, X.; Wei, Q. CoFeOx(OH)y/CoOx(OH)y Core/Shell Structure with Amorphous Interface as an Advanced Catalyst for Electrocatalytic Water Splitting. *Electrochim. Acta* **2020**, *341*, 136038. https://doi.org/10.1016/J.ELECTACTA.2020.136038.

(176) Hessels, J.; Detz, R. J.; Koper, M. T. M.; Reek, J. N. H. Rational Design Rules for Molecular Water Oxidation Catalysts Based on Scaling Relationships. *Chem. Eur. J.* **2017**, *23* (65), 16413–16418. https://doi.org/10.1002/CHEM.201702850.

(177) Duan, L.; Tong, L.; Xu, Y.; Sun, L. Visible Light-Driven Water Oxidation—from Molecular Catalysts to Photoelectrochemical Cells. *Energy Environ. Sci.* **2011**, *4* (9), 3296–3313. https://doi.org/10.1039/C1EE01276B.

(178) Romain, S.; Vigara, L.; Llobet, A. Oxygen−Oxygen Bond Formation Pathways Promoted by Ruthenium Complexes. *Acc. Chem. Res.* **2009**, *42* (12), 1944–1953. https://doi.org/10.1021/ar900240w.

(179) Gersten, S. W.; Samuels, G. J.; Meyer, T. J. Catalytic Oxidation of Water by an Oxo-Bridged Ruthenium Dimer. *J. Am. Chem. Soc.* **1982**, *104* (14), 4029–4030. https://doi.org/10.1021/JA00378A053/ASSET/JA00378A053.FP.PNG_V03.

(180) Duan, L.; Fischer, A.; Xu, Y.; Sun, L. Isolated Seven-Coordinate Ru(IV) Dimer Complex with [HOHOH]-Bridging Ligand as an Intermediate for Catalytic Water Oxidation. *J. Am. Chem. Soc.* **2009**, *131* (30), 10397–10399. https://doi.org/https://doi.org/10.1021/JA9034686.

(181) Wang, L.; Duan, L.; Wang, Y.; Ahlquist, M. S. G.; Sun, L. Highly Efficient and Robust Molecular Water Oxidation Catalysts Based on Ruthenium Complexes. *Chem. comm.* **2014**, *50* (85), 12947–12950. https://doi.org/10.1039/C4CC05069J.

(182) Duan, L.; Bozoglian, F.; Mandal, S.; Stewart, B.; Privalov, T.; Llobet, A.; Sun, L. A Molecular Ruthenium Catalyst with Water-Oxidation Activity Comparable to That of Photosystem II. *Nat. Chem* **2012**, *4* (5), 418–423. https://doi.org/10.1038/nchem.1301.

(183) Kamire, R. J.; Materna, K. L.; Hoffeditz, W. L.; Phelan, B. T.; Thomsen, J. M.; Farha, O. K.; Hupp, J. T.; Brudvig, G. W.; Wasielewski, M. R. Photodriven Oxidation of Surface-Bound Iridium-Based Molecular Water-Oxidation Catalysts on Perylene-3,4-Dicarboximide-Sensitized TiO2 Electrodes Protected by an Al2O3 Layer. *J. Phys. Chem. C* **2017**, *121* (7), 3752–3764. https://doi.org/https://doi.org/10.1021/ACS.JPCC.6B11672.

(184) Thomsen, J. M.; Huang, D. L.; Crabtree, R. H.; Brudvig, G. W. Iridium-Based Complexes for Water Oxidation. *Dalton Trans.* **2015**, *44* (28), 12452–12472. https://doi.org/10.1039/C5DT00863H.

(185) McDaniel, N. D.; Coughlin, F. J.; Tinker, L. L.; Bernhard, S. Cyclometalated Iridium(III) Aquo Complexes: Efficient and Tunable Catalysts for the Homogeneous Oxidation of Water. *J. Am. Chem. Soci.* **2008**, *130* (1), 210–217. https://doi.org/10.1021/ja074478f.

(186) Hull, J. F.; Balcells, D.; Blakemore, J. D.; Incarvito, C. D.; Eisenstein, O.; Brudvig, G. W.; Crabtree, R. H. Highly Active and Robust Cp* Iridium Complexes for Catalytic Water Oxidation. *J. Am. Chem. Soc.* **2009**, *131* (25), 8730–8731. https://doi.org/10.1021/ja901270f.

(187) Blakemore, J. D.; Schley, N. D.; Balcells, D.; Hull, J. F.; Olack, G. W.; Incarvito, C. D.; Eisenstein, O.; Brudvig, G. W.; Crabtree, R. H. Half-Sandwich Iridium Complexes for Homogeneous Water-Oxidation Catalysis. *J. Am. Chem. Soc.* **2010**, *132* (45), 16017–16029. https://doi.org/10.1021/ja104775j.

(188) Naruta, Y.; Sasayama, M.; Sasaki, T. Oxygen Evolution by Oxidation of Water with Manganese Porphyrin Dimers. *Angew. Chem., Int. Ed.* **1994**, *33* (18), 1839–1841. https://doi.org/10.1002/anie.199418391.

(189) Limburg, J.; Vrettos, J. S.; Liable-Sands, L. M.; Rheingold, A. L.; Crabtree, R. H.; Brudvig, G. W. A Functional Model for O-O Bond Formation by the O_2-Evolving Complex in Photosystem II. *Science (1979)* **1999**, *283* (5407), 1524–1527. https://doi.org/10.1126/science.283.5407.1524.

(190) Baffert, C.; Artero, V.; Fontecave, M. Cobaloximes as Functional Models for Hydrogenases. 2. Proton Electroreduction Catalyzed by Difluoroborylbis(Dimethylglyoximato)Cobalt(II) Complexes in Organic Media. *Inorg. Chem.* **2007**, *46* (5), 1817–1824. https://doi.org/10.1021/IC061625M/SUPPL_FILE/IC061625MSI20061116_042029.PDF.

(191) Muckerman, J. T.; Fujita, E. Theoretical Studies of the Mechanism of Catalytic Hydrogen Production by a Cobaloxime. *Chem. Comm.* **2011**, *47* (46), 12456–12458. https://doi.org/10.1039/C1CC15330G.

(192) Solis, B. H.; Hammes-Schiffer, S. Substituent Effects on Cobalt Diglyoxime Catalysts for Hydrogen Evolution. *J. Am. Chem. Soc.* **2011**, *133* (47), 19036–19039. https://doi.org/https://doi.org/10.1021/JA208091E.

(193) Cline, E. D.; Adamson, S. E.; Bernhard, S. Homogeneous Catalytic System for Photoinduced Hydrogen Production Utilizing Iridium and Rhodium Complexes. *Inorg. Chem.* **2008**, *47* (22), 10378–10388. https://doi.org/10.1021/IC800988B.

(194) Bhugun, I.; Lexa, D.; Savéant, J. M. Homogeneous Catalysis of Electrochemical Hydrogen Evolution by Iron(0) Porphyrins. *J. Am. Chem. Soc.* **1996**, *118* (16), 3982–3983. https://doi.org/10.1021/JA954326X.

(195) Gong, M.; Wang, D. Y.; Chen, C. C.; Hwang, B. J.; Dai, H. A Mini Review on Nickel-Based Electrocatalysts for Alkaline Hydrogen Evolution Reaction. *Nano Res.* **2016**, *9* (1), 28–46. https://doi.org/10.1007/S12274-015-0965-X/METRICS.

(196) Papageorgiou, N. Counter-Electrode Function in Nanocrystalline Photoelectrochemical Cell Configurations. *Coord Chem Rev* **2004**, *248* (13–14), 1421–1446. https://doi.org/10.1016/J.CCR.2004.03.028.

(197) Rahman, M. Y. A.; Salleh, M. M.; Talib, I. A.; Yahaya, M. Solid State Photoelectrochemical Cells Utilising Graphite Thin Films Counter Electrode. *Ionics (Kiel)* **2005**, *11* (3–4), 275–280. https://doi.org/10.1007/BF02430389/METRICS.

(198) Lin, C. Y.; Mersch, D.; Jefferson, D. A.; Reisner, E. Cobalt Sulphide Microtube Array as Cathode in Photoelectrochemical Water Splitting with Photoanodes. *Chem. Sci.* **2014**, *5* (12), 4906–4913. https://doi.org/10.1039/C4SC01811G.

(199) Zhang, S.; Li, X.; Yun, K.; Yu, F.; Hua, J. Effects of Electrolytes on the Photocurrent of N-Annulated Perylene-Sensitized Photoelectrochemical Cells Based on NiO as Photocathode. *ChemElectroChem* **2018**, *5* (21), 3198–3205. https://doi.org/10.1002/CELC.201801038.

(200) Krawicz, A.; Yang, J.; Anzenberg, E.; Yano, J.; Sharp, I. D.; Moore, G. F. Photofunctional Construct That Interfaces Molecular Cobalt-Based Catalysts for H2 Production to a Visible-Light-Absorbing Semiconductor. *J. Am. Chem. Soc.* **2013**, *135* (32), 11861–11868. https://doi.org/10.1021/JA404158R.

(201) Li, F.; Zhang, B.; Li, X.; Jiang, Y.; Chen, L.; Li, Y.; Sun, L.; Li, F.; Zhang, B.; Jiang, Y.; Chen, L.; Li, Y.; Sun, L.; Li, X. Highly Efficient Oxidation of Water by a Molecular Catalyst Immobilized on Carbon Nanotubes. *Angew. Chem. Int. Ed.* **2011**, *50* (51), 12276–12279. https://doi.org/10.1002/ANIE.201105044.

(202) Eberhart, M. S.; Wang, D.; Sampaio, R. N.; Marquard, S. L.; Shan, B.; Brennaman, M. K.; Meyer, G. J.; Dares, C.; Meyer, T. J. Water Photo-Oxidation Initiated by Surface-Bound Organic Chromophores. *J. Am. Chem. Soc.* **2017**, *139* (45), 16248–16255. https://doi.org/https://doi.org/10.1021/jacs.7b08317.

(203) Shi, X.; Cai, L.; Ma, M.; Zheng, X.; Park, J. H. General Characterization Methods for Photoelectrochemical Cells for Solar Water Splitting. *ChemSusChem* **2015**, *8* (19), 3192–3203. https://doi.org/10.1002/cssc.201500075.

(204) Wang, X. L.; Huang, J. F.; Liu, J. M.; Tsiakaras, P. Recent Advances in Metal-Free Photosensitizers for Dye-Sensitized Photoelectrochemical Cells. *Coord. Chem. Rev.* **2025**, *522*, 216143. https://doi.org/10.1016/J.CCR.2024.216143.

(205) Allen J. Bard; Larry R. Faulkner. *Electrochemical Methods: Fundamentals and Applications, 2nd Edition*; New York, USA: Wiley, 2002.

(206) Selli, E.; Chiarello, G. L.; Quartarone, E.; Mustarelli, P.; Rossetti, I.; Forni, L. A Photocatalytic Water Splitting Device for Separate Hydrogen and Oxygen Evolution. *Chem. comm.* **2007**, No. 47, 5022–5024. https://doi.org/10.1039/B711747G.

(207) Araujo, M. N.; Vargas, S. R.; Soares, L. A.; Trindade, L. F.; Fuess, L. T.; Adorno, M. A. T. Rapid Method for Determination of Biogas Composition by Gas Chromatography Coupled to a Thermal Conductivity Detector (GC-TCD). *J. Environ. Anal. Chem.* **2023**. https://doi.org/10.1080/03067319.2023.2210055.

(208) Zhong, D. K.; Gamelin, D. R. Photo-Electrochemical Water Oxidation by Cobalt Catalyst ("Co-Pi")/α-Fe2O3 Composite Photoanodes: Oxygen Evolution and Resolution of a Kinetic Bottleneck. *J. Am. Chem. Soc.* **2010**, *132* (12), 4202–4207. https://doi.org/10.1021/JA908730H.

(209) Singh, Z.; Donnarumma, P. R.; Majewski, M. B. Molecular Copper(I)-Copper(II) Photosensitizer-Catalyst Photoelectrode for Water Oxidation. *Inorg. Chem.* **2020**, *59* (18), 12994–12999. https://doi.org/https://doi.org/10.1021/ACS.JPCC.6B11672.

(210) Chen, Z.; Jaramillo, T. F.; Deutsch, T. G.; Kleiman-Shwarsctein, A.; Forman, A. J.; Gaillard, N.; Garland, R.; Takanabe, K.; Heske, C.; Sunkara, M.; McFarland, E. W.; Domen, K.; Milled, E. L.; Dinh, H. N. Accelerating Materials Development for Photoelectrochemical Hydrogen Production: Standards for Methods, Definitions, and Reporting Protocols. *J. Mater. Res.* **2010**, *25* (1), 3–16. https://doi.org/10.1557/JMR.2010.0020/METRICS.

(211) Li, Z.; Luo, W.; Zhang, M.; Feng, J.; Zou, Z. Photoelectrochemical Cells for Solar Hydrogen Production: Current State of Promising Photoelectrodes, Methods to Improve Their Properties, and Outlook. *Energy Environ. Sci.* **2013**, *6* (2), 347–370. https://doi.org/10.1039/C2EE22618A.

Chapter 2

Outline of the work

This Ph.D. research work concerned the design, synthesis and transformation of new photoactive compounds for application in photocatalysis.

The main section of the work focused on the preparation and characterization of new organic dyes designed to function as anodic photosensitizers in Dye-Sensitized Photoelectrochemical Cells (DSPECs) for water-splitting. Indeed, as widely discussed in the introduction, the dye is pivotal for achieving intense visible light absorption and triggering the water oxidation reaction at the catalytic active site. Consequently, the design of dye molecules with tailored spectro-electrochemical properties is a critical factor in enhancing the performance of these devices.

In addition to this main subject, the research work also explored the potential of near-ultraviolet (UV) and visible light irradiation as a powerful mean for enabling efficient and selective chemical transformations in synthetic chemistry. This part of the activity was carried out in the course of a six month internship in the group of Prof. Dr. Daniele Leonori at RWTH Aachen University (Germany). This dual focus highlights the versatility of photochemical approaches in both energy conversion and molecular synthesis applications.

In line with the various topics addressed during the research, the discussion will be organized into three chapters, the contents of which are briefly outlined below.

- In Chapter 3, we will present the results of our activity dealing with the modeling, synthesis, and characterization of two novel families of D-A-π-A organic dyes. Our aim in this work was to develop new small molecules characterized by strong absorption in the visible region and energy levels optimized for efficient electron transfer in DSPECs. The two dye families were designed with distinct central chromophores: compounds **1a-c**, incorporating a 2,3-diphenylquinoxaline core, and compounds **PP2a-c**, featuring a 2,3-diphenylpyrido[3,4-*b*]pyrazine core. In the case of dyes **1a-c**, three different donor groups of moderate strength were introduced to modulate the energies of the respective HOMO levels and enable the electron transfer from the chosen Ru-based molecular water oxidation catalyst (WOC). Conversely, for dyes **PP2a-c,** three different acceptor/anchor groups were introduced to modulate the energies of the respective LUMO levels, thereby making electron transfer from the oxidized form of the dye to the semiconductor conduction band thermodynamically favored.

  First, a comprehensive computational study, conducted in collaboration with the group of Prof. Adalgisa Sinicropi at the University of Siena, will be presented. This will be followed by a detailed discussion of the synthetic methodologies and spectro-electrochemical characterization carried out for both dye families.

For dyes **1a-c**, the characterization discussion will address both their behaviour in solution and their properties after adsorption onto electrodes composed of thin films of nanocrystalline TiO_2. This section includes an investigation of the charge transfer processes between the dyes and the semiconductor, utilizing femtosecond Transient Absorption Spectroscopy (TAS) studies, conducted in collaboration with the group of Dr. Andrea Barbieri and Dr. Barbara Ventura at ISOF-CNR, Bologna. Additionally, the results of the DS-PEC photoanode fabrication and spectro-electrochemical experiments, aimed at evaluating the new dyes as anodic sensitizers for water splitting in DSPEC under a co-loading approach, will be presented in detail. This work was carried out in collaboration with Dr. Alessandra Sanson's group at ISSMC-CNR, Faenza.

- In Chapter 4, the work conducted to explore different types chromophore/catalyst assemblies, alternative to conventional co-loading strategies, is presented. Indeed, to overcome unfavorable recombination dynamics, our approach involves synthetizing a new metal-free sensitizer-WOC covalent adduct (dyad), in which the catalyst is positioned farther from the electrode surface. In this context, with the aim to obtain a molecular system with a high molar attenuation coefficient and a broad absorption spectrum in the visible region, we took the molecular structure of the previously tested dye **1a** as a starting point, and adapted it to incorporate a crucial peripheral pyridine moiety, essential for coordinating a Ru(bda) unit, chosen also in this case as the water oxidation catalyst, thus forming the dyad.A comprehensive discussion of the design pathways and attempted synthetic routes leading to the successful preparation of the catalytic dyad **D1A2** will be provided. Additionally, the full characterization of the resulting system using various absorption and emission spectroscopy techniques, along with cyclic voltammetry, will be presented, supporting the successful assembly of the dyad.

- In Chapter 5, the research activity carried out during the internship will be described. The project focused on the development of innovative synthetic methodologies utilizing UV and visible light. The work was built upon the group expertise on the photodecomposition of aryl azides into singlet nitrene species, that results, upon formation of seven-membered ring azepine intermediate, in the incorporation of different nucleophiles in *ortho*- position, together with the formal 1,2-shift of the nitrogen functionality. Building on this, the goal of this activity was to create new photochemical techniques for the migration of N-functional groups on aromatic rings but without the need to introduce a second functionality, facilitating the conversion of arylazides into anilines with a regioisomeric substitution pattern. Before describing the ex-

perimental work, a brief general introduction on synthetic photochemical approaches is provided in this chapter. Then, a comprehensive discussion on the synthetic design plan, and the reaction development, as well as a broad substrate scope evaluation, are presented. Additionally, the possibility of employing the key reaction intermediates for the synthesis of diverse ortho-substituted anilines, overcoming limitations of traditional methods and expanding the scope of accessible molecular architectures, will be discussed

Chapter 3

Synthesis, characterization and application of novel organic dyes as anodic sensitizers in photoelectrochemical cells

3.1 Introduction

In the field of artificial photosynthesis, dye-sensitized photoelectrochemical cells (DSPECs) have been extensively investigated in recent years as a promising system to produce solar fuels from water and sunlight.[1] As already discussed in the previous chapters, the major bottleneck in the design of efficient and durable water splitting cells is the catalytic four-electron oxidation of water. Therefore, the design of suitable photosensitizers (PS) and water oxidation catalysts (WOCs), as fundamental elements of a photoanode, stands as a crucial point.[2] However, while the development of WOCs has been the subject of several studies,[3–6] the design of novel photosensitizers for photoanode application has been less developed.

It is worth remembering that the dye represents the heart of the device, having the key roles of absorbing sunlight and transferring the photogenerated electrons into the conduction band (CB) of the semiconductor. Therefore, the optimal dye must: (i) present an intense visible light absorption, possibly stretching to the near-infrared (NIR) region; (ii) possess anchoring groups providing robust linkages to the SC surface under aqueous condition; (iii) have an excited-state oxidation potential more negative than the CB edge of the *n*-type SC and a ground-state oxidation potential more positive than the catalytic onset potential of the WOC; (iv) be easy to synthesize and purify; and (v) be not toxic. In addition, the structure of the dye should allow optimal tuning of its optical (wide and strong light harvesting) and electronic properties, and ensure proper interface and solubility characteristics. Combining all these stringent requirements in the same molecule represents the principal challenge in this field. So far, most studies of dye-sensitized photoanodes have employed $[Ru(bpy)_3]^{2+}$derivatives as photosensitizers, due to their stability in water and suitable electronic and optical properties.[7,8] Meanwhile, metal-free organic dyes have been only scantly investigated.[9] This fact is even more surprising if we consider the massive literature on organic dyes available for other solar-related applications, such as DSSCs or dye sensitized photocatalytic hydrogen generation.[10–12] Despite that, replacing Ru-based dyes with fully organic sensitizers in photoelectrochemical cells could be potentially advantageous thanks to their properties of lower cost, absence of critical or precious metals, simple synthesis and tunable spectroscopic properties.

To date, many of the reports dealing with the use of organic dyes for DS-PEC describe the application of small and relatively simple donor-acceptor molecules, mostly relying on the use of triphenylamine as principal donor unit. Representative D-π-A dyes that summarize the current state of the art, and their corresponding water splitting performances, are shown in Figure 3.1.[13–16]

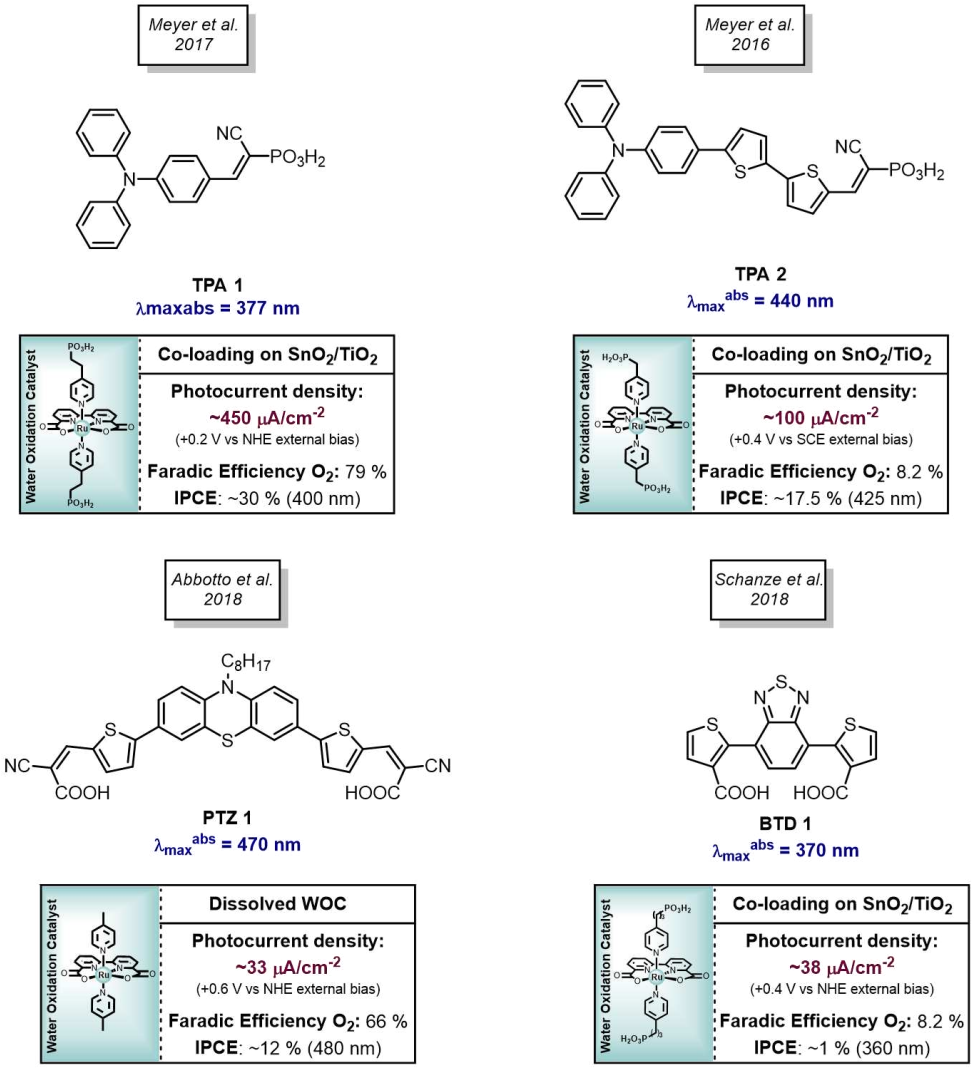

Figure 3.1Representative metal-free organic dyes reported in literature for photoanode sensitization and corresponding performance metrics.

As can be seen, most of these dyes have maximum absorption wavelengths below 450 nm and weak light-harvesting ability in the middle of the visible region, where the emission spectrum of sunlight is maximized. From this results, then, it appears clear that the design of novel molecules with a broad optical response, appropriate energy levels, and good stability is still an open field.

3.2 Aim of the work

Building on the concepts outlined in the previous paragraph, the goal of this project was the development of novel donor-π-acceptor (D-π-A) organic sensitizers showing both improved light-harvesting capability and optimized electrochemical properties for employment in PA-DSPEC.
To achieve this goal, we designed the structures of the new compounds according to the following basic principles: (i) in their conjugated structure, the dyes should feature a chromophore able to impart strong absorption in the visible region, possibly with maximum close to 500 nm; (ii) the

sensitizers should present donor groups of moderate strength, so as to modulate their ground-state oxidation potentials (E_{ox}) and make them compatible with the most common WOCs (*e.g.* Ru-based complexes); (iii) alkyl chains present on the compounds structures could make them more soluble in common organic solvents, facilitating their purification and subsequent handling; (iv) the compounds structures should be easily obtained through a modular synthetic sequence allowing late-stage differentiation. For what concerns the first point, extending the conjugation across D-A architecture is a commonly applied strategy to widen the spectral window. However, cell degradation phenomena have been observed occasionally when longer π-conjugated chromophores have been used as sensitizers. Another possible strategy to extend the absorption window is the incorporation of an auxiliary acceptor in the form of an additional electron-accepting group into the π-bridge. This strategy effectively reduces the HOMO–LUMO bandgap and stabilizing the LUMO[17] and leading to a red-shifted absorption profile. Moreover, the incorporated auxiliary acceptor unit was demonstrated to facilitate the electron transfer from the donor to the acceptor/anchor group.[18] Based on the above considerations, we designed two new families of dyes, compounds **1a-c** and compounds **PP2a-c**, featuring a 2,3-diphenylquinoxaline and 2,3-diphenylpyrido[3,4-*b*]pyrazine core, respectively, as their main chromophore (Figure 3.2). Such central units were selected since they had been already successfully incorporated as auxiliary acceptors in several organic dyes for dye-sensitized solar cells, showing impressive photovoltaic performances and intense light absorption in the visible region.[19] The latter, as mentioned above, is a consequence of the electron-accepting properties provided by the pyrazine ring found in the two moieties. This property is enhanced for pyrido[3,4-*b*]pyrazines, displaying an additional imine nitrogen atom on the pyridine ring.[20,21]

In compounds **1a-c**, the quinoxaline unit has been linked to two thiophene rings, introduced to further extend the conjugation length of the molecules and thus red-shift their absorption spectra. For what concerns the anchoring function, a typical cyanoacrylic acid moiety was chosen in all cases. On the contrary, three different mono- or dialkoxy-substituted benzene rings were employed as the donor groups. These donor moieties were selected due to their weaker electron-donating ability compared to the common donor groups of DSSC sensitizers (*e.g.* triarylamines, indolines)[18], with the aim to obtain compounds with relatively low HOMO energy levels, and thus make electron transfer from the reduced form of the WOC to the oxidized dyes thermodynamically favored. By varying the number and substitution patterns of alkoxy substituents in compounds **1a-c**, we expected to induce changes in the electronic structures of the dyes, allowing us to modulate their E_{ox} values and therefore evaluate the influence of this parameter on device performances.

Finally, the donor groups were decorated with branched or linear alkyl chains to improve the compounds solubility and possibly reduce aggregation upon binding on the semiconductor surface.

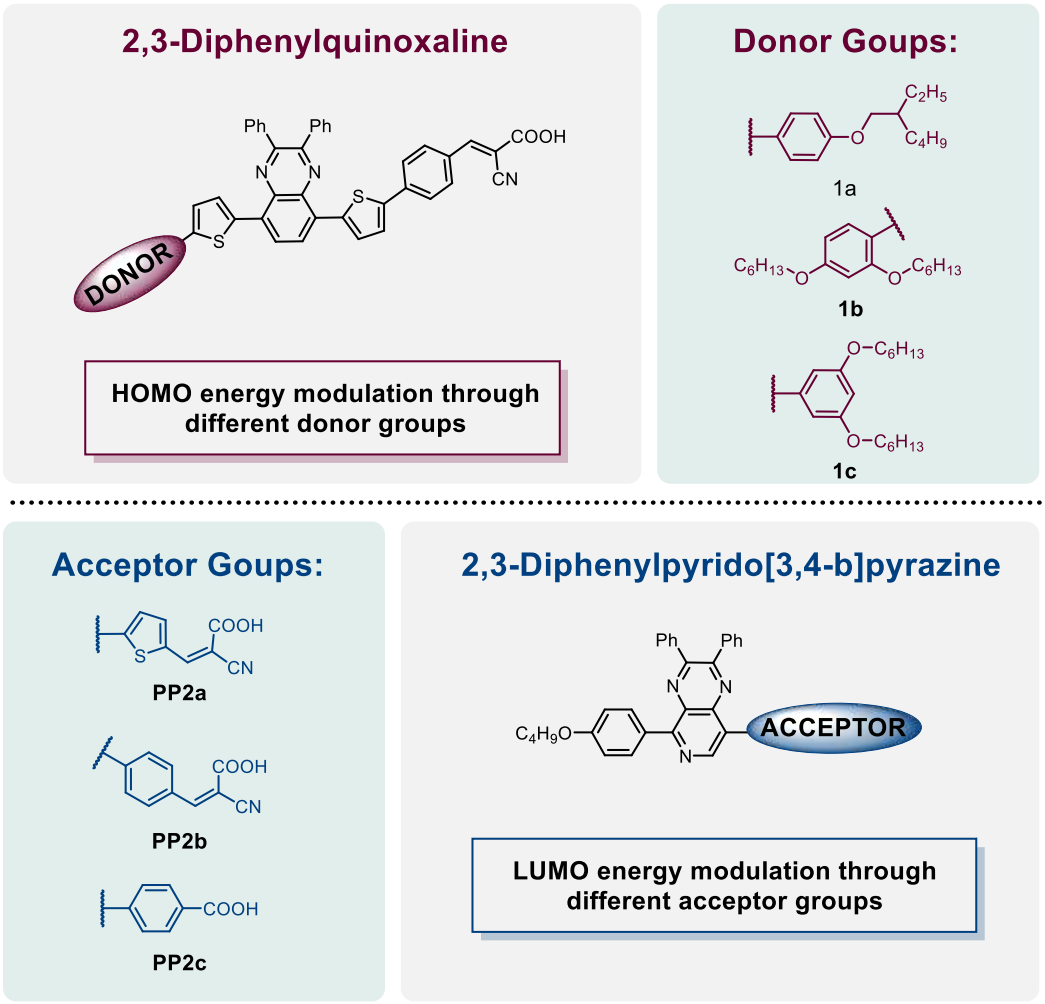

*Figure 3.2 Structure of organic dyes **1a-c** (top) and **PP2a-c** (bottom) designed in this project.*

A similar approach was followed for the design of compound **PP2a-c.** As it can be easily noted, here the two thiophene rings, used in the previous case as π-spacers, were not employed. In this case the more electron-withdrawing pyrido[3,4-*b*]pyrazine unit was directly linked to the donor/acceptor moieties. Once again, a mono-alkoxy-substituted benzene ring was selected as common donor groups, meanwhile three different acceptor/anchor groups were employed. By progressively reducing the electron-withdrawing strength of the acceptor/anchor unit from compound **PP2a** to **PP2c**, we expected to obtain compounds with increasingly high LUMO energy levels, making electron transfer from the oxidized form of the dye to the conduction band of the semiconductor thermodynamically favored.

Once the initial design of the novel compounds was established, the selected structures were investigated computationally by means of Density Functional Theory (DFT) and Time Dependent Density Functional Theory (TD-DFT) methods, to model their molecular and electronic properties

and simulate their main light-absorption features. Then, the compounds were prepared by application of a concise synthetic sequence featuring Pd-catalyzed arylation reactions as the key C-C bond-forming steps. The optical and electrochemical properties of all dyes were assessed to have a first evaluation of their suitability as sensitizers for use in DSPECs. Spectroscopic and electrochemical features of dyes **1a-c** were studied both in solution and after adsorption on electrodes made of thin films of nanocrystalline TiO_2, which included the investigation of the charge transfer processes between the dyes and the semiconductor by means of femtosecond Transient Absorption Spectroscopy (TAS) studies. Additionally, the known ruthenium complex [**Ru(bda)(PyP)$_2$]** (bda = 2,2′- bipyridyl-6,6′-dicarboxylic acid; PyP = pyridin-4-methyl phosphonic acid) was then selected as a water oxidation catalyst to work in combination with dyes **1a-c** and was prepared by adapting a reported procedure. Finally, photoanodes sensitized with the new dyes and decorated with the chosen WOC were tested in water splitting DS-PEC with a 0.1 M aq. Na_2SO_4 electrolyte, to determine their relative performances. On the other hand, the capability of dyes **PP2a-c** to work as anodic sensitizers was first investigated by spectroscopic and electrochemical characherization in solution.

For clarity, the synthetic approach developed for each family of dyes, and the corresponding spectro-electrochemical characterization, will be discussed individually in the following sections (paragraph 3.4 and 3.5).

3.3 Computational studies

The correlation between the molecular structures and the optoelectronic properties of the designed dyes was investigated by means of computational methods based on density functional theory (DFT) and time-dependent DFT (TD-DFT). [22,23] The computational study was carried out in collaboration with the group of Prof. Adalgisa Sinicropi (University of Siena). A complete investigation was conducted for the entire series of compounds **1a-c**, while compound **PP2a** was selected as model substrate for the pyrido[3,4-*b*]pyrazine family. First, the structures of the compounds in the singlet ground state (S0) were minimized in vacuum at the B3LYP/6-31G* level (Figure 3.3). As can be seen, the structures of dyes **1a-c** were very similar and sufficiently planar, with dihedral angles comprised between approx. 11.0° and 26.5°, allowing to maintain a proper conjugation along the entire molecular scaffold. Analogous features could be found for **PP2a.** Subsequently, B3LYP/6-31G* single-point calculations at ground-state optimized geometries were carried out to obtain the distribution and energy of the respective frontier molecular orbitals (FMOs), including the effects of the chosen solvent, dichloromethane (DCM), by using the polarizable continuum

model (PCM). As can be noticed from Figure 3.4, for all quinoxaline-based dyes the highest occupied molecular orbitals (HOMO) were mainly localized on the donor part of the molecules, with a significant contribution from the intermediate quinoxaline ring. On the other hand, the lowest unoccupied molecular orbitals (LUMO) were located for the most part on the acceptor cyanoacrylic group, with a smaller contribution coming from the central bridging unit. For compound **PP2a** a less pronounced spatial separation of the orbitals can be noticed (Figure 3.4, right).

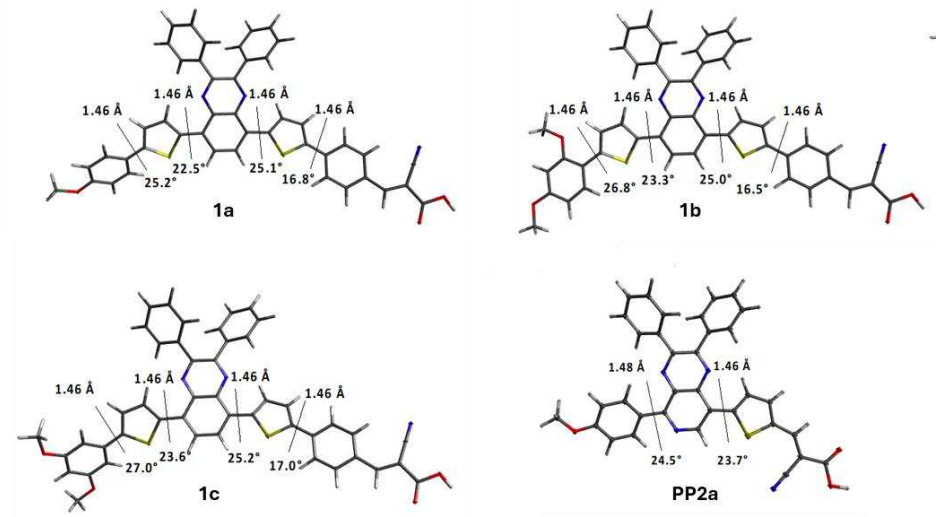

*Figure 3.3 Optimized DFT geometries of compounds **1a-c** and **PP2a** in vacuum computed at the B3LYP/6-31G* level.*

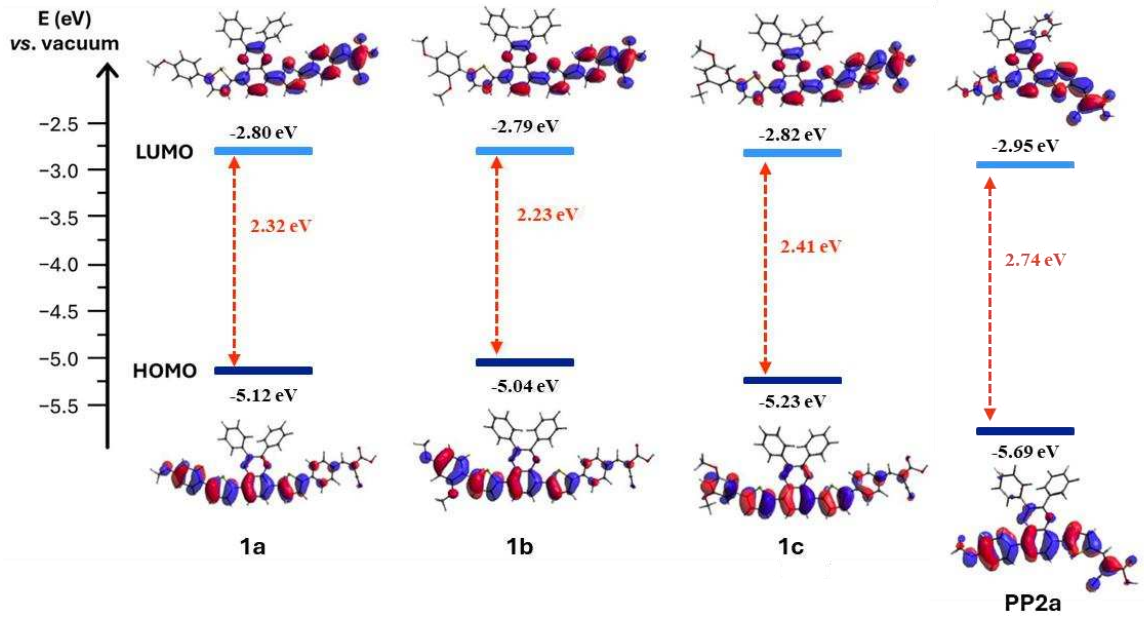

*Figure 3.4 Energies and electron density spatial distributions of the FMOs of dyes **1a-c** and dye **PP2a** in DCM solution.*

In terms of computed orbital energies, the LUMOs of all three quinoxaline-based dyes were found to be in similar positions, which can be attributed to the common acceptor/anchoring group present

in each compound. When compared to dye **1a**, the HOMO of dye **1b** was slightly destabilized (approx. 0.1 eV), likely due to the additional electron-donating alkoxy group placed in conjugation with its unsaturated backbone. In contrast, the HOMO of compound **1c**, which contains two alkoxy groups in the *meta* positions, showed a stabilization of roughly the same magnitude. Therefore, dye **1b** exhibited the smallest HOMO-LUMO energy gap, followed by **1a** and **1c**. On the other hand, as a result of the less conjugated structure and the presence of a stronger auxiliary acceptor, compound **PP2a** shows a higher HOMO-LUMO energy gap with a deep HOMO level calculated at −5.69 eV *vs.* vacuum.

TD-DFT calculations were then employed to assess the spectroscopic properties of the compounds, once again in DCM solution. The funda mental properties investigated were the maximum absorption wave length (λ_{max}^{abs}), the vertical excitation energy (E_{exc}), the oscillator strength (*f*) and the percentage composition of the transition in terms of molec ular orbitals. They were calculated at the TD-CAM-B3LYP/6-311+G(2d,p) and TD-MPW1K/6-311+G(2d,p) levels of theory, including the solvent effect by means of PCM. The results are reported in Table 3.1.

*Table 3.1 TD-DFT absorption maxima (in nm), excitation energies (E_{exc} in eV), oscillator strengths (f) and contributions (%) to the $S_0 \rightarrow S_1$ transition in DCM of compounds **1a-c** and **PP2a**.*

Dye	TD-CAM-B3LYP				MPW1K			
	λ_{max}^{abs}	E_{exc}	f	Comp. (%)	λ_{max}^{abs}	E_{exc}	f	Comp. (%)
1a	493	2.52	1.80	69 (H → L)	519	2.39	1.79	80 (H → L)
1b	498	2.49	1.80	66 (H → L)	526	2.36	1.78	78 (H → L)
1c	486	2.55	1.77	75 (H → L)	509	2.43	1.78	83 (H → L)
PP2a	441	2.81	1..17	87 (H → L)	452	2.75	1.14	93 (H → L)

As it can be noticed, dyes **1a-c** present a main transition in the visible region, in the 486-526 nm (2.55-2.36 eV) range, depending on the functional used. The most red-shifted absorption was exhibited by compound **1b**, owing to its stronger donor group with two alkoxy chains in 2- and 4-position, while the weaker electron-donating capacity of the *bis-meta*-substituted ring of **1c** was evidenced by its slightly blue-shifted transitions. Meanwhile, as expected from the larger energy band gap, compound **PP2a** shows blue-shifted absorption with a maximum wavelength calculated at ca 440-450 nm (depending on the functional used). In all cases, the oscillator strengths are high, suggesting a strong light absorption capability, and the corresponding bands are found to stem mostly from HOMO → LUMO transitions.

In general, the obtained results indicated the existence of a good degree of intramolecular charge

transfer (ICT) upon photoexcitation and suggests the possibility of an intense light absorption via HOMO–LUMO transitions. Based on the above computational investigation, all the designed compounds show appropriate electronic and spectroscopic properties for employment in photoelectrochemical cells, and therefore their preparation was subsequently investigated.

3.4 Quinoxaline-based sensitizers

3.4.1 Design pathway and retrosynthetic analysis

The synthetic strategy employed to prepare the designed quinoxaline-based sensitizers relies on the use of Pd-catalyzed C-C bond forming reactions for linking donor/π-spacer and acceptor moieties. As widely known, Pd-catalyzed cross-coupling reactions such as Suzuki–Miyaura, Stille-Migita, Negishi, Sonogashira, *etc.* have become indispensable in organic synthesis. While these reactions enable the construction of C–C bonds with high selectivity, the prerequisite functionalization of substrates with expensive organometallic reagents and, often, toxic metallic byproducts generated in stoichiometric quantities still represents a serious drawback.[24] In recent decades, direct C–H (hetero)arylation, has therefore emerged as an attractive alternative strategy.[25]
Conceptually, direct (hetero)arylation allows the formation of a new carbon−carbon bond starting from a (hetero)aromatic halide and a (hetero)arene, bearing one or more C(sp^2)−H bonds, without the need for preformed organometallic reagents, improving several aspects such as synthesis time, waste generation, and atom economy. The reaction usually requires a precatalyst, which typically is either $Pd(OAc)_2$ or $Pd_2(dba)_3$, a phosphine ligand, an excess amount of a base (usually a carbonate) in combination with a catalytic amount of a carboxylic acid (usually pivalic acid).[26]
The generic reaction mechanism (Scheme 3.1) involves an oxidative addition of the aryl bromide to the Pd(0) complex (**A**) and the interaction of the pivalate anion with the catalytic complex to give intermediate **B**. Then, the arene is subjected to concerted metalation/deprotonation (CMD) process through transition state **C**, which evolves to the complex **D**. From here, two possible reaction pathways can be discerned: in the first one, pivalic acid is eliminated (**E**) and then the reductive elimination of the biaryl takes place, while, in the second case, the pivalate anion remains bound to the palladium metal (**F**) even after the formation of the new C–C bond.

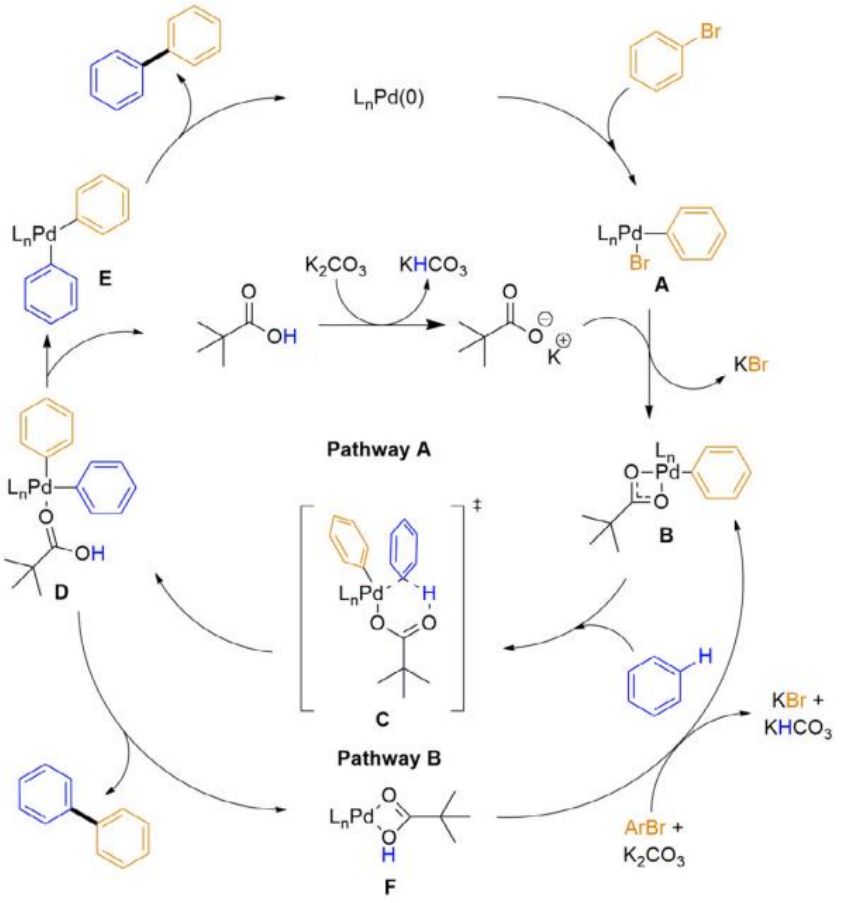

Scheme 3.1 The *proposed mechanism of direct arylation through concerted metalation/deprotonation (CMD).*[26]

The CMD pathway guides the regioselectivity of the direct arylation reaction towards the most acidic C-H bond of the arene, making thiophenes and furans ideal candidates for functionalization at the C-2 position. For these reasons, the direct arylation reaction has been widely used in the past decade for the preparation of small conjugated organic molecules and polymers with applications in optoelectronics.[27,28]

On the basis of the above discussion, the retrosynthetic analysis followed for the preparation of dyes **1a-c** (Scheme 3.2) was elaborated considering direct aryltaion reactions as principal protocols the construction of key C–C bonds.

To prepare compounds **1a-c**, the process begins with the removal of cyanoacetic acid (**15**), yielding aldehyde **14a-c** (disconnection ***A***). The following steps involve the disconnections of the alkoxy-phenyl donor (disconnection ***B***) and benzaldehyde acceptor group (disconnection ***C***). For these important steps we chose to perform a double direct arylation protocol starting from intermediate **6**, in order to avoid the use of any preformed organometallic reagent and reduce the number of synthetic and purification steps as much as possible. Finally, intermediate **6** can be obtained by a telescopic reduction/condensation reaction of intermediate **4** (disconnection ***D***), that results from

the Stille cross-coupling reaction between the two commercially available starting materials, 4,7-dibromobenzo[*c*][1,2,5]thiadiazole (**2**) and tributyl(thiophen-2-yl)stannane (**3**). From this discussion, it clearly emerges that the corresponding synthesis would represent a convergent approach, granting access to all the desired dyes through a late state diversification of the common intermediate **8.**

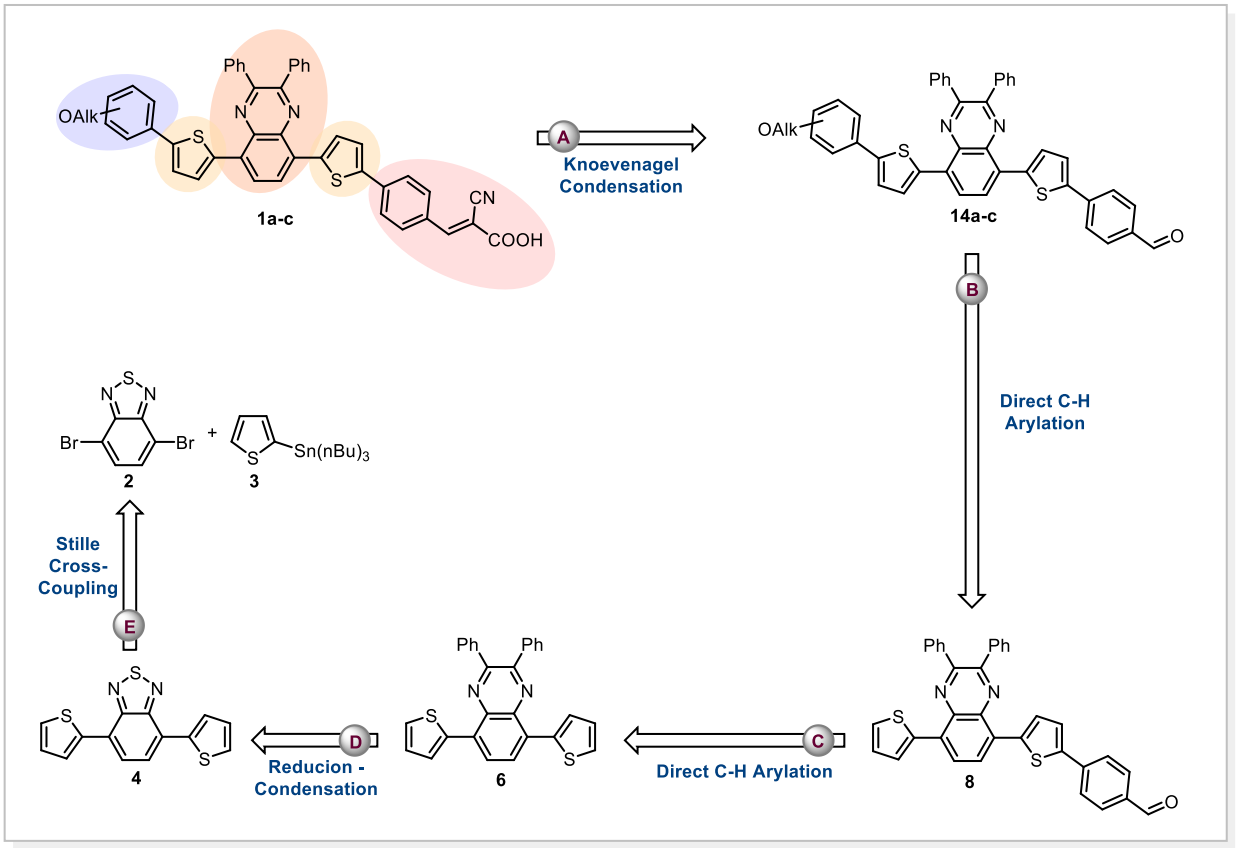

Scheme 3.2 Retrosynthetic approach for the synthesis of compounds **1a-c**. Colors represent the different building blocks: donor (purple), π (yellow), auxiliary acceptor (orange), acceptor (pink).

3.4.2 Synthesis of dyes 1a-c

The synthetic route followed to obtain common intermediate **8** needed for the preparation of dyes **1a-c** is presented in Scheme 3.3.

By subjecting 4,7-dibromo-2,1,3-benzothiadiazole (**2**) to a Stille-Migita reaction with tributyl(thiophen-2-yl)stannane (**3**) in the presence of $Pd(PPh_3)_2Cl_2$ as catalyst, bis-thiophen-2-yl derivative **4** could be obtained in high yield.

The benzothiadiazole ring of compound **4** was then converted to a quinoxaline system by means of a reduction with elemental zinc in acetic acid, followed by trapping of the resulting diamine with 1,2-diphenylethane-1,2-dione (benzil, **5**) in ethanol (EtOH), providing the desired compound **6** in 92 % yield. At this stage, the insertion of the acceptor moiety of the final sensitizers was

achieved through a direct arylation reaction of compound **6** with 4-bromobenzaldehyde **7**, in the presence of a palladium complex as the catalyst.

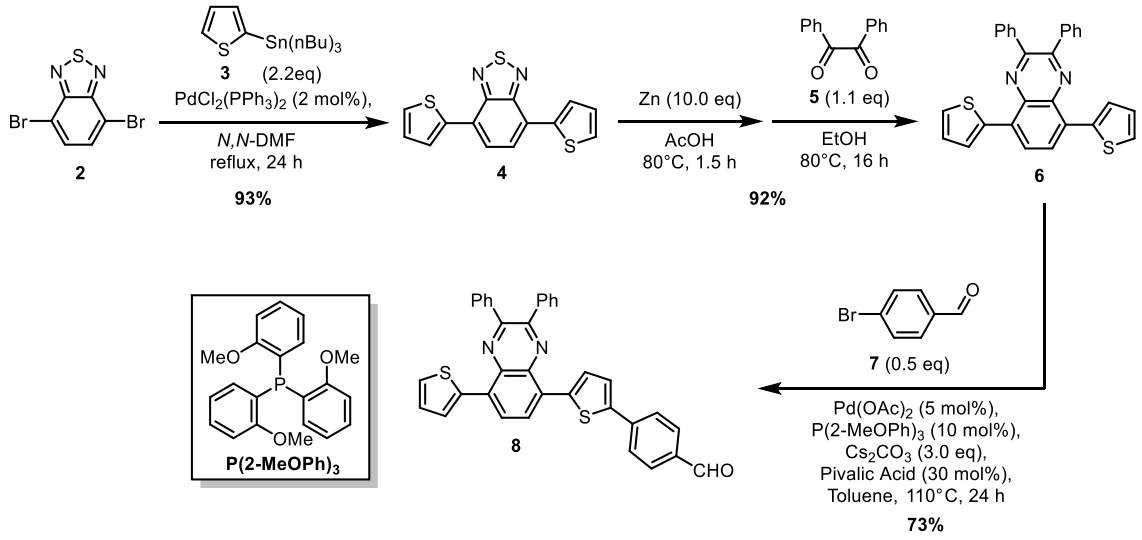

*Scheme 3.3 Synthetic route and preparation of intermediate **8.***

To maximize the yield of key intermediate 8, a short optimization of the reaction protocol was carried out, varying the nature of the phosphine ligand and the base (Table 3.2).

Table 3.2 *Optimization of the reaction conditions for the preparation of intermediate **8***[a]

Entry	Base	Ligand	Yield (%)[b]	S.M. recovery (%)[d]
1	K_2CO_3	PCy_3HBF_4	18%	69%
2	Cs_2CO_3	PCy_3HBF_4	31%	67%
3	Cs_2CO_3	CataCXium A®	46%	62%
4	**Cs_2CO_3**	**P(2-MeOPh)$_3$**	**73%**	**43%**
5[e]	Cs_2CO_3	P(2-MeOPh)$_3$	70%	50%
6[f]	Cs_2CO_3	P(2-MeOPh)$_3$	67%	50%

[a] **6** (0.27 mmol, 2.0 eq), 4-bromobenzaldehyde (**7**, 0.135 mmol,1.0 eq), $Pd(OAc)_2$ (5 mol%), ligand (10 mol%), base (3.0 eq), pivalic acid (30 mol%), toluene, 110°C, 24 h, if not stated otherwise; [b] Isolated product yield after column chromatography; [d] Referred to the initial amount of reagent **6**; [e] Scaled-up reaction: **6** (2.24 mmol), **7** (1.12 mmol), reaction time 16 h; [f] reaction time 1.5 h.

The best conditions turned out to be the following: $Pd(OAc)_2$ (5 mol%), P(2-MeOPh)$_3$ (10 mol%), Cs_2CO_3 (3.0 eq.), pivalic acid (30 mol%) in toluene at 110°C for 24 h. Under such conditions, the desired product could be obtained in 73% yield on a small-scale reaction (0.27 mmol of quinoxaline **6,** entry 4), which was essentially maintained at 70% when scaling up to 2.24 mmol of substrate (entry 5), demonstrating the robustness of the protocol. Importantly, most of the unreacted compound **6** could be recovered after flash column chromatography, and the reaction time could be also decreased to 1.5 h (entry 6), albeit at the cost of a slightly reduced yield (67%).

At this stage, driven by the will to develop a concise synthetic pathway that allows a late-stage diversification, we then attempted the introduction of 4-hydroxyphenyl moiety *via* direct arylation (Scheme 3.4, ***A***). Unfortunately, by subjecting compound **8** to similar conditions to those employed for the previous C-H coupling, in the presence of 4-bromohydroxyphenol (**9**), the desired product **10** was detected only in traces and almost no conversion of aldehyde **8** was observed. A slightly better result was obtained when compound **11** (where hydroxyl function was protected with a trimethylsilyl group) was used as aryl bromide (Scheme 3.4, B). However, even in this case, the desired product was obtained with a very low yield of 10%.

Based on these results, we decided then to change our approach and attempt the direct arylation of intermediate **8** with the appropriate arylbromides **13a-c** (Scheme 3.4, **C**), already bearing a different number of alkoxy-substituents arranged in different substitution patterns. The reactions proceeded once again under similar conditions to those employed for the coupling between compounds **6** and **7**, allowing to isolate advanced intermediates **14a-c** in 80–93% yield, where the lower yield of aldehyde **14a** was mostly due to its lower solubility, and thus more difficult handling, compared to **14b-c**.

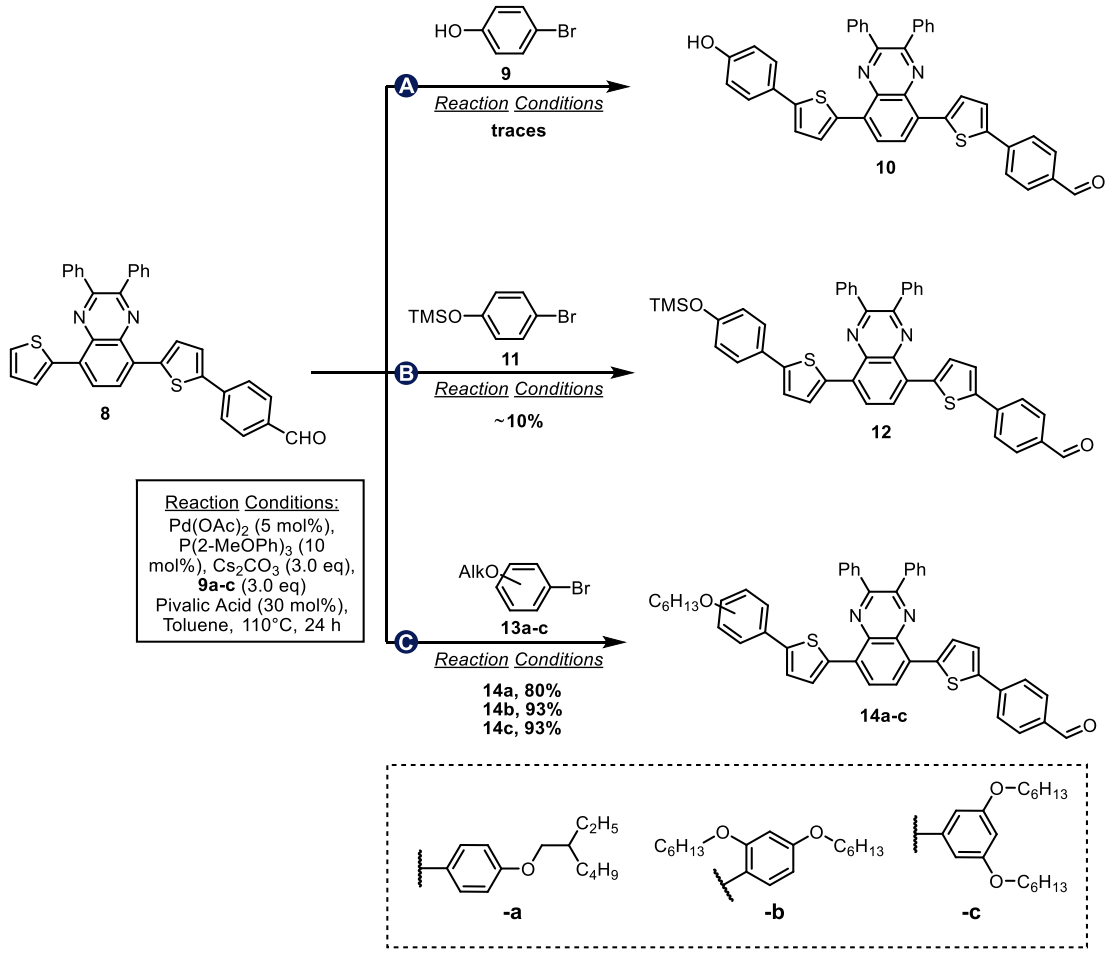

Scheme 3.4 Attempted direct arylation reactions for the insertion of the donor unit.

Finally, the desired dyes **1a-c** were obtained in good yields (82–89%) by condensation of aldehydes **14a-c** with cyanoacetic acid in the presence of a catalytic amount of piperidine (Scheme 3.5). Compounds **1a-c** could not be purified using flash column chromatography, due to the interaction of the anchoring group with the silica stationary phase, and therefore were isolated by means of recrystallization from ethanol.

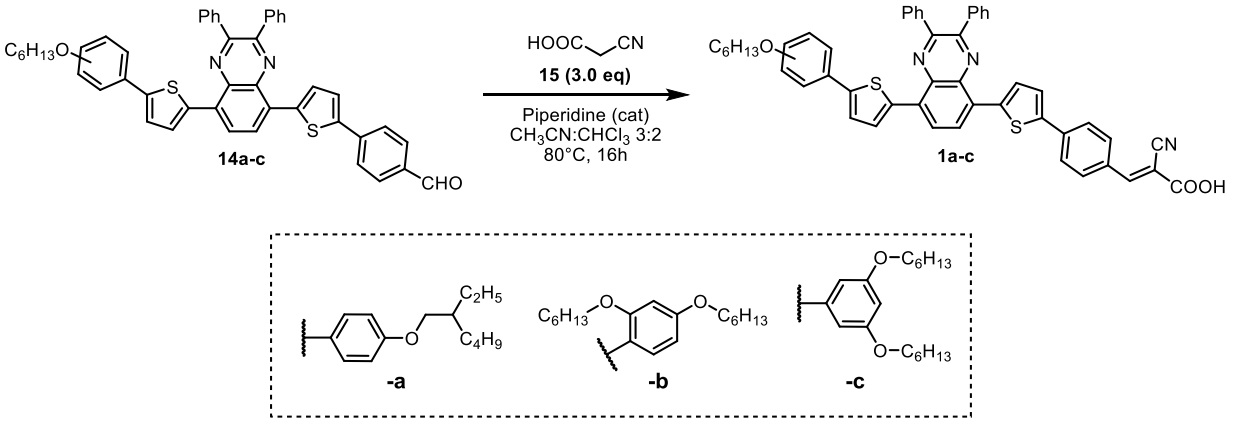

*Scheme 3.5 Knoevenagel condensation of aldehydes **14a-c** with cyanoacetic acid.*

3.4.3 Spectro-electrochemical characterization

3.4.3.1 Characterization in solution

A detailed spectro-electrochemical characterization was performed for dyes **1a-c** in solution. The results discussed below have been obtained in collaboration with the group of Dr. Andrea Barbieri (*CNR-ISOF, Bologna*). The UV-Vis absorption and fluorescence emission spectra of compounds **1a-c** were recorded at room temperature in both DCM (Figure 3.5, left) and THF (Figure 3.5, right) solution and their main features are listed in Table 3.3.

*Table 3.3 Main spectroscopic properties of dyes **1a-c** in DCM and THF solution.*

Dye	Solvent	λ_{max}^{abs} (nm)	$\varepsilon \times 10^4$ (M^{-1} cm^{-1})	λ_{max}^{emi} (nm)	ϕ	τ (ns)	$^{a}E_{0\text{-}0}$ (eV)[a]
1a	DCM	492	2.39	647	-	-	2.17
		334	3.14				
	THF	498	3.36	632	0.310	5.43	2.18
		334	4.05				
1b	DCM	503	2.27	664	-	-	2.14
		337	3.11				
	THF	499	1.93	646	0.429	6.28	2.15

		347	3.42				
1c	DCM	490	2.72	617	-	-	2.22
		330	3.07				
	THF	488	2.62	610	0.535	7.16	2.23
		347	4.77				

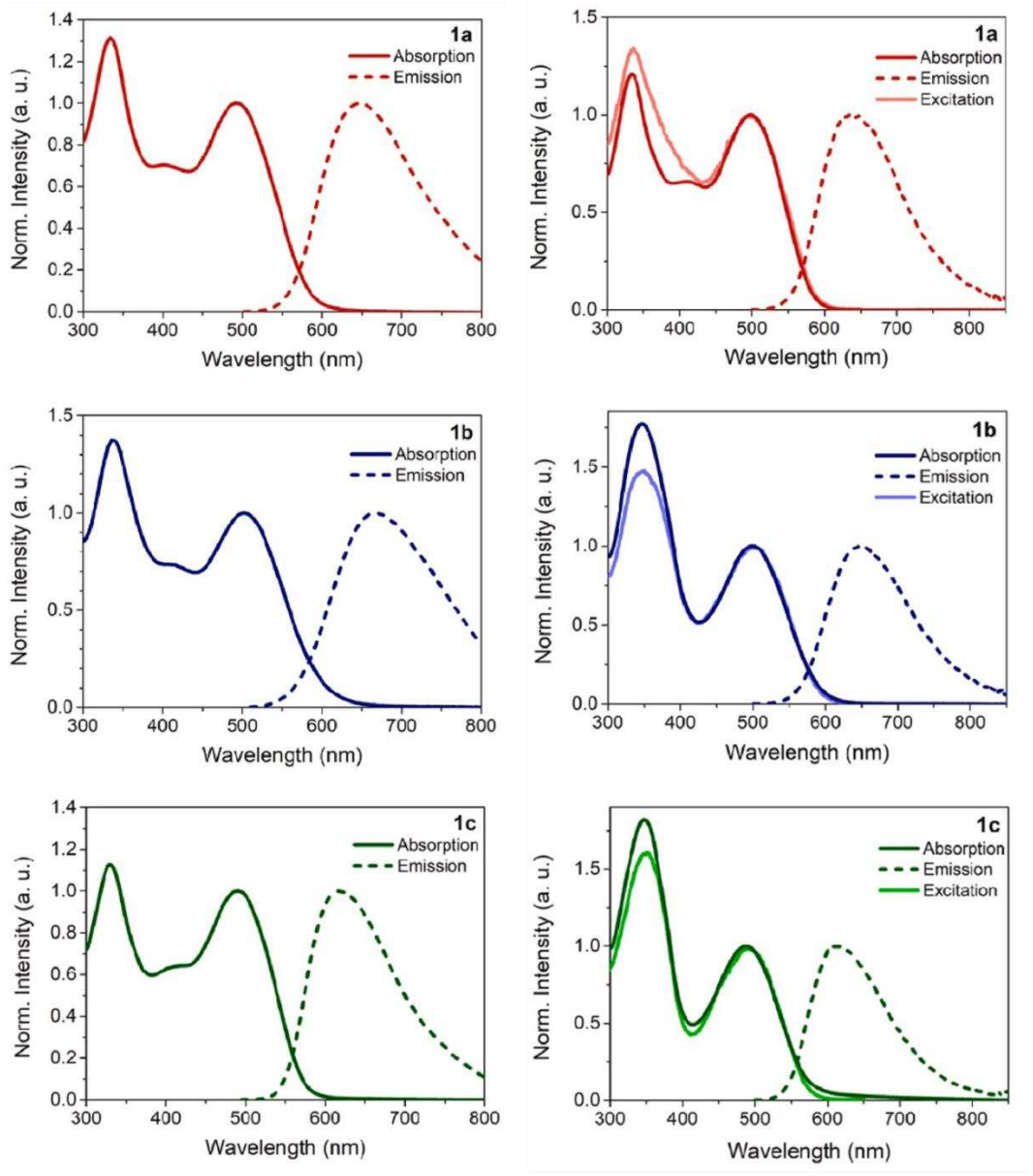

*Figure 3.***5** *UV–Vis absorption, emission and excitation spectra of dyes* ***1a-c*** *in DCM (left) and THF (right) solution at room temperature.*

By comparison with the values resulting from the TD-DFT investigations (see paragraph 3.3), it can be seen that a very good agreement with the experimental data was obtained when using the CAM-B3LYP functional for calculations (Table 3.1), with differences between the computational and experimental E_{exc} values lower than 0.1 eV in all cases.

Whereas the absorption maxima did not change much in passing from DCM to THF, a significant red-shift (7–18 nm) was observed for the emission profiles of the dyes in the more polar DCM. When excited near their maximum absorption in THF solution, the dyes exhibited a notable fluorescence emission, with maxima in the 610–646 nm range, quantum yields (FQY, ϕ) comprised between 0.31 and 0.54 and excited state lifetimes (τ, obtained from the corresponding time-resolved fluorescence spectra reported in Figure 3.6) comprised between 5 and 7 ns in THF.

Furthermore, excitation spectra were also measured for all dyes in THF solution. The corresponding excitation profiles, monitored at the maximum emission wavelength, followed those of the corresponding absorption spectra, indicating that, regardless the excitation energy, emission always occurred from the lowest singlet excited state (S_1), according to Kasha's rule.[29] From the intersection of the normalized absorption and emission spectra, the corresponding energies of the $S_0 \rightarrow S_1$ zero-zero transition (also known as optical band gap, $E_{0\text{-}0}$) could be determined, yielding values in the 2.14–2.23 eV range. It can be noted that the largest value of Stokes' shift (approx. 0.5–0.6 eV, 4100-4900 cm^{-1}) and smaller $E_{0\text{-}0}$ were shown by compound **1b**, probably owing to its stronger donor group compared to the other two compounds, and therefore to its more pronounced donor-acceptor character.

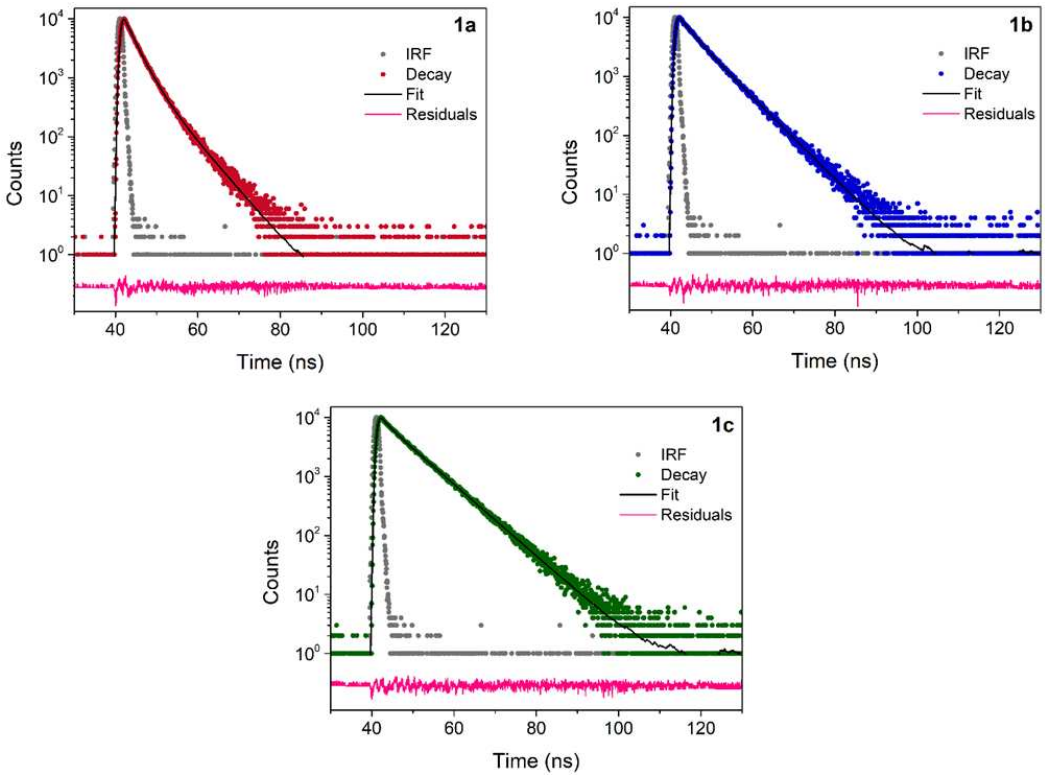

*Figure 3.6 Fluorescence (λ_{exc} = 440 nm) decay spectra for compounds **1a-c** recorded in THF solution at room temperature. IRF = Instrument response function.*

Subsequently, to gain further insight into the electronic structures of the dyes and the properties of their excited states, additional experiments were carried out in a DCM:MeOH 1:1 frozen matrix at

77K. Compared to the experiments in THF at room temperature, the emission spectra are only slightly affected by changes in matrix and temperature. The main difference is a better-resolved vibrational progression, which is not apparent in the emissions from fluid solution at room temperature. In contrast, at low temperatures, the excitation spectra show a significant bathochromic shift, suggesting a larger dipole moment of the ground state compared to the excited state. At low temperatures, the reorganization of solvent dipoles that normally stabilize the ground state in solution is hindered, leading to a destabilization of the ground state in the frozen matrix. Meanwhile, the energy of the excited state remains largely unchanged. This results in a reduced energy difference between the ground and excited states, which in turn causes the observed red-shift in the spectra (Figure 3.7, left).

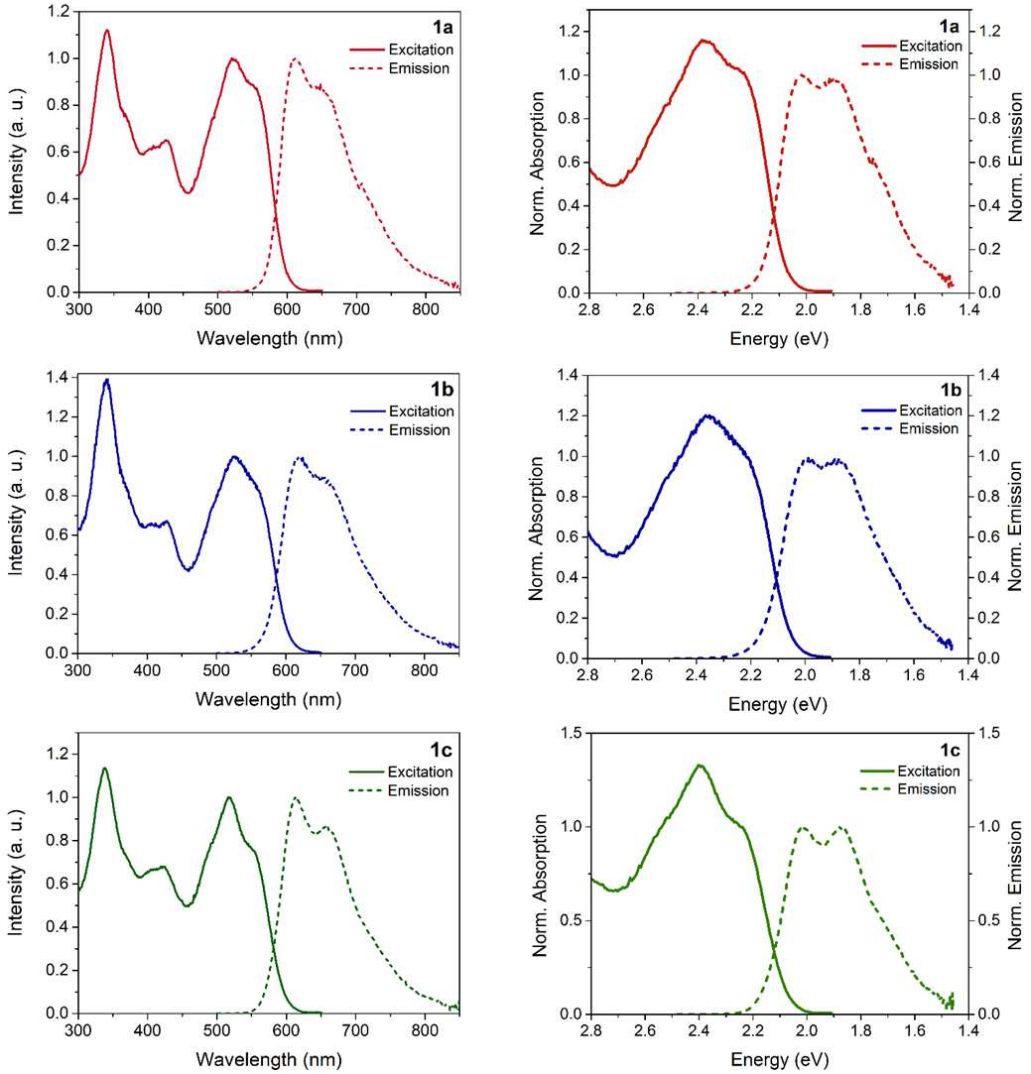

*Figure 3.7 Excitation (λ_{emi} = 700 nm) and emission (λ_{exc} = 440 nm) spectra of dyes **1a-c** in frozen DCM/MeOH 1:1 matrix at 77 K (left); Excitation and emission spectra of dyes **1a-c** in frozen DCM/MeOH 1:1 matrix at 77K, in energy scale after Jacobian transformation (right).*

Further spectroscopic information can be obtained from the energy-scaled spectra. To correctly convert the data recorded in wavelength units (λ) to energy (E) scale, the intensity of the bands themselves must be scaled using the Jacobian transformation, according to equation (3.1):

$$f(E) = f(\lambda)\frac{d\lambda}{dE} = f(\lambda)\frac{d}{dE}\left(\frac{hc}{E}\right) = -f(\lambda)\frac{hc}{E^2} \qquad (3.1)$$

where h is Planck's constant, c is the speed of light and E is the energy of the transition. The minus sign here can be ignored as it simply reflects the different directions of integration in wavelength and energy. Therefore, to correctly convert the data recorded in wavelength units to the energy scale, not only must the latter be converted using the well-known relationship E = hc / λ, but the signal intensities must also be scaled by hc / E^2. This process is called a Jacobian transformation.[30] The excitation spectra and emission spectra transformed according to the above procedure and reported in energy scale (E, eV) are illustrated in Figure 3.7 (right).

From the intersection between the two spectra it is possible to estimate the energy difference between the vibrational ground levels of the electronic ground state and first excited state of the molecule ($E_{0\text{-}0}$), in the absence of perturbations due to the presence of solvent dipoles. The corresponding values are reported in Table 3.4. All analyzed compounds **1a-c** showed practically coincident $E_{0\text{-}0}$ values, further confirming the similarity of the nature of their excited states. Compounds **1a** and **1b** with the alkoxy groups –OR in *para-* and *ortho-* positions of the terminal phenyl ring present similar values of Stokes' shift (approx. 1300 cm^{-1}) and excited state lifetimes of ~ 5.3 ns. Conversely, compound **1c**, featuring the alkoxy groups in *meta-* position, presents different values of $\Delta\lambda$ ~ 1700 cm^{-1} and τ = 7.2 ns. This highlights the effect exerted by the substituents positions on the photophysical properties of this series of dyes.

Table 3.4 *Main absorption and emission parameters of the sensitizers in frozen matrix at 77K.*

Dye	λ_{max}^{abs} (nm)[b]	λ_{max}^{emi} (nm)[c]	τ (ns)[c]	$\Delta\lambda$ (cm^{-1})[d]	$E_{0\text{-}0}$ (eV)[e]
1a	340, 425, 520	613	5.33	1270	2.12
1b	343, 428, 524	620	5.23	1360	2.11
1c	339, 424, 516	615	7.22	1680	2.12

[a] In DCM/MeOH 1:1 mixture; [b] Obtained from excitation spectra (λ_{emi} = 700 nm); [c] Obtained from emission spectra (λ_{exc} = 440 nm and λ_{exc} = 375 nm for emission and lifetime measurements, respectively); [d] Stokes' shift calculated from the energy difference between the band with the lowest excitation energy and the band with the highest emission energy, considering the spectra reported in energy scale. [e] Values estimated from the intersection between the normalized excitation and emission spectra reported in energy scale.

To achieve crucial insights into the thermodynamics of the electron injection as well as of the dye regeneration processes in dye-sensitized systems, electrochemical measurements were carried out

by recording the corresponding cyclic voltammetry (CV) experiments, using tetrabutylammonium hexafluophosphate ($TBAPF_6$) 0.1 M in DCM as the supporting electrolyte and the ferrocenium/ferrocene (Fc^+/Fc) redox couple as an internal standard. The ground state-oxidation potentials (E_{ox}) of all three dyes were determined, allowing to calculate the energy level positions of their frontier orbitals. The obtained results are summarized in Table 3.5. As can be seen from Figure 3.8, upon application of positive potentials compounds **1a-c** exhibited quasi-reversible first oxidation waves, which were followed by a second oxidation at more positive potentials. After conversion according to literature reports,[31] their E_{ox} values resulted in +1.19 V (**1a**), +1.08 V (**1b**) and +1.33 V (**1c**) *vs.* NHE, respectively. As expected, the trend observed in the E_{ox} values of the dyes thus followed the order of relative strength of their donor groups, with **1c** > **1a** > **1b**. Accordingly, the electrochemical analysis showed that in the case of dye **1b** the E_{ox} value measured in solution was very close to the reported onset of catalysis of a typical Ru^{II}(bda)-based complex (E_{onset}, approx. +1.1 V *vs.* NHE)[32], suggesting that a relatively small thermodynamic driving force for hole transfer to the catalyst could exist for such dye. Compound **1a** and **1c** have, on the contrary, E_{ox} potentials above the threshold value which should ensure a proper regeneration process.

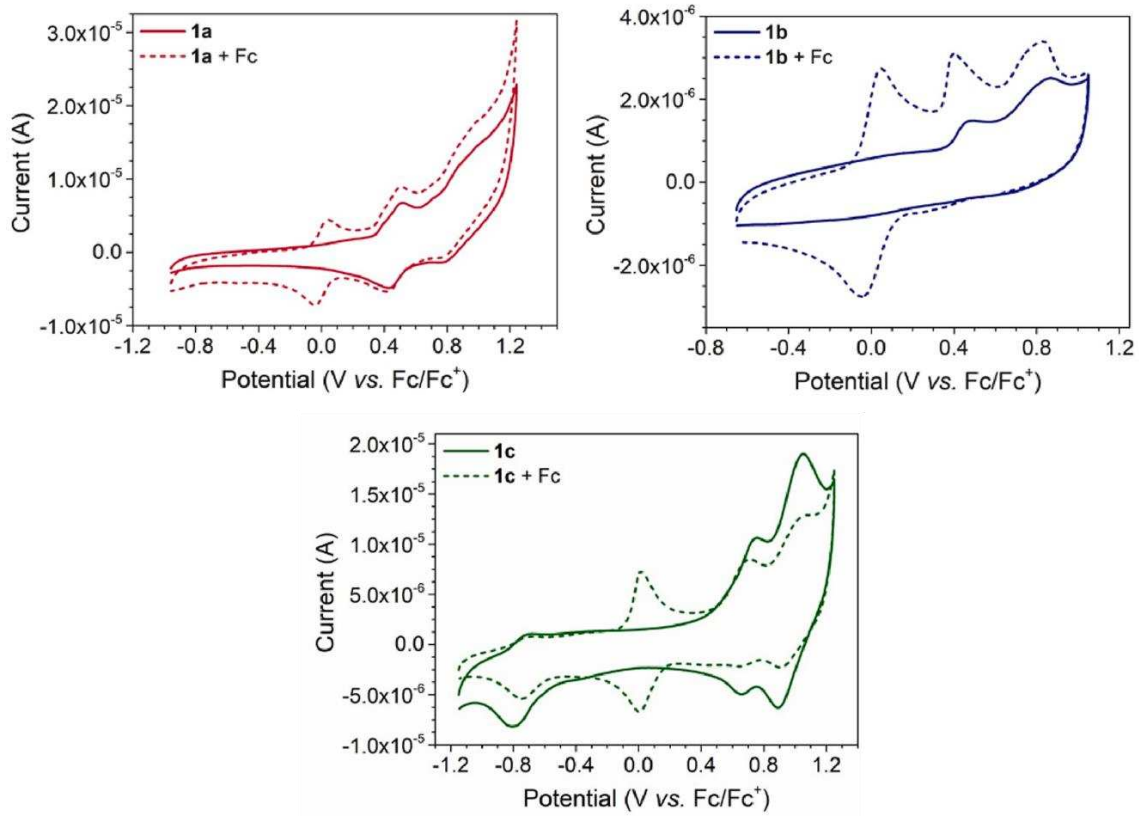

*Figure 3.8 Cyclic voltammetry plots of dyes **1a-c** in DCM solution, both without (solid lines) and with (dotted lines) ferrocene as an internal standard.*

*Table 3.5 Electrochemical properties of dyes **1a-c** in DCM solution.*

Dye	E_{ox} (V) *vs.* Fc^+/Fc	E_{ox} (V) *vs.* NHE[a]	E^*_{ox} (V) *vs.* NHE[b]
1a	+0.47	+1.19	−0.98
1b	+0.36	+1.08	−1.06
1c	+0.61	+1.33	−0.89

[a] Calculated by adding +0.72 V to the potential *vs.* Fc^+/Fc[31]; [b] Calculated from the E_{ox} and $E_{0\text{-}0}$ values according to the formula: $E^*_{ox} = E_{ox} - (E_{0\text{-}0}/e)$

The excited state oxidation potentials (E^*_{ox}) of the dyes were then assessed by subtracting the previously determined $E_{0\text{-}0}$ values from the E_{ox} resulting from cyclic voltammetry, yielding values of −0.98, −1.06 and −0.89 V *vs.* NHE for **1a**, **1b** and **1c**, respectively. The obtained values were largely more negative than the conduction band energy of TiO_2 (approx. −0.5 V *vs.* NHE), supporting a proper electron injection from the excited state of the dye to the semiconductor during cell operation.

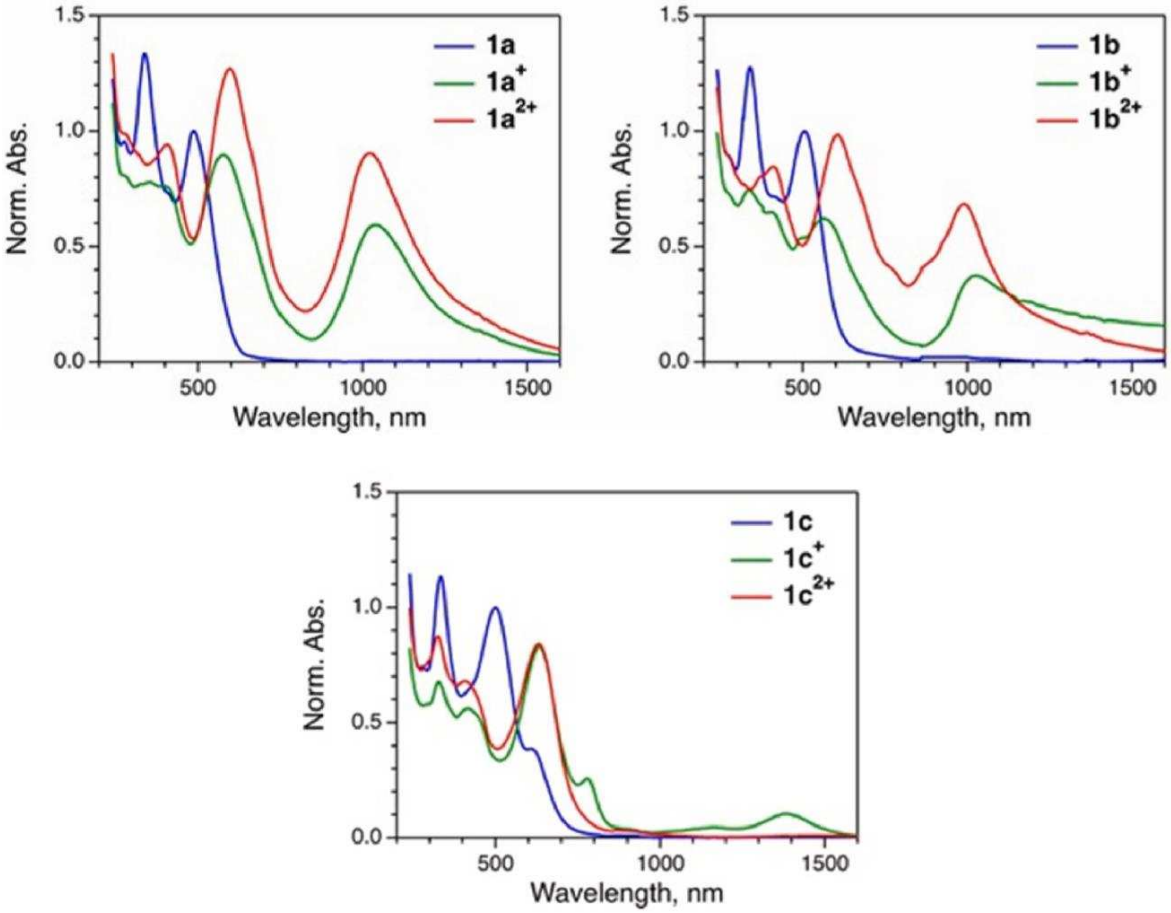

*Figure 3.9 Absorption spectra of the neutral and cationic species of dyes **1a-c** in dichloromethane solution containing $TBAPF_6$ 0.1 M as supporting electrolyte.*

To further investigate the spectroscopic behaviour of the oxidized dyes, a complete spectro-electrochemical study was performed in DCM solution. Absorption spectra across the UV–vis–NIR

range (200–1600 nm) (Figure 3.9) were recorded under potentiostatic conditions at three distinct potentials: (1) below the first oxidation potential (E_{ox}), corresponding to the neutral species, (2) between the first and second oxidation potentials (E_{ox2}), representing the monocationic species, and (3) above the second oxidation potential (di-cation). The corresponding values are reported in Table 3.6.

The absorption spectra obtained at potentials below E_{ox} (Figure 3.9, blue curves) closely match those recorded at open circuit for all dyes **1a-c**, consistent with the absorption of the neutral species. For the cationic forms of dyes **1a** and **1b**, observed at potentials between E_{ox} and E_{ox2} (green curves) and above E_{ox2} (red curves), the spectra exhibit two notable features: (i) a clear red-shift of the two main absorption bands in the visible region, and (ii) the appearance of a strong new low-energy absorption band peaking around 1000 nm. In contrast, for compound **1c**, while a red shift in the visible region is still observed for the cationic species, the absorption band in the NIR region is less intense compared to **1a** and **1b**.

*Table 3.6 Absorption maxima of compounds **1a-c** at different oxidation potentials in dichloromethane solution containing $TBAPF_6$ 0.1 M at room temperature*

Dye	λ_{max}^{abs} (nm)	λ_{max}^{abs} (nm) $E < E_{ox}$	λ_{max}^{abs} (nm) $E_{ox} < E < E_{ox2}$	λ_{max}^{abs} (nm) $E > E_{ox2}$
1a	336, 492	336, 492	352, 576, 1038	407, 596 1022
1b	339, 503	339, 503	336, 563 1028	409, 605 990
1c	333, 502	333, 502	327, 410, 633, 1381	330, 416, 494, 622,

3.4.3.2 Spectroscopic characterization on TiO_2 films

Dye-sensitized films were obtained by immersing the electrodes for 4 h in 2×10^{-4} M solutions of the dyes in THF, and their UV–Vis absorption spectra are reported in Figure 3.10.

Compared to the spectra in solution, compound **1a** showed a noticeable blue-shift in its absorption maximum (from 482 nm to 498 nm), while the absorption maxima of dyes **1b** and **1c** shifted by no more than 2 nm compared to THF. In all cases, the absorption peaks were broader than those observed in solution, and a red-shifted onset around 650 nm was evident. The dye loading on TiO_2 (in mol/cm²) was determined using Meyer's method[33], based on the following equation 3.2:

$$\Gamma = A(\lambda)/[10^3 \cdot \varepsilon(\lambda)] \qquad (3.2)$$

where A(λ) and ε(λ) represent the absorbance and molar absorptivity at wavelength λ of each dye. The calculated dye loadings were 4.1×10^{-8} mol/cm² for **1a**, 9.3×10^{-8} mol/cm² for **1b**, and 6.4×10^{-8} mol/cm² for **1c**, which are in line with the values reported for other organic dyes in previous studies.[15,34,35]

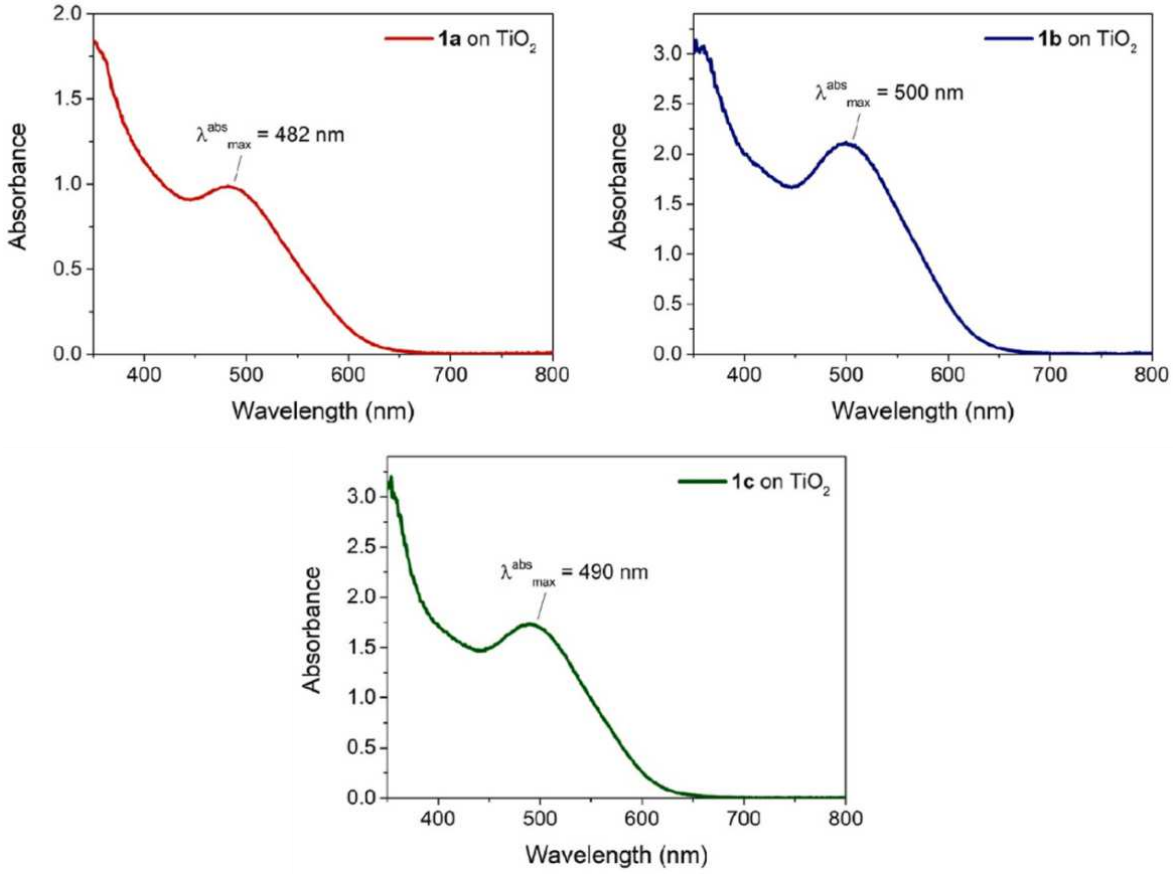

*Figure 3.10 UV-Vis absorption spectra of dyes **1a-c** adsorbed on mesoporous TiO_2 films.*

3.4.3.3 Transient absorption spectroscopy

To better understand the individual processes occurring after light absorption, we investigated the dynamics of photoexcitation and charge transfer of the dyes adsorbed onto mesoporous TiO_2 films using femtosecond transient absorption spectroscopy (TAS) in the visible and near infrared (NIR) regions. This study was done in collaboration with the research group of Dr. Barbara Ventura and Dr. Andrea Barbieri (*CNR-ISOF, Bologna*).

TAS is a time-resolved technique used to explore the excited-state dynamics and reaction pathways of molecules and materials following photoexcitation. In a typical experiment, the ground-state absorption spectrum of the sample is first recorded. A pump pulse then excites the sample, and after a controlled time delay (τ), a probe light measures the changes in the absorption spectrum induced by the excitation. The differential absorption spectrum (ΔA) is calculated using the equation 3.3:

$$\Delta A = A_{\text{after pump}} - A_{\text{ground-state}} \quad (3.3)$$

By systematically varying the delay time (τ) between the pump and probe pulses and recording the ΔA at each time point, a time-resolved profile of ΔA as a function of τ and wavelength (λ) can be generated. This provides a detailed map of how the sample's absorption properties evolve over time, offering valuable insights into transient states, energy transfer, and reaction dynamics.
In general, ΔA is composed of a series of contributions:

- Ground-state bleach: When a significant portion of molecules is excited from the ground state to an excited state, fewer molecules remain available to absorb light at the ground-state absorption wavelengths. This depletion manifests as a negative contribution in ΔA spectrum.
- Stimulated emission (SE): This process occurs when the system is already excited by a pump pulse and a subsequent probe photon induces the excited molecule to return to its ground state. The resulting trend on ΔA spectrum appears as a negative band, typically observed in the wavelength region corresponding to the fluorescence emission of the molecule. This negative signal arises because stimulated emission reduces the net absorption at these wavelengths. The spectral profile of this negative band often overlaps with other features, such as the ground-state bleach, making it challenging to deconvolute the two signals.
- Excited-state absorption (ESA): In this process, molecules that have been promoted to an excited state by the initial pump pulse can undergo further excitation to higher-energy excited states when interacting with the probe pulse. This occurs if the probe photon energy matches the transition energy between the populated excited state and the higher excited states. ESA contributes positively to the ΔA spectrum in regions where these higher excited-state transitions are optically allowed.

Keeping in mind this real-time spectroscopic technique, TiO_2 films sensitized with dyes **1a-c** were excited at 500 nm and their transient spectra recorded in the 0.1 ps -6.1 ns time interval. The results were then analyzed by simultaneously fitting all the kinetic traces with a combination of exponential functions (global analysis), and using a kinetic scheme based on a sequential decay. Besides kinetic constants, the global analysis also retrieved the correspondent spectral components, indicated as Evolution Associated Difference (EAD) spectra.
As can be seen in Figure 3.11 (left) the spectral region below 510 nm has been omitted because of the strong noise due to the intense ground state absorption. In general, the spectral features were similar across all three dyes, with first broad band in the 600–800 nm region, an intense band at ca. 900 nm and a broad absorption in the NIR between 1200 nm and 1600 nm. The corresponding back electron-transfer kinetic traces are shown in Figure 3.11 (right). Interestingly, the formation

of a band at ca. 830 nm is clearly observable: it appears with a kinetics in the order of few hundreds of ps, after a fast decay of the signal in the same region, and decays on longer time scales.

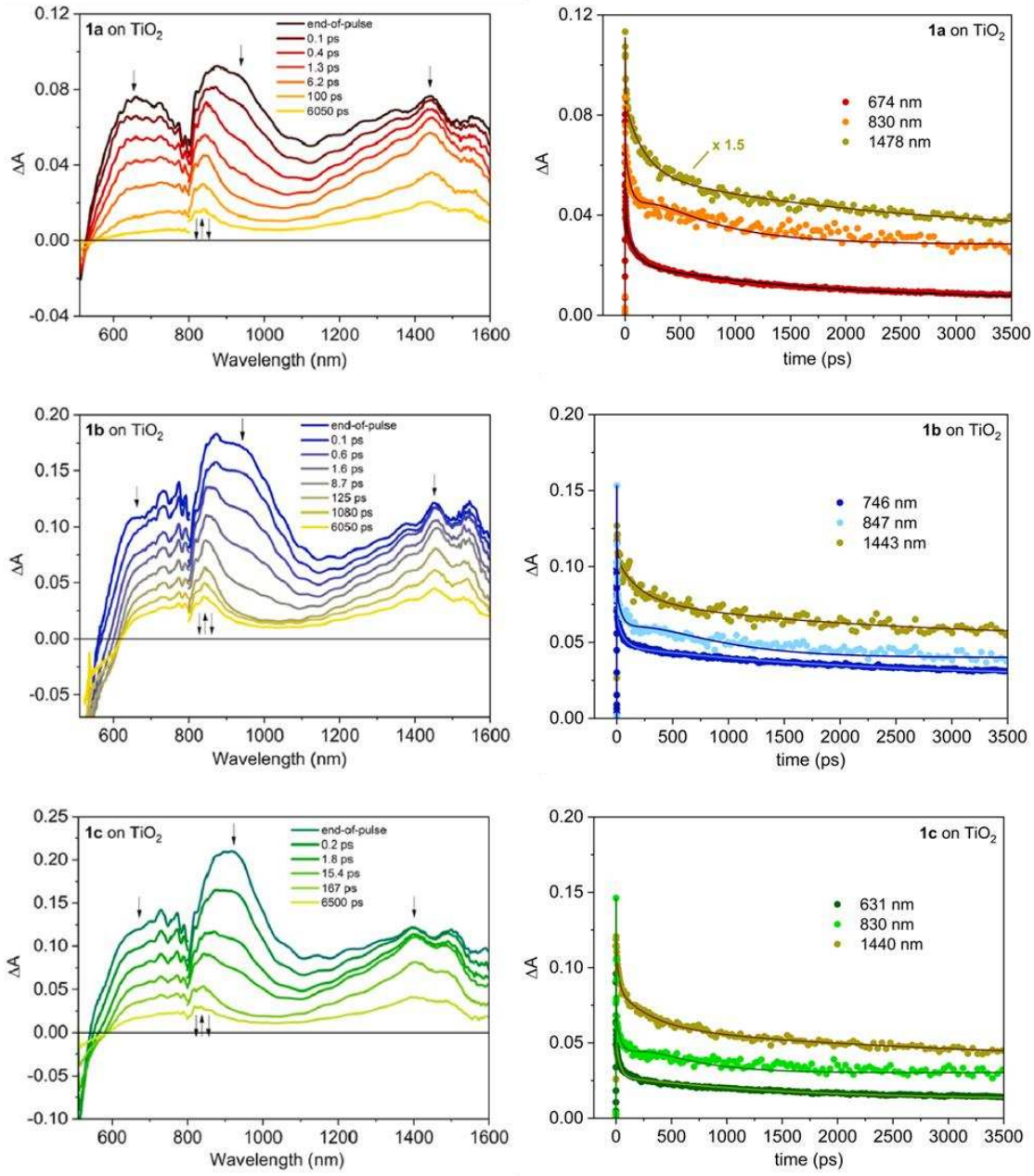

*Figure 3.11 Transient absorption spectra at different delays of dyes **1a-c** (left) and ΔA temporal evolution at selected wavelengths for **1a-c** (right) adsorbed on mesoporous TiO_2 films.*

As anticipated before, in order to rationalize the obtained data, a global fit analysis has been performed on the transient matrices and the corresponding EAD spectra are reported in Figure 3.12.

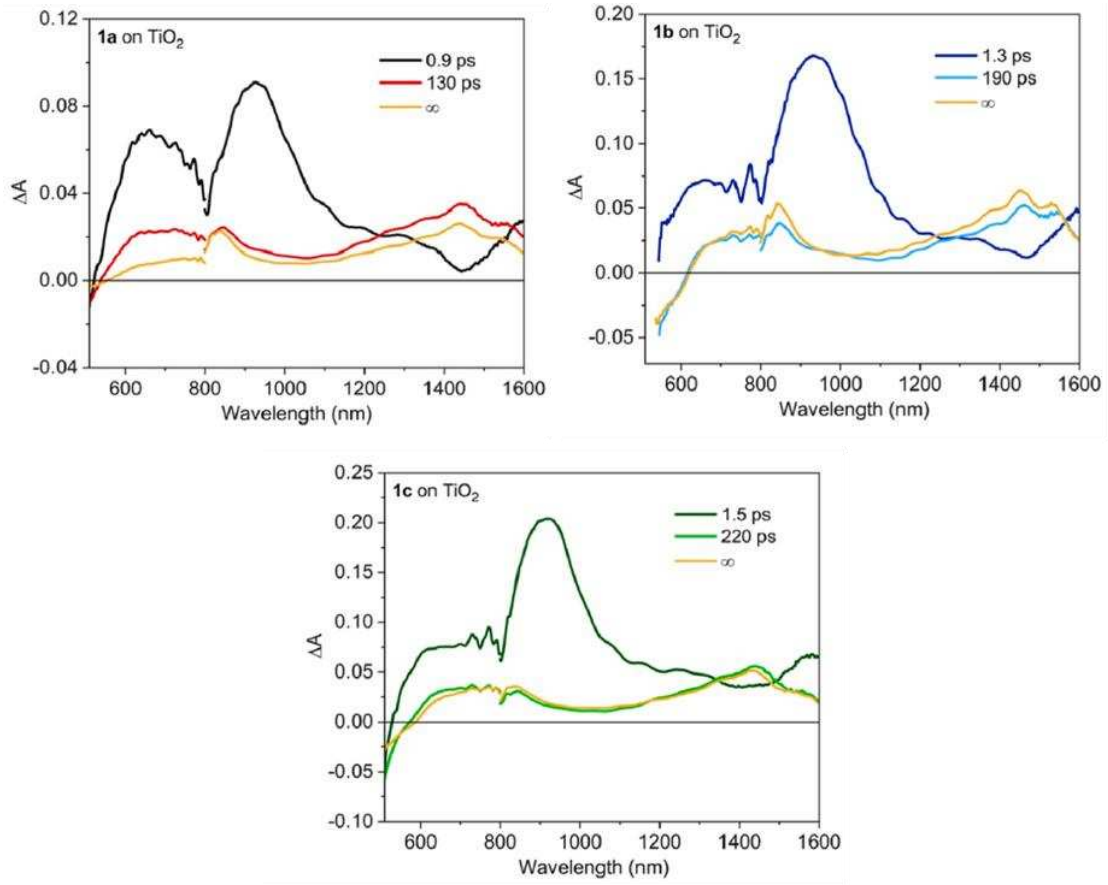

Figure 3.12 Evolution Associated Difference Spectra and lifetimes obtained from Global Analysis of the transient data.

As can be seen, in all cases, a fast component with a timescale of 1–2 ps is observed, characterized by a broad absorption band in the 600–800 nm range and a pronounced peak around 920 nm. The analysis also reveals two additional components, which differ significantly from the fast component in both their spectral features and kinetic behavior. These components have nearly identical spectra, featuring a broad band between 600 and 800 nm, a peak near 830 nm, and a broad absorption feature in the 1200–1600 nm range. The corresponding time constants are approximately 100–200 ps and >5 ns, with the latter effectively exhibiting an infinite lifetime within the experimental time window. The first fast component is assigned to the radical cation of the molecule, generated upon electron injection into TiO_2, as its spectrum closely matches that of the oxidized dye observed in spectro-electrochemical analysis shown in the previous paragraphs. This suggests that electron injection from the dye's singlet excited state into TiO_2 is an ultrafast process occurring within the time resolution of the instrument (300 fs). Similar ultrafast injection dynamics have been reported in titania-supported DSSCs.[36] In contrast, the spectral distribution of the components with longer lifetimes can be attributed to contributions from the dye cation, as well as from both trapped and conduction electrons generated upon injection. These electrons are known to exhibit absorption

bands around 800 nm and above 1200 nm, respectively.[37] The growth of the band at 830 nm (Figure 3.11, right) testifies the slower accumulation of the trapped electrons with respect to the fast injection event. Interestingly, as mentioned above, these spectra decay with two different time con stants: 100–200 ps and >5 ns, as indicated by the global fit (Fig. 9, right). This behavior can be interpreted considering that charge recombination can occur from two types of electron-hole pairs, one where the electron is still electrostatically bound to the dye cation (interfacial charge-transfer complex) and one where the electron has become a "free" carrier.[38] The "infinite" lifetime is thus indicative of the presence of free electrons that will give origin to the photocurrent. It can be noticed that the short lifetime (1–2 ps) observed for the first component associated with the radical cation of the dye is justified by the absence of an external circuit that promotes the movement of the electron once generated. Part of the formed cations will thus recombine quickly and, given the high attenuation coefficient of these species, their transient features dominate the spectra at short time delays.

3.4.4 Application of dyes 1a-c as anodic sensitizers in DSPEC

In agreement with the general structure of *n*-type DS-PEC described above (see Chapter 1), we planned to fabricate devices presenting a photoanode functionalized with dyes **1a-c** and a suitable water oxidation catalyst. Accordingly, we selected the known ruthenium complex **[Ru(bda)(PyP)$_2$]** (Figure 3.13) to work in combination with the novel dyes **1a-c**.
The resulting DS-PEC, and in particular its photoanode, are also schematically represented in Figure 3.12.

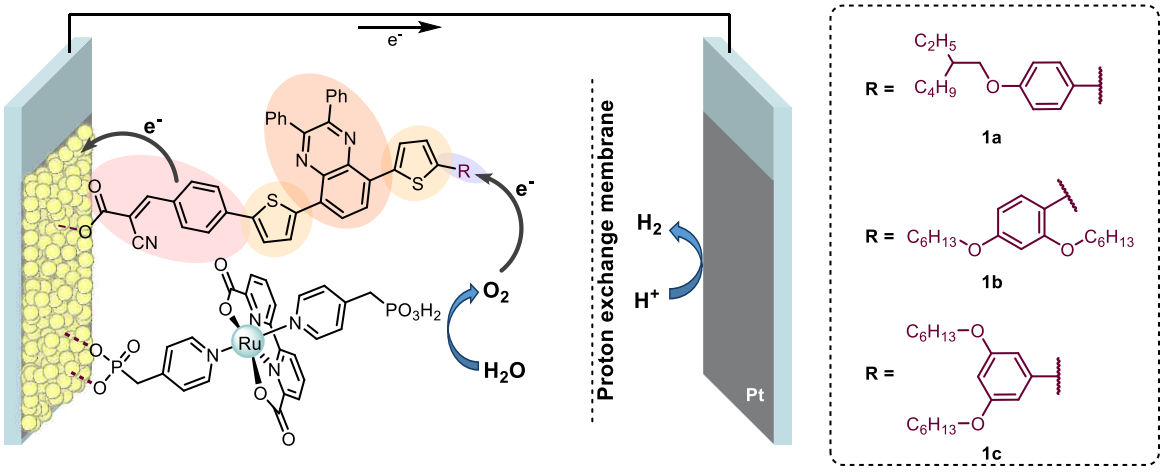

*Figure 3.13 Schematic representation of a DS-PEC with a photoanode functionalized with dyes **1a-c** and catalyst **[Ru(bda)(PyP)$_2$]** .*

Among all reported Ru-based water oxidation catalysts we choose **[Ru(bda)(PyP)$_2$]** due to its two phosphonate anchoring groups, which enable stable attachment to TiO_2, and its straightforward synthesis from commercially available starting materials. Furthermore, previous reports have demonstrated sustained photocurrent density in an aqueous solution when **[Ru(bda)(PyP)$_2$]** was employed as WOC for water splitting DSPEC in combination with D-π-A organic dyes as sensitizers. [16]

For the functionalization of the photoelectrodes we decided to apply the so-called co-loading approach, where chromophores and catalysts are deposited onto the oxide surface through simple soaking procedures.[39] This procedure can occur simultaneously or sequentially, with the electrode being immersed in a solution containing the chromophores, catalysts, or both.[40–42] Despite some drawbacks, such as rapid electron-hole recombination at the molecule-electrode interface and a difficult-to-control adsorption ratio of catalyst and photosensitizer, this approach offers a simple, straightforward and effective method to assemble PA-DS-PECs.

In the next paragraphs, the synthesis of the chosen Ru-based WOC will be described, followed by the spectroscopic and electrochemical characterization of the functionalized photoelectrodes, using both stationary and time-resolved techniques. Finally, the performances of the resulting DS-PEC in a three-electrode cell configuration will be discussed.

3.4.4.1 Synthesis of [Ru(bda)(PyP)$_2$] complex

Initially, we attempted the synthesis of **[Ru(bda)(PyP)$_2$]** by repeating the general procedure described in the literature to access this class of compounds[16] (Scheme 3.6).

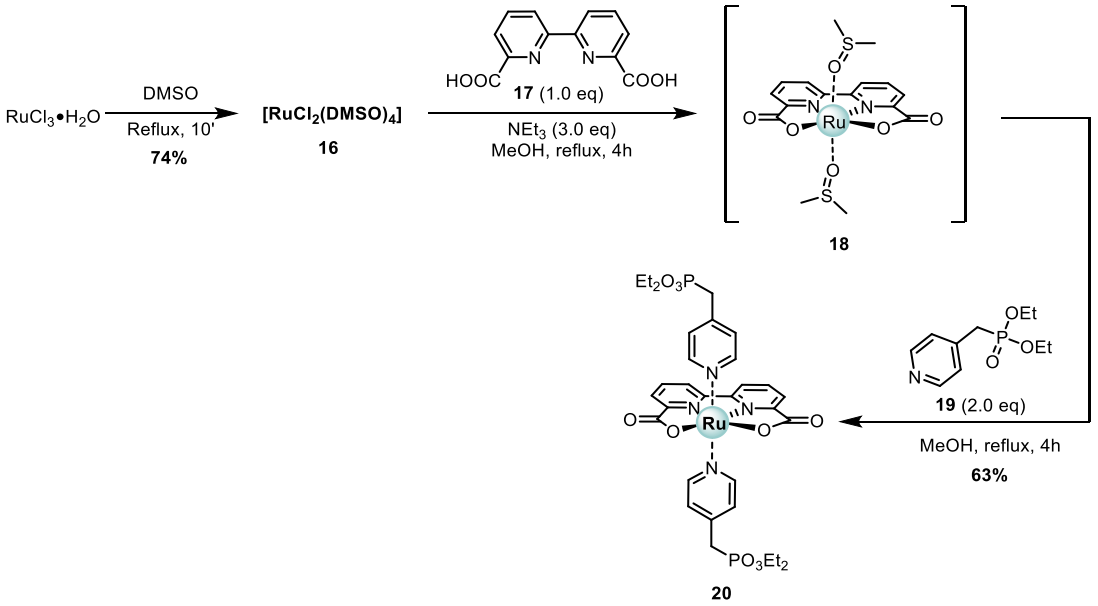

*Scheme 3.6 Synthesis of intermediate **20.***

Accordingly, **[$RuCl_2(DMSO)_4$]** (**16**) was prepared by refluxing $RuCl_3 \cdot 3H_2O$ in DMSO for 10 minutes. The obtained precursor was then reacted with the tetradentate ligand 2, 2′-bipyridine-6,6′-dicarboxylic acid (bda, **16**) and NEt_3 to form the intermediate **[Ru(bda)$(DMSO)_2$]** (**18**). Without any isolation step, intermediate **18** was treated in situ with diethyl pyridin-4-ylmethylphosphonate (**19**), leading to the di-phosphonic ester complex **20** in 63% yield.

At this stage, multiple attempts to obtain the final product after conversion of the phosphonic ester moieties to the free acids, summarized in Table 3.7, were unsuccessful (Scheme 3.7).

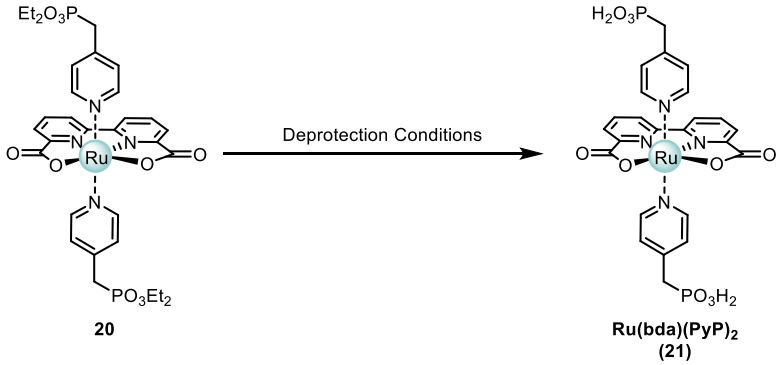

20 **Ru(bda)$(PyP)_2$ (21)**

Scheme 3.7 *Attempted deprotection of complex **20** with trimethylsilyl halides.*

Table 3.7 Attempted reaction condition for the deprotection of complex 19

Entry	Deprotection conditions	Yield of 21 (%)
1[b]	$(CH_3)_3SiI$, DCM, rt, **16 h** then MeOH, rt, 2 h	n.d
2	$(CH_3)_3SiI$, DCM, rt, 16 h then MeOH, rt, **8 h**	n.d
3	$(CH_3)_3SiI$, DCM, rt, **24 h** then MeOH, rt, 2 h	n.d
4	**$(CH_3)_3SiBr$**, DCM, rt, 16 h then MeOH, rt, 2 h	n.d
5	$(CH_3)_3SiBr$, DCM, rt, **72 h** then MeOH, rt, 2 h	n.d
6	$(CH_3)_3SiBr$, **Acetonitrile**, rt, 16 h then MeOH, rt, 2 h	n.d

n.d.= Not determined

Indeed, when either $(CH_3)_3SiBr$ or $(CH_3)_3SiI$ were used as the deprotecting reagent under different reaction conditions[16], a complex mixture of products was obtained, from which we were not able to isolate **[Ru(bda)(PyP)$_2$]** (**21**) in pure form, also due to its limited solubility in typical organic solvents.

To overcome these problems, we modified the procedure to bypass the deprotection step (Scheme 3.8). In this revised method, **[Ru(bda)(DMSO)$_2$]** (**18**) was prepared once again from **[RuCl$_2$(DMSO)$_4$]** (**16**) under similar conditions as the previous synthesis. This time, however, the product was isolated by centrifugation and washed with cold methanol. Intermediate **18** was then directly reacted with free pyridin-4-ylmethylphosphonic acid (**22**) in a 4:1 MeOH/HFIP mixture (HFIP = 1,1,1,3,3,3-hexafluoro-2-propanol). The use of HFIP proved essential to dissolve the otherwise rather insoluble acid **22**, allowing a more efficient formation of the final product, which could then be isolated in good yield by centrifugation and washing with DCM and methanol. Also in the case of **[Ru(bda)(PyP)$_2$]**, we found that the use of HFIP greatly helped to properly dissolve the compound, facilitating its isolation and further manipulation (see below).

The desired product was finally characterized by ^{1}H-, ^{13}C- and ^{31}P-NMR spectroscopy. Due to partial oxidation under air, with consequent formation of less soluble paramagnetic species, NMR spectra of the catalyst were recorded in the presence of a small amount of hydroquinone as a reducing agent.

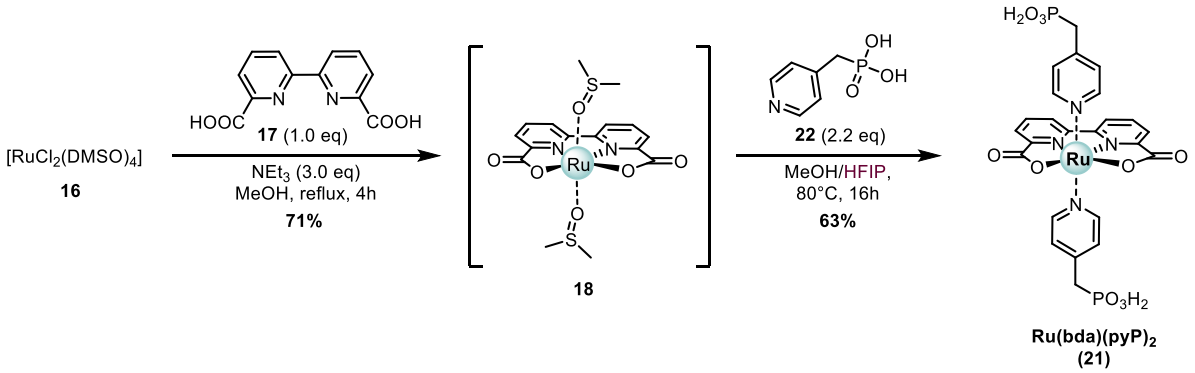

*Scheme 3.8 Synthesis of water oxidation catalyst **[Ru(bda)(PyP)$_2$]**.*

3.4.4.2 Spectro-electrochemical characterization of [Ru(bda)(PyP)$_2$]

The optical properties of **[Ru(bda)(PyP)$_2$]** were initially studied using UV-vis absorption spectroscopy in a MeOH/HFIP (9:1) solution. As shown in the recorded spectra (Figure 3.14, left) the compound exhibits a broad absorption in the visible region, with an onset just below 600 nm. The absorption is more pronounced between 300–450 nm and weaker in the 450–600 nm range. This spectroscopic behavior is in agreement with the reported examples in literature.

The spectroscopic behavior of **[Ru(bda)(PyP)$_2$]** was further examined after adsorption on mesoporous TiO_2 films. Electrodes decorated only with the **[Ru(bda)(PyP)$_2$]** catalyst were prepared by dipping them in a 1.0×10^{-4} M solution of the complex in a MeOH/HFIP 9:1 mixture for 4 h. The recorded UV-Vis absorption spectra shown in Figure 3.14 (right), resembles the one recorded in solution, but with a relatively weaker absorption encompassing the visible region in the 400–575 nm range.

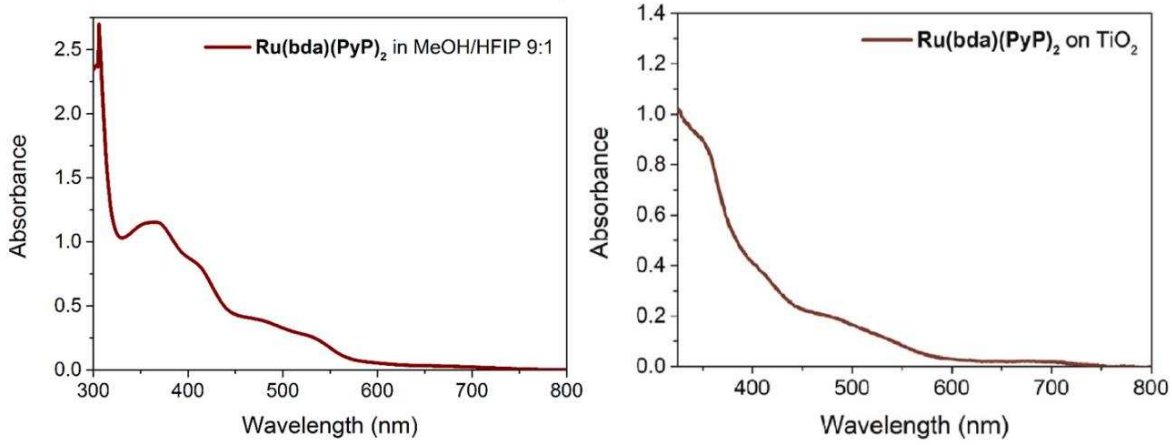

*Figure 3.14 Normalized UV-Vis absorption spectra of **[Ru(bda)(pyP)$_2$]** in solution (left) and adsorbed on mesoporous TiO_2 films (right).*

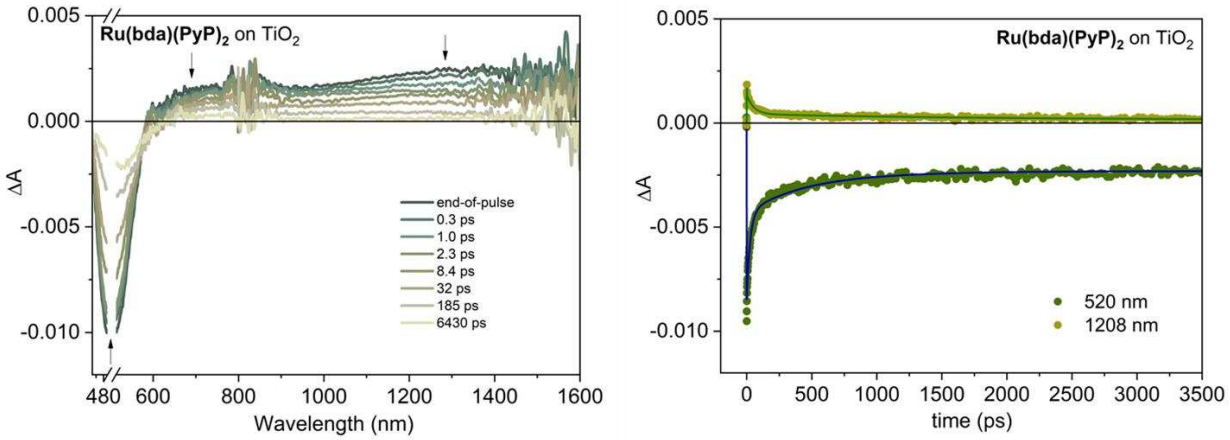

*Figure 3.15 Transient absorption spectra at different delays of complex **[Ru(bda)(PyP)$_2$]** adsorbed on TiO_2 films (left); ΔA temporal evolution at selected wavelengths. λ_{exc} = 500 nm, E = 3 μJ/pulse (right).*

TAS experiments were also performed on the complex **[Ru(bda)(PyP)$_2$]** adsorbed onto TiO_2. The transient spectra display ground-state bleaching around 500 nm and a broad, featureless positive signal extending up to 1600 nm (Figure 3.15, left). No rise in the signal was observed, and the decay follows a multi-exponential profile across the entire spectral range, with lifetimes of approximately 0.5, 50, and 500 ps, along with an "infinite" component, which is most prominent in

the bleaching band (Figure 3.15, right). The short components can be attributed to electron injection from the triplet excited state of the Ru complex into TiO_2, while the infinite lifetime suggests a slow recovery of the complex's ground state, likely due to charge recombination occurring over longer timescales. Overall, the transient signal can be interpreted as a combination of absorption from the triplet state of the complex, its oxidized form, and free electrons in the conduction band of TiO_2.[43–45]

3.4.4.3 Preparation and characterization of the photoanodes

DS-PEC photoanodes were obtained following a co-adsorption approach realized by immersion of FTO/nc-TiO_2 films in a mixed solution of one of the dyes **1a-c** and **[Ru(bda)(PyP)$_2$]** in a MeOH/THF/HFIP 70:25:5 solvent mixture for 4 h. The concentrations of the dye and the catalyst in this staining solution were 2.0×10^{-4} M and 1.0×10^{-4} M, respectively.

Prior to the photoelectrochemical experiments in DSPEC, the obtained electrodes were fully characterized from a photo-electrochemical point of view.

The UV-vis absorption spectra reported in Figure 3.16, show profiles similar to those of the individual dyes. However, for compound **1a**, a red shift of the absorption maximum to 489 nm was observed, likely due to reduced dye aggregation on the TiO_2 surface as a result of co-adsorption. Unfortunately, we were unable to separate the absorption features of the dyes from those of the ruthenium catalyst in the recorded spectra, preventing the estimation of their relative loading on the semiconductor surface using Meyer's method as described above.

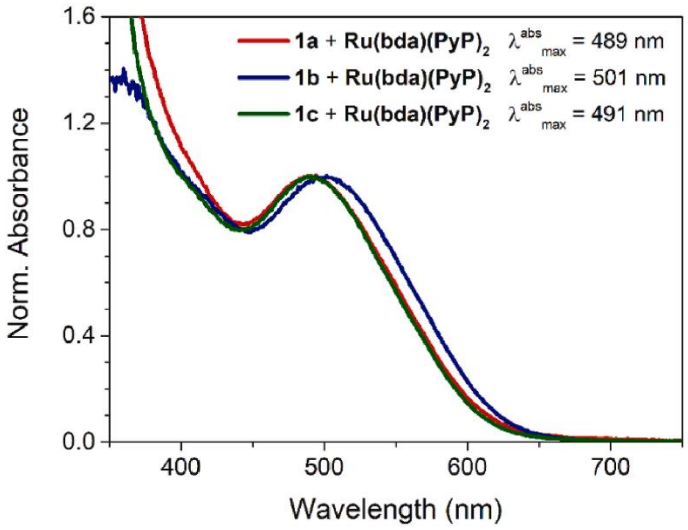

*Figure 3.16 Normalized UV–Vis absorption spectra of dyes **1a-c** and complex **[Ru(bda)(PyP)$_2$]** co-adsorbed on TiO_2.*

For what concern TAS experiments, when co-adsorbed with the complex **[Ru(bda)(PyP)$_2$]** on TiO_2, dyes **1a-c** show transient spectral features very similar to those observed for the bare dyes. The EAD spectra obtained by global analysis (Figure 3.17) reveals three main components with spectral distributions similar to those seen in the previous case. However, the second component now shows a slightly shorter lifetime, in the range of 100–130 ps, suggesting a faster charge recombination in the interfacial electron-hole pairs. Overall, the presence of the Ru complex does not significantly influence the charge injection or charge recombination processes within the timescale of the TAS experiment, which is not surprising considering that the dye regeneration process mediated by the catalyst usually occurs on much longer timescales. Furthermore, since the transient absorption features of the bare complex adsorbed on TiO_2 are weak, they are barely detectable in the spectra of the co-adsorbed samples.

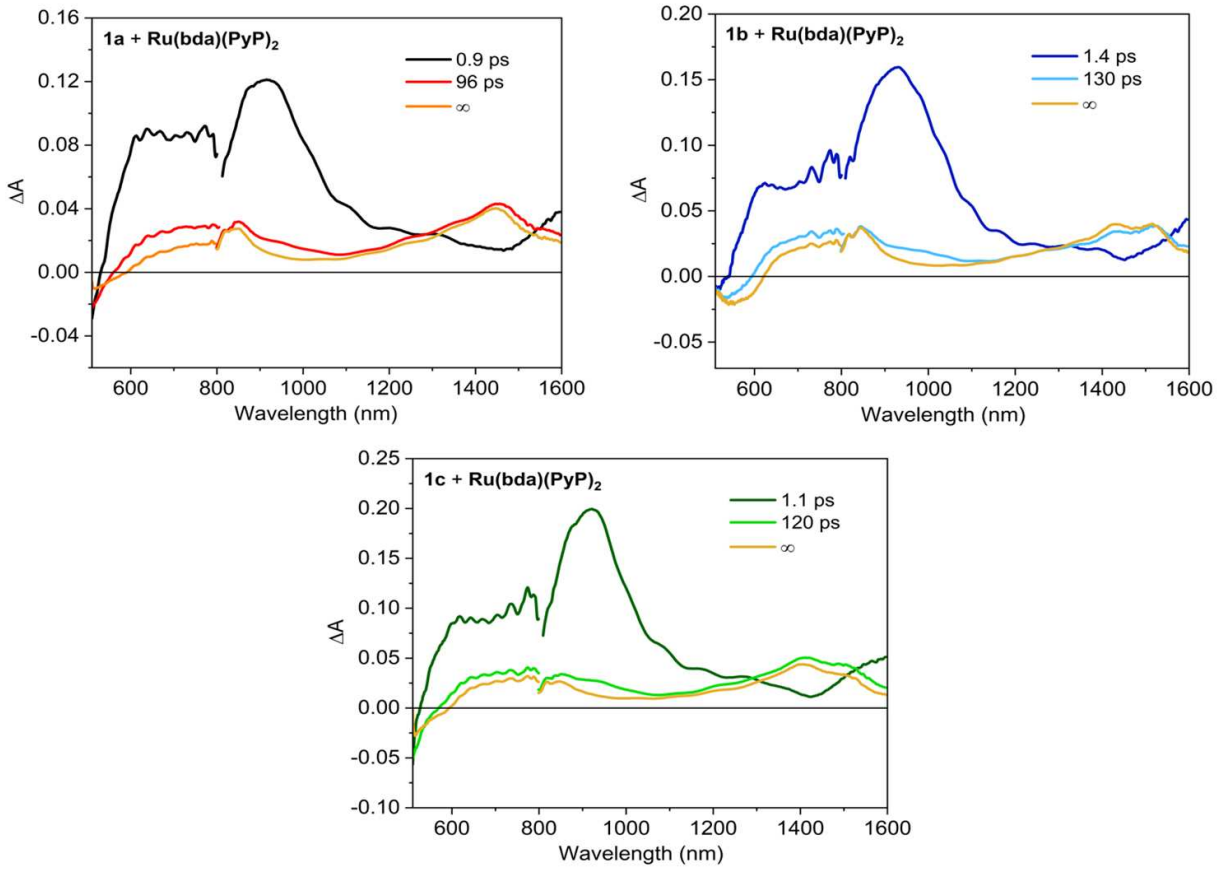

Figure 3.17 *Evolution Associated Difference Spectra and lifetimes obtained from Global Analysis of the transient data of dyes* ***1a-c*** *and complex* ***[Ru(bda)(PyP)$_2$]*** *co-adsorbed on TiO_2 films.*

The electrochemical properties of the dye-sensitized photoanodes were also investigated recording the cyclic voltammetry (CV) traces of the FTO/nc-TiO_2 electrodes in dark conditions (Figure 3.18, right), using a three-electrodes cell setup with the functionalized films as working electrodes, a Saturated Calomel Electrode (SCE) as the reference electrode, a platinum wire as the counter electrode and phosphate buffer (pH = 6.6) as the electrolyte.

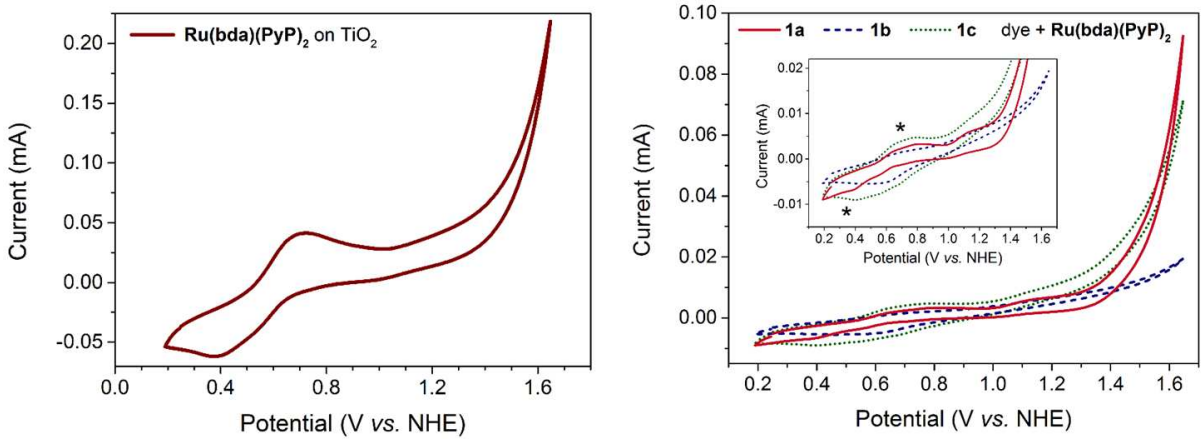

*Figure 3.18 CV scan of a FTO/TiO₂/**[Ru(bda)(PyP)₂]** electrode (left); FTO/TiO₂/dye + **[Ru(bda)(PyP)₂]** electrodes (right, **1a**: red solid line; **1b**: blue dashed line; **1c**: green dotted line), immersed in 0.1 M phosphate buffer solution at pH = 6.6.*

The CV traces of the photoanodes functionalized with both the dyes and the catalyst (Figure 3.18, right), display a small reversible peak at $E_{1/2}$ ~ +0.6 V *vs.* NHE and an anodic wave with an onset potential of approx. +1.1 V vs. NHE. By comparison with the CV traces of the electrodes functionalized with only **[Ru(bda)(pyP)₂]** (Figure 3.18, left) the small reversible peak at $E_{1/2}$ ~ +0.6 V *vs.* NHE could be assigned to the Ru^{II}/Ru^{III} redox couple, whereas the anodic wave at positive potentials indicated that the water oxidation reaction occurred.[43,46] Therefore, the presence of the Ru-catalyst could be confirmed in all the samples, although, as can be seen in the zoom of the plots in Figure 3.18 (right), the electrode sensitized with **1b** shows a less evident peak at $E_{1/2}$ ~ +0.6 V *vs.* NHE and also a smaller water oxidation wave at positive potentials, suggesting that it could be less efficient in promoting the desired reaction, compared to dye **1a,c**.

3.4.4.4 Photoelectrochemical experiments

As a final part of our study on the quinoxaline-based sensitizers, the capability of the new dyes to work as sensitizers for DS-PEC photoanodes was preliminarily assessed by measuring the relative photocurrent response in a photoelectrochemical cell with a three-electrode configuration. The dye-sensitized photoanodes (prepared in the same manner described above) were used as working electrodes, an Ag/AgCl (KCl sat.) aqueous electrode as reference electrode and platinum wire as the counter electrode, while aq. Na_2SO_4 0.1 M (pH = 6.5) was employed as the electrolyte.

To evaluate the best external bias to be used in the photoelectrochemical measurements, linear sweep voltammetry (LSV) was performed on the differently sensitized photoanodes, scanning the potential range from −0.2 to 0.7 V *vs* NHE. The experiments were conducted under chopped illumination (100 mW cm^{-2}, AM 1.5 calibrated with a reference silicon solar cell), to highlight the different response of the electrode materials and confirm their photoactive behavior.

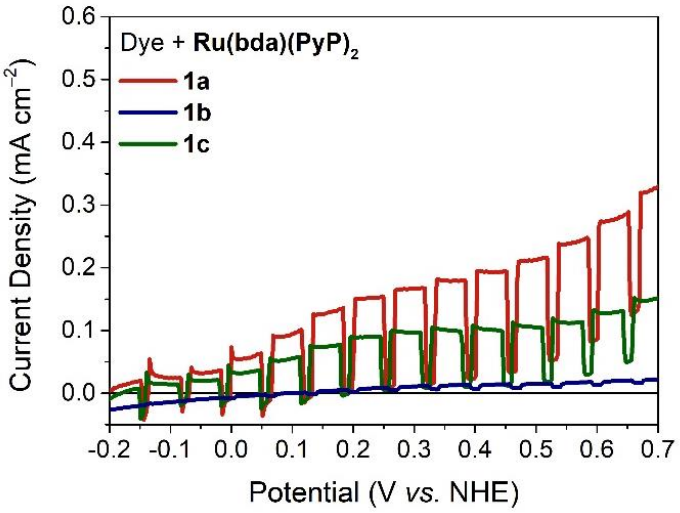

*Figure 3.19 LSV traces of DS-PEC fabricated with FTO/nc-TiO_2/dye + **[Ru(bda)(PyP)$_2$]** working electrodes under chopped AM 1.5 illumination.*

Clearly, the largest photocurrent was provided by dye **1a** (Figure 3.19, red line), with an onset at around − 0.2 V *vs.* NHE and the maximum value of approx. 150 μA cm^{-2} in the +0.4–0.5 V vs. NHE range, calculated as difference between illuminated and dark conditions. This outcome can be rationalized considering that compound **1a** shows the best combination of intense light absorption and well-aligned electrochemical features in quinoxaline-based dye series. Specifically, the HOMO and LUMO energy levels of dye **1a** have the best matching with the catalytic onset potential of the Ru-based WOC and the CB of TiO_2, respectively. Furthermore, its smaller $E_{0\text{-}0}$ value ensures enhanced overlap with the solar emission spectrum, contributing to its higher efficiency. Dye **1c** (Figure 3.19, green line) displayed a similar behavior, although its photocurrent was lower, peaking at around 85 μA cm^{-2} within the same potential range. In contrast, the electrode sensitized with dye **1b** (Figure 3.19, blue line) showed minimal activity under illumination, with a photocurrent only slightly above the dark current.

Building on the results from the LSV experiments, subsequent chronoamperometric (CA) measurements were conducted at a fixed bias of +0.5 V *vs.* NHE to optimize the photocurrent response (Figure 3.20). Current traces were recorded over a 100-second period, under chopped illumination. After an initial decay-attributable to rapid electron injection from the excited dye into the TiO_2 conduction band, followed by fast charge recombination due to the kinetic limitations of the dye regeneration process by the WOC[47], the photocurrents stabilized for the remainder of the experiment. These results were consistent with those from the LSV measurements. Electrodes incorporating dyes **1a** and **1c** yielded stable currents of approximately 145 μA cm^{-2} and 82 μA cm^{-2}, respectively, while the electrode sensitized with dye **1b** showed the lowest photocurrent, at around 6 μA cm^{-2}.

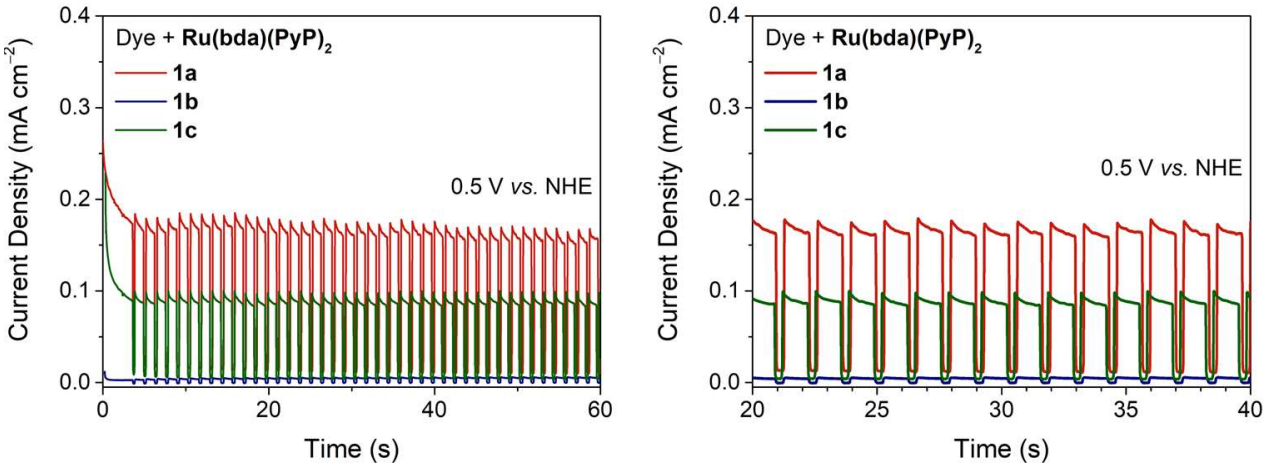

*Figure 3.20 CA of DS-PEC fabricated with FTO/nc-TiO_2/dye + **[Ru(bda)(PyP)$_2$]** working electrodes under hopped AM 1.5 illumination from 0 to 60 s (left); zoom of panel in the 20–40 s range (right).*

The lack of activity shown by the electrodes containing dye **1b** could be tentatively explained by taking into account its oxidation potentials. The electrochemical analysis discussed above (see paragraph 3.4.3.1) showed that, in the case of dye **1b**, the E_{ox} value measured in solution (+1.08 V vs. NHE) was very close to the reported onset of catalysis of **[Ru(bda)(pyP)$_2$]** (E_{onset}, approx. +1.1 V vs. NHE) suggesting that a relatively small thermodynamic driving force for hole transfer to the catalyst could exist for such dye. In addition, with a value of 9.3×10^{-8} mol/cm^2, dye **1b** presented also the highest loading on TiO_2, suggesting that an insufficient amount of the catalyst could be adsorbed on the semiconductor surface when applying the "co-adsorption" method described above.

Based on these observations, we hypothesized that the regeneration of dye **1b** could be improved by increasing the relative amount of catalyst adsorbed on the semiconductor compared to the dye. To test this supposition, we employed a "sequential" adsorption approach, where the bare TiO_2 electrodes were first immersed in a 1.0×10^{-4} M catalyst solution for 4 hours, followed by immersion in a 2.0×10^{-4} M solution of dye **1b** (Figure 3.21). By initiating the sensitization process with the immersion of the photoanode in a solution containing only the catalyst, we aimed to maximize the amount of catalyst anchored on the semiconductor surface and enhance the water oxidation reaction capacity.

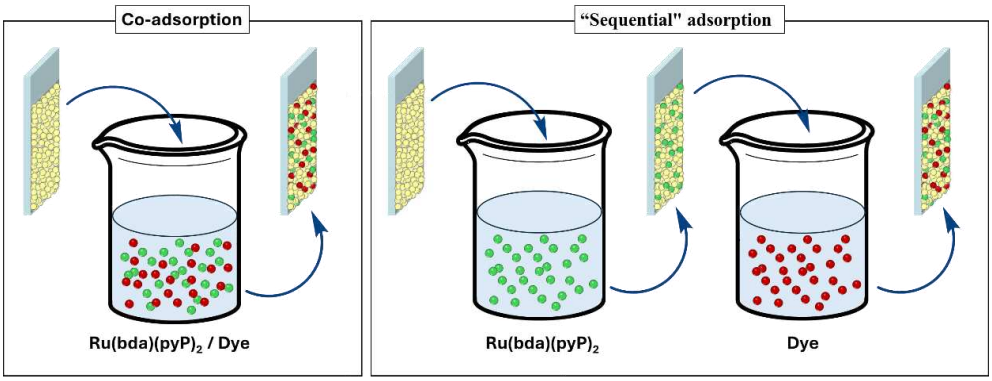

Figure 3.21 Schematic representation of the co-adsorption method (left) and the "sequential" adsorption approach (right).

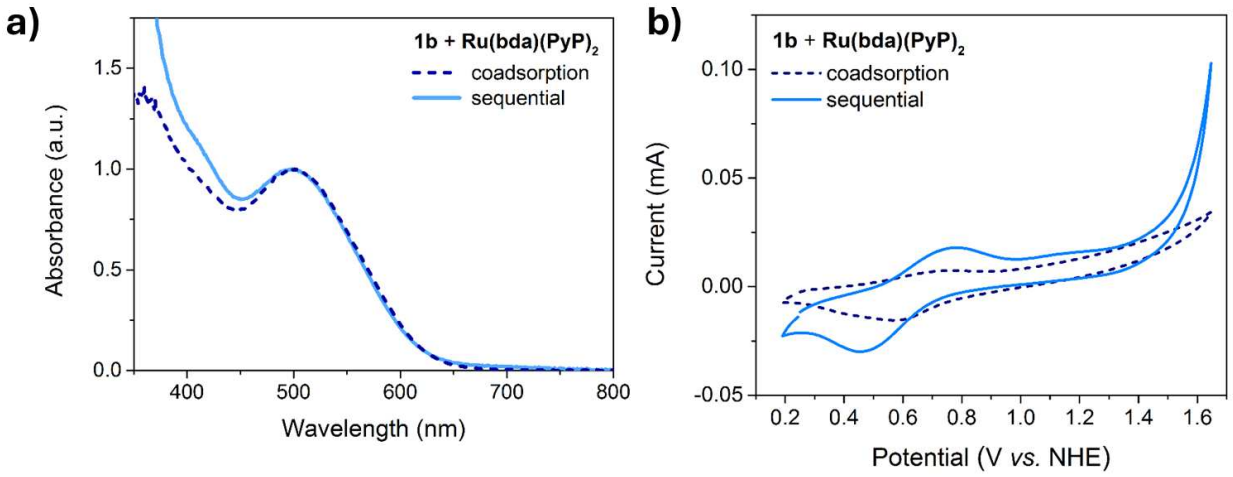

*Figure 3.22 a) Comparison between the normalized UV-Vis absorption spectra of FTO/TiO$_2$/**1b**+**[Ru(bda)(PyP)$_2$]** electrodes obtained with the "co-adsorption" (blue dashed line) and "sequential" (light blue solid line) staining procedures; b) CV scans of FTO/TiO$_2$ /**1b** + **[Ru(bda)(PyP)$_2$]** electrodes, immersed in 0.1 M phosphate buffer solution at pH = 6.6. "Coadsorption" staining procedure, blue dashed line; "sequential" staining procedure, light blue solid line.*

Comparing the normalized UV–Vis absorption spectra of electrodes prepared with the two methods (Figure 3.22, left), we found a higher relative absorbance for the "sequential" sample in the 350–500 nm range, where the catalyst absorbs more light. Furthermore, in the CV curves (Figure 3.22, right), the redox peak corresponding to the Ru^{II}/Ru^{III} couple was more pronounced for the "sequential" sample. In addition, an intense electrocatalytic anodic wave (onset at ca. +1.1 V vs. NHE) comparable with the one seen previously for dyes **1a,c** was observed. This observation suggested that the electrode, prepared using the sequential method, could have significantly higher catalytic activity compared to the one prepared using the co-adsorption procedure.

Encouraged by these results, we performed LSV experiments using the FTO/nc-TiO$_2$/**1b** + **[Ru(bda)(PyP)$_2$]** electrodes, obtained by the "sequential" adsorption method, as working electrodes under the same experimental conditions described previously.

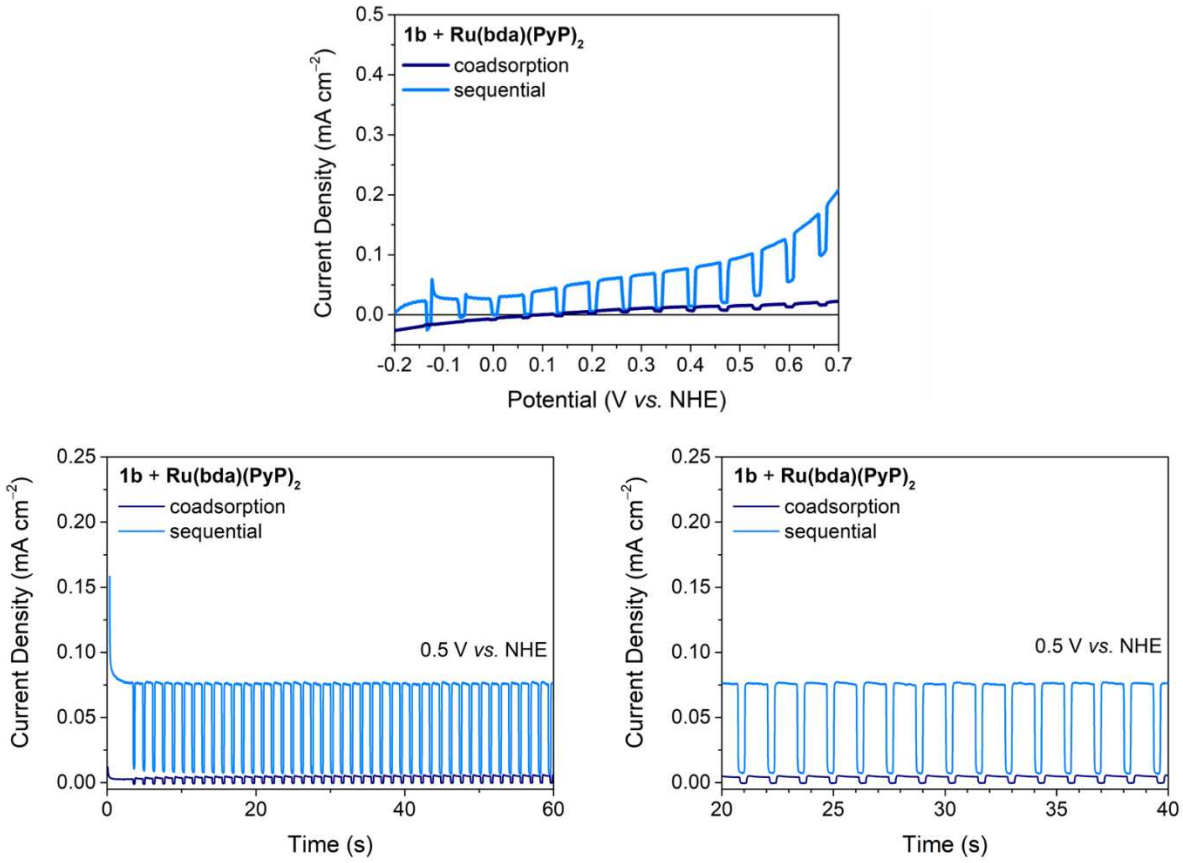

*Figure 3.23 Comparison of the LSV traces of DS-PEC fabricated with FTO/nc-TiO_2/**1b** + **[Ru(bda)(PyP)$_2$]** working electrodes obtained with the "co-adsorption" and "sequential" methods (top); CA of the same cells (bottom left); zoom of panel in the 20–40 s range (bottom right); under chopped AM 1.5 illumination.*

As illustrated in Figure 3.22, the investigated sample displayed notable improvement in photocurrent, reaching approximately 63 μA cm^{-2} within the +0.4 to +0.5 V vs. NHE potential range. This observation was further confirmed by the following CA measurements conducted at +0.5 V vs. NHE (Figure 3.23,bottom), where a relatively stable photocurrent of around 68 μA cm^{-2} was sustained throughout the entire duration of the experiment. Although the photocurrent generated by the "sequential" **1b + [Ru(bda)(PyP)$_2$]** photoelectrodes remained lower than the one produced by dyes **1a,c**, this result highlighted the potential of tuning the performance of DS-PEC systems through adjustments in the sensitization procedure, in response of the specific structural and electrochemical features of their molecular components.

3.5 Pyrido[3,4-*b*]pyrazine-based sensitizers

After completing the investigation of compounds 1a–c, we turned our focus to the second family of pyrido[3,4-b]pyrazine-based sensitizers **PP2a-c**. These dyes were initially synthesized using Pd-catalyzed cross-coupling reactions and subsequently characterized in solution. The synthesis and characterization details are outlined in the following sections.

3.5.1 Design pathway and retrosynthetic analysis

With the aim of developing a concise and common synthetic pathway for the designed family of dyes, we decided to first investigate the synthesis of compound **PP2a** as a model substrate and later extend the optimized approach to compounds **PP2b-c**

Scheme 3.9 shows the retrosynthetic approach devised to highlight the most important disconnections in the structure of dye **PP2a**.

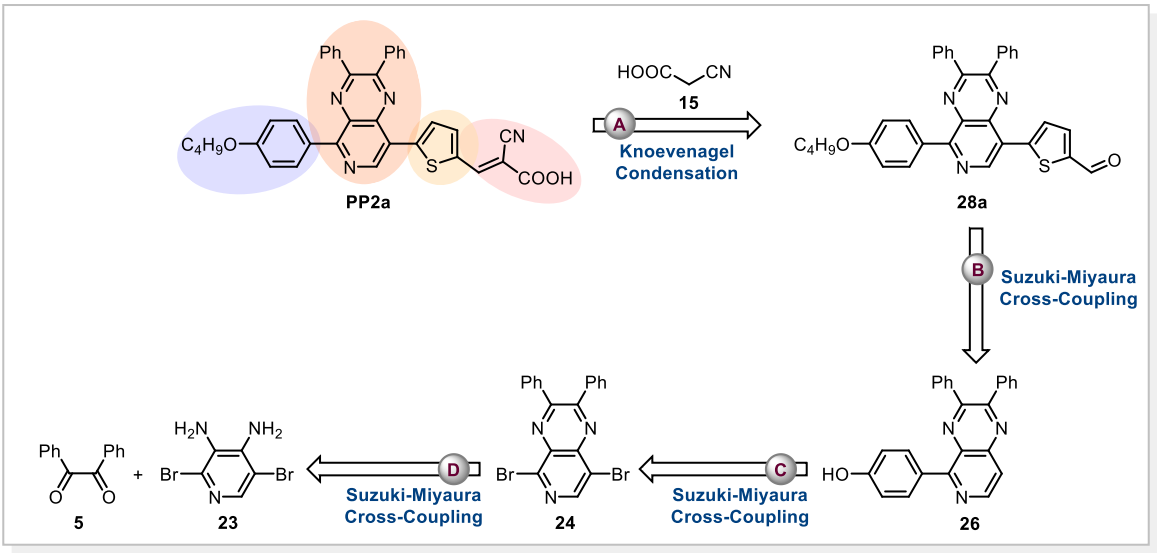

*Scheme 3.9 Retrosynthetic approach for the synthesis of compound **PP2a**. Colors represent the different building blocks: donor (purple), π (yellow), auxiliary acceptor (orange), acceptor (pink).*

In agreement with the retrosynthetic analysis shown above, after a first fragmentation of the cyanoacrylic acid moiety to yield aldehyde **28a**, the two main disconnections (***B*** and ***C***) concerned the removal of the acceptor and then donor groups from the central pyrido[3,4-*b*]pyrazine core. Then, the latter was divided to release the starting materials benzil (**5**) and 3,4-diamino-2,5-dibromopyridine (**23**).

Considering the forward synthetic route, the procedure chosen to connect the donor and acceptor units to the pyrido[3,4-*b*]pyrazine central core of **24** was once again based on Pd-catalyzed cross-couplings as key reactions. Unlike the preparation of dyes **1a-c**, here we preferred the Suzuki–Miyaura reaction over direct arylation protocol. Indeed, while direct C–H arylation reactions between arenes and aromatic halides have been reported in literature, this procedure often suffers from poor regioselectivity. This is due to the presence in many arenes of C–H bonds with comparable reactivity, often resulting in mixtures of regioisomers. Without directing groups or inherent electronic or steric biases, it is challenging to control the arylation site. In order to optimize the key C-C bond formation step we decided to investigate the Suzuki-Miyaura reaction both under

thermal and microwave (MW)-assisted conditions. The details of the optimization process are discussed below.

3.5.1.1 Optimization of the Suzuki-Miyaura reaction and synthesis of dye PP2a

In the last decades, the application of MW irradiation as a heating source in synthetic organic chemistry has become progressively more popular, in response to the need of developing more environmentally friendly processes in terms of sustainable chemistry[48]. MW heating offers a distinct advantage over conventional heating because it directly transfers energy to the reacting molecules, leading to a rapid increase in temperature without significant energy loss. In contrast, conventional heating is slower due to the need to transfer heat through the walls of the vessel, which results in energy dissipation before reaching the reacting molecules. MW heating takes advantage of the ability of mobile electric charges in liquids or conducting ions in solids to convert electromagnetic energy into heat. On the other hand, conventional heating relies on thermal conduction and convection to transfer heat. MW heating is particularly advantageous in chemical processes as it significantly reduces reaction times from hours or even days to just minutes or seconds. Moreover, it aligns with the principles of green chemistry by minimizing side reactions, increasing reaction yields, and improving reproducibility.[49] For these reasons, we decided to test its employment also in our sequence to prepare dye **PP2a**.

Prior to optimizing the Suzuki-Miyaura reaction, the needed pyrido[3,4-*b*]pyrazine central core (**24**) was successfully synthetized. The desired product could be obtained through a condensation reaction, conducted in acetic acid at 100°C for 2h, between the two commercially available starting materials: 2,5-dibromopyridine-3,4-diamine (**23**) and benzil (**5**). Under this condition, compound **24** was obtained in high yield.

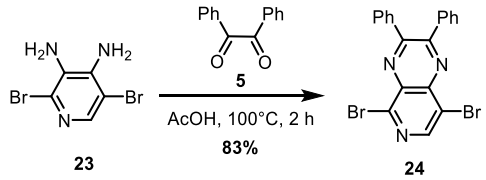

*Scheme 3.10 Synthesis of intermediate **24**.*

For what concern the Suzuki-Miyaura coupling several reports in literature have demonstrated that, with pyrido[3,4-*b*]pyrazine, the reaction occurs preferentially at the more electron deficient 4-carbon position in (highlighted with a red dot in Scheme 3.11) of pyridine derivatives.[20,50,51] Therefore, in order to obtain the desired dye **PP2a**, we started our investigation by optimizing the

coupling between the 5,8-dibromo-2,3-diphenylpyrido[3,4-*b*]pyrazine (**24**) and (4-hydroxybenzene)boronic acid (**25**) (Scheme 3.11) under both thermal and microwave-assisted conditions (Table 3.8).

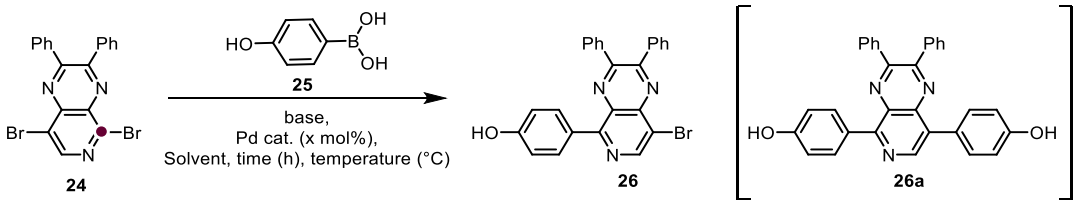

*Scheme 3.11 Synthesis of intermediate **26.***

*Table 3.8 Optimization of the reaction conditions for the preparation of intermediate **26**[a].*

Entry	24:25 ratio	"Pd"/Ligand (x mol%)	Solvent	T/t	Yield 26 (%)[d]	24:26:26a[e]
Thermal Heating						
1[b]	1:1	$Pd_2(dba)_3$ / SPhos (1.5:3 mol%)	THF:H_2O 3:1	80°C/24 h	0 %	-
2[b]	1:1	$Pd(PPh_3)_4$ (3 mol%)	THF:H_2O 3:1	80°C/24 h	15%	83:15:traces
3[b]	1:1	$Pd(PPh_3)_4$ (3 mol%)	Toluene: EtOH: H_2O 2:1:1	80°C/24 h	36%	0:36:12
4[b]	1:1.5	$Pd(PPh_3)_4$ (3 mol%)	THF:H_2O 3:1	80°C/24 h	43%	41:43:7
5[b]	1:2	$Pd(PPh_3)_4$ (3 mol%)	THF:H_2O 3:1	80°C/24 h	50%	30:50:10
Microwave Irradiation						
6[b]	1:1	$Pd(PPh_3)_4$ (3 mol%)	THF:H_2O 3:1	80°C/30'	8%	75:8:8
7[b]	1:1	$Pd(PPh_3)_4$ (3 mol%)	THF:H_2O 3:1	120°C/30'	8%	48:8:12
8[c]	1:1	$Pd(dppf)Cl_2$ (3 mol%)	Toluene: MeOH 1:1	80°C/30'	48%	24:48:traces
9[c]	**1:1.5**	**$Pd(dppf)Cl_2$ (3 mol%)**	**Toluene: MeOH 1:1**	**80°C/30'**	**70%**	**8:70:10**
10[c]	1:2	$Pd(dppf)Cl_2$ (3 mol%)	Toluene: MeOH 1:1	80°C/30'	59%	0:59:27

[a] **24** (0.227 mmol); [b] K_2CO_3 (15.0 eq) was used as base; [c] KF (6.0 eq) was used as base; [d] Isolated product yield after column chromatography; [e] Isolated products ratios.

After varying the catalyst, solvent mixture, base, stoichiometry ratio between the reagents, temperature and time, we found that the best protocol for the synthesis of intermediate **26** was represented by the microwave-assisted reaction conducted in the presence of $Pd(dppf)Cl_2$ (3 mol%) as catalyst, KF (6.0 eq.) as base, in toluene and methanol (MeOH) 1:1 at 80°C for 30 min (entry 9). Under these conditions the desired product was obtained with a good yield of 70% on a 0.227 mmol scale.

Encouraged by this result we moved further and investigated the second coupling between aldehyde **27a** and the obtained intermediate **26** (Scheme 3.12). Also in this case we performed a short optimization of the reaction conditions and explored again both thermal and MW-assisted procedures (Table 3.9).

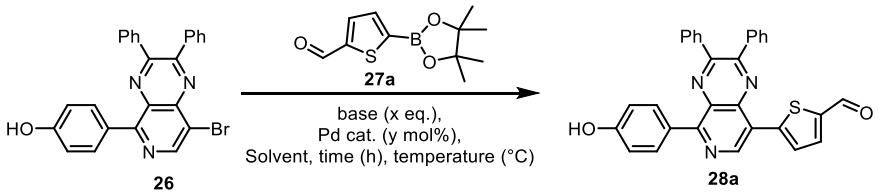

*Scheme 3.12 Synthesis of intermediate **28a-***

*Table 3.9 Optimization of the reaction conditions for the preparation of intermediate **28a**[a].*

Entry	26:27a ratio	"Pd"/Ligand (x mol%)	Solvent	T/t	Yield 28a (%)[d]	26:28a (%)
			Thermal Heating			
1[b]	1:3	$Pd(PPh_3)_4$ (3 mol%)	THF:H_2O 3:1	80°C/24 h	41%	39:41
			Microwave Irradiation			
1[b]	1:3	$Pd(PPh_3)_4$ (3 mol%)	THF:H_2O 3:1	80°C/30'	25%	63:25
3[c]	**1:3**	**$Pd(dppf)Cl_2$ (3 mol%)**	**Toluene: MeOH 1:1**	**80°C/30'**	**62%**	**35:62**

[a] **26** (0.220 mmol); [b] K_2CO_3 (15.0 eq) was used as base; [c] KF (6.0 eq) was used as base; [d] Isolated product yield after column chromatography; [d] Isolated products ratios.

The optimized conditions found for the preparation of intermediate **26** turned out to also work best for the synthesis of compound **28a** (entry 3). The same protocol, performed with an excess of compound **27a**, allowed us to obtain intermediate **28a** with a good yield of 62%.

Furthermore, since both Suzuki-Miyaura couplings could be conducted under the same reaction conditions, we decided to explore the synthesis of compound **28a** using a one-pot telescopic approach (Scheme 3.13). In this method, the process begins with the MW-assisted Suzuki-Miyaura reaction between **24** and **25**. After 30 minutes of irradiation at 80°C, the entire catalytic system is reintroduced into the reaction mixture along with boronic acid **27a**, required for the second cross-coupling step. The resulting mixture is then subjected to MW irradiation once again.

Due to the complexity of the mixture deriving from the double cross-coupling reaction, compound **28a** could not be isolated in pure form by classic flash column chromatography in this case. To overcome this problem, we decided to attempt the subsequent alkylation step leading to compound **30a** directly on the crude mixture of the double cross-coupling transformation (Scheme 3.13).

The introduction of the *n*-butane chain on the free –OH group was performed using a large excess of *n*-bromobutane (10.0 eq) and K_2CO_3 as the base, in *N,N*-DMF at 90°C for 4h. To our delight,

the alkylation procedure succeeded, and intermediate **30a** could be easily separated from the other components of the crude reaction mixture, allowing its isolation with a good overall yield of 54% over 3 steps. Therefore, the telescopic strategy offers not only better performances when compared to the previously described step-wise protocol (54% of yield over 3 steps *vs.* 43% over two steps), but also a more concise and straightforward approach, characterized by a lower number of steps requiring work-up and purification processes.

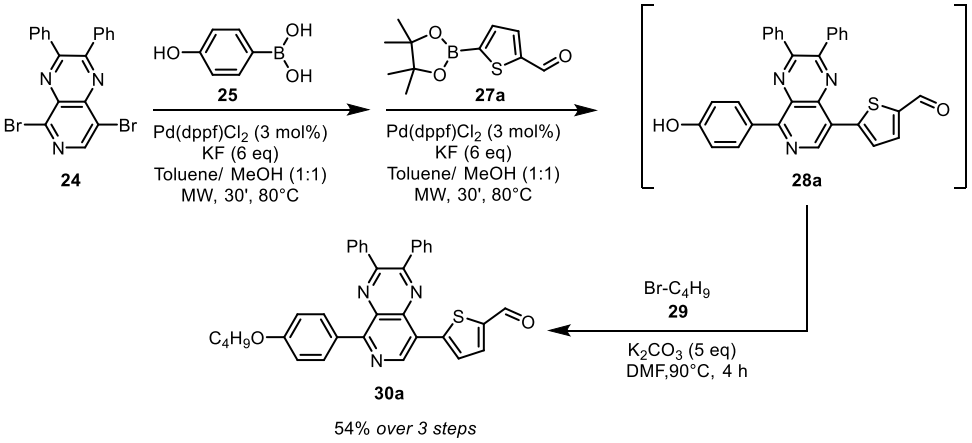

*Scheme 3.13 Synthesis of intermediate **19**: with a one-pot telescopic approach.*

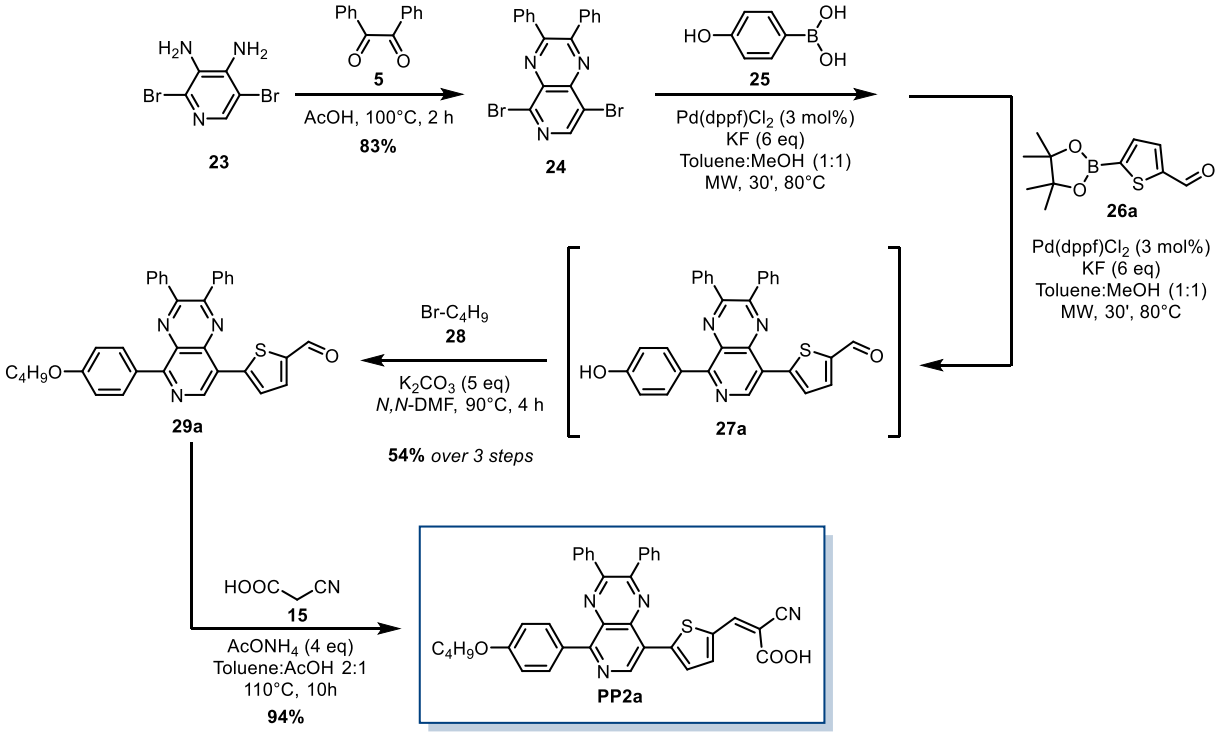

*Scheme 3.14 Overall synthetic pathway for the synthesis of dye **PP2a.***

Finally, by subjecting intermediate **30a** to a Knoevenagel reaction with cyanoacetic acid (**15**) in an acidic environment, the desired dye **PP2a** could be obtained with a high yield of 94%.

Based on the above description, the overall synthetic pathway for its preparation is summarized in Scheme 3.14. Besides the synthetic steps already described above, the scheme reports also the preparation of the pyrido[3,4-*b*]pyrazine central core (**24**) that can be easily obtained through a condensation reaction, conducted in acetic acid at 100°C for 2h, between the two commercially available starting materials: 2,5-dibromopyridine-3,4-diamine (**23**) and benzil (**5**)**.**

3.5.1.2 Synthesis of dyes PP2b,c

Encouraged by the results obtained for dye **PP2a**, we decided to expand the developed pathway to the synthesis of dyes **PP2b,c.** The overall synthetic pathway is presented in Scheme 3.15.

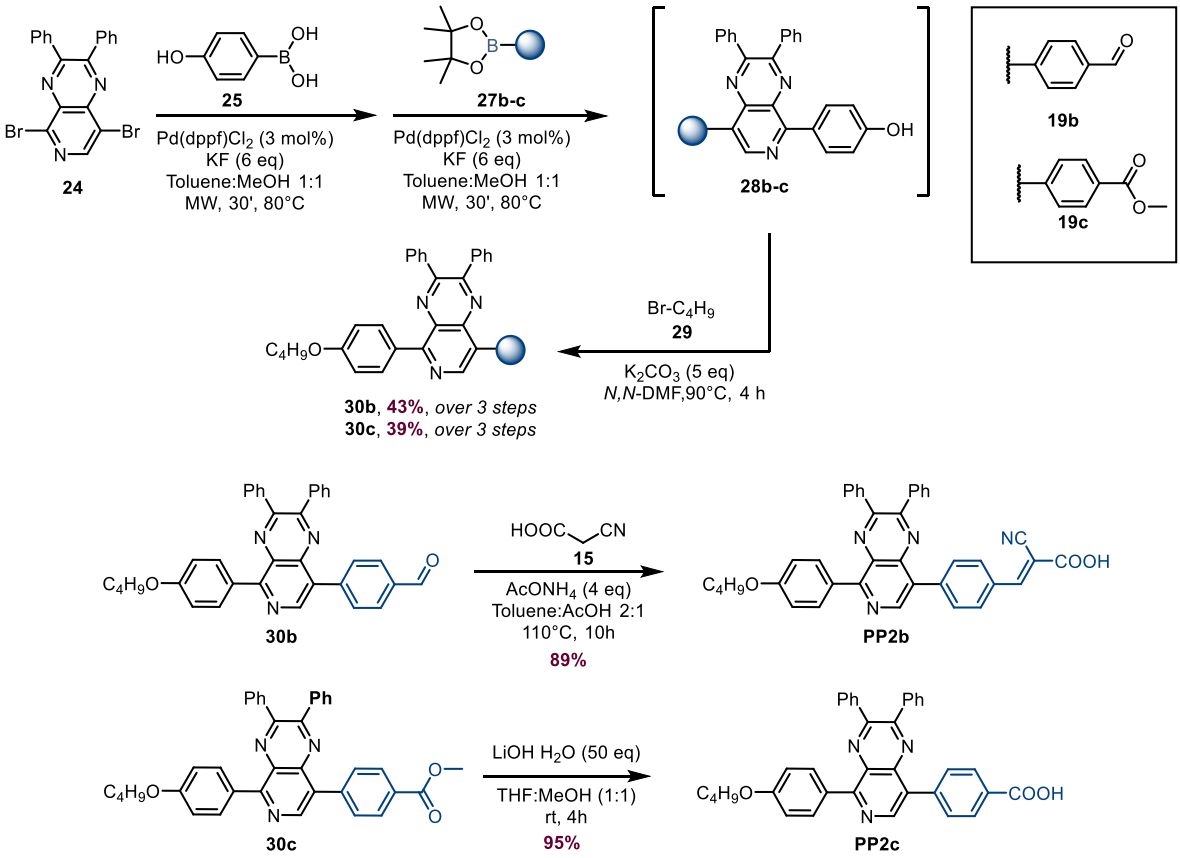

*Scheme 3.15 Overall synthetic pathway for the synthesis of dye **PP2b-c.***

As can be seen, the telescopic double Suzuki-Miyaura followed by alkylation allowed us to obtain the key intermediates **30b-c** with good yields of 39-43% over 3 steps. Then, by subjecting intermediate **30b** to a Knoevenagel reaction with cyanoacetic acid (**15**) and ammonium acetate in a toluene:acetic acid mixture at 110°C for 10h, the desired dye **PP2b** could be obtained with high yield of 89%. Meanwhile, the basic hydrolysis of ester **30c** with LiOH in a toluene:MeOH mixture, at room temperature for 4h, led to dye **PP2c** with an excellent yield of 95%. Compounds **PP2a-c** could not be purified using flash column chromatography, due to the interaction of the anchoring

group with the silica stationary phase, and therefore were isolated by means of recrystallization from ethanol.

3.5.2 Spectro-electrochemical characterization

The absorption spectra of the pyrido[3,4-*b*]pyrazine-based dyes **PP2a-c** in DCM are shown in Figure 3.24. Their absorptions, molar extinction coefficients, and optical band gap ($E_{0\text{-}0}$) are summarized in Table 3.10. The UV-vis spectra of **PP2a** exhibit three major prominent bands, two appearing around in the visible region around 390-450 nm and the third in the near UV around 310 nm. By comparison with other pyrido[3,4-*b*]pyrazine-based dyes reported in literature[20], the latter can be ascribed to a localized aromatic π–π* transition from the donor group to the pyrido[3,4-*b*]pyrazine moiety, meanwhile the absorption at 390-450 nm may be attributed to the ICT transition from the alkoxy-phenyl ring to the cyanoacetic acceptor unit.

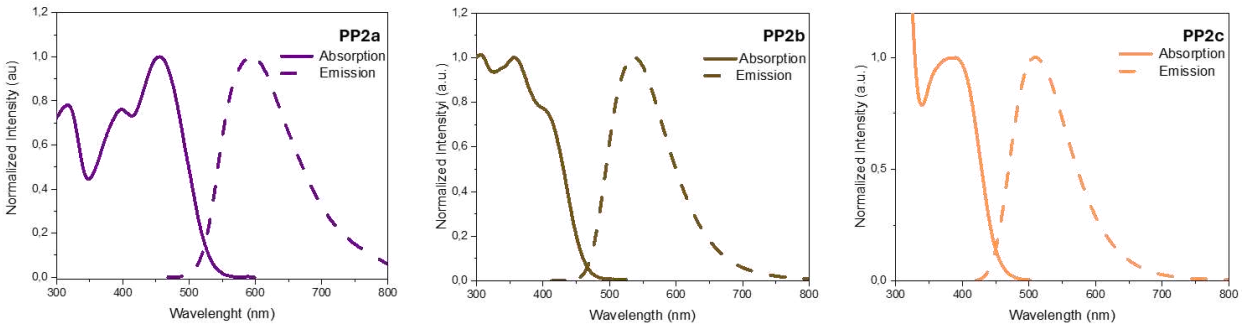

*Figure 3.24 UV–Vis absorption and emission spectra of dyes **PP2a-c** in DCM.*

*Table 3.10 Main spectroscopic properties of dyes **PP2a-c** in DCM.*

Dye	λ^{abs}_{max} (nm)	$\varepsilon \times 10^4$ (M^{-1} cm^{-1})	λ^{emi}_{max} (nm)	$^{a}E_{0\text{-}0}$ (eV)[a]
PP2a	456 (398) 316	2.51	594	2.42
PP2b	357 (406)	2.33	537	2.66
PP2c	389	2.02	525	2.75

[a] Estimated based on the intersection of the normalized absorption and emission spectra.

Varying the π-bridge from thiophene to benzene as was done for the dye **PP2b** leads to a significant difference in the absorption features demonstrating that modulation of the electron density distribution of FMOs of D–A–π–A type dyes may be achieved through alterations of the π-bridges. In particular, dye **PP2b** shows a strong blue-shift in the absorption spectra with a major prominent band at 357 nm and a minor shoulder at 406 nm, as a consequence of the less planar, and thus less

conjugated, structure of the compound incorporating the benzene ring compared to thiophene, resulting in a less pronounced push-pull system. When cyanoacrylic acid moiety was changed to a simple carboxylic acid a blue-shift of *ca*. 17 nm was observed, with dye **PP2c** showing a maximum at 389 nm. This result was unexpected, as a simple change in the anchor group typically does not have such significant impact on the electron density distribution. However, the relatively simple design of the dye, featuring a short conjugation system, may provide a key explanation for this observation. The molar attenuation coefficients (ε) range from 2.02×10^4 $M^{-1}cm^{-1}$ for dye **PP2c** to 2.51×10^4 $M^{-1}cm^{-1}$ for dye **PP2a.**

When excited near their absorption maxima, the dyes exhibited a notable fluorescence emission, with maxima in the 520–590 nm range. The large Stokes shift (ca. 130-180 nm) indicates good intramolecular charge transfer character in the singlet excited state of dyes **PP2a-c.** From the intersection of the normalized absorption and emission spectra, the corresponding optical band gap $E_{0\text{-}0}$ could be determined, yielding values in the 2.42–2.75 eV range. As can be seen, compound **PP2b** exhibited the largest Stokes shift, approximately 180 nm. This observation suggests that replacing the π-bridge from thiophene to benzene may enhance planarity in the excited state S_1, potentially boosting optical properties, including a larger Stokes shift. Meanwhile the smaller $E_{0\text{-}0}$ was shown by compound **PP2a**, probably owing to its stronger donor-acceptor character.

The spectro-electrochemical characterization of the new dyes was thus completed by recording the corresponding cyclic voltammetries (CV) in DCM solution, in order to determine their ground-state oxidation potentials E_{ox} and calculate the energy level positions of their frontier orbitals (Figure 3.25).

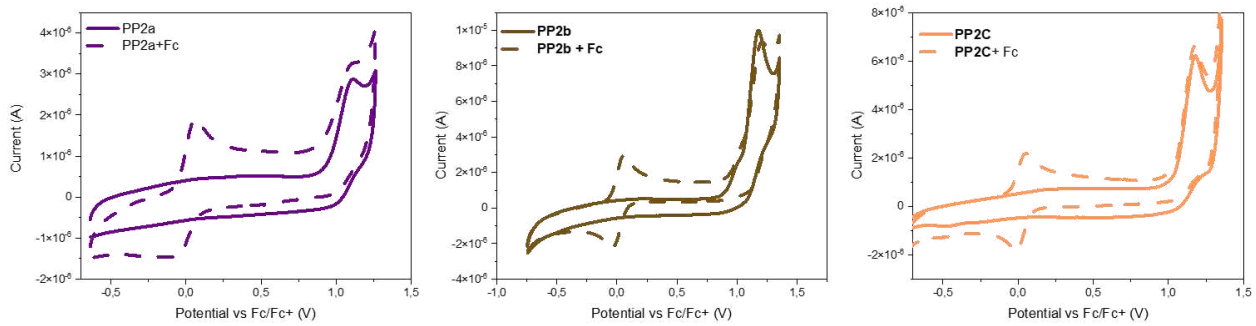

*Figure 3.25 Ciclic voltammetry plots of dyes **PP2a-c** in DCM solution, both without and with ferrocene as an internal standard.*

*Table 3.11 electrochemical properties of dyes **PP2a-c** in DCM solution.*

Dye	E_{ox} (V) *vs.* Fc^+/Fc	E_{ox} (V) *vs.* NHE[a]	E^*_{ox} (V) *vs.* NHE[b]
PP2a	+1.03	+1.75	−0.67
PP2b	+1.11	+1.83	−0.83
PP2c	+1.11	+1.83	−0.92

[a] Calculated by adding +0.72 V to the potential *vs.* Fc^+/Fc[31]; [b] Calculated from the E_{ox} and $E_{0\text{-}0}$ values according to the formula: $E^*_{ox} = E_{ox} - (E_{0\text{-}0}/e)$

Upon application of positive potentials, the dyes showed single quasi-reversible oxidation waves corresponding to an oxidation/re-reduction process. After conversion according to literature reports, their E_{ox} values resulted +1.75 V (**PP2a**), +1.83 V (**PP2b**) and +1.83 V (**PP2c**) *vs.* NHE, respectively (Table 3.11). Therefore, all dyes bring sufficient energy offsets for regeneration by the typical Ru^{II}(bda)-based complex (E_{onset}, approx. +1.1 V *vs.* NHE). The excited state oxidation potentials (E^*_{ox}) of the dyes were then assessed by subtracting the previously determined $E_{0\text{-}0}$ values from the E_{ox} resulting from cyclic voltammetry, yielding values of −0.67 V, −0.83 V and −0.92 V *vs.* NHE for **PP2a**, **PP2b** and **PP2c**, respectively. As expected, the trend observed in the values of the dyes followed the order of relative electron-withdrawing ability of their acceptor/anchor groups, with **PP2c** < **PP2b** < **PP2a**. Accordingly, the electrochemical analysis showed that in the case of dye **PP2a** the value measured in solution was very close to the reported conduction band edge of TiO_2 (approx.–0.5 V vs. NHE) suggesting that a smaller thermodynamic driving force for electron transfer to the semiconductor may exist for such dye. Further investigation for this class of chromophores must be continued on TiO_2 films.

3.6 Conclusions

In conclusion, we designed, synthesized, and characterized two families of organic dyes as sensitizers for DSPEC applications: compounds **1a-c**, featuring a quinoxaline core, and compounds **PP2a-c**, built on a pyrido[3,4-*b*]pyrazine core. With the help of DFT and TD-DFT computational studies, the structures of the dyes were designed to optimize light absorption and energy levels for efficient electron transfer in DSPECs. Key design choices included using donor/acceptor groups that moderate the dyes' ground state-/excited state-oxidation potentials, extending π-conjugation to shift absorption toward longer wavelengths, and adding alkyl chains to improve solubility and reduce aggregation on semiconductor surfaces.

The structures of dyes **1a-c** presented a common 2,3-diphenyl-5,8-dithienylquinoxaline central core and three different alkoxy-substituted benzene rings as donor groups of moderate strength.

The varying number of substituents and the different substitution patterns of the donor groups were expected to alter the energy of the corresponding HOMO levels, allowing a fine tuning of the dyes ground state oxidation potentials and affecting the efficiency of their regeneration by the WOC. The dyes were prepared through a multistep synthetic sequence, featuring two consecutive direct arylation reactions as the key carbon-carbon bond forming steps. By applying such procedures, it was possible to sequentially introduce both the acceptor and the donor groups while reducing the number of steps compared to typical cross-coupling procedures, keeping the overall synthetic route concise.

Firstly, the spectroscopic and electrochemical properties of compounds **1a-c** were determined both in solution and upon adsorption on mesoporous TiO_2 thin films. In agreement with the results of the computational studies, all compounds presented marked visible light absorption in solution. After adsorption on the semiconductor, spectral profiles were only slightly affected, although a small blue shift of the absorption maxima and a broadening of the main visible absorption bands could be observed. Electrochemical analysis in DCM solution confirmed the expected impact of the relative strength of different donor groups on the ground state oxidation potentials of the compounds, with E_{ox} values increasing in the order **1b** < **1a** < **1c**.

As a final part of our study of the quinoxaline-based dyes, we investigated the capability of the new chromophores to work as anodic sensitizers in photoelectrochemical cells for water splitting application. As a WOC to work in combination with the dyes, we selected compound **[Ru(bda)(PyP)$_2$]**, thanks to its simple symmetric structure and the possibility to prepare it from readily available, commercial starting materials. Its synthetic protocol was slightly modified compared to literature reports, and it was found that using HFIP as a co-solvent was crucial both to improve the efficiency of its formation and facilitate its subsequent purification and handling. CV experiments indicated that the onset of electrochemical water oxidation with **[Ru(bda)(PyP)$_2$]** adsorbed on TiO_2 occurred at around +1.1 V vs. NHE, which was considered compatible with the ground state oxidation potentials of all dyes, although in the case of compound **1b** its lower E_{ox} value measured in solution could point to a less efficient dye-regeneration process in comparison to sensitizers **1a,c**.

Before carrying out the photoelectrochemical tests, the dynamics of photoexcitation and charge transfer of the dyes adsorbed on mesoporous TiO_2 films were studied by means of TAS technique. The results evidenced ultrafast electron injection processes taking place within the time resolution of the instrument, with formation of both dye-bound (lifetime 100–200 ps) and long-lived (>5 ns), "free" charge carriers for all the tested systems, the latter being able to give rise to photocurrent in PEC cells.

Finally, the ability of the new dyes to work as anodic sensitizers in DS-PEC devices was preliminarily assessed by means of photoelectrochemical tests in a three-electrodes cell setup. Our study revealed that when the dyes and WOC were deposed on the electrode semiconductor by means of a "co-adsorption" procedure, the best performance was yielded by dye **1a**, which provided a photocurrent density of approx. 150 μA cm^{-2} at +0.5 V vs. NHE external bias. In contrast, dye **1c** yielded a lower current of around 85 μA cm^{-2} under the same conditions, while dye **1b** exhibited almost no activity. For the latter, we attributed the poor performance to a possible ineffective dye regeneration by the WOC, which was likely due to both a lower driving force, as previously discussed, and insufficient catalyst loading arising from the co-adsorption method.

To address this limitation, we explored an alternative staining approach in which the WOC was first deposited on TiO_2, followed by the dye. This sequential deposition method led to a noticeable improvement photocurrent density of approx. 63 μA cm^{-2} at +0.5 V vs. NHE external bias. These findings suggest that further optimization of electrode fabrication, functionalization protocols, and exploration of different dye-catalyst combinations are necessary to enhance the system's performance. Therefore, additional experiments are currently underway.

Overall, we can conclude that dye **1a** emerged as the most promising candidate, exhibiting a well-balanced combination of photophysical and electrochemical properties. It demonstrated strong and broad absorption (λ_{abs}^{max}~ 500 nm), well-matched ground- and excited-state oxidation potentials, and an optimal adsorption density on TiO_2, which contributed to its superior photocurrent performance in the series.

Considering the second sensitizers series, the structures of dyes **PP2a-c** presented a pyrido[3,4-*b*]pyrazine central core and three different acceptor/anchor groups of moderate strength. By varying the acceptor moiety of the dye we expected to alter the energy of the corresponding LUMO levels, allowing a fine tuning of the dyes excited state oxidation potentials and affecting the efficiency of electron injection into the CB of TiO_2. The dyes were prepared also in this case through a multistep synthetic sequence, featuring a telescopic double microwave -assisted Suzuki-Miyaura reaction as the key carbon-carbon bond forming steps.

The capability of the new chromophores to work as anodic sensitizers in photoelectrochemical cells for water splitting application was first investigated by performing a complete spectro-electrochemical characterization in DCM solution. **PP2a-c** showed a narrower, but still appropriate,visible light absorption compared to dyes **1a-c**, with maxima λ_{max}^{abs} centered around 390-450 nm. This result suggests that the increased electron acceptor capacity of the pyrido[3,4-*b*]pyrazine central core is probably not sufficient to compensate the less extended π-conjugation of dyes **PP2a-c**.

Electrochemical analysis in DCM solution confirmed the expected impact of the relative strength of different acceptor on the oxidation potentials of the compounds, with excited -state oxidation potentials (E^*_{OX}) values decreasing for compound **PP2a-c** in the order **PP2a < PP2b < PP2c**. Notably, spectroscopic and electrochemical studies confirmed the dyes' suitability for DSPEC applications.

3.7 Materials and methods

3.7.1 General synthetic remarks

All commercially available compounds were purchased from Merck KGaA, Fluorochem Ltd., and T.C.I. Europe Co. Ltd., and were used without further purification unless otherwise stated. 4,7-dibromobenzo[c][1,2,5]thiadiazole (**2**), 2-(tributylstannyl)thiophene (**3**), benzil (**5**), 2,5-dibromopyridine-3,4-diamine (**23**), (4-hydroxyphenyl)boronic acid (**25**), 5-(4,4,5,5-tetramethyl-1,3,2-dioxaborolan-2-yl)thiophene-2-carbaldehyde (**27a**), 4-(4,4,5,5-tetramethyl-1,3,2-dioxaborolan-2-yl)benzaldehyde (**27b**), methyl 4-(4,4,5,5-tetramethyl-1,3,2-dioxaborolan-2-yl)benzoate (**27c**), $RuCl_3 \bullet 3H_2O$, and 2,2′-bipyridine-6,6′-dicarboxylic acid (**17)** were obtained from the above mentioned commercial suppliers. 1-Bromo-4-((2-ethylhexyl)oxy)benzene **(14a)**,[52] 1-bromo-2,4-bis(hexyloxy)benzene **(14b)**[53] and 1-bromo-3,5-bis(hexyloxy)benzene (**14c**)[54] were prepared according to the previously published synthetic procedures. Before use, Zn dust was stirred in a 1M HCl aqueous solution for 15 min, then it was filtered and washed with water, ethanol and diethyl ether, in this order, to remove adventitious traces of zinc oxides. The resulting activated Zn dust was dried under vacuum and could be stored for months under nitrogen atmosphere. Anhydrous toluene, N,N-dimethylformamide (DMF), tetrahydrofuran (THF), and dichloromethane (DCM) were obtained after drying with a PureSolv Micro apparatus (Inert). Palladium-catalyzed reactions were carried out under a dry nitrogen atmosphere using Schlenk techniques. Reactions were monitored by TLC on Kieselgel 60 F254 (Merck) aluminum sheets and the products were visualized by exposing the plate to UV light or by staining it with a basic aqueous potassium permanganate ($KMnO_4$) solution. Flash column chromatography was performed using Merck Kieselgel 60 (300–400 mesh) as the stationary phase. ^{1}H NMR spectra were recorded at 200–400 MHz, and ^{13}C NMR spectra were recorded at 50.3–100.6 MHz, respectively, on Varian Gemini/Mercury/INOVA instruments. Chemical shifts (δ) are reported in parts per million (ppm) and are referenced to the residual solvent peak ($CDCl_3$, δ = 7.26 ppm for ^{1}H NMR and δ = 77.16 ppm for ^{13}C NMR; CD_2Cl_2, δ = 5.32 ppm for ^{1}H NMR and δ = 53.84 ppm for ^{13}C NMR; THF-d_8, δ = 1.72, 3.58 ppm for ^{1}H NMR and δ = 25.31, 67.21 ppm for ^{13}C NMR). The following abbreviations are used to indicate

the multiplicity: s, singlet; d, doublet; t, triplet; q, quartet; m, multiplet; bs, broad signal. ESI-MS spectra were obtained by direct injection of the sample solution using a Thermo Scientific LCQ-FLEET instrument, while HRMS spectra were measured using a Thermo Scientific LTQ Orbitrap (FT-MS) instrument (carried out at the Interdepartmental Center for Mass Spectroscopy of the University of Florence, CISM); both are reported as *m/z*.

3.7.2 Synthetic procedures

4,7-Di(thiophen-2-yl)benzo[c][1,2,5]thiadiazole (4)

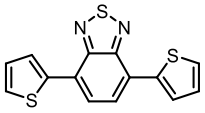

4,7-Dibromobenzo[c][1,2,5]thiadiazole (**2**, 1.00 g, 3.40 mmol, 1.0 eq.) and $PdCl_2(PPh_3)_2$ (0.047 g, 0.068 mmol, 2.0 mol%) were added to a Schlenk tube and put under inert atmosphere by performing three vacuum-nitrogen cycles. The solids were then dissolved in dry DMF (25 mL) and the solution was stirred for 5 min. Then, 2-(tributylstannyl) thiophene (**3**, 2.79 g, 7.48 mmol, 2.2 eq.) was added via syringe and the reaction was stirred at reflux for 24 h. The reaction mixture was allowed to cool down to room temperature, then water (25 mL) was added, and the mixture was extracted with DCM (3 × 25 mL). The organic phases were combined and dried over anhydrous Na_2SO_4, filtered and the solvent evaporated under reduced pressure. The crude was purified by recrystallization from ethanol to give compound **4** as a bright yellow solid (0.950 g, 3.16 mmol, 93% yield). ^{1}H-NMR (400 MHz, $CDCl_3$) δ = 8.13 (dd, J = 3.7, 1.1 Hz, 2H), 7.89 (s, 2H), 7.46 (dd, J = 5.1, 1.1 Hz, 2H), 7.22 (dd, J = 5.1, 3.7 Hz, 2H) ppm. Spectroscopic data are in agreement with those reported in the literature.[55]

2,3-Diphenyl-5,8-di(thiophen-2-yl)quinoxaline (6)

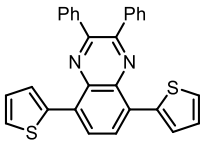

In a round bottom flask 4,7-di(thiophen-2-yl)benzo[c][1,2,5]thiadiazole (**4**, 0.950 g, 3.16 mmol, 1.0 eq.) and zinc powder (2.07 g, 31.6 mmol, 10 eq.) were suspended in glacial acetic acid (25 mL). The reaction mixture was vigorously stirred at 80°C for 1.5 h to obtain a complete conversion of the starting material as assessed by TLC (eluent: petroleum ether/DCM 4:1 v/v). The mixture was then cooled to room temperature and filtered. The filtrate was poured in water and extracted

with diethyl ether (3 × 30 mL). The combined organic phases were dried over Na_2SO_4, filtered, and the solvent evaporated under reduced pressure. Without any further purification, the crude mixture was then dissolved in ethanol (20 mL) and benzil (**5**, 0.731 g, 3.48 mmol, 1.1 eq.) was subsequently added. The reaction mixture was then vigorously stirred at 80°C for 16 h. After cooling down to room temperature, the mixture was filtered through a fritted funnel and the solid residue washed with cold ethanol, to afford compound **6** as a yellow solid (1.30 g, 2.91 mmol, 92% yield). ^{1}H-NMR (400 MHz, $CDCl_3$) δ = 8.16 (s, 2H), 7.89 (dd, J = 3.8, 1.1 Hz, 2H), 7.82–7.71 (m, 4H), 7.53 (dd, J = 5.1, 1.1 Hz, 2H), 7.45–7.37 (m, 6H), 7.19 (dd, J = 5.2, 3.8 Hz, 2H). Spectroscopic data are in agreement with those reported in the literature.[56]

General procedure for the synthesis of compounds **14a-c** (GP1)

4-(5-(2,3-Diphenyl-8-(thiophen-2-yl)quinoxalin-5-yl)thiophen-2-yl) benzaldehyde (**8**), the appropriate aryl bromide **13a-c** (3.0 eq.) and Cs_2CO_3 (3.0 eq.) were added to a Schlenk tube and put under inert atmosphere by performing three vacuum-nitrogen cycles. The solids were dissolved in dry toluene (3 mL) and a solution of $Pd(OAc)_2$ (5 mol%), P (2-MeOPh)$_3$ (10 mol%) and pivalic acid (30 mol%) in toluene (1 mL) was added. The reaction mixture was stirred at 110°C for 24 h. After cooling down to room temperature, water (5 mL) was added and the mixture extracted with DCM (3 × 10 mL). The combined organic phases were dried over anhydrous Na_2SO_4, filtered, and the solvent evaporated under reduced pressure. Crude products were then purified by flash column chromatography to give the desired compounds **14a-c** in pure form.

4-(5-(2,3-Diphenyl-8-(thiophen-2-yl)quinoxalin-5-yl)thiophen-2-yl) benzaldehyde (8)

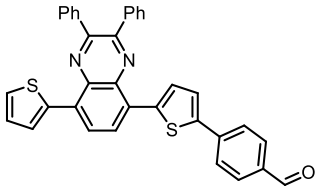

2,3-Diphenyl-5,8-di(thiophen-2-yl)quinoxaline (**6**, 1.00 g, 2.24 mmol, 2.0 eq.), 4-bromobenzaldehyde (**7**, 207 mg, 1.12 mmol, 1.0 eq.), Cs_2CO_3 (2.19 g, 3.36 mmol, 3.0 eq), $Pd(OAc)_2$ (13 mg, 0.056 mmol, 5 mol%), P(2-MeOPh)$_3$ (39 mg, 0.112 mmol, 10 mol%) and pivalic acid (34 mg, 0.336 mmol, 30 mol%) were added to a Schlenk tube and put under inert atmosphere by performing three vacuum-nitrogen cycles. The solids were then dissolved in dry toluene (32 mL) and the reaction mixture was vigorously stirred at 110°C for 24 h. The solution was cooled to room temperature, diluted with DCM (20 mL), filtered over a pad of Celite®, and washed with water (2 ×

30 mL) and brine (30 mL). The organic phase was dried over Na_2SO_4, filtered, and the solvent evaporated under reduced pressure. The crude product was purified by flash column chromatography (SiO_2, gradient from petroleum ether/ DCM 75:15 to petroleum ether/DCM 50:50) to afford compound **8** (434 mg, 0.788 mmol, 70% yield) as a dark yellow solid. ^{1}H-NMR (400 MHz, $CDCl_3$) δ = 10.01 (s, 1H), 8.14 (s, 2H), 7.92–7.85 (m, 4H), 7.81 (d, *J* = 8.0 Hz, 2H), 7.80–7.72 (m, 4H), 7.54 (d, *J* = 5.1 Hz, 1H), 7.51 (d, *J* = 4.1 Hz, 1H) 7.48–7.30 (m, 6H), 7.19 (dd, *J* = 5.1, 3.7 Hz, 1H) ppm. ^{13}C-NMR (100 MHz, $CDCl_3$) δ = 191.7, 152.0, 151.8, 145.1, 140.6, 140.3, 138.64, 138.58, 137.3, 137.2, 135.0, 131.8, 130.67, 130.66, 130.6, 129.39, 129.36, 129.3, 128.41, 128.36, 127.60, 127.56, 127.0, 126.8, 126.7, 125.8, 124.9 ppm. MS (ESI) *m/z*: $[M+H]^+$ calcd. for $C_{35}H_{23}N_2OS_2$ 551.1; found: 551.3.

4-(5-(8-(5-(4-((2-Ethylhexyl)oxy)phenyl)tiophen-2-yl)-2,3-diphenylquinoxalin-5-yl)tiophen-2-yl)benzaldehyde (14a)

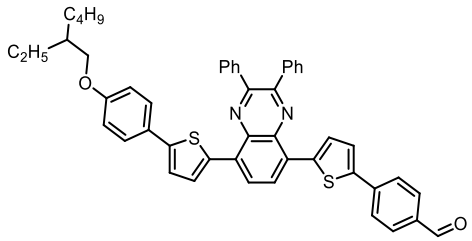

Prepared following general procedure GP1, using 4-(5-(2,3-diphenyl-8-(thiophen-2-yl)quinoxalin-5-yl)thiophen-2-yl)benzaldehyde (**8**) (50 mg, 0.091 mmol, 1.0 eq.), 1-bromo-4-((2-ethylhexyl)oxy)benzene (**13a**, 78 mg, 0.273 mol, 3.0 eq.), Cs_2CO_3 (89 mg, 0.273 mmol, 3.0 eq.), $Pd(OAc)_2$ (2 mg, 0.009 mmol, 10 mol%), P(2-MeOPh)$_3$ (6 mg, 0.018 mmol, 20 mol%) and pivalic acid (3 mg, 0.027 mmol, 30 mol%). The crude product was purified by flash column chromatography (SiO_2, petroleum ether/THF 85:15 v/v) to afford compound **14a** as a red solid (55 mg, 0.073 mmol, 80% yield). ^{1}H-NMR (400 MHz, THF-d_8) δ = 9.95 (s, 1H), 8.27-8.19 (m, 2H), 7.97–7.85 (m, 6H), 7.83–7.75 (m, 4H), 7.65- 7.58 (m, 3H), 7.46–7.35 (m, 7H), 7.30 (d, *J* = 3.9 Hz, 1H), 6.96 (d, *J* = 8.6 Hz, 2H), 3.92 (d, *J* = 5.9 Hz, 2H), 1.50-1.53 (m, 4H), 1.34-1.38 (m, 4H), 1.01–0.90 (m, 6H) ppm. ^{13}C-NMR (100 MHz, THF-d_8) δ = 191.3, 160.4, 152.8, 152.7, 148.7, 146.2, 141.3, 141.0, 139.9, 138.1, 137.6, 136.6, 132.8, 131.7, 131.1, 130.1, 130.0, 129.11, 129.08, 128.8, 128.5, 127.60, 127.55, 127.0, 126.4, 125.7, 122.6, 115.8, 71.3, 40.7, 31.7, 30.2, 25.0, 24.2, 14.6, 11.7 ppm. Note: not all carbon signals are visible in the ^{13}C-NMR spectrum due to fortuitous overlaps of aromatic peaks. MS (ESI) *m/z*: $[M+H]^+$ calcd for $C_{49}H_{43}N_2O_2S_2$ 755.3; found: 755.3.

4-(5-(8-(5-(2,4-Bis(Hexyloxy)phenyl)tiophen-2-yl)-2,3-diphenylquinoxalin-5-yl)tiophen-2-yl)benzaldehyde (14b)

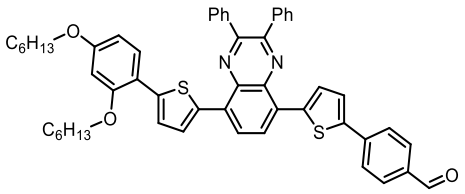

Prepared following general procedure GP1, using 4-(5-(2,3- diphenyl-8-(thiophen-2-yl)quinoxalin-5-yl)thiophen-2-yl)benzaldehyde (**8**) (50 mg, 0.091 mmol, 1.0 eq.), 1-bromo-2,4-*bis*(hexyloxy)benzene (**13b**, 97 mg, 0.273 mmol, 3.0 eq.), Cs_2CO_3 (89 mg, 0.273 mmol, 3.0 eq.), $Pd(OAc)_2$ (2 mg, 0.009 mmol, 10 mol%), P(2-MeOPh)$_3$ (6 mg, 0.018 mmol, 20 mol%) and pivalic acid (3 mg, 0.027 mmol, 30 mol%). The crude product was purified by flash column chromatography (SiO_2, gradient from petroleum ether/DCM 90:10 v/v to petroleum ether/DCM 60:40 v/v) to afford compound **14b** as a red solid (70 mg, 0.085 mmol, 93 % yield). ^{1}H-NMR (400 MHz, CD_2Cl_2) δ = 9.96 (s, 1H), 8.11–8.05 (m, 2H), 7.89–7.84 (m, 3H), 7.82–7.72 (m, 7H), 7.59 (d, *J* = 8.3 Hz, 1H), 7.57–7.48 (m, 2H), 7.46–7.35 (m, 6H), 6.57–6.52 (m, 2H), 4.07 (t, *J* = 6.6 Hz, 2H), 4.00 (t, *J* = 6.6 Hz, 2H), 1.79-1.81 (m, 4H), 1.55–1.45 (m, 4H), 1.41–1.35 (m, 4H), 1.33–1.29 (m, 4H), 0.94 (t, *J* = 7.0 Hz, 3H), 0.86 (t, *J* = 7.0 Hz, 3H) ppm. ^{13}C-NMR (100 MHz, CD_2Cl_2) δ = 191.2, 160.0, 156.5, 151.6, 151.5, 144.7, 143.3, 140.2, 140.1, 138.7, 137.2, 137.0, 136.7, 135.0, 132.1, 130.5, 130.4, 130.2, 129.7, 129.1, 128.9, 128.8, 128.1, 127.4, 127.1, 126.5, 126.4, 125.4, 124.6, 124.4, 116.2, 105.7, 99.9, 68.8, 68.2, 31.6, 31.5, 29.3, 29.0, 25.8, 25.7, 22.6, 22.5, 13.80, 13.77 ppm. MS (ESI) *m/z*: $[M+H]^+$ calcd. for $C_{53}H_{51}N_2O_3S_2$ 827.3; found: 827.4.

4-(5-(8-(5-(3,5-Bis(hexyloxy)phenyl)thiophen-2-yl)-2,3-diphenylquinoxalin-5-yl)thiophen-2-yl)benzaldehyde (14c)

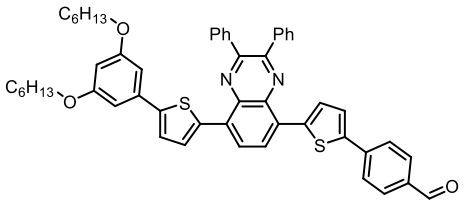

Prepared following general procedure GP1, using 4-(5-(2,3- diphenyl-8-(thiophen-2-yl)quinoxalin-5-yl)thiophen-2-yl)benzaldehyde (**8**) (40 mg, 0.073 mmol, 1.0 eq.), 1-bromo-3,5-*bis*(hexyloxy)benzene (**13c**, 78 mg, 0.219 mmol, 3.0 eq.), Cs_2CO_3 (71 mg, 0.219 mmol, 3.0 eq.), $Pd(OAc)_2$ (2 mg, 0.008 mmol, 10 mol%), P(2-MeOPh)$_3$ (5 mg, 0.015 mmol, 20 mol%) and pivalic acid (2 mg, 0.022 mmol, 30 mol%). The crude product was purified by flash column chromatography (SiO_2, gradient from petroleum ether/DCM 90:10 v/v to petroleum ether/DCM 60:40 v/v) to afford compound **14c** as a red solid (56 mg, 0.068 mmol, 93 % yield). ^{1}H-NMR (400 MHz, $CDCl_3$) δ = 9.99 (s, 1H), 8.07 (br s, 2H), 7.88 (d, *J* = 8.1 Hz, 2H), 7.83–7.73 (m, 8H), 7.49–7.32 (m, 8H), 6.85-

6.81 (m, 2H), 6.43 (s, 1H), 4.00 (t, J = 6.5 Hz, 4H), 1.88–1.76 (m, 4H), 1.56–1.45 (m, 4H), 1.43–1.32 (m, 8H), 0.94 (t, J = 6.7 Hz, 6H) ppm. ^{13}C-NMR (100 MHz, $CDCl_3$) δ = 191.6, 160.8, 151.79, 151.77, 147.7, 145.1, 140.6, 140.3, 138.7, 137.8, 137.2, 136.4, 135.1, 131.7, 130.8, 130.7, 130.6, 130.6, 130.4, 129.4, 129.2, 128.4, 128.3, 127.6, 126.7, 126.3, 125.7, 124.9, 123.2, 104.5, 101.0, 68.3, 31.8, 29.5, 26.0, 22.8, 14.2 ppm. Note: not all carbon signals are visible in the ^{13}C-NMR spectrum due to fortuitous overlaps of aromatic peaks. MS (ESI) *m/z*: $[M+H]^+$ calcd for $C_{53}H_{51}N_2O_3S_2$ 827.3; found: 827.4.

General procedure for the synthesis of compounds **1a-c** (GP2)

The appropriate aldehyde **14a-c** was added to a Schlenk tube, put under inert atmosphere by performing three vacuum-nitrogen cycles and dissolved in a mixture of $CHCl_3$/CH_3CN 3:2 *v/v* (10 mL). Cyanoacetic acid (**15**, 10 eq.) and piperidine (0.3 eq.) were then added and the reaction mixture was stirred at 90°C for 16 h. After cooling down to room temperature, water (5 mL) was added and the mixture was extracted with DCM (3 × 10 mL). The combined organic phases were dried over anhydrous Na_2SO_4, filtered, and the solvent evaporated under reduced pressure. The crude mixture was washed several times with cold ethanol to give the corresponding compounds **1a-c**.

3-(4-(5-(8-(5-(4-((2-Ethylhexyl)oxy)phenyl)thiophen-2-yl)-2,3- diphenylquinoxalin-5-yl)thiophen-2-yl)phenyl)-2-cyanoacrylic acid (1a)

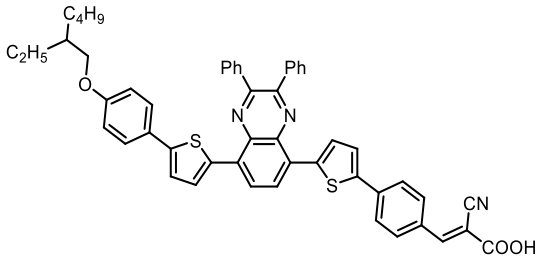

Prepared following general procedure GP2, using 4-(5-(8-(5-(4-((2-ethylhexyloxy)phenyl)tiophen-2-yl)-2,3-diphenylquinoxaline-5-yl)tiophen-2-yl)benzaldehyde (**14a**, 55 mg, 0.073 mmol, 1.0 eq.), cyanoacetic acid (**15**, 60 mg, 0.715 mmol, 10 eq.) and piperidine (2 mg, 0.022 mmol, 0.3 eq.). The crude mixture was washed several times with cold ethanol to afford compound **1a** as a red solid (49 mg, 0.060 mmol, 82% yield). ^{1}H-NMR (400 MHz, THF-d_8) δ = 8.27–8.19 (m, 3H), 8.09 (d, J = 8.4 Hz, 2H), 7.95 (d, J = 4.0 Hz, 1H), 7.92 (d, J = 3.9 Hz, 1H), 7.85 (d, J = 8.4 Hz, 2H), 7.84–7.76 (m, 5H), 7.67–7.56 (m, 3H), 7.47–7.36 (m, 7H), 7.31 (d, J = 3.9 Hz, 1H), 6.96 (d, J = 8.7 Hz, 2H), 3.95–3.90 (m, 2H), 1.63–1.44 (m, 4H), 1.43–1.32 (m, 4H), 1.01–0.90 (m, 6H) ppm. ^{13}C-NMR (100 MHz, THF-d_8) δ = 164.1, 160.4, 153.9, 152.8, 152.7, 148.7, 146.2, 141.1, 140.2, 139.9, 138.1, 137.7, 132.8, 131.7, 131.2, 130.1, 130.0, 129.2, 129.1, 128.8, 128.6, 128.5,

127.6, 127.3, 127.0, 126.5, 125.9, 122.6, 121.8, 116.7, 115.9, 112.8, 103.6, 71.3, 40.7, 31.7, 30.8, 30.2, 24.1, 14.6, 11.7 ppm. Not all carbon signals are visible in the ^{13}CNMR spectrum due to fortuitous overlaps of aromatic peaks. HRMS (ESI) *m/z*: $[M+H]^+$ calcd for $C_{52}H_{44}N_3O_3S_2$ 822.2819; found 822.2821.

3-(4-(5-(8-(5-(2,4-Bis(hexyloxy)phenyl)thiophen-2-yl)-2,3-diphenylquinoxalin-5-yl)thiophen-2-yl)phenyl)-2-cyanoacrylic acid (1b)

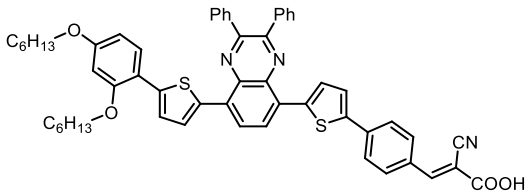

Prepared following general procedure GP2, using 4-(5-(8-(5-(2,4-bis (hexyloxy)phenyl)tiophen-2-yl)-2,3-diphenylquinoxalin-5-yl)tiophen2-yl)benzaldehyde (**14b,** 70 mg, 0.085 mmol, 1.0 eq.), cyanoacetic acid (**15**, 72 mg, 0.846 mmol, 10 eq.) and piperidine (2 mg, 0.025 mmol, 0.3 eq.). The crude mixture was washed several times with cold ethanol to afford compound **1b** as a red solid (62 mg, 0.069 mmol, 82% yield). ^{1}H-NMR (400 MHz, THF-d$_8$) δ = 8.32–8.20 (m, 3H), 8.11 (d, *J* = 8.2 Hz, 2H), 8.00–7.96 (m, 2H), 7.88 (d, *J* = 8.1 Hz, 2H), 7.84–7.77 (m, 4H), 7.67–7.61 (m, 2H), 7.53 (d, *J* = 4.0 Hz, 1H), 7.45–7.36 (m, 7H), 6.62 (d, *J* = 2.5 Hz, 1H), 6.56 (dd, *J* = 8.5, 2.4 Hz, 1H), 4.09 (t, *J* = 6.5 Hz, 2H), 4.01 (t, *J* = 6.4 Hz, 2H), 1.83–1.76 (m, 4H), 1.55–1.46 (m, 4H), 1.42–1.35 (m, 4H), 1.33–1.26 (m, 4H), 0.97–0.91 (m, 3H), 0.88–0.82 (m, 3H) ppm. ^{13}C-NMR (100 MHz, THF-d$_8$) δ = 164.1, 161.2, 157.7, 153.9, 152.76, 152.75, 146.1, 144.8, 141.3, 140.3, 140.1, 140.0, 138.4, 138.2, 137.7, 133.5, 132.8, 131.8, 131.7, 130.9, 130.1, 129.9, 129.7, 129.14, 129.08, 128.5, 128.3, 127.8, 127.3, 126.5, 125.9, 125.2, 117.6, 116.7, 111.7, 106.8, 103.6, 101.1, 69.7, 68.8, 32.8, 32.7, 30.5, 30.2, 27.0, 26.9, 23.7, 23.6, 14.6, 14.6 ppm. HRMS (ESI) *m/z*: $[M+H]^+$ calcd for $C_{56}H_{52}N_3O_4S_2$ 894.3394; found 894.3391.

3-(4-(5-(8-(5-(3,5-Bis(hexyloxy)phenyl)thiophen-2-yl)-2,3-diphenylquinoxalin-5-yl)thiophen-2-yl)phenyl)-2-cyanoacrylic acid (1c)

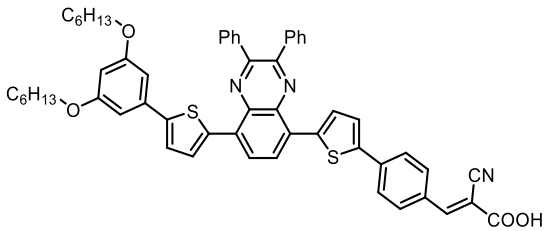

Prepared following general procedure GP2, using 4-(5-(8-(5-(3,5-bis(hexyloxy)phenyl)thiophen-2-yl)-2,3-diphenylquinoxalin-5-yl)thiophen-2-yl)benzaldehyde (**14c**, 56 mg, 0.068 mmol, 1.0 eq.),

cyanoacetic acid (**15**, 58 mg, 0.677 mmol, 10 eq.) and piperidine (2 mg, 0.020 mmol, 0.3 eq.). The crude mixture was washed several times with cold ethanol to afford compound **1c** as a red solid (54 mg, 0.060 mmol, 89% yield). ^{1}H-NMR (400 MHz, THF-d_8) δ = 8.28 (s, 2H), 8.23 (s, 1H), 8.10 (d, *J* = 8.5 Hz, 2H), 7.99 (d, *J* = 4.0 Hz, 1H), 7.95 (d, *J* = 4.0 Hz, 1H), 7.87 (d, *J* = 8.4 Hz, 2H), 7.86–7.79 (m, 5H), 7.64 (d, *J* = 4.0 Hz, 1H), 7.48–7.37 (m, 7H), 6.87 (d, *J* = 2.1 Hz, 2H), 6.42 (t, *J* = 2.1 Hz, 1H), 4.02 (t, *J* = 6.4 Hz, 4H), 1.84–1.79 (m, 4H), 1.59–1.50 (m, 4H), 1.38-1.41 (m, 8H), 0.99–0.92 (m, 6H) ppm. ^{13}C-NMR (100 MHz, THF-d_8) δ = 164.1, 161.9, 153.9, 152.9, 152.8, 148.8, 146.3, 141.0, 140.2, 139.9, 139.8, 138.4, 138.1, 138.0, 137.3, 132.8, 132.5, 131.8, 131.7, 131.4, 130.2, 130.0, 129.2, 129.1, 128.7, 128.4, 127.6, 127.1, 126.5, 125.9, 123.8, 116.7, 104.8, 103.5, 101.7, 96.2, 68.8, 32.8, 30.5, 27.0, 24.0, 14.6 ppm. HRMS (ESI) *m/z* $[M+H]^+$ calcd for $C_{56}H_{52}N_3O_4S_2$ 894.3394; found 894.3398.

5,8-Dibromo-2,3-diphenylpyrido[3,4-*b*]pyrazine (24)

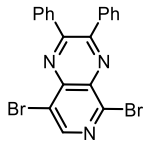

2,5-Dibromopyridine-3,4-diamine (**23**,1.0 g, 3.72 mmol, 1.0 eq.) and benzil (**5**, 0.79 g, 4.09 mmol, 1.1 eq.) were dissolved in acetic acid (10 mL) and the reaction mixture was vigorously stirred at 100 °C for 2 h. After cooling down to room temperature, the mixture was filtered through a fritted funnel and the solid residue was washed with cold ethanol, to afford compound **24** as a pale yellow solid (1.35 g, 3.07 mmol, 83% yield). ^{1}H-NMR (400 MHz, $CDCl_3$) *δ* = 8.76 (s, 1H), 7.70–7.61 (m, 4H), 7.49–7.42 (m, 2H), 7.42–7.34 ppm (m, 4H). Spectroscopic data are in agreement with those reported in the literature.[20]

General procedure for the synthesis of compounds **22a-c** (GP3)

Compound **16** was dissolved in anhydrous toluene (3 mL) together with [Pd(dppf)Cl_2] (3 mol%) and the reaction mixture was introduced in a microwave vial equipped with a magnetic stirrer. 4-(Hydroxybenzene)boronic acid (**17**, 1.5 eq.) and KF (6.0 eq.) were dissolved in MeOH (3 mL), and the resulting solution was transferred into the microwave vial. The reaction mixture was heated under microwave irradiation at 80°C for 30 min. After cooling to room temperature the microwave vial was opened and the appropriate boronic ester **19a-c** (3.0 eq), [Pd(dppf)Cl_2] (3 mol%.) and KF (6.0 eq.) were added. The obtained reaction mixture was subjected again to microwave irradiation at 80°C for 30 min. After cooling down to room temperature, water (5 mL) was added and the mixture extracted with DCM (3 × 10 mL). The combined organic phases were dried over anhydrous Na_2SO_4, filtered, and the solvent evaporated under reduced pressure. Without any further

purification, the crude mixture was then dissolved in dry DMF (4 mL). *n*-Bromobutane (9.0 eq) and K_2CO_3 (5.0 eq.) were added and the reaction mixture was then stirred at 90°C for 4 h. After cooling down to room temperature, water (5 mL) was added and the mixture extracted with DCM (3×10 mL). The combined organic phases were dried over anhydrous Na_2SO_4, filtered, and the solvent evaporated under reduced pressure. Crude products were then purified by flash column chromatography to give the desired compounds **22a-c** in pure form.

5-(5-(4-Butoxyphenyl)-2,3-diphenylpyrido[3,4-*b*]pyrazin-8-yl)thiophene-2-carbaldehyde (30a)

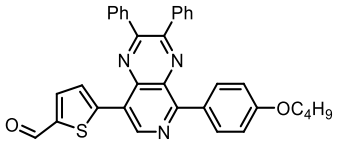

Prepared following general procedure GP3, using 5,8-dibromo-2,3-diphenylpyrido[3,4-*b*]pyrazine (**24**, 100 mg, 0.227 mmol, 1.0 eq.), (4-hydroxybenzene)boronic acid (**25**, 47 mg, 0.340 mmol, 1.5 eq.), [Pd(dppf)Cl_2] (5 mg, 0.007 mmol, 3.0 mol%.) and KF (79 mg, 1.39 mmol, 6.0 eq.), 5-(4,4,5,5-tetramethyl-1,3,2-dioxaborolan-2-yl)thiophene-2-carbaldehyde (**27a**, 162 mg, 0.680 mmol, 3.0 eq.), *n*-bromobutane (**29**, 280 mg, 2.04 mmol, 9.0 eq.) and K_2CO_3 (157 mg, 1.13 mmol, 5.0 eq.). The crude product was purified by flash column chromatography (SiO_2, gradient from petroleum ether/EA 90:10 v/v to petroleum ether/EA 80:20 v/v) to afford compound **30a** as a red solid (66 mg, 0.122 mmol, 54% yield). ^{1}H-NMR (400 MHz, THF-d_8) δ = 9.96 (s, 1H), 9.33 (s, 1H), 8.51 (d, *J* = 8.5 Hz, 2H), 8.09 (d, *J* = 3.9 Hz, 1H), 7.89 (d, *J* = 4.0 Hz, 1H), 7.77 (d, *J* = 7.1 Hz, 2H), 7.66 (d, *J* = 7.1 Hz, 2H), 7.48 – 7.31 (m, 6H), 7.04 (d, *J* = 8.6 Hz, 2H), 4.08 (t, *J* = 6.4 Hz, 2H), 1.87 – 1.75 (m, 2H), 1.62 – 1.48 (m, 2H), 1.01 (t, *J* = 7.4 Hz, 3H) ppm. ^{13}C-NMR (400 MHz, THF-d_8) δ = 183.5, 162.0, 159.1, 156.5, 154.4, 147.0, 146.0, 145.5, 141.2, 139.8, 139.3, 139.1, 136.5, 134.6, 134.1, 131.5, 131.1, 130.8, 130.2, 129.3, 129.2, 128.0, 124.0, 114.7, 68.5, 32.5, 20.3, 14.4 ppm. MS (ESI) *m/z*: $[M+H]^+$ calcd for $C_{34}H_{28}N_3O_2S$ 542.2; found: 542.3

4-(5-(4-Butoxyphenyl)-2,3-diphenylpyrido[3,4-*b*]pyrazin-8-yl)benzaldehyde (30b)

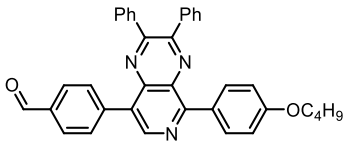

Prepared following general procedure GP3, using 5,8-dibromo-2,3-diphenylpyrido[3,4-*b*]pyrazine (**24**, 100 mg, 0.227 mmol, 1.0 eq.), (4-hydroxybenzene)boronic acid (**25**, 47 mg, 0.340 mmol, 1.5 eq.), [Pd(dppf)Cl_2] (5 mg, 0.007 mmol, 3.0 mol%.) and KF (79 mg, 1.39 mmol, 6.0 eq.), 4-(4,4,5,5-

tetramethyl-1,3,2-dioxaborolan-2-yl)benzaldehyde (**27b**, 158 mg, 0.680 mmol, 3.0 eq.), *n*-bromobutane (**29**, 280 mg, 2.04 mmol, 9.0 eq.) and K_2CO_3 (157 mg, 1.13 mmol, 5.0 eq.). The crude product was purified by flash column chromatography (SiO_2, gradient from petroleum ether/EA 99:1 v/v to petroleum ether/EA 90:10 v/v) to afford compound **30b** as a red solid (52 mg, 0.097 mmol, 43% yield). ^{1}H-NMR (400 MHz, $CDCl_3$) δ = 10.13 (s, 1H), 8.94 (s, 1H), 8.36 (d, *J* = 8.8 Hz, 2H), 8.08 – 8.03 (m, 4H), 7.68 – 7.58 (m, 4H), 7.44 – 7.31 (m, 6H), 7.14 – 7.06 (m, 2H), 4.10 (t, *J* = 6.5 Hz, 2H), 1.89 – 1.80 (m, 2H), 1.61 – 1.49 (m, 2H), 1.02 (t, *J* = 7.3 H, 3H). ^{13}C-NMR m(400 MHz, $CDCl_3$) δ = 192.2, 161.2, 159.0, 156.0, 153.4, 145.1, 141.9, 141.3, 138.3, 138.0, 135.8, 133.7, 133.4, 131.5, 130.4, 130.2, 130.2, 130.1, 129.7, 128.6, 114.4, 68.0, 31.4, 19.4, 14.0 ppm. Note: not all carbon signals are visible in the ^{13}C-NMR spectrum due to fortuitous overlaps of aromatic peaks. MS (ESI) *m/z*: $[M+H]^+$ calcd for $C_{36}H_{30}N_3O_2$ 536.2; found: 536.3

Methyl 4-(5-(4-Butoxyphenyl)-2,3-diphenylpyrido[3,4-*b*]pyrazin-8-yl)benzoate (22c)

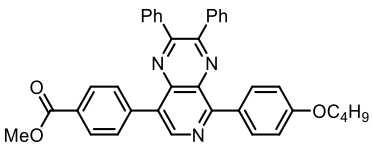

Prepared following general procedure GP3, using 5,8-dibromo-2,3-diphenylpyrido[3,4-*b*]pyrazine (**24**, 100 mg, 0.227 mmol, 1.0 eq), (4-hydroxybenzene)boronic acid (**25**, 47 mg, 0.340 mmol, 1.5 eq.), [Pd(dppf)Cl_2] (5 mg, 0.007 mmol, 3.0 mol%.) and KF (79 mg, 1.39 mmol, 6.0 eq.), methyl 4-(4,4,5,5-tetramethyl-1,3,2-dioxaborolan-2-yl)benzoate (**27c**, 178 mg, 0.680 mmol, 3.0 eq.), *n*-bromobutane (**29**, 280 mg, 2.04 mmol, 9.0 eq.) and K_2CO_3 (157 mg, 1.13 mmol, 5.0 eq.). The crude product was purified by flash column chromatography (SiO_2, gradient from petroleum ether/EA 95:5 v/v to petroleum ether/EA 85:15 v/v) to afford compound **30c** as a red solid (48 mg, 0.085 mmol, 37% yield). ^{1}H-NMR (400 MHz, THF-d_8) δ = 8.94 (s, 1H), 8.48 (d, *J* = 8.5 Hz, 2H), 8.17 (d, *J* = 8.0 Hz, 2H), 8.02 (d, *J* = 8.1 Hz, 2H), 7.74 – 7.54 (m, 4H), 7.40 – 7.27 (m, 6H), 7.06 (d, *J* = 8.4 Hz, 2H), 4.09 (t, *J* = 6.4 Hz, 2H), 3.91 (s, 3H), 1.89 – 1.75 (m, 2H), 1.64 – 1.45 (m, 2H), 1.02 (t, *J* = 7.4 Hz, 3H) ppm. ^{13}C-NMR (400 MHz, THF-d_8) δ = 167.1, 161.8, 159.5, 156.4, 153.8, 147.0, 142.5, 141.2, 140.0, 139.7, 134.6, 134.1, 133.0, 131.8, 131.4, 131.1, 131.0, 130.5, 130.1, 129.7, 129.2, 129.2, 114.6, 111.7, 68.5, 52.3, 32.5, 20.3, 14.4 ppm. MS (ESI) *m/z*: $[M+H]^+$ calcd for $C_{37}H_{32}N_3O_3$ 566.2; found: 566.4

3-(5-(8-(4-Butoxyphenyl)-2,3-diphenylpyrido[3,4-*b*]pyrazin-5-yl)thiophen-2-yl)-2-cyanoacrylic acid (PP2a)

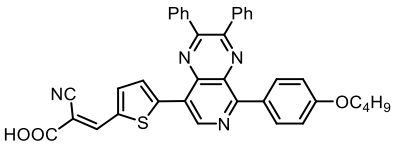

Compound **30a** (57 mg, 0.105 mmol, 1.0 eq.) was added into a Schlenk tube, put under inert atmosphere by performing three vacuum-nitrogen cycles and dissolved in a mixture of toluene and glacial/acetic acid 2/1 v/v (6 mL), then cyanoacetic acid (**15**, 45 mg, 0.526 mmol, 5.0 eq.) and ammonium acetate (8 mg, 0.105 mmol, 1.0 eq.) were added. The resulting mixture was stirred at 110°C for 4 hours, then cooled down to room temperature. After dilution with DCM, the organic phase was washed twice with HCl (aq.) 0.1 M and the solvent evaporated. The crude mixture was washed with several portions of ethanol, ethyl acetate (EA) and *n*-pentane to afford compound **PP2a** as a dark orange solid (60 mg, 0.099 mmol, 94% yield). ^{1}H-NMR (400 MHz, THF-d_8) δ = 9.40 (s, 1H), 8.52 (d, J = 8.9 Hz, 2H), 8.44 (bs, 1H), 8.09 (d, J = 4.1 Hz, 1H), 7.96 – 7.86 (m, 3H), 7.74 – 7.67 (m, 2H), 7.47 – 7.31 (m, 6H), 7.10 – 7.02 (m, 2H), 4.09 (t, J = 6.4 Hz, 2H), 1.87 – 1.78 (m, 2H), 1.62 – 1.49 (m, 2H), 1.02 (t, J = 7.4 Hz, 3H). ^{13}C-NMR (100 MHz, THF-d_8) δ = 164.3, 162.0, 159.0, 156.7, 154.4, 147.3, 146.7, 145.4, 140.9, 140.3, 140.0, 138.9, 138.9, 134.4, 131.9, 131.1, 131.1, 130.6, 130.2, 129.6, 129.4, 129.3, 127.4, 123.9, 117.1, 114.7, 99.9, 32.5, 30.8, 20.3, 14.4. HRMS (ESI) *m/z* $[M+H]^+$ calcd for $C_{37}H_{29}N_4O_3S$ 609.1960; found 609.1983.

3-(4-(5-(4-Butoxyphenyl)-2,3-diphenylpyrido[3,4-b]pyrazin-8-yl)phenyl)-2-cyanoacrylic acid (PP2b)

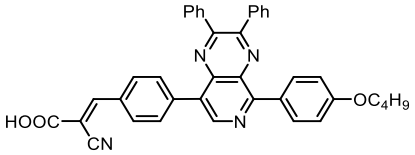

Compound **30b** (52 mg, 0.097 mmol, 1.0 eq.) was added to a Schlenk tube, put under inert atmosphere by performing three vacuum-nitrogen cycles and dissolved in a mixture of toluene and glacial/acetic acid 2/1 v/v (6 mL), then cyanoacetic acid (**15**, 41 mg, 0.485 mmol, 5.0 eq.) and ammonium acetate (7 mg, 0.097 mmol, 1.0 eq.) were added. The resulting mixture was stirred at 110°C for 4 hours, then cooled down to room temperature. After dilution with DCM, the organic phase was washed twice with HCl (aq.) 0.1 M and the solvent evaporated. The crude mixture was washed with several portions of ethanol, EA and *n*-pentane to afford compound **PP2b** as a yellow solid (52 mg, 0.086 mmol, 89% yield). ^{1}H-NMR (400 MHz, THF-d_8) δ = 8.97 (s, 1H), 8.54 – 8.43 (m, 2H), 8.36 (s, 1H), 8.23 (d, J = 8.5 Hz, 2H), 8.12 (d, J = 8.4 Hz, 2H), 7.70 – 7.61 (m, 4H), 7.42 – 7.27 (m, 7H), 7.12 – 7.02 (m, 2H), 4.09 (t, J = 6.3 Hz, 2H), 1.88 – 1.76 (m, 2H), 1.63 – 1.49 (m, 2H), 1.01 (t, J = 7.4 Hz, 3H). ^{13}C NMR (100 MHz, THF-d_8) δ = 164.2, 161.8, 159.6, 156.4, 154.3,

153.9, 147.1, 142.6, 141.3, 140.0, 139.7, 134.6, 134.1, 132.6, 132.4, 131.6, 131.3, 131.1, 131.1, 131.0, 130.7, 130.5, 130.1, 129.2, 129.2, 116.6, 114.6, 68.5, 32.5, 20.3, 14.4. HRMS (ESI) *m/z* $[M+H]^+$ calcd for $C_{39}H_{31}N_4O_3$ 603.2396; found 603.2382

4-(5-(4-butoxyphenyl)-2,3-diphenylpyrido[3,4-*b*]pyrazin-8-yl)benzoic acid (PP2c)

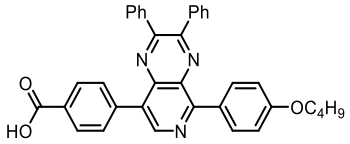

Compound **30c** (48 mg, 0.085 mmol, 1.0 eq.) was added to a Schlenk tube, put under inert atmosphere by performing three vacuum-nitrogen cycles and dissolved in THF (3 mL). A solution of $LiOH \cdot H_2O$ (178 mg, 4.24 mmol, 50.0 eq) in MeOH (3 mL) was then added. The resulting mixture was stirred at room temperature for 4 hours. HCl (aq.) 0.1 M (30 mL) was then added to induce precipitation od the crude and the solid was collected by centrifugation (4000 rpm, 10 min, rt).The crude mixture was washed with several portions of ethanol, EA and *n*-pentane to afford compound **PP2c** as a yellow solid (44 mg, 0.080 mmol, 94% yield). ^{1}H-NMR (400 MHz, CD_2Cl_2/HFIP-d_2 6/1 v/v) δ = 8.77 (d, J = 1.4 Hz, 1H), 8.30 (d, J = 8.1 Hz, 2H), 8.08 – 7.97 (m, 4H), 7.67 – 7.59 (m, 4H), 7.52 – 7.43 (m, 2H), 7.42 – 7.34 (m, 4H), 7.23 – 7.16 (m, 2H), 4.14 (t, J = 6.3 Hz, 2H), 1.92 – 1.78 (m, 2H), 1.61 – 1.47 (m, 2H), 1.02 (t, J = 7.4 Hz, 3H). ^{13}C-NMR (100 MHz, CD_2Cl_2/HFIP-d_2 6/1 v/v) δ = 171.2, 162.1, 160.9, 158.9, 156.2, 143.9, 143.4, 140.5, 138.4, 138.3, 135.0, 133.7, 133.5, 131.8, 131.5, 131.1, 131.0, 130.9, 130.7, 129.7, 129.5, 128.5, 122.8, 115.9, 111.5, 31.8, 19.8, 13.8. HRMS (ESI) *m/z* $[M+H]^+$ calcd for $C_{36}H_{30}N_3O_3$ 552.2287; found 552.2286.

$[RuCl_2(DMSO)_4]$(16)

$RuCl_3 \bullet 3H_2O$ (1.00 g, 3.82 mmol, 1.0 eq) was refluxed in DMSO (10 mL) for 10 min under air until the solution turned yellow. After cooling to room temperature, acetone (30 mL) was added to induce product precipitation. The resulting precipitate was then filtered and washed with acetone and diethyl ether to afford the desired product as a yellow solid (1.38 g, 2.85 mmol, 74% yield). ^{1}H NMR (400 MHz, D_2O): δ 3.49 (s, 6H), 3.47 (s, 6H), 3.39 (s, 6H), 2.72 (s, 6H). Spectroscopic data are in agreement with those reported in the literature.[57]

[Ru(bda)(DMSO)$_2$] (18)

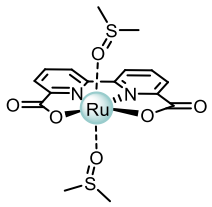

2,2′-bipyridine-6,6′-dicarboxylic acid (**17**, 350 mg, 0.722 mmol, 1.0 eq.) and **[RuCl$_2$(DMSO)$_{4v}$]** (176 mg, 0.722 mmol, 1.0 eq.) were added to a Schlenk tube and put under inert atmosphere by performing three vacuum-nitrogen cycles. The solids were then suspended in dry methanol (15 mL) and the solution degassed by bubbling N_2 for 15 min. Et_3N (439 mg, 4.33 mmol, 6.0 eq.) was then added, and the mixture was heated up and stirred under reflux for 4 h. After cooling to room temperature, the reaction mixture was centrifuged (4000 rpm, 10 min, rt). The resulting precipitate was then washed with cold methanol to afford the desired product as a dark brown solid (251 mg, 0.502 mmol, 70% yield). ^{1}H NMR (400 MHz, DMSO-d$_6$) δ = 8.64 (d, J = 8.0 Hz, 2H), 8.14 (t, J = 7.9 Hz, 2H), 8.02 (d, J = 7.8 Hz, 2H), 2.52 (s, 6H) ppm. Spectroscopic data are in agreement with those reported in the literature. [58]

[Ru(bda)(PyP)$_2$] (21)

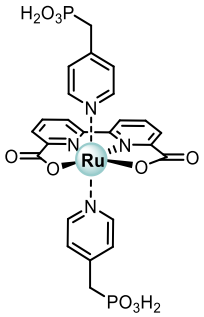

[Ru(bda)(DMSO)$_2$] (117 mg, 0.234 mmol, 1.0 eq.) was added to a Schlenk tube, put under inert atmosphere by performing three vacuum-nitrogen cycles, and suspended in dry methanol (10 mL). The mixture was degassed by bubbling N_2 for 15 min and heated at 60°C. Then a solution of (pyridin-4-ylmethyl)phosphonic acid (**25**, 89 mg, 0.515 mmol, 2.2 eq.) in a HFIP/methanol 1:4 (5 mL) mixture, previously prepared in another Schlenk tube under inert atmosphere and pre-heated at 60°C, was added via a gas-tight syringe. The reaction mixture was vigorously stirred at 80°C for 16 h. After cooling to room temperature, the volume of the solvent was reduced to ca. 8 mL. The mixture was centrifuged (4000 rpm, 10 min, rt). The resulting solid was washed with DCM and methanol, to afford the desired product as dark brown solid (110 mg, 0.200 mmol, 68% yield). Note: due to partial oxidation under air, with consequent formation of less soluble paramagnetic

species, NMR spectra of the catalyst were recorded in the presence of a small amount of hydroquinone as a reducing agent. ^{1}H NMR (400 MHz, CD_3OD + Hydroquinone) δ 8.55 (dd, J = 8.0, 1.1 Hz, 2H), 8.01 (d, J = 7.7 Hz, 2H), 7.87 (t, J = 7.9 Hz, 2H), 7.71 (d, J = 6.0 Hz, 4H), 7.14 (dd, J = 6.6, 2.3 Hz, 4H), 3.04 (d, J = 22.5 Hz, 4H) ppm. ^{31}P NMR (162 MHz, CD_3OD + Hydroquinone) δ = 17.50 ppm. MS (ESI) *m/z*: $[M]^+$ calcd for $C_{24}H_{22}N_4O_{10}P_2Ru$ 690.0; found: 689.8.

3.7.3 Spectroscopic characterization

UV-Vis spectra in different solvents were measured on diluted solutions of the compounds (approx. 10^{-5} M) either with a *Shimadzu* UV-2600 or a *Perkin Elmer* Lambda 950 UV-vis-NIR spectrometer. UV-Vis absorption spectra of the same compounds adsorbed on TiO_2 were recorded with a *Shimadzu* UV-2600 spectrometer in transmission mode after the sensitization of thin, transparent semiconductor films (thickness approx. 5 μm, for details on their preparation see below, Section 3.7.5). Steady state fluorescence emission and excitation spectra of the dyes at room temperature were obtained either with a *Jasco* FP-8300 or a *Hamamatsu* Edinburgh FLS920 spectrofluorometer. Excitation and emission spectra of the compounds in a frozen MeOH/DCM 1:1 matrix at 77 K were obtained with the same Edinburgh FLS920 spectrofluorometer, using quartz tubes dipped in liquid nitrogen in a quartz Dewar as sample containers.

Time-correlated single photon counting (TCSPC) experiments for the determination of the excited states lifetimes were carried out with an IBH time-correlated single-photon counting apparatus with nanoLED excitation source at 375 nm.

Pump-probe transient absorption measurements on the dyes and catalyst adsorbed on TiO_2 films were performed with an *Ultrafast Systems* HELIOS (HE-VIS-NIR) femtosecond transient absorption spectrometer by using, as excitation source, a *Newport* Spectra Physics Solstice-F-1K-230 V laser system, combined with a TOPAS Prime (TPR-TOPAS-F) optical parametric amplifier (pulse width: 100 fs, 1 kHz repetition rate) tuned at 500 nm. The pump energy on the sample was 3 μJ/pulse. Probe beams with a generated continuum both in the visible range (450-800 nm) and in the NIR range (800-1600 nm) have been employed and the spectra have been merged in the analysis. The overall time resolution of the system is 300 fs. Surface Xplorer V4 software from *Ultrafast Systems* was used for data acquisition and analysis. The 3D data surfaces were corrected for the chirp of the probe pulse prior to analysis. The estimated error on transient absorbance lifetimes is 10%.

3.7.4 Electrochemical and spectroelectrochemical characterization

Cyclic voltammetries (CV) of the dyes in DCM solution were recorded with an *Agilent* B2901 precision SMU using a glassy carbon electrode as the working electrode, a platinum wire as the counter electrode, and an $Ag/AgNO_3$ (0.01 M in CH_3CN) pseudo-reference electrode. 0.1 M $TBAPF_6$ was used as the supporting electrolyte, with a scan speed of 100 mV s^{-1}. Curves were recorded first in the absence and then in the presence of ferrocene (Fc), used as an internal standard. The E_{ox} of the compounds were referenced to that of the $Fc^{+/0}$ couple, and the latter was used to set the potential scale assuming its redox potential to be equal to 0.72 V *vs.* NHE in DCM, according to the literature.[31]

CVs of the FTO/TiO_2/**dye + [Ru(bda)(PyP)$_2$]** electrodes, employed as working electrodes, were recorded with a *Metrohm Autolab* PGSTAT 302N + FRA32M electrochemical workstation, using a Saturated Calomel Electrode (SCE) as the reference electrode and a platinum wire as the counter electrode, and the data were recorded and elaborated by Nova 1.6 software. Measurements were performed in a 0.1 M phosphate buffer solution (pH = 6.6), between −0.05 V and +1.4 V *vs.* SCE at scan rate of 50 mV s^{-1} (3 cycles). Prior to each measurement, electrolytic solutions were degassed with argon for 10 minutes.

The in situ UV-vis-NIR spectroelectrochemical measurements were carried out with a *Metrohm Autolab* PGSTAT204 potentiostat/galvanostat and a *Perkin Elmer* Lambda 950 spectrophotometer in a thin layer quartz glass spectroelectrochemical cell (*ALS*, model SEC-C). A platinum gauze was used as the working electrode, a platinum wire was the counterelectrode while the reference electrode was made by Ag/Ag^+ in $AgNO_3$ 0.01 M in acetonitrile (*ALS*, model RE-7). Tetrabutylammonium hexafluophosphate ($TBAPF_6$) 0.1 M in dichloromethane was used as the electrolyte. All the solutions were deaerated for 15 min in argon and the cuvette was sealed for maintaining the argon atmosphere during the experiments. The spectroelectrochemical tests were carried out at room temperature.

3.7.5 Photoelectrode preparation and staining procedure

10×10 cm FTO-coated conducting glass sheets (TEC 8 Ω sq^{-1}, GreatCell solar) were cleaned in an ultrasonic bath by the following procedure: (a) immersion in soapy water (15'), followed by rinsing with demineralized water (3×); (b) immersion in demineralized water (15'), followed by rinsing with acetone (3×); (c) immersion in acetone (15'). The sheets were then immersed for 10 seconds in boiling *iso*-propanol, followed by drying.

The mesoporous TiO_2 layer was deposited on the FTO glass by printing a single layer of a commercially available nanocrystalline TiO_2 paste (DyeSol TiO_2 Paste DSL 18NR-T, mechanically stirred for 20' prior to use) in 1.0×1.0 cm^2 spots, using an *Aurel* C920 semi-automatic screen printer. The plates were left to sit in an EtOH-fumes-filled chamber for 30" before drying at 120 °C for 30 min, then sintered according to the following programmed ramp: 15' at 350 °C, 30' at 375 °C, 1 h at 450 °C, and 1 h at 500 °C. The active area of the resulting mesoporous semi-transparent TiO_2 films was 1.0 cm^2 and the plates were cut into 2.5×2.5 cm^2 slides.

For the preparation of the co-adsorption staining solutions, dyes **1a-c** were first dissolved in the appropriate volume of anhydrous and degassed THF, then the same volume of anhydrous and degassed MeOH was added to obtain 4×10^{-4} M solutions of the dyes in a THF/MeOH 1:1 (v/v) mixture. In another container, **[Ru(bda)(PyP)$_2$]** was dissolved in a small amount of HFIP, and then anhydrous and degassed MeOH was added to obtain a 2×10^{-4} M solution of the catalyst in a MeOH/HFIP 9:1 (v/v) mixture. Finally, the dye and catalyst individual solutions were mixed in a 1:1 ratio to obtain the desired co-adsorption staining solution, with concentrations of 2×10^{-4} M (dye) and 1×10^{-4} M (catalyst) in a MeOH/THF/HFIP 70:25:5 (v/v) mixture. The staining solutions for the sequential procedure were instead obtained by simply diluting to double volume the above-mentioned individual dye (**1b**) and catalyst solutions, obtaining the same final concentrations of 2×10^{-4} M (dye) and 1×10^{-4} M (catalyst).

The slides with the printed TiO_2 films were heated on a hot plate at 80°C for at least one hour. For the co-adsorption procedure, while still warm, they were then immersed in the appropriate combined **1a-c+[Ru(bda)(PyP)$_2$]** solution for 4 h, after which the electrodes were rinsed with ethanol and dried under airflow. For the sequential adsorption procedure, they were instead immersed first, when still warm, in the **[Ru(bda)(PyP)$_2$]** solution for 4 h, followed by rinsing with ethanol and immersion in the **1b** solution for another 4h; finally, also in this case they were rinsed with ethanol and dried under airflow.

3.7.6 Photoelectrochemical measurements

The photoelectrochemical tests were conducted in a three-electrode cell setup with a *Metrohm* Autolab PGSTAT 302N + FRA32M electrochemical workstation, using the dye-sensitized and catalyst-functionalized electrodes as working electrodes, an Ag/AgCl/KCl (3 M) reference electrode and a platinum wire as the counter electrode, and the data were recorded and elaborated by Nova 1.6 software. The electrolyte was constituted by a 0.1 M Na_2SO_4 (Sigma Aldrich, ≥99.9%) solution in demineralized water (pH = 6.5), which was degassed for 10' with Ar prior to each measurement. The working electrode was illuminated with simulated solar radiation (100 mW

cm^{-2} AM 1.5) obtained using a *LOT-ORIEL* Solar Simulator, calibrated with a reference silicon solar cell. A mask was placed on the working electrode so that the illuminated area was 0.5 cm^2. Linear sweep voltammetry (LSV) measurements were conducted under chopped illumination, scanning potentials from −0.5 to +1.3 V *vs.* Ag/AgCl (in the oxidation direction), with a scan rate of 50 mV s^{-1}. Potentials were then referenced to NHE according to the following equation: $E_{NHE} = E_{Ag/AgCl} + 0.2$ V. Chronoamperometry (CA) measurements were conducted for 100 s under the same illumination conditions, measuring the current produced by the cells at a fixed potential of +0.3 V *vs.* Ag/AgCl (equal to +0.5 V *vs.* NHE).

3.8 References

(1) Yu, Z.; Li, F.; Sun, L. Recent Advances in Dye-Sensitized Photoelectrochemical Cells for Solar Hydrogen Production Based on Molecular Components. *Energy Environ. Sci.* 2015, *8* (3), 760–775. https://doi.org/10.1039/C4EE03565H.

(2) Ding, X.; Zhang, L.; Wang, Y.; Liu, A.; Gao, Y. Design of Photoanode-Based Dye-Sensitized Photoelectrochemical Cells Assembling with Transition Metal Complexes for Visible Light-Induced Water Splitting. *Coord. Chem. Rev.* 2018, *357*, 130–143. https://doi.org/10.1016/j.ccr.2017.10.020.

(3) Concepcion, J. J.; Tsai, M. K.; Muckerman, J. T.; Meyer, T. J. Mechanism of Water Oxidation by Single-Site Ruthenium Complex Catalysts. *J. Am. Chem. Soc.* 2010, *132* (5), 1545–1557. https://doi.org/10.1021/JA904906V.

(4) Ruttinger, W.; Dismukes, G. C. Synthetic Water-Oxidation Catalysts for Artificial Photosynthetic Water Oxidation. *Chem. Rev.* 1997, *97* (1), 1–24. https://doi.org/10.1021/CR950201Z.

(5) Blakemore, J. D.; Crabtree, R. H.; Brudvig, G. W. Molecular Catalysts for Water Oxidation. *Chem. Rev.* 2015, *115* (23), 12974–13005. https://doi.org/10.1021/acs.chemrev.5b00122.

(6) Duan, L.; Bozoglian, F.; Mandal, S.; Stewart, B.; Privalov, T.; Llobet, A.; Sun, L. A Molecular Ruthenium Catalyst with Water-Oxidation Activity Comparable to That of Photosystem II. *Nat. Chem* 2012, *4* (5), 418–423. https://doi.org/10.1038/nchem.1301.

(7) Li, L.; Duan, L.; Xu, Y.; Gorlov, M.; Hagfeldt, A.; Sun, L. A Photoelectrochemical Device for Visible Light Driven Water Splitting by a Molecular Ruthenium Catalyst Assembled on Dye-Sensitized Nanostructured TiO2. *Chem. comm.* 2010, *46* (39), 7307. https://doi.org/10.1039/c0cc01828g.

(8) Brennaman, M. K.; Dillon, R. J.; Alibabaei, L.; Gish, M. K.; Dares, C. J.; Ashford, D. L.; House, R. L.; Meyer, G. J.; Papanikolas, J. M.; Meyer, T. J. Finding the Way to Solar Fuels with Dye-Sensitized Photoelectrosynthesis Cells. *J. Am. Chem. Soc.* 2016, *138* (40), 13085–13102. https://doi.org/10.1021/jacs.6b06466.

(9) Decavoli, C.; Boldrini, C. L.; Manfredi, N.; Abbotto, A. Molecular Organic Sensitizers for Photoelectrochemical Water Splitting. *Eur. J. Inorg. Chem.* 2020, *2020* (11–12), 978–999. https://doi.org/10.1002/ejic.202000026.

(10) Ji, J.; Zhou, H.; Eom, Y. K.; Kim, C. H.; Kim, H. K. 14.2% Efficiency Dye-Sensitized Solar Cells by Co-sensitizing Novel Thieno[3,2- *b*]Indole-Based Organic Dyes with a Promising Porphyrin Sensitizer. *Adv. Energy Mater.* 2020, *10* (15). https://doi.org/10.1002/aenm.202000124.

(11) Zhang, L.; Yang, X.; Wang, W.; Gurzadyan, G. G.; Li, J.; Li, X.; An, J.; Yu, Z.; Wang, H.; Cai, B.; Hagfeldt, A.; Sun, L. 13.6% Efficient Organic Dye-Sensitized Solar Cells by Minimizing Energy Losses of the Excited State. *ACS Energy Lett.* 2019, *4* (4), 943–951. https://doi.org/10.1021/acsenergylett.9b00141.

(12) Ren, Y.; Zhang, D.; Suo, J.; Cao, Y.; Eickemeyer, F. T.; Vlachopoulos, N.; Zakeeruddin, S. M.; Hagfeldt, A.; Grätzel, M. Hydroxamic Acid Pre-Adsorption Raises the Efficiency of Cosensitized Solar Cells. *Nature* 2023, *613* (7942), 60–65. https://doi.org/10.1038/s41586-022-05460-z.

(13) Eberhart, M. S.; Wang, D.; Sampaio, R. N.; Marquard, S. L.; Shan, B.; Brennaman, M. K.; Meyer, G. J.; Dares, C.; Meyer, T. J. Water Photo-Oxidation Initiated by Surface-Bound Organic Chromophores. *J. Am. Chem. Soc.* 2017, *139* (45), 16248–16255. https://doi.org/10.1021/jacs.7b08317.

(14) Manfredi, N.; Boldrini, C. L.; Abbotto, A. Organic Sensitizers for Photoanode Water Splitting in Dye-Sensitized Photoelectrochemical Cells. *ChemElectroChem* 2018, *5* (17), 2395–2402. https://doi.org/10.1002/CELC.201800592.

(15) Eom, Y. K.; Nhon, L.; Leem, G.; Sherman, B. D.; Wang, D.; Troian-Gautier, L.; Kim, S.; Kim, J.; Meyer, T. J.; Reynolds, J. R.; Schanze, K. S. Visible-Light-Driven Photocatalytic Water Oxidation by a π-Conjugated Donor-Acceptor-Donor Chromophore/Catalyst Assembly. *ACS Energy Lett.* 2018, *3* (9), 2114–2119. https://doi.org/10.1021/ACSENERGYLETT.8B01020/SUPPL_FILE/NZ8B01020_SI_001.PDF.

(16) Wee, K. R.; Sherman, B. D.; Brennaman, M. K.; Sheridan, M. V.; Nayak, A.; Alibabaei, L.; Meyer, T. J. An Aqueous, Organic Dye Derivatized SnO2/TiO2 Core/Shell Photoanode. *J. Phys. Chem. A* 2016, *4* (8), 2969–2975. https://doi.org/10.1039/c5ta06678f.

(17) Tripathi, A.; Ganjoo, A.; Chetti, P. Influence of Internal Acceptor and Thiophene Based π-Spacer in D-A-π-A System on Photophysical and Charge Transport Properties for Efficient DSSCs: A DFT Insight. *Solar Energy* 2020, *209*, 194–205. https://doi.org/10.1016/j.solener.2020.08.084.

(18) Ji, J.-M.; Zhou, H.; Kim, H. K. Rational Design Criteria for D–π–A Structured Organic and Porphyrin Sensitizers for Highly Efficient Dye-Sensitized Solar Cells. *J.Mater. Chem. A* 2018, *6* (30), 14518–14545. https://doi.org/10.1039/C8TA02281J.

(19) Al-Marhabi, A. R.; El-Shishtawy, R. M.; Al-Footy, K. O. An Overview of Metal-Free Diazine-Based Dyes for Dye-Sensitized Solar Cells: Synthesis, Optical, and Photovoltaic Properties. *Mater. Today Sustainability* 2024, *28*, 101014. https://doi.org/10.1016/j.mtsust.2024.101014.

(20) Ying, W.; Yang, J.; Wielopolski, M.; Moehl, T.; Moser, J.-E.; Comte, P.; Hua, J.; Zakeeruddin, S. M.; Tian, H.; Grätzel, M. New Pyrido[3,4-b]Pyrazine-Based Sensitizers for Efficient and Stable Dye-Sensitized Solar Cells. *Chem. Sci.* 2014, *5* (1), 206–214. https://doi.org/10.1039/C3SC51844B.

(21) Yashwantrao, G.; Saha, S. Perspective on the Rational Design Strategies of Quinoxaline Derived Organic Sensitizers for Dye-Sensitized Solar Cells (DSSC). *Dyes Pigm.* 2022, *199*, 110093. https://doi.org/10.1016/j.dyepig.2022.110093.

(22) Kohn, W.; Sham, L. J. Self-Consistent Equations Including Exchange and Correlation Effects. *Phys. Rev.* 1965, *140* (4A), A1133. https://doi.org/10.1103/PHYSREV.140.A1133/FIGURE/1/THUMB.

(23) Adamo, C.; Jacquemin, D. The Calculations of Excited-State Properties with Time-Dependent Density Functional Theory. *Chem. Soc. Rev.* 2013, *42* (3), 845–856. https://doi.org/10.1039/C2CS35394F.

(24) RCS Catalysis Series. *New Trends in Cross-Coupling*; Colacot, T., Ed.; Royal Society of Chemistry: Cambridge, 2014. https://doi.org/10.1039/9781782620259.

(25) D'Amico, F.; Papucci, C.; Franchi, D.; Reginato, G.; Calamante, M.; Zani, L.; Dessì, A.; Mordini, A. Sustainable Pd-Catalyzed Direct Arylation of Thienyl Derivatives with (Hetero)Aromatic Bromides under Air in Deep Eutectic Solvents. *ACS Sustainable Chem. Eng.* 2022, *10* (9), 3037–3047. https://doi.org/10.1021/acssuschemeng.1c08466.

(26) Zani, L.; Dessì, A.; Franchi, D.; Calamante, M.; Reginato, G.; Mordini, A. Transition Metal-Catalyzed Cross-Coupling Methodologies for the Engineering of Small Molecules with Applications in Organic Electronics and Photovoltaics. *Coord. Chem. Rev.* 2019, *392*, 177–236. https://doi.org/10.1016/j.ccr.2019.04.007.

(27) Papucci, C.; Ventura, F.; Franchi, D.; Dessi, A.; Pucci, A.; Reginato, G.; Mordini, A.; Calamante, M.; Zani, L. A Direct Arylation Approach for the Preparation of Benzothiadiazole-Based Fluorophores for Application in Luminescent Solar Concentrators. *Synlett* 2023, *34* (12), 1462–1466. https://doi.org/10.1055/a-2059-3372.

(28) Nitti, A.; Po, R.; Bianchi, G.; Pasini, D. Direct Arylation Strategies in the Synthesis of π-Extended Monomers for Organic Polymeric Solar Cells. *Molecules* 2016, *22* (1), 21. https://doi.org/10.3390/molecules22010021.

(29) Kasha, M. Characterization of Electronic Transitions in Complex Molecules. *Discuss. Faraday Soc.* 1950, *9*, 14. https://doi.org/10.1039/df9500900014.

(30) Mooney, J.; Kambhampati, P. Get the Basics Right: Jacobian Conversion of Wavelength and Energy Scales for Quantitative Analysis of Emission Spectra. *J. Phys. Chem. Lett* 2013, *4* (19), 3316–3318. https://doi.org/10.1021/jz401508t.

(31) Aranzaes, J. R.; Daniel, M.-C.; Astruc, D. Metallocenes as References for the Determination of Redox Potentials by Cyclic Voltammetry — Permethylated Iron and Cobalt Sandwich Complexes, Inhibition by Polyamine Dendrimers, and the Role of Hydroxy-Containing Ferrocenes. *Can. J. Chem.* 2006, *84* (2), 288–299. https://doi.org/10.1139/v05-262.

(32) Zhang, B.; Sun, L. Artificial Photosynthesis: Opportunities and Challenges of Molecular Catalysts. *Chem. Soc. Rev.* 2019, *48* (7), 2216–2264. https://doi.org/10.1039/C8CS00897C.

(33) Chen, Z.; Concepcion, J. J.; Jurss, J. W.; Meyer, T. J. Single-Site, Catalytic Water Oxidation on Oxide Surfaces. *J. Am. Chem. Soc.* 2009, *131* (43), 15580–15581. https://doi.org/10.1021/ja906391w.

(34) Yamamoto, M.; Nishizawa, Y.; Chábera, P.; Li, F.; Pascher, T.; Sundström, V.; Sun, L.; Imahori, H. Visible Light-Driven Water Oxidation with a Subporphyrin Sensitizer and a Water Oxidation Catalyst. *Chem. Comm.* 2016, *52* (94), 13702–13705. https://doi.org/10.1039/c6cc07877j.

(35) Decavoli, C.; Boldrini, C. L.; Trifiletti, V.; Luong, S.; Fenwick, O.; Manfredi, N.; Abbotto, A. Dye–Catalyst Dyads for Photoelectrochemical Water Oxidation Based on Metal-Free Sensitizers. *RSC Adv.* 2021, *11* (10), 5311–5319. https://doi.org/10.1039/D0RA10971A.

(36) Gierszewski, M.; Glinka, A.; Grądzka, I.; Gierczyk, B.; Ziółek, M. Testing New Concepts in Solar Cells Sensitized with Indoline Dyes—Alkoxysilyl Anchoring Group, Molecular Capping, and Cobalt-Based Electrolyte. *J. Phys. Chem. C* 2018, *122* (45), 25764–25775. https://doi.org/10.1021/acs.jpcc.8b06389.

(37) Yoshihara, T.; Katoh, R.; Furube, A.; Tamaki, Y.; Murai, M.; Hara, K.; Murata, S.; Arakawa, H.; Tachiya, M. Identification of Reactive Species in Photoexcited Nanocrystalline TiO 2 Films by Wide-Wavelength-

Range (400−2500 Nm) Transient Absorption Spectroscopy. *J. Phys. Chem.B* 2004, *108* (12), 3817–3823. https://doi.org/10.1021/jp031305d.

(38) Virkki, K.; Tervola, E.; Ince, M.; Torres, T.; Tkachenko, N. V. Comparison of Electron Injection and Recombination on TiO 2 Nanoparticles and ZnO Nanorods Photosensitized by Phthalocyanine. *R. Soc. Open Sci.* 2018, *5* (7), 180323. https://doi.org/10.1098/rsos.180323.

(39) Zhao, Y.; Swierk, J. R.; Megiatto, J. D.; Sherman, B.; Youngblood, W. J.; Qin, D.; Lentz, D. M.; Moore, A. L.; Moore, T. A.; Gust, D.; Mallouk, T. E. Improving the Efficiency of Water Splitting in Dye-Sensitized Solar Cells by Using a Biomimetic Electron Transfer Mediator. *Proc. Natl Acad. Sci.* 2012, *109* (39), 15612–15616. https://doi.org/https://doi.org/10.1073/PNAS.1118339109.

(40) Alibabaei, L.; Dillon, R. J.; Reilly, C. E.; Brennaman, M. K.; Wee, K. R.; Marquard, S. L.; Papanikolas, J. M.; Meyer, T. J. Chromophore-Catalyst Assembly for Water Oxidation Prepared by Atomic Layer Deposition. *ACS Appl. Mater. Interfaces* 2017, *9* (44), 39018–39026. https://doi.org/https://doi.org/10.1021/ACSAMI.7B11905.

(41) Glasson, C. R. K.; Song, W.; Ashford, D. L.; Vannucci, A.; Chen, Z.; Concepcion, J. J.; Holland, P. L.; Meyer, T. J. Self-Assembled Bilayers on Indium-Tin Oxide (SAB-ITO) Electrodes: A Design for Chromophore-Catalyst Photoanodes. *Inorg. Chem.* 2012, *51* (16), 8637–8639. https://doi.org/https://doi.org/10.1021/IC300636W.

(42) Hanson, K.; Torelli, D. A.; Vannucci, A. K.; Kyle Brennaman, M.; Luo, H.; Alibabaei, L.; Song, W.; Ashford, D. L.; Norris, M. R.; K Glasson, C. R.; Concepcion, J. J.; Meyer, T. J.; Hanson, K.; Torelli, D. A.; Vannucci, A. K.; Brennaman, M. K.; Luo, H.; Alibabaei, L.; Song, W.; Ashford, D. L.; Norris, M. R.; K Glasson, C. R.; Concepcion, J. J.; Meyer, T. J. Self-Assembled Bilayer Films of Ruthenium(II)/Polypyridyl Complexes through Layer-by-Layer Deposition on Nanostructured Metal Oxides. *Angew. Chem. Int. Ed.* 2012, *124* (51), 12954–12957. https://doi.org/10.1002/ANGE.201206882.

(43) Grądzka, I.; Gierszewski, M.; Karolczak, J.; Ziółek, M. Comparison of Charge Transfer Dynamics in Polypyridyl Ruthenium Sensitizers for Solar Cells and Water Splitting Systems. *Phys. Chem. Chem. Phys.* 2018, *20* (11), 7710–7720. https://doi.org/10.1039/C8CP00258D.

(44) Juozapavicius, M.; Kaucikas, M.; van Thor, J. J.; O'Regan, B. C. Observation of Multiexponential Pico- to Subnanosecond Electron Injection in Optimized Dye-Sensitized Solar Cells with Visible-Pump Mid-Infrared-Probe Transient Absorption Spectroscopy. *J. Phys. Chem. C* 2013, *117* (1), 116–123. https://doi.org/10.1021/jp309732z.

(45) Kallioinen, J.; Lehtovuori, V.; Myllyperkiö, P.; Korppi-Tommola, J. Transient Absorption Studies of the Ru(Dcbpy)2(NCS)2 Excited State and the Dye Cation on Nanocrystalline TiO2 Film. *Chem. Phys. Lett.* 2001, *340* (3–4), 217–221. https://doi.org/10.1016/S0009-2614(01)00398-0.

(46) Gao, Y.; Zhang, L.; Ding, X.; Sun, L. Artificial Photosynthesis – Functional Devices for Light Driven Water Splitting with Photoactive Anodes Based on Molecular Catalysts. *Phys. Chem. Chem. Phys.* 2014, *16* (24), 12008. https://doi.org/10.1039/c3cp55204g.

(47) Kirner, J. T.; Stracke, J. J.; Gregg, B. A.; Finke, R. G. Visible-Light-Assisted Photoelectrochemical Water Oxidation by Thin Films of a Phosphonate-Functionalized Perylene Diimide Plus CoO *x* Cocatalyst. *ACS Appl. Mater. Interfaces* 2014, *6* (16), 13367–13377. https://doi.org/10.1021/am405598w.

(48) Mehta, V. P.; Van der Eycken, E. V. Microwave-Assisted C–C Bond Forming Cross-Coupling Reactions: An Overview. *Chem. Soc. Rev.* 2011, *40* (10), 4925. https://doi.org/10.1039/c1cs15094d.

(49) Rahman, M.; Ghosh, S.; Bhattacherjee, D.; Zyryanov, G. V.; Kumar Bagdi, A.; Hajra, A. Recent Advances in Microwave-assisted Cross-Coupling Reactions. *Asian J. Org. Chem.* 2022, *11* (8). https://doi.org/10.1002/ajoc.202200179.

(50) Liu, B.; Giordano, F.; Pei, K.; Decoppet, J.; Zhu, W.; Zakeeruddin, S. M.; Grätzel, M. Molecular Engineering of Pyrido[3,4- *b*]Pyrazine-Based Donor–Acceptor–Π-Acceptor Organic Sensitizers: Effect of Auxiliary Acceptor in Cobalt- and Iodine-Based Electrolytes. *Chem. Eur. J.* 2015, *21* (51), 18654–18661. https://doi.org/10.1002/chem.201503514.

(51) Shen, Z.; Zhang, X.; Giordano, F.; Hu, Y.; Hua, J.; Zakeeruddin, S. M.; Tian, H.; Grätzel, M. Significance of π-Bridge Contribution in Pyrido[3,4-b]Pyrazine Featured D–A–π–A Organic Dyes for Dye-Sensitized Solar Cells. *Mater. Chem. Front.* 2017, *1* (1), 181–189. https://doi.org/10.1039/C6QM00119J.

(52) Qiao, H.; Deng, Y.; Peng, R.; Wang, G.; Yuan, J.; Tan, S. Effect of π-Spacers and Anchoring Groups on the Photovoltaic Performances of Ullazine-Based Dyes. *RSC Adv.* 2016, *6* (74), 70046–70055. https://doi.org/10.1039/C6RA11918B.

(53) Almenningen, D. M.; Haga, B. S.; Hansen, H. E.; Buene, A. F.; Hoff, B. H.; Gautun, O. R. Adamantyl Side Chains as Anti-Aggregating Moieties in Dyes for Dye-Sensitized Solar Cells. *Chem. Eur. J.* 2022, *28* (51). https://doi.org/10.1002/chem.202201726.

(54) Liu, D.; Chen, M.; Li, K.; Li, Z.; Huang, J.; Wang, J.; Jiang, Z.; Zhang, Z.; Xie, T.; Newkome, G. R.; Wang, P. Giant Truncated Metallo-Tetrahedron with Unexpected Supramolecular Aggregation Induced Emission Enhancement. *J. Am. Chem. Soc.* 2020, *142* (17), 7987–7994. https://doi.org/10.1021/jacs.0c02366.

(55) Pratap Tripathi, N.; Gupta, V.; Tarun, T.; Kumar Pandey, U.; Sengupta, S. Functionalized Benzothiadiazole Non-Fused A−D−A'−D−A Small Molecules for Effective Electron Mobilities and Metal-free Photocatalysis. *Chem. Eur. J.* 2023, *29* (26). https://doi.org/10.1002/chem.202203951.

(56) Putri, S. K.; Kim, Y. H.; Whang, D. R.; Lee, M. S.; Kim, J. H.; Chang, D. W. Step-by-Step Improvement in Photovoltaic Properties of Fluorinated Quinoxaline-Based Low-Band-Gap Polymers. *Org. Electron.* 2017, *47*, 14–23. https://doi.org/10.1016/j.orgel.2017.04.025.

(57) Karges, J.; Stokes, R. W.; Cohen, S. M. Photorelease of a Metal-Binding Pharmacophore from a Ru(<scp>ii</Scp>) Polypyridine Complex. *Dalton Trans.* 2021, *50* (8), 2757–2765. https://doi.org/10.1039/D0DT04290K.

(58) Gao, Y.; Ding, X.; Liu, J.; Wang, L.; Lu, Z.; Li, L.; Sun, L. Visible Light Driven Water Splitting in a Molecular Device with Unprecedentedly High Photocurrent Density. *J. Am. Chem. Soc.* 2013, *135* (11), 4219–4222. https://doi.org/10.1021/ja400402d.

Chapter 4

Synthetic approaches to the construction of a dye-catalyst molecular dyad

4.1 Introduction

In the previous chapter, it was shown how functionalized DS-PEC photoanodes can be fabricated by applying the concept of co-loading of a dye and a water oxidation catalyst. However, such arrangement presents inherent limitations such as rapid electron-hole recombination at the molecule-electrode interface, which limits overall efficiency, and a difficult-to-control ratio of the adsorbed catalyst and photosensitizer. To overcome these problems, alternative strategies have been investigated over the years. In 2012, Meyer and coworkers[1] introduced an innovative co-loading strategy that improves the dye-catalyst assembly on metal oxide surfaces. This method relies on the formation of a catalyst overlayer on a chromophore monolayer. Initially, a layer of chromophores is covalently attached to the oxide surface. Subsequently, catalyst units are linked to the surface using long-chain -(CH_2)- phosphonate linkers, positioning each catalyst above a corresponding chromophore. This design places the WOC further away from the electrode surface limiting charge recombination (Figure 4.1).

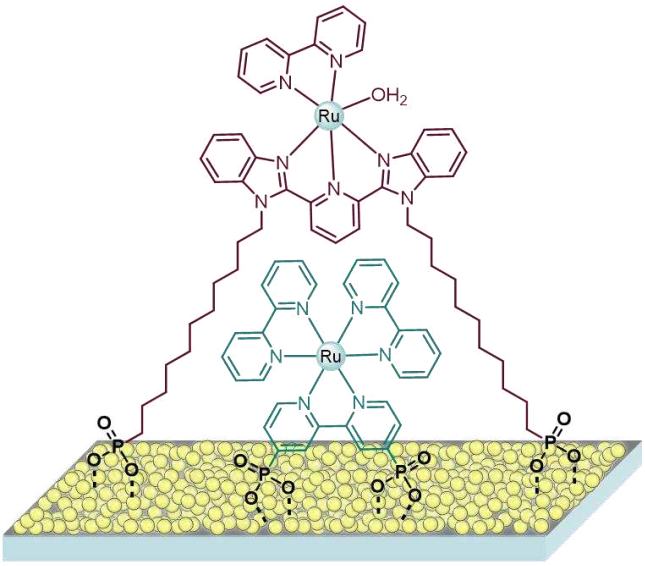

Figure 4.1 Examples of molecular overlayer strategy.

More generally, the unfavorable electron recombination dynamics on the SC surface can be overcome by linking the chromophore to the catalyst through different types of bridge, forming a dyadic system, and thus boosting dye regeneration kinetics. In this approach, the WOC can either be connected to the dye exploiting supramolecular interactions or form a covalent bond with it.

The first strategy has been reported several times in the literature. In 2012, Meyer and co-workers described for the first time the "layer-by-layer" assembly strategy (**Ru1-Zr^{4+}-RuCat1**) where phosphonate/Zr^{IV} coordination linkages were employed for the construction of multiple chromophore-catalyst sites on nanocrystalline metal oxide surfaces (Figure 4.2a).[2] In this approach Ru-

dyes endowed with multiple phosphonate functional groups were adsorbed as the first layer on the SC. Uncoordinated phosphonate groups oriented away from the SC surface and towards the solution were then used to coordinate Zr^{IV} centers of $ZrOCl_2$. The second layer was then formed by soaking in a solution containing a phosphonate-derivatized water oxidation catalyst (**RuCat1**), thereby completing the synthesis of the assembly. A slower back electron transfer kinetics was demonstrated by TAS experiments for TiO_2 film functionalized with the **Ru1-Zr^{4+}-RuCat1** assembly compared with TiO_2 film functionalized by co-adsorption.

Later on, Abbotto and co-workers reported a novel photosensitizer-catalyst dyad based on robust and, at the same time, flexible host-guest non-covalent interactions through the use of calix[4]arene cavities. In particular, by covalently linking the calix[4]arenes moiety with an easy-to-synthesize metal-free organic dye-sensitizer, they were able to immobilize a commonly used WOC such as Ru(bda)(Pic)$_2$ *via* formation of a host-guest supramolecular assembly, achieving a more efficient photoinduced water splitting (Figure 4.2b).[3]

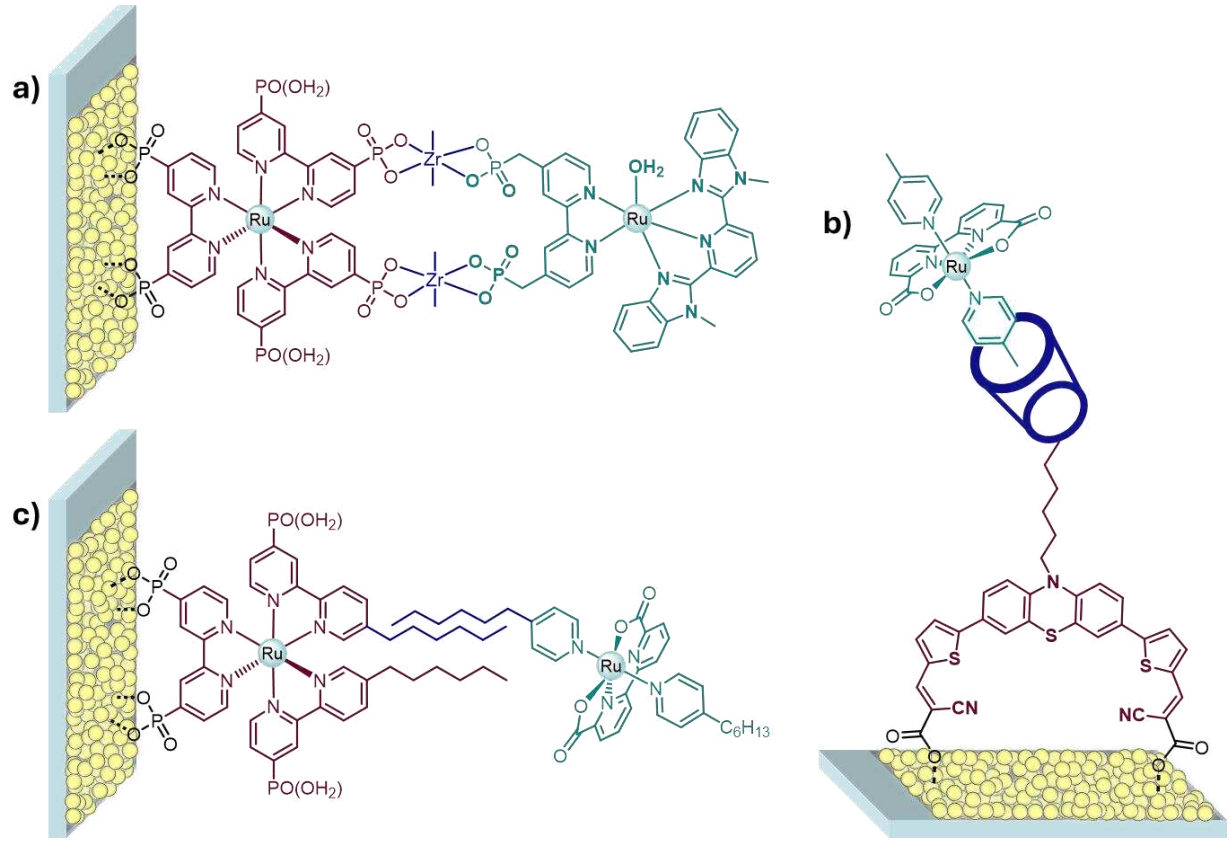

Figure 4.2 Examples of chromophore–catalyst assemblies based on supramolecular non-covalent interaction. a) "layer-by-layer" strategy; b) host-guest strategy; c) self-assembled bilayer strategy.

More recently, Concepcion and co-workers explored an alternative approach that utilizes self-assembled bilayers (SAB) of the two components, formed by noncovalent interactions between long alkyl chains decorating both the chromophore and catalyst. This strategy provides easy access to

a variety of combinations of catalysts and chromophores with precise control of the chromophore–catalyst ratio without complicated synthetic procedures (Figure 4.2c).[4]

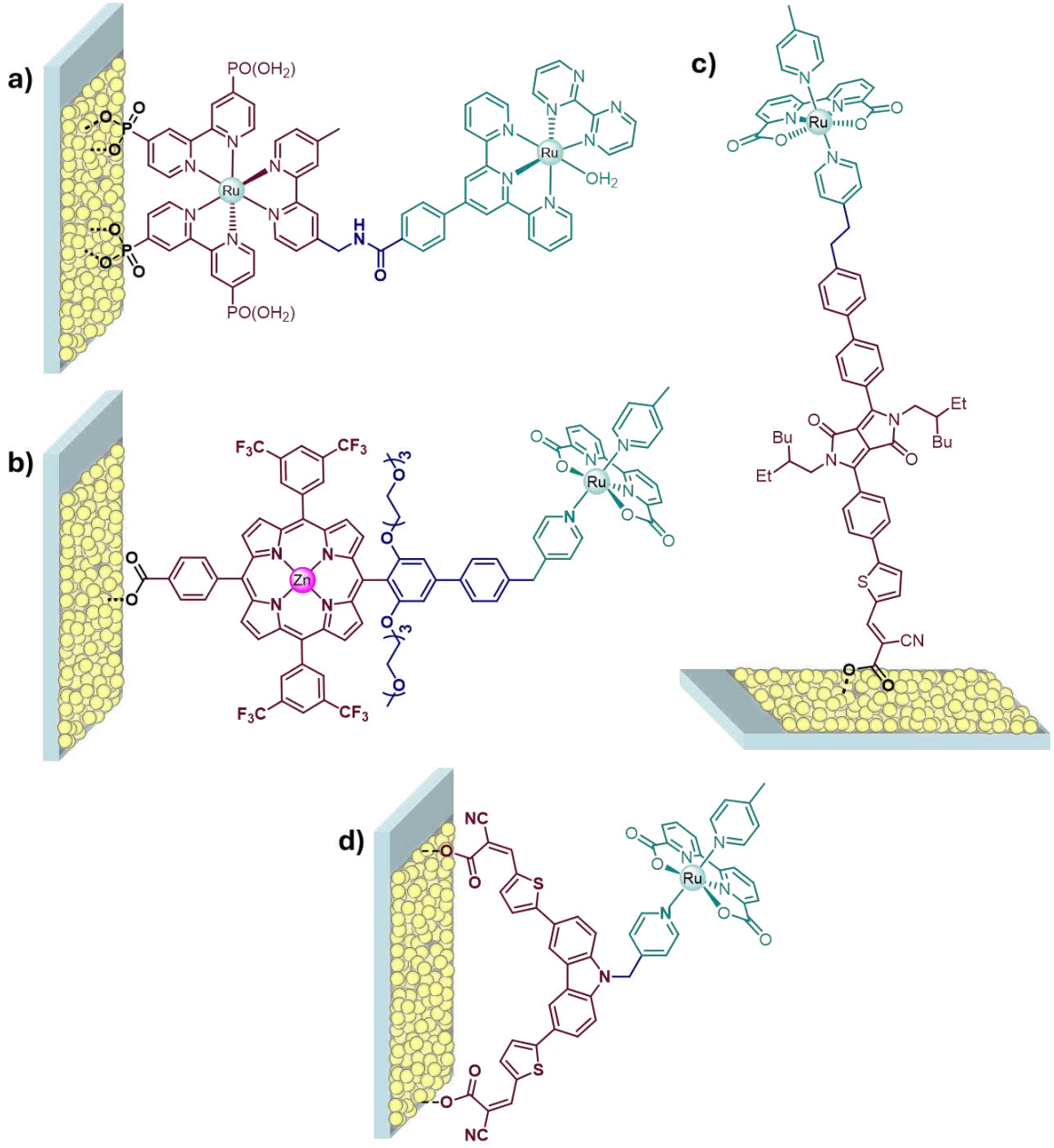

Figure 4.3 Examples of covalently linked chromophore–catalyst assemblies: a) amide bridge; b) dialkoxybiphenyl bridge; c) and d) alkyl bridge.

Compared to supramolecular chromophore-catalyst assemblies, covalently linked assemblies (Figure 4.3) offer significant advantages such as a more chemically stable linkages between the chromophore and catalyst and faster charge transfer kinetics between them, while suppressing back electron transfer between the semiconductor and the catalyst. However, the intrinsic advantages of this approach are often offset by the significant synthetic challenges posed by the preparation of compounds characterized by high molecular complexity.

Several examples of covalent linked dyads, exploring different types of bridge systems for linking the two key elements, have been reported. Most of these assemblies rely on the use of metal-based dyes and [Ru^{II}(bda)]-type derivatives as water oxidation catalyst. Meanwhile, the use of organic dyes has been less investigated.

Famous among metal-based covalent dyads are the amide-linked **Ru2-RuCat2** assembly[5] (Figure 4.3, a) and the ruthenium-based WOC–zinc porphyrin sensitizer (**Ru-ZnP**, Figure 4.3, b)[6]. The former assembly combines a light-harvesting chromophore (**Ru2**) and water oxidation catalyst (**RuCat**) linked by a synthetically flexible saturated bridge designed to enable long-lived charge-separated states. When compared with the constituent monomers, the **Ru2-RuCat2** assembly displayed, as expected, higher injection yields and slower back electron transfer rates.

In the **Ru-ZnP** dyad, the benchmark **[Ru(bda)(pic)$_2$]** was linked to a zinc porphyrin through one of its axial ligands, while the electronic conjugation between the dye and the catalyst was interrupted with a methylene bridge to avoid, once again, back electron transfer reactions. Moreover, the long alkoxyl chains present in the structure of the porphyrin-based dye generate a protective layer preventing protons to approach the SC. The performance of the corresponding DSPEC was demonstrated to be superior to those of the reference systems with co-adsorption of individual Ru(bda) and ZnP as well as with ZnP solely, corroborating the advantage of the covalent linking approach over the noncovalent one.

As already anticipated above, the use of organic dyes in catalytic dyads has been less explored. In 2020, Reisner and co-workers reported the first example of an organic dye-ruthenium catalyst dyad consisting of a DPP dye and a [Ru^{II}(bda)]-type complex, linked through an alkyl spacer chain (Figure 4.3c).[7] Good results were obtained when the dyad was integrated in a TiO_2-based photoanode for light-driven water oxidation, with photocurrents reaching ca. 140 $\mu A\ cm^{-2}$. This example is particularly significant as it demonstrates the potential for using metal-free sensitizers in the development of covalently linked catalyst dyads.

In the same year, Abbotto and co-workers[8] reported organic dye-ruthenium catalyst dyad consisting of a Cbz-based dye, functionalized with pyridine linkers, and a [Ru^{II}(bda)]-type complex. However in this example the catalytic system could not be individually prepared and isolated, but its formation was rather completed directly on the electrode surface, starting from the corresponding synthetic precursors. Despite this, optical, electrochemical, and XPS experiments confirmed the formation of the dyad on the SC film.

4.2 Design and synthesis of novel organic dye -catalyst dyads

With the aim of exploring different types of dye/catalyst photoanode-sensitization strategies, in this part of work we focused our attention on the development of novel covalent dye-catalyst dyads incorporating organic sensitizers. For this purpose, driven by the good photocurrent values obtained in DS-PEC sensitized with compound **1a** (Figure 4.4, top) of the quinoxaline-based series, we decided to explore the possibility of achieving the desired catalytic assembly by strategically modifying the structure of such dye as shown in Figure 4.4 (bottom).

As can be seen, the acceptor portion was not altered; therefore **Ru-D1A1** can be immobilized on a porous TiO_2 electrode *via* a cyanoacrylic acid anchoring group, which allows the localization of the LUMO near the electrode surface, facilitating electron injection into the bulk of the TiO_2 semiconductor.

On the other hand, the donor side of the molecule was adapted to incorporate the crucial pyridine moiety, essential for coordinating the designed dye with the Ru(bda) unit, chosen also in this case as the water oxidation catalyst (WOC). To introduce the terminal pyridine unit on the dye structure, we planned to use one of the so-called "click" reactions, whose concept was defined in 2001 by Kolb, Finn and Sharpless as a mean to bind two molecular building blocks together in a facile, selective, and high-yielding reaction under mild, water-tolerant conditions with little or no by-products.[9]

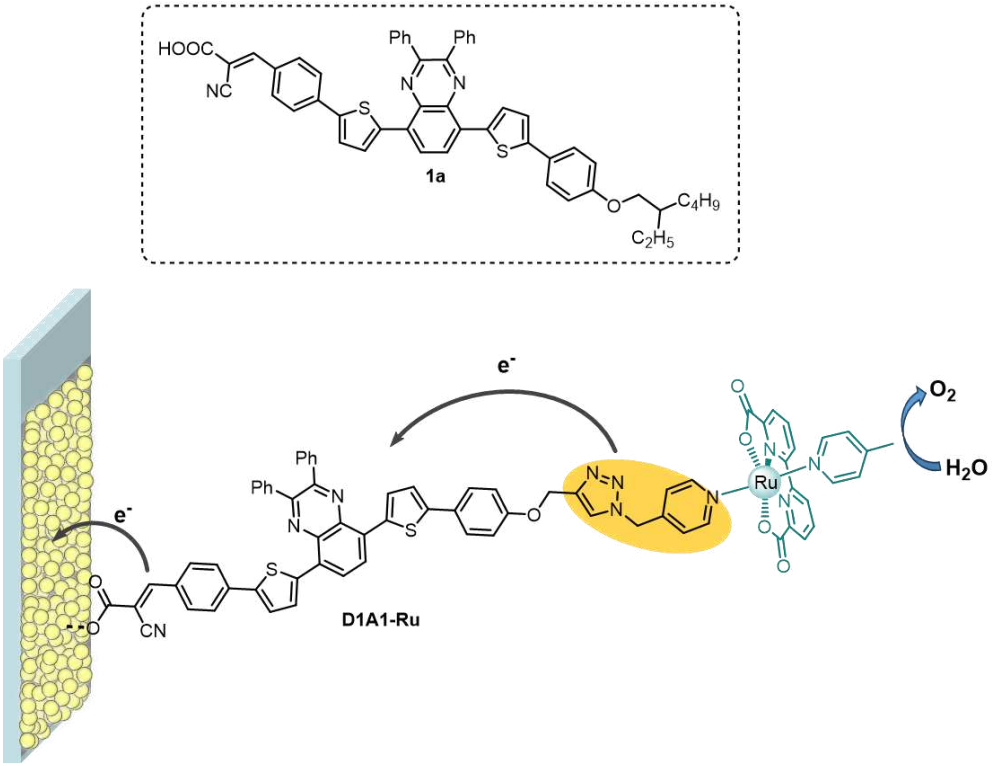

*Figure 4.4 Structure of dye **1a** (top); Designed structure of the proposed dye-catalyst dyad **DIA1-Ru.***

The most used "click" reaction that can fulfill these conditions is the CuI-catalyzed azide/alkyne cycloaddition (CuAAC)[10], reported independently by the research groups of Fokin, Sharpless[9] and Meldal[11] in 2001. Indeed, the non-catalyzed azide/alkyne reaction has been known since 1893 as Huisgen reaction, and produces a mixture of 1,4 and 1,5-disubstitution products[12] whereas, the CuAAC reaction of terminal alkynes is completely regioselective in the formation of the 1,4-di-substituted triazoles. The reasons for its success are that this "click" reaction is very easy to carry out, widely applicable and high yielding without producing by-products. Indeed, it is unaffected by a variety of functional groups and can be achieved with many sources of catalysts and solvents, including aqueous systems. For all these reasons in our design it was decided to use a triazole cycle as bridge system of the molecular dyad **Ru-D1A1**.

4.2.1 Retrosynthetic analysis

The synthetic pathway for the target chromophore was designed based on insights gained for the synthesis of the reference dye **1a** (see chapter 3, paragraph 3.4.2).

Thus, to reduce chromophore **D1A1** to its essential building blocks, a retrosynthetic approach involving five key steps was envisioned (Scheme 4.1). The process begins with the removal of cyanoacetic acid (**15**), yielding aldehyde **38** (disconnection ***A***). The next step (disconnection ***B***) involves the breaking of the 1,2,3-triazole bridge, resulting in the pyridine fragment **36** and intermediate **37**.

From intermediate **37**, a disconnection of the C–O bond (disconnection ***C***) produces propargyl bromide together with intermediate **32**, which contains a free hydroxyl group. The subsequent step involves the disconnection (***D***) of the hydroxyphenyl donor group leading to intermediate **8**. From this stage the retrosynthetic pathway resembles that seen for the reference dye **1a,** involving: the disconnection of benzaldehyde acceptor unit (disconnection ***E***) and the following break of the C-N bond of the quinoxaline central core (Disconnection ***F***) leading diketone **5** and compound **4** (that can be obtained as already described in chapter 3, paragraph 3.4.1).

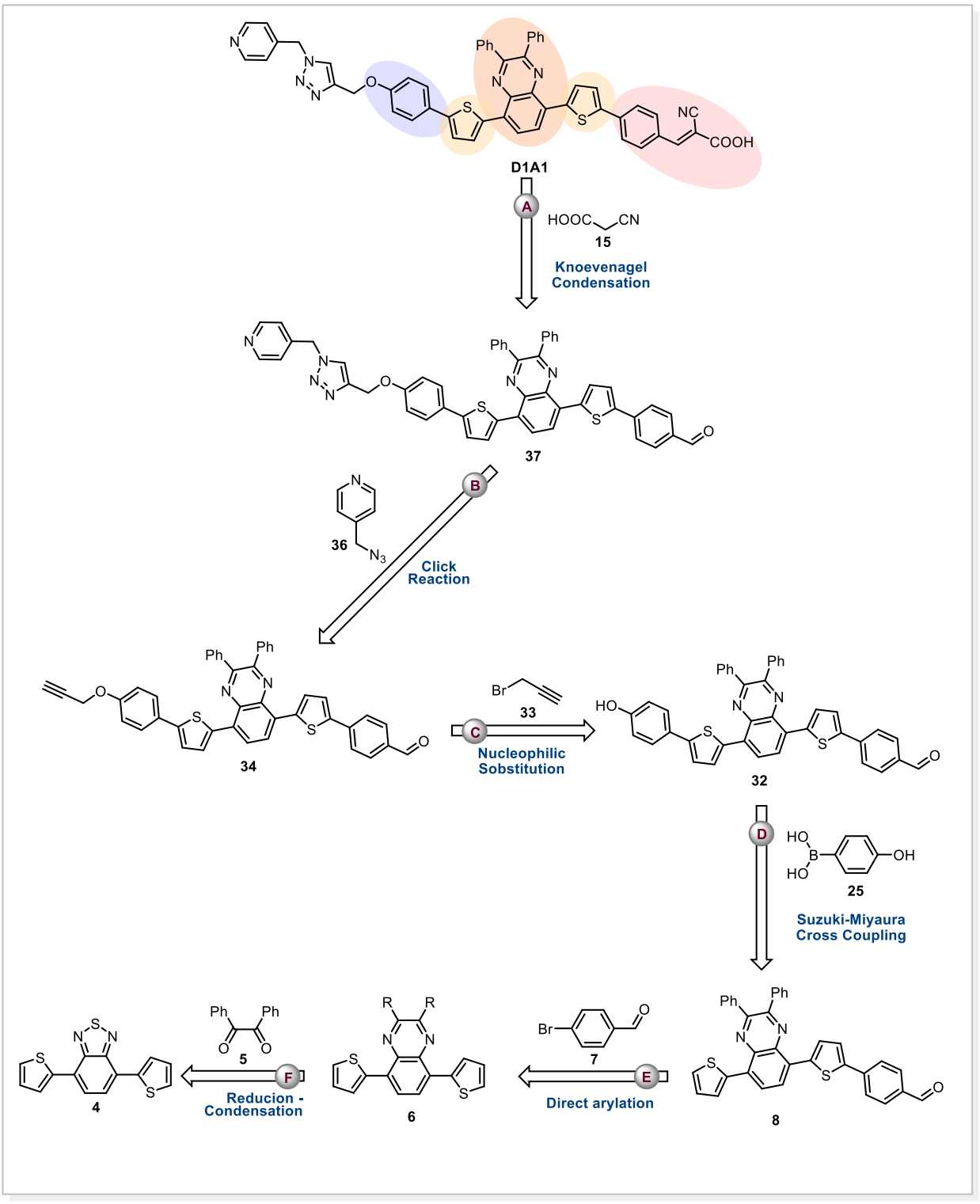

*Scheme 4.1 Retrosynthetic approach for the synthesis of compounds **D1A1**. Colors represent the different building blocks: donor (purple), π-bridge (yellow), auxiliary acceptor (orange), acceptor (pink).*

4.2.2 Synthesis of dye D1A1

Building on the above discussion, we begin the synthesis of the desired dye **D1A1** starting from the previously synthetized intermediate **8** (see chapter 3, paragraph 3.4.2). Here, to introduce the

donor moiety, unlike what was done for the synthesis of dye **1a**, we chose to follow the halogenation pathway, followed by Suzuki-Miyaura cross-coupling, rather than employing a direct arylation protocol (Scheme 4.2). This decision was based on previous observations, where C-H activation reactions proved to be unsuccessful when 4-bromophenol was used as an aryl bromide.

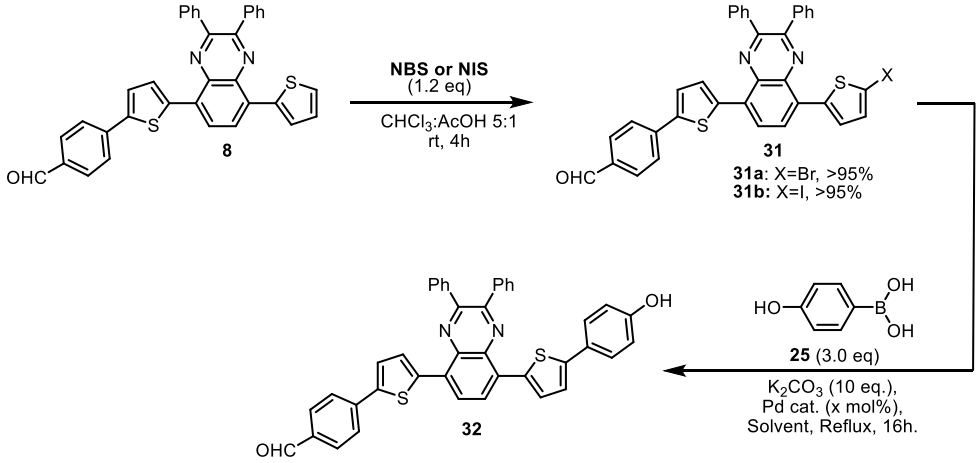

*Scheme 4.2 Synthesis of intermediate **32.***

To maximize the yield of intermediate **32**, a short optimization of the Suzuki-Miyaura reaction protocol was carried out, varying the nature of the catalyst, ligand, solvent and the halogen atom on intermediates **31a,b** (Table 4.1). The latter were first obtained in quantitative yield by reacting compound **8** with either *N*-bromosuccinimide (NBS) or *N*-iodosuccinimide (NIS), in a mixture of $CHCl_3$:AcOH 5:1 at room temperature for 4h.

Table 1 *Optimization of the reaction conditions for the preparation of intermediate **32***[a]

Entry	31 (-X)	"Pd"/Ligand (x mol%)	Solvent	T/t	Yield (%)[b]
1	Br	$Pd(PPh_3)_4$ (5.0 mol%)	Toluene:H_2O 2:1	Reflux/16 h	<5 %
2	Br	$Pd(PPh_3)_4$ (5.0 mol%)	1,4-Dioxane:H_2O 2:1	Reflux/16 h	<5%
3	Br	$Pd(PPh_3)_4$ (5.0 mol%)	THF: H_2O 2:1	Reflux/16 h	10%
4	I	$Pd(PPh_3)_4$ (5.0 mol%)	THF:H_2O 2:1	Reflux/16 h	46%
5	I	$Pd_2(dba)_3$ / SPhos (2.5/5.0 mol%)	THF:H_2O 2:1	Reflux/16 h	91%

[a]**31a,b** (0.079 mmol, 1.0 eq), **25** (0.237 mmol, 3.0 eq) K_2CO_3 (0.110 mmol, 10.0 eq); [b] Isolated product yield after column chromatography.

The best result was obtained when iodide **31b** was used as the substrate and the reaction was conducted under the following conditions: $Pd_2(dba)_3$ (2.5 mol%), S-Phos (5 mol%), K_2CO_3 (10.0 eq.), in THF/H_2O 2:1 at reflux for 16 h. With this protocol, the desired product **32** could be obtained with an excellent yield of 91%.

As mentioned in paragraph 4.2.1, the approach we chose to incorporate the pyridine moiety (essential for coordination with the Ru-bda unit), relies on a click reaction. This method necessitates the prior synthesis of the two reaction partners, each equipped with the appropriate azide/alkyne functional groups. Therefore, in our pathway to the dye **D1A1**, we continued with the synthesis of intermediate **34,** featuring a propargyl unit, and of the azido-methyl-pyridine unit **36** (Scheme 4.3, first two rows).

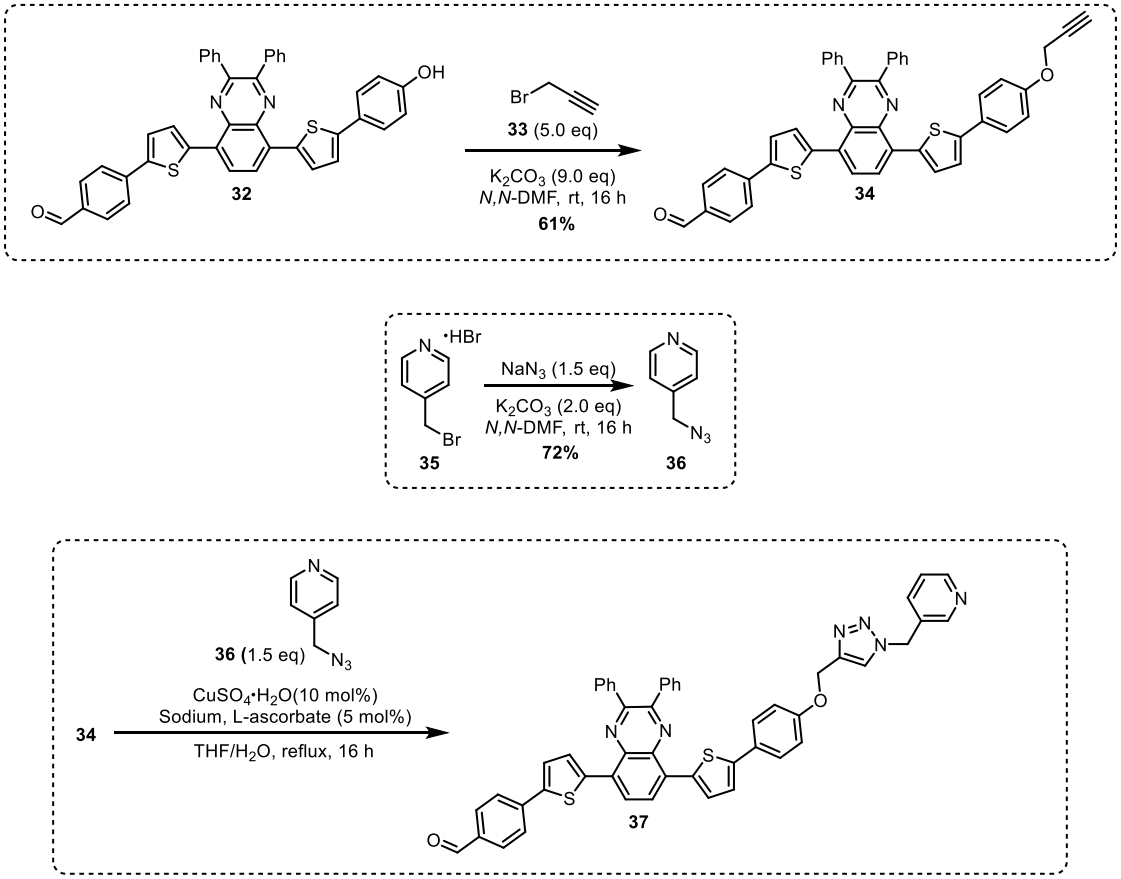

*Scheme 4.3 Attempted synthesis of dye **D1A1.***

The two fragments were obtained under similar conditions by reaction of the precursors **32** and **35** with propargyl bromide **33** and sodium azide, respectively. The reactions were accomplished by mixing the reagents in *N,N*-DMF, heating at 90°C and stirring for 6 h. Under these conditions the two desired products were obtained with a good yield of 61-72%.

Finally, compound **34** was subjected to CuAAC conditions in the presence of azide **36**. Full conversion of the starting materials was observed, but unfortunately the obtained product resulted completely insoluble in a wide range of common organic solvents.

This outcome prevented us from advancing along the planned synthetic route, and forced us to reconsider the chosen molecular design in order to resolve the solubility issues encountered with compound **37**.

4.2.3 Adapted molecular design - dye D1A2

In view of the negative results discussed above, the original design of the dye was revised, leading to the development of compound **D1A2** (Figure 4.5).

As can be seen, we decided to reduce the molecular complexity by avoiding the inclusion of the triazole bridge, with the aim to decrease the length of the system and improve solubility. Differently from dye **D1A1**, in **D1A2** the pyridine unit is directly attached to the donor portion through a simple alkyl bridge. In addition, we also envisioned that solubility could be enhanced by introducing long alkyl chains on the phenyl groups in position 2,3 of the central quinoxaline core, helping to avoid the formation of aggregates. In this regard, we reasoned that one of the easiest ways to attach such substituents to the aromatic rings would be through the use of alkynyl bridges, since the required carbon-carbon bonds could then be simply formed by Sonogashira-type or related cross- coupling reactions. The presence of long alkyl chains in those positions could also prove beneficial after dye adsorption on TiO_2, preventing aggregation phenomena and thus the occurrence of intermolecular charge transfer processes upon light absorption by the sensitizer.

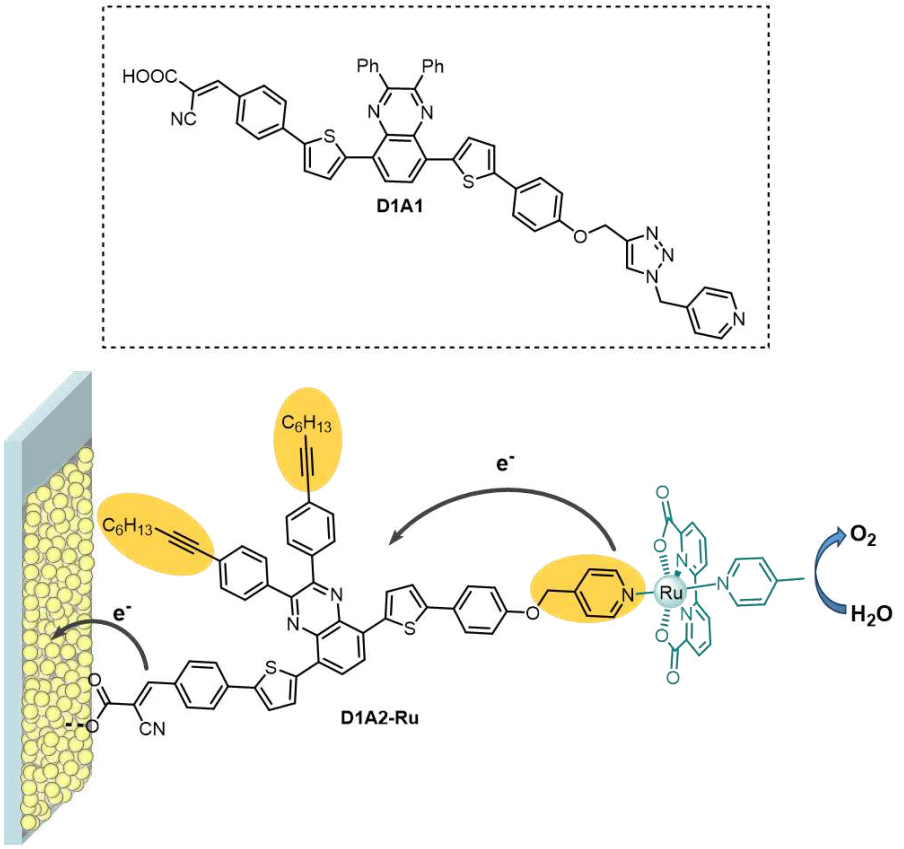

*Figure 4.5 Structure of dye **D1A1** (top); Designed structure of adapted dye-catalyst dyad **DIA2-Ru.***

Once again we started our path for obtaining the desired catalytic dyad by attempting the synthesis of dye **D1A2**. The retrosynthetic analysis and the following synthetic approach are described in detail in the next paragraphs.

4.2.3.1 Retrosynthetic analysis

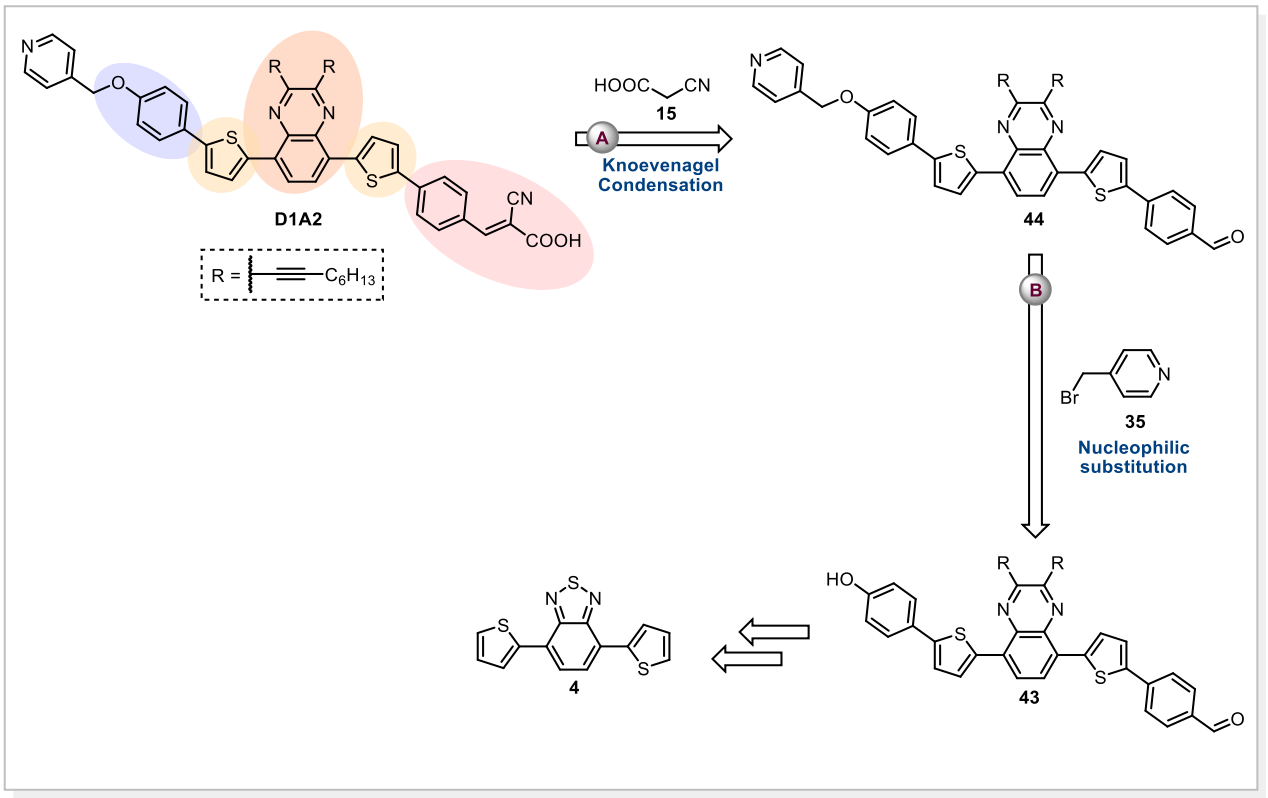

*Scheme 4.4 Retrosynthetic approach for the synthesis of compounds **D1A2**. Colors represent the different building blocks: donor (purple), π-bridge (yellow), auxiliary acceptor (orange), acceptor (pink).*

As can be seen from Scheme 4.4, the retrosynthetic pathway resembles that seen for dye **D1A1** with the main difference that after the removal of cyanoacetic acid (**15**) to leave aldehyde **44** (disconnection ***A***), the following step involves the disconnection (***B***) of a C-O bond to leave the pyridine fragment **35** and intermediate **43**, having a free hydroxyl group.

From this stage the pathway follows that discussed previously leading to the starting material compound **4**.

4.2.3.2 Synthetic pathway to dye D1A2 and molecular dyad Ru-D1A2

The synthetic strategy followed for the preparation of dye **D1A2** is shown in Scheme 4.5.

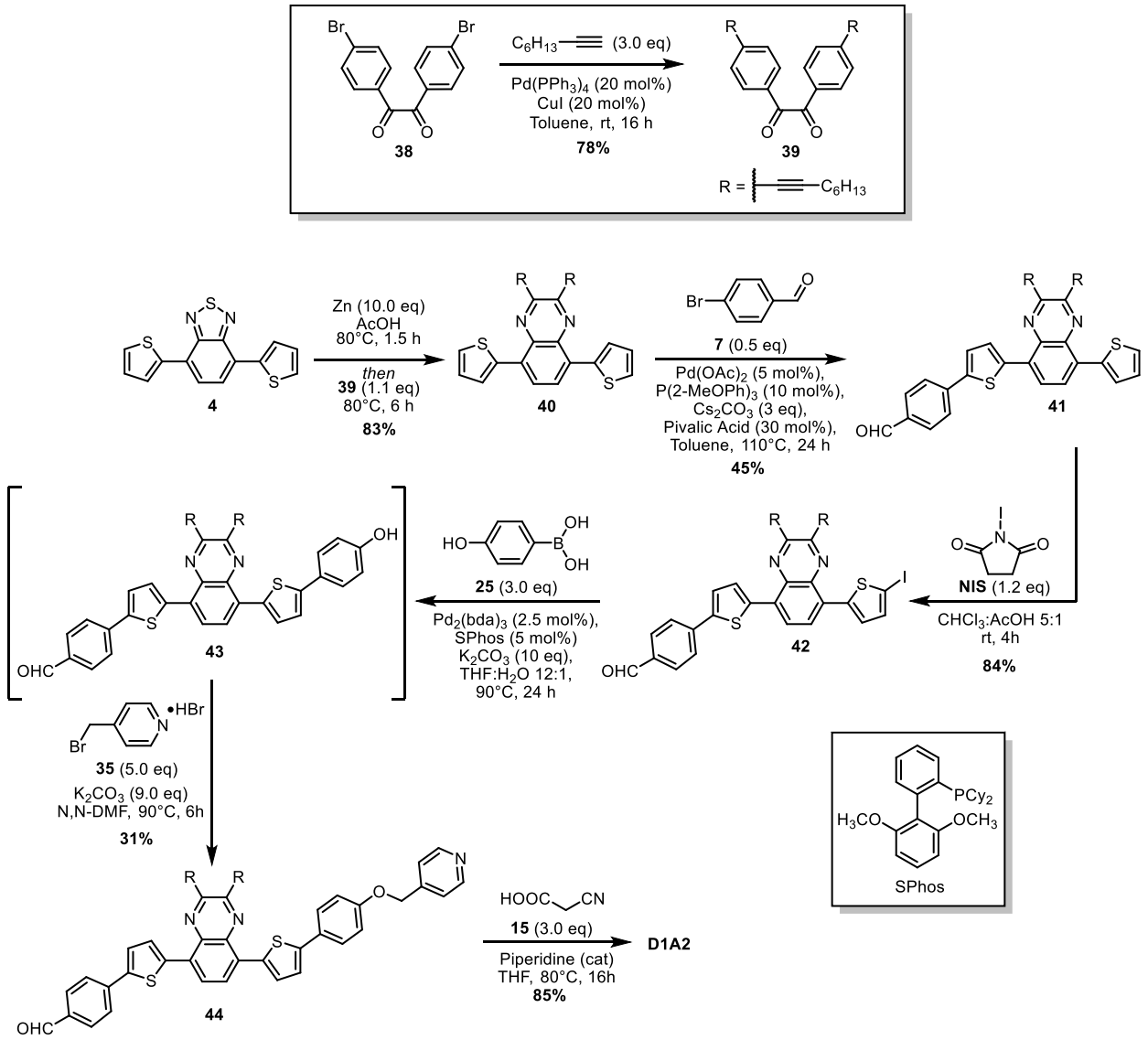

*Scheme 4.5 Synthetic route for the synthesis of dye **D1A2.***

First, we focused on the preparation of diketone **39**, essential for the incorporation of the two alkynyl chains on the quinoxaline core, starting from the commercially available 4-4'-dibromo-benzil **38.** By subjecting the latter compound to a Sonogashira reaction with 1-octyne in the presence of $Pd(PPh_3)_4$, CuI as catalysts and NEt_3 as base, at room temperature for 16 h, compound **39** could be obtained with a good yield of 78% on gram scale. It is important to highlight that when this reaction was attempted with a lower catalyst loading (10 mol%), a significantly lower yield of only 22% was obtained.

With the desired diketone in hand, we moved forward and performed the transformation of the benzothiadiazole ring of compound **4** into the quinoxaline system by means of the standard two-

step procedure already described in chapter 3 (paragraph 3.4.2), consisting of a reduction of the starting material with elemental zinc, followed by trapping of the resulting diamine with diketone **39**. Unlike what was seen for dye **1a**, here the telescopic reduction-condensation reactions were both performed in acetic acid. This procedure eliminated the need for a complicated work-up step typically associated with the reduction reaction. Often, this step involves the precipitation of large quantities of zinc salts, which are challenging to separate from the solution due to the formation of a complex emulsion during the extraction phase. Instead, in this case the excess zinc was removed by simple filtration from the reaction mixture, and then diketone **39** was directly added to the same solution, simplifying the overall process. Under these conditions, intermediate **40** could be obtained with a good yield of 83%. The insertion of the benzaldehyde acceptor portion was achieved through a direct arylation reaction performed under the best conditions found for reference dye **1a** (see chapter 3, paragraph 3.4.2, table 3.2). By reacting intermediate **40** with benzaldehyde **7** in the presence of $Pd(OAc)_2$ (5 mol%), $P(2\text{-}MeOPh)_3$ (10 mol%), Cs_2CO_3 (3.0 eq.) and pivalic acid (30 mol%) in toluene at 110°C for 24 h, the desired product **41** could be obtained in 45% yield. The reaction was conducted with an excess of intermediate **40** to avoid the formation of the undesired *bis*-arylation product. Importantly, most of the unreacted compound **40** (ca. 43%) could be recovered after product purification by flash column chromatography.

The following iodination of the resulting intermediate **41** was performed by reaction with *N*-iodosuccinimide (NIS) in a mixture of $CHCl_3$:AcOH 5:1. Purification by flash column chromatography gave the desired clean product **42** with a good yield of 84%. At this stage, the insertion of the 4-hydroxyphenyl donor unit was conducted by subjecting iodide **42** to a Suzuki-Miyaura reaction with boronic acid **25** under the following conditions: $Pd_2(dba)_3$ (2.5 mol%), S-Phos (5 mol%), K_2CO_3 (10 eq) in a mixture of THF:H_2O 12:1 at 80°C for 16 h. Despite several efforts of purification *via* flash column chromatography, we were not able to isolate the desired clean product **43**, mostly due to its low solubility in common chromatographic solvents. Therefore, we decided to directly use the crude reaction mixture and attempt the following nucleophilic substitution reaction with 4-(bromomethyl)pyridine hydrobromide (**35**). This was accomplished by mixing the reagents in *N,N*-DMF, heating at 90°C and stirring for 6 h. Thanks to the introduction of the pyridine moiety, the solubility of compound **44** was slightly improved compared to previous intermediate **43,** allowing its isolation in pure form by flash column chromatography with a moderate yield of 31 % over 2 steps. It is important to highlight that the tested reaction conditions for the conversion of compound **41** to **44**, via intermediate **43**, were not fully optimized. We anticipate that especially the yield of the Suzuki-Miyaura step could be significantly improved by testing different catalyst and/or Pd-ligands, as well as different reaction times and temperatures.

As a final step of our synthesis, a Knoevenagel condensation of intermediate **44** with cyanoacetic acid (**15**) in the presence of piperidine afforded dye **D1A2** with a good yield of 85%. The compound was purified by precipitation, and its composition and purity were confirmed by ^{1}H-NMR, ^{13}C-NMR and high-resolution mass spectrometry experiments.

With dye **D1A2** in hand, we finally attempted the formation of the molecular dyad by reacting it with ruthenium complex **[Ru(bda)(pic)(dmso)]**, presenting a labile DMSO ligand, as shown in Scheme 4.3. The complex was synthetized following a previously reported procedure,[13] by reacting **[Ru(bda)(dmso)$_2$]** (see chapter 3, paragraph 3.4.4.1) with 4-picoline, in MeOH at 80°C for 16 h. Under these conditions, **[Ru(bda)(pic)(dmso)]** was obtained with a moderate yield of 24%.

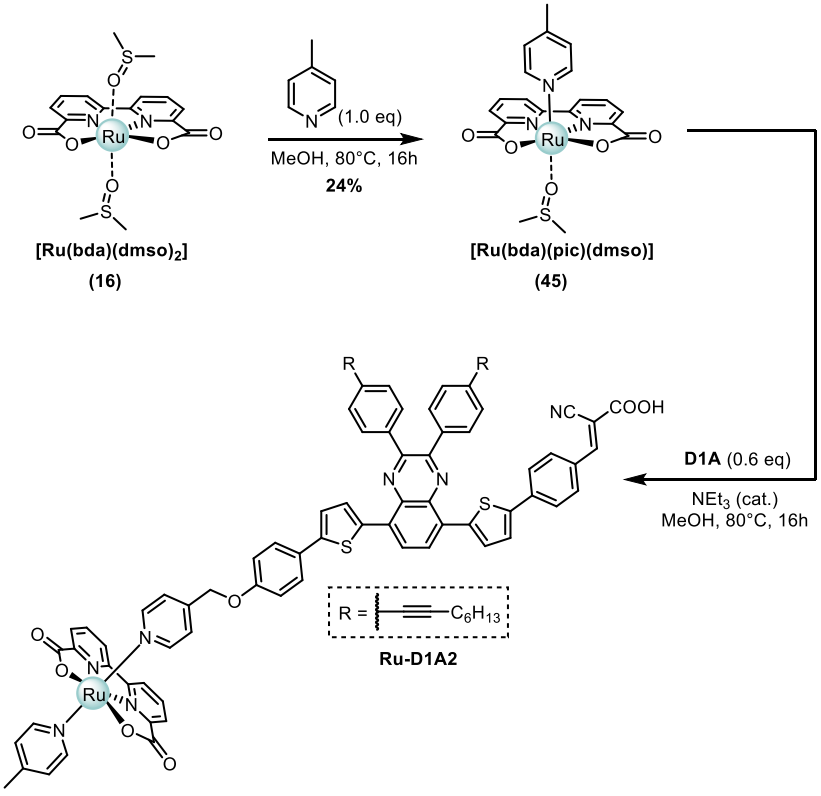

*Scheme 4.3 Synthesis of the dye-catalyst **Ru-D1A2** dyad.*

Reaction of the obtained **[Ru(bda)(pic)(dmso)]** complex with dye **D1A2** in MeOH under reflux in the presence of catalytic amounts of triethylamine afforded the dye-catalyst assembly **Ru-D1A2**. Unfortunately, due to its low solubility and partial oxidation under air, with consequent formation of less soluble paramagnetic Ru^{III} species, dyad **Ru-D1A2** could not be characterized by NMR spectroscopy. However, accurate mass spectrometry and spectroscopic characterization (see below) allowed us to confirm the formation of the desired product.

4.2.3.3 Spectroscopic and electrochemical characterization

Both synthetized dye **D1A2** and dye-catalyst assembly **Ru-D1A2** were fully characterized in dichloromethane solution. The main spectroscopic features are listed in Table 4.2.

We started our investigation by comparing the spectro-electrochemical properties of dye **D1A2** with those of reference dye **1a** (Figure 4.6) (see chapter 3, paragraph 3.4.3.1).

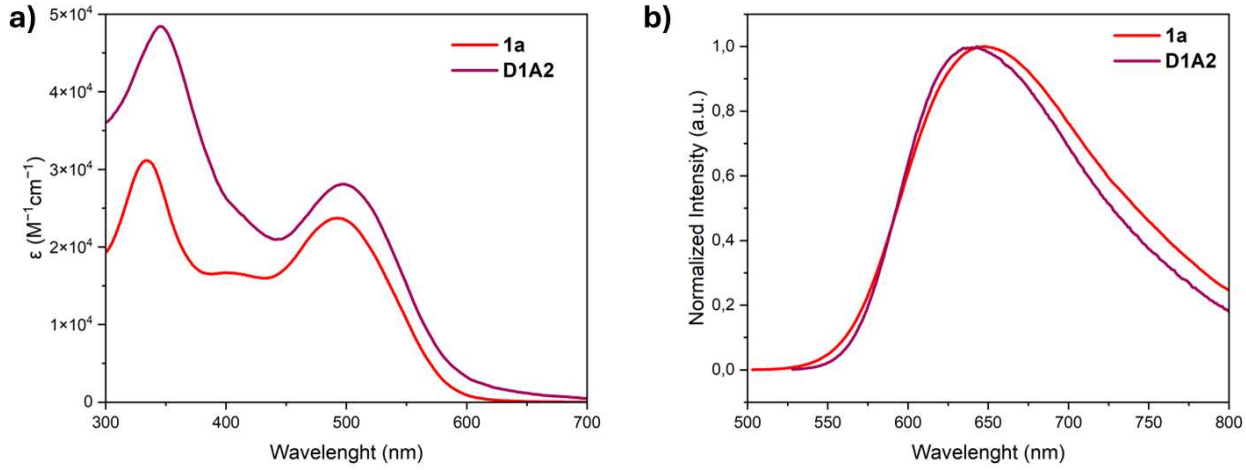

*Figure 4.6 a) UV-vis absorption spectra of dye **1a** and dye **D1A2** in DCM solution; b) Normalized emission spectra of dye **1a** and dye **D1A2** in DCM solution.*

As can be seen from the overlapped absorption spectra reported in Figure 4.6a, the optical response of dye **D1A2** is comparable to that of the reference dye **1a**, highlighting that the structural modifications made to adapt the molecular structure did not significantly alter its key spectroscopic characteristics. The absorption spectrum of dye **D1A2** shows an intense band at 497 nm (ε = 2.80 × 10^4 M^{-1} cm^{-1}), matching the region of highest irradiance of the solar spectrum, and a tailing absorption up to 630 nm. The second band at 347 nm, attributed to local π-π* absorption, exhibits a molar attenuation coefficient higher than that of dye **1a** in the same range (ε = 4.84 × 10^4 $M^{-1}cm^{-1}$ compared to 3.14 × 10^4 M^{-1} cm^{-1}), likely due to the additional presence of the alkynyl chains on the quinoxaline core. Upon photoexcitation at 497 nm, the emission spectrum of dye **D1A2** shows a broad band centered at 643 nm, consistent with that of dye **1a** (Figure 4.6b). From the intersection of the normalized absorption and emission spectra, the corresponding $E_{0\text{-}0}$ could be determined, yielding a value of 2.18 eV.

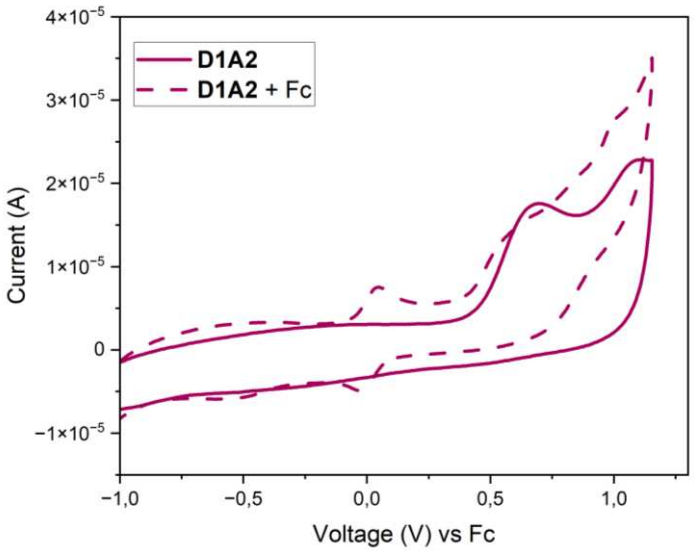

*Figure 4.7 Cyclic voltammetry plots of dye **D1A2** in DCM solution, both without and with ferrocene as an internal standard.*

*Table 4.2 Main spectroscopic and electrochemical properties of dyes **1a** and **D1A2**, and dyad **Ru-D1A2** in DCM solution.*

Dye	λ_{max}^{abs} (nm)	$\varepsilon \times 10^4$ (M^{-1} cm^{-1})	λ_{max}^{emi} (nm)	$E_{0\text{-}0}$ (eV)[a]	E_{ox} (V) *vs.* Fc^+/Fc	E_{ox} (V) *vs.* NHE[b]	E^*_{ox} (V) *vs.* NHE[c]
1a	492 334	2.39 3.14	647	2.17	+0.47	+1.19	−0.98
D1A2	497 347	2.80 4.84	643	2.18	+0.54	+1.26	−0.92
Ru-D1A2	505 349 302	2.87 5.13 5.34	653	2.14	+0.04 +0.46	+0.76 +1.18	−0.96

[a] Estimated based on the intersection of the normalized absorption and emission spectra; [b] Calculated by adding +0.72 V to the potential measured *vs.* Fc^+/Fc[14]; [c] Calculated from the E_{ox} and $E_{0\text{-}0}$ values according to the formula: $E^*_{ox} = E_{ox} - (E_{0\text{-}0}/e)$

The characterization in solution continued by measuring the ground-state oxidation potential of **D1A2** by means of cyclic voltammetry experiments, using 0.1 M $TBAPF_6$ in DCM as the supporting electrolyte and the ferrocenium/ferrocene redox couple as an internal standard. As can be seen from Figure 4.7, dye **D1A2** shows an irreversible oxidation wave with a potential of +1.26 V *vs.* NHE (calculated at the half-peak potentials $E^{(p/2)}$)[7]. The excited state oxidation potential of the dye was then assessed by subtracting the previously determined $E_{0\text{-}0}$ value from the E_{ox} resulting from cyclic voltammetry, yielding a value of −0.92 V vs. NHE.

Regarding the characterization of the catalytic assembly **Ru-D1A2**, due to the break in conjugation between the dye and the catalyst, caused by the alkyl-bridge, only a marginal change in the **D1A2** absorption spectrum is observed upon complexation with the Ru center (Figure 4.8a). Interestingly, however, besides the two main absorption bands at 349 and 504 nm, attributable to dye **D1A2**, the dyad also features an additional strong absorption band at 301 nm, which, as demonstrated in several reports in literature, is characteristic of Ru(bda)-complexes.[7] Upon photoexcitation at 504 nm, the emission spectrum of dyad **Ru-D1A2** shows a broad band centered at 653 nm, consistent with that of dye **D1A2** (Figure 4.8b).

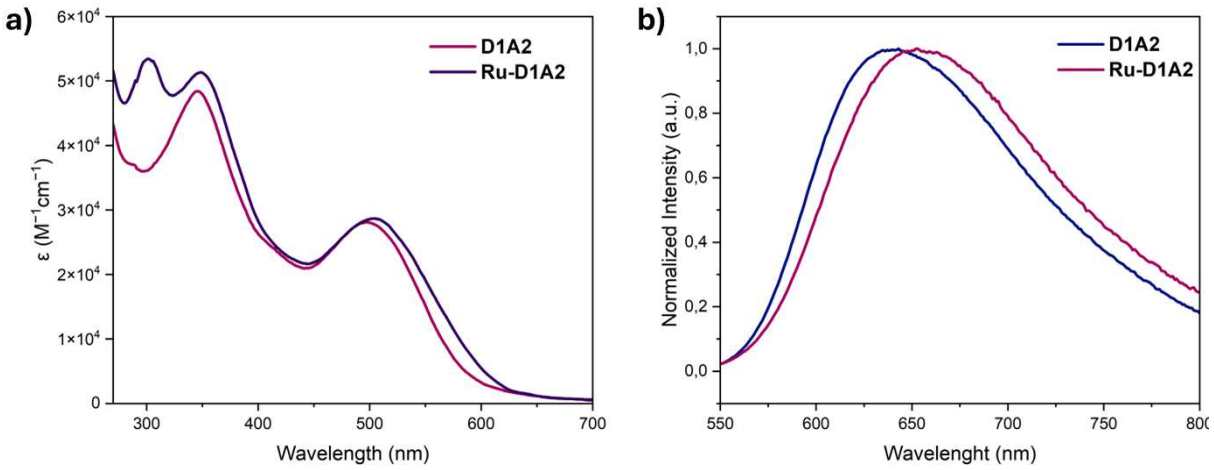

*Figure 4.8 a) UV-vis absorption spectra of dye **D1A2** and dyad **Ru-D1A2** in DCM solution; b) Normalized emission spectra of dye **D1A2** and dyad **Ru-D1A2** in DCM solution.*

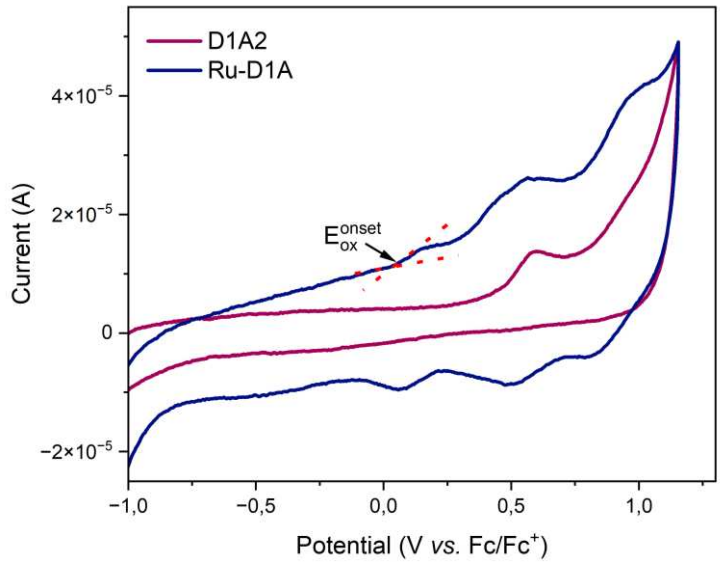

*Figure 4.9 Cyclic voltammetry plots of dye **D1A2** and dyad **Ru-D1A2** in DCM solution.*

The formation of a complex between dye **D1A2** and the Ru-based catalyst was further confirmed by means of cyclic voltammetry experiments using 0.1 M $TBAPF_6$ in DCM as the supporting

electrolyte. As can be seen from the overlapped traces shown in Figure 4.9, besides the oxidation wave at ca. +1.18 V *vs.* NHE, attributed to the **D1A2** unit, **Ru-D1A2** features a reversible oxidation with an E_{ox}^{onset} potential calculated at ca. +0.76 V *vs.* NHE that can be assigned to the Ru^{III}/Ru^{II} couple.[15]

Further confirmation of the formation of the desired molecular assembly was obtained by high-resolution mass spectrometry. Indeed, the recorded spectrum shows a peak at *m/z*=1454.3812 in agreement with that calculated $[M+H]^+$ fragment at *m/z*=1454.3822

4.3 Conclusions

In conclusion, in this part of work we focused our attention on the design, synthesis, and characterization of an organic dye-ruthenium catalyst dyad, consisting of a quinoxaline-based dye connected to a [Ru(bda)]-type complex, for application in PA-DS-PECs for water splitting.

After the unsuccessful synthesis of the designed D-A-π-A sensitizer **D1A1** due to serious solubility problems, we designed an adapted chromophore **D1A2** with the aim to address the encountered issues.

With our delight, **D1A2** was successfully synthesized and fully characterized from a spectroscopic and electrochemical point of view. The synthesis was based on a desymmetrisation via direct arylation of the quinoxaline-thiophene central core **41** with bromobenzaldehyde, followed by a telescopic Suzuki cross-coupling/nucleophilic substitution reaction sequence to insert the hydroxyphenyl donor moiety and link it with the alkyl-pyridine coordination unit, respectively.

Dye **D1A2** showed a λ_{max}^{abs} well-centered in the visible region (497 nm) with a good ε value (2.80×10^4 M^{-1} cm^{-1}) and λ_{max}^{emi}at 643 nm. E_{ox} was calculated to be at around +1.26 V vs. NHE, a value more positive than the catalytic onset potential of the chosen Ru(bda)-WOC, suggesting an effective regeneration of the dye in the device. At the same time, $E_{ox}^{*}$was calculated to be at −0.92 V vs. NHE, which is more negative than the conduction band of TiO_2 (approx. −0.57 V vs. NHE)[16], suggesting that electron injection from the excited state of the dye to the semiconductor CB would be feasible for **D1A2**.

After evaluating the spectroscopic properties of dye **D1A2**, we attempted complexation of the dye to the **[Ru(bda)(pic)(dmso)]** moiety by simple reaction in methanol of the two reaction partners. Despite issues of low solubility and partial oxidation under air, with consequent formation of paramagnetic species that prevented characterization by NMR spectroscopy, the successful formation of the desired catalytic dyad could be confirmed by spectro-electrochemical characterization in

solution. First, UV-Vis absorption spectra showed a clear additional band center at 302 nm, assigned to the Ru-bda complex.[7] Furthermore, CV traces recorded in DCM highlighted the presence of an additional oxidation wave in the +0.6-0.7 V (*vs.* NHE) region, compatible with that reported in literature for the Ru^{III}/Ru^{II} couple.

Driven by this exciting results, further spectroscopic and electrochemical characterization, as well as experiments in DS-PEC system, are currently ongoing for compound **Ru-D1A2**.

4.4 Synthetic Procedures

For general synthetic remarks see chapter 3, paragraph 3.7.1

4-(5-(8-(5-Bromothiophen-2-yl)-2,3-diphenylquinoxalin-5-yl)thiophen-2-yl)benzaldehyde (31a)

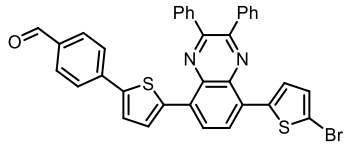

Compound **8** (50 mg, 0.091 mmol, 1.0 eq.) was dissolved in a mixture of CH_3Cl/AcOH 5:1 (6 mL). Then *N*-bromosuccinimide (18 mg, 0.100 mmol, 1.2 eq.) was added at room temperature, and the resulting solution was stirred for 4h. Then, water was added, and the mixture was extracted with DCM (3 × 10 mL). The organic phases were combined and dried over anhydrous Na_2SO_4, filtered and the solvent evaporated under reduced pressure. The crude product was purified by flash column chromatography (SiO_2, gradient from petroleum ether/DCM 90:10 to petroleum ether/DCM 70:30) to afford compound **31a** (56 mg, 0.089 mmol, 97% yield) as an orange solid.

^{1}H NMR (400 MHz, $CDCl_3$) δ 10.01 (s, 1H), 8.11 (d, J =8.1 Hz, 2H), 7.91 (d, J = 8.2 Hz, 2H), 7.86 (d, J = 4.0 Hz, 1H), 7.81 (d, J = 8.2 Hz, 2H), 7.77 – 7.70 (m, 4H), 7.58 (d, J = 4.0 Hz, 1H), 7.51 (d, J = 4.0 Hz, 1H), 7.46 – 7.38 (m, 6H), 7.12 (d, J = 4.0 Hz, 1H). ^{13}C NMR (100 MHz, $CDCl_3$) δ 191.6, 152.2, 145.4, 140.6, 140.2, 139.7, 138.6, 138.3, 137.2, 136.9, 135.1, 131.1, 130.9, 130.70, 130.66, 130.6, 129.4, 129.3, 128.5, 128.4, 127.8, 126.8, 125.8, 124.9, 117.5. *Note: not all carbon signals are visible in the ^{13}C-NMR spectrum due to fortuitous overlaps of aromatic peaks.*

MS (ESI) *m/z*: $[M+H]^+$ calcd for $C_{35}H_{22}BrN_2OS_2$ 630.6.; found: 630.1.

4-(5-(8-(5-Iodothiophen-2-yl)-2,3-diphenylquinoxalin-5-yl)thiophen-2-yl)benzaldehyde (31b)

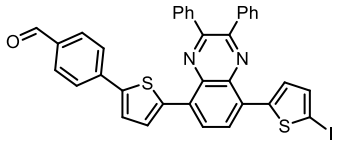

Compound **8** (90 mg, 0.163 mmol, 1.0 eq.) was dissolved in a mixture of CH_3Cl/AcOH 5:1 (6 mL). Then *N*-iodosuccinimide (41 mg, 0.180 mmol, 1.2 eq.) was added at room temperature, and the resulting solution was stirred for 4h. Then, water was added, and the mixture was extracted with DCM (3 × 10 mL). The organic phases were combined and dried over anhydrous Na_2SO_4, filtered and the solvent evaporated under reduced pressure. The crude product was purified by flash column chromatography (SiO_2, gradient from petroleum ether/DCM 90:10 to petroleum ether/DCM 70:30) to afford compound **31b** (104 mg, 0.154 mmol, 94% yield) as an orange solid. ^{1}H-NMR (400 MHz, $CDCl_3$) δ 9.96 (s, 1H), 8.14 – 8.04 (m, 2H), 7.96 – 7.89 (m, 2H), 7.85 – 7.77 (m, 8H), 7.73 (d, *J* = 4.3 Hz, 1H), 7.55 (d, *J* = 4.3 Hz, 1H), 7.49 – 7.41 (m, 5H), 7.34 – 7.29 (m, 1H). ^{13}C-NMR (100 MHz, $CDCl_3$) *δ* 191.9, 148.9, 148.9, 144.9, 144.8, 142.2, 142.0, 141.7, 138.78, 138.76, 138.3, 138.2, 136.5, 131.6, 129.9, 129.84, 129.81, 129.3, 129.24, 129.22, 129.14, 129.12, 127.74, 127.71, 127.2, 127.1, 126.8, 126.0, 75.3. MS (ESI) *m/z*: $[M+H]^+$ calcd for $C_{35}H_{22}IN_2OS_2$ 677.6.; found: 677.3.

4-(5-(8-(5-(4-Hydroxyphenyl)thiophen-2-yl)-2,3-diphenylquinoxalin-5-yl)thiophen-2-yl)benzaldehyde (32)

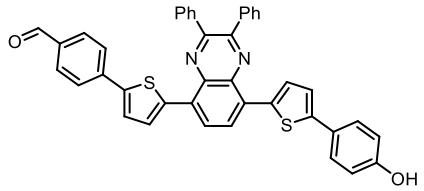

Compound **31b** (104 mg, 0.154 mmol, 1.0 eq.) and $Pd_2(dba)_3$ (4 mg, 0.024 mmol, 2.5 mol%), SPhos (3 mg, 0.008 mmol, 5 mol%) and 4-hydroxyphenyl boronic acid (**25**, 64 mg, 0.461 mmol, 3.0 eq.) were added to a Schlenk tube and put under inert atmosphere by performing three vacuum-nitrogen cycles. The solids were then dissolved in dry THF (10 mL) and K_2CO_3 (212 mg, 1.54 mmol, 10.0 eq.), previously solubilized in H_2O (5 mL), was subsequently added. The reaction mixture was then vigorously stirred under reflux for 16 h. The solution was cooled to room temperature, diluted with DCM (20 mL) and washed with water (2 × 20 mL) and brine (20 mL). The organic phase was dried over Na_2SO_4, filtered, and the solvent evaporated under reduced pressure. The crude product was purified by flash column chromatography (SiO_2, gradient from petroleum

ether/EA 80:20 to petroleum ether/EA 50:50) to afford compound **32** (90 mg, 0.140 mmol, 91% yield) as red solid.

^{1}H-NMR (400 MHz, THF-*d8*) δ 9.98 (s, 1H), 8.48 (s, 1H), 8.35 – 8.25 (m, 2H), 8.02 (d, *J* = 3.9 Hz, 1H), 7.97 (d, *J* = 3.9 Hz, 1H), 7.94 – 7.90 (m, 4H), 7.87 – 7.80 (m, 4H), 7.66 (d, *J* = 3.9 Hz, 1H), 7.61 – 7.53 (m, 2H), 7.48 – 7.37 (m, 6H), 7.29 (d, *J* = 3.8 Hz, 1H), 6.80 (d, *J* = 8.4 Hz, 2H). ^{13}C NMR (100 MHz, THF-*d8*) δ 191.3, 158.9, 152.83, 152.78, 149.2, 146.2, 141.3, 141.1, 140.0, 138.2, 137.3, 136.7, 133.0, 131.7, 131.1, 130.1, 130.0, 129.12, 129.09, 129.0, 128.5, 127.8, 127.6, 127.3, 127.1, 126.4, 125.8, 122.3, 116.8. *Note: not all carbon signals are visible in the ^{13}C-NMR spectrum due to fortuitous overlaps of aromatic peaks.* MS (ESI) *m/z*: $[M+H]^+$ calcd for $C_{41}H_{27}N_2O_2S_2$ 643.8; found: 643.2.

4-(5-(2,3-Diphenyl-8-(5-(4-(prop-2-yn-1-yloxy)phenyl)thiophen-2-yl)quinoxalin-5-yl)thiophen-2-yl)benzaldehyde (34)

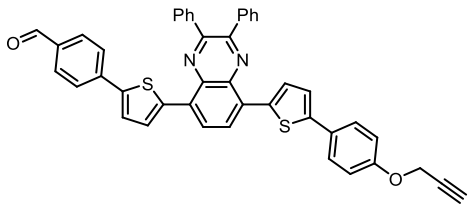

Compound **32 (**90 mg, 0.140 mmol, 1.0 eq) and K_2CO_3 (174 mg, 1.26 mmol, 9.0 eq.) were dissolved in *N,N*-DMF (6 mL). Propargyl bromide (**33**, 83 mg, 0.70 mmol, 5.0 eq.) was then added and the reaction mixture was vigorously stirred at 90°C for 6 h. The solution was cooled to room temperature, diluted with DCM (15 mL) and washed with water (2 × 20 mL) and brine (20 mL). The organic phase was dried over Na_2SO_4, filtered, and the solvent evaporated under reduced pressure. The crude product was purified by flash column chromatography (SiO_2, gradient from petroleum ether/DCM 80:20 to petroleum ether/DCM 40:60) to afford compound **34** (45 mg, 0.047 mmol, 31% yield) as a red solid. ^{1}H-NMR (400 MHz, THF-*d8*) *δ* 9.96 (s, 1H), 8.30 – 8.22 (m, 2H), 7.97 (d, *J* = 4.0 Hz, 1H), 7.94 (d, *J* = 4.0 Hz, 1H), 7.91 – 7.88 (m, 4H), 7.82 – 7.78 (m, 4H), 7.67 – 7.61 (m, 3H), 7.46 – 7.37 (m, 6H), 7.34 (d, *J* = 3.9 Hz, 1H), 7.03 (d, *J* = 8.7 Hz, 2H), 4.77 (d, *J* = 2.3 Hz, 2H), 3.02 (t, *J* = 2.4 Hz, 1H). ^{13}C NMR (100 MHz, THF-*d8*) *δ* 191.3, 158.8, 152.9, 152.8, 148.4, 146.3, 141.3, 141.0, 139.9, 138.1, 137.9, 136.7, 132.8, 131.7, 131.3, 131.1, 130.1, 130.0, 129.3, 129.13, 129.10, 128.8, 128.5, 127.6, 127.1, 126.4, 125.8, 122.9, 116.3, 79.8, 77.0, 56.6. *Note: not all carbon signals are visible in the ^{13}C-NMR spectrum due to fortuitous overlaps of aromatic peaks.* MS (ESI) *m/z*: $[M+H]^+$ calcd for $C_{44}H_{29}N_2O_2S_2$ 681.8; found: 681.5.

1,2-*Bis*(4-(oct-1-yn-1-yl)phenyl)ethane-1,2-dione (39)

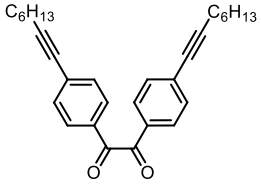

4,4'-Dibromobenzil (**38**, 1.00 g, 2.72 mmol, 1.0 eq.), $Pd(PPh_3)_4$ (0.628 g, 0.54 mmol, 20 mol%) and CuI (0.104 g, 0.54 mmol, 20 mol%), were added to a Schlenk tube and put under inert atmosphere by performing three vacuum-nitrogen cycles. The solids were then dissolved in a mixture of toluene and triethylamine 2/1 v/v (45 mL) and the solution was degassed by bubbling N_2 for 15 min. Then, 1-octyne (0.898 g, 8.15 mmol, 3.0 eq.) was added via syringe. After stirring at room temperature for 24 h, water was added, and the mixture was extracted with DCM (3 × 25 mL). The organic phases were combined and dried over anhydrous Na_2SO_4, filtered and the solvent evaporated under reduced pressure. The crude product was purified by flash column chromatography (SiO_2, gradient from petroleum ether to petroleum ether/EA 95:5) to afford compound **39** (0.901 g, 2.11 mmol, 78% yield) as a light yellow solid. ^{1}H-NMR (400 MHz, $CDCl_3$) δ 7.66 (d, J = 8.5 Hz, 4H), 7.27 (d, J = 8.4 Hz, 4H), 2.21 (t, J = 7.1 Hz, 4H), 1.54 – 1.29 (m, 4H), 1.29 – 1.15 (m, 4H), 1.13 – 1.05 (m, 8H), 0.73 – 0.62 (m, 6H). ^{13}C-NMR (100 MHz, $CDCl_3$) δ 193.6, 132.1, 131.5, 131.3, 129.8, 96.3, 80.2, 31.4, 28.7, 28.6, 22.7, 19.7, 14.2. MS (ESI) *m/z*: $[M+H]^+$ calcd for $C_{30}H_{35}0_2$ 427.3; found: 427.5.

2,3-*Bis*(4-(oct-1-yn-1-yl)phenyl)-5,8-di(thiophen-2-yl)quinoxaline (40)

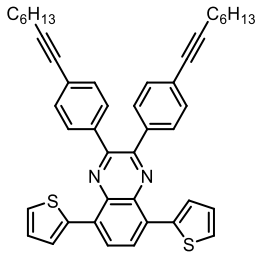

In a round bottom flask, 4,7-di(thiophen-2-yl)benzo[c][1,2,5]thiadiazole (**4,** 300 mg, 1.0 mmol, 1.0 eq.) and zinc powder (653 mg, 9.99 mmol, 10 eq.) were suspended in glacial acetic acid (10 mL). The reaction mixture was vigorously stirred at 80°C for 1.5 h to obtain a complete conversion of the starting material as assessed by TLC (eluent: petroleum ether/DCM 4:1 v/v). The mixture was then cooled to room temperature and filtered to remove the excess of unreacted Zn. Without any further purification, diketone **39** (469 mg, 1.10 mmol, 1.1 eq.) was added to the reaction mixture, which was then vigorously stirred at 80°C for 6 h. After cooling down to room temperature, the mixture was poured in water and extracted with diethyl ether (3 × 30 mL). The organic phases

were combined and dried over anhydrous Na_2SO_4, filtered and the solvent evaporated under reduced pressure. The crude product was purified by flash column chromatography (SiO_2, gradient from petroleum ether/DCM 90:10 to petroleum ether/ DCM 70:30) to afford compound **40** (547 mg, 0.83 mmol, 83% yield) as an orange solid. ^{1}H-NMR (400 MHz, $CDCl_3$) δ 8.14 (s, 2H), 7.85 (d, J = 3.8 Hz, 2H), 7.66 (d, J = 7.8 Hz, 4H), 7.52 (d, J = 5.1 Hz, 2H), 7.41 (d, J = 8.4 Hz, 4H), 7.22 – 7.14 (m, 2H), 2.43 (t, J = 7.0 Hz, 4H), 1.67 – 1.54 (m, 4H), 1.53 – 1.43 (m, 4H), 1.40 – 1.27 (m, 8H), 0.92 (t, J = 6.8 Hz, 6H).^{13}C-NMR (100 MHz, $CDCl_3$) δ 151.0, 138.6, 137.4, 137.1, 131.5, 131.2, 130.3, 129.0, 127.2, 126.6, 126.4, 124.9, 92.5, 80.3, 31.4, 28.7, 28.6, 22.6, 19.5, 14.1. MS (ESI) *m/z*: $[M+H]^+$ calcd for $C_{44}H_{43}N_2S_2$ 664.0; found: 664.2.

4-(5-(2,3-*Bis*(4-(oct-1-yn-1-yl)phenyl)-8-(thiophen-2-yl)quinoxalin-5-yl)thiophen-2-yl)benzaldehyde (41)

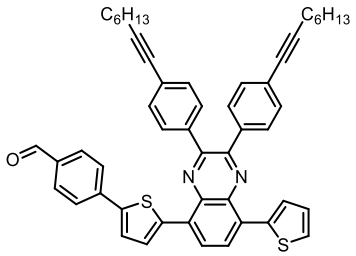

Compound **40** (547 mg, 0.82 mmol, 2.0 eq.), 4-bromobenzaldehyde (**7**, 76 mg, 0.41 mmol, 1.0 eq.), Cs_2CO_3 (404 mg, 1.24 mmol, 3.0 eq.), $Pd(OAc)_2$ (5 mg, 0.021 mmol, 5 mol%), P(2-MeOPh)$_3$ (15 mg, 0.041 mmol, 10 mol%) and pivalic acid (13 mg, 0.124 mmol, 30 mol%) were added to a Schlenk tube and put under inert atmosphere by performing three vacuum-nitrogen cycles. The solids were then dissolved in dry toluene (16 mL) and the reaction mixture was vigorously stirred at 110°C for 24 h. The solution was cooled to room temperature, diluted with DCM (20 mL), filtered over a pad of Celite®, and washed with water (2 × 30 mL) and brine (30 mL). The organic phase was dried over Na_2SO_4, filtered, and the solvent evaporated under reduced pressure. The crude product was purified by flash column chromatography (SiO_2, gradient from petroleum ether/ DCM 80:20 to petroleum ether/DCM 50:50) to afford compound **41** (141 mg, 0.184 mmol, 45% yield) as an orange solid. ^{1}H-NMR (400 MHz, $CDCl_3$) δ 10.02 (s, 1H), 8.14-11 (m, 2H), 7.92 (d, J = 8.3 Hz, 2H), 7.89 – 7.77 (m, 4H), 7.72 – 7.59 (m, 4H), 7.56 – 7.49 (m, 2H), 7.47 – 7.37 (m, 4H), 7.22 – 7.16 (m, 1H), 2.46-2.42 (m, 4H), 1.71 – 1.57 (m, 4H), 1.55 – 1.42 (m, 4H), 1.40 – 1.32 (m, 8H), 0.96 – 0.88 (m, 6H). ^{13}C-NMR (100 MHz, $CDCl_3$) δ 191.7, 151.4, 151.2, 145.3, 140.6, 140.2, 138.6, 137.5, 137.3, 137.2, 135.1, 131.9, 131.7, 131.6, 130.7, 130.6, 130.4, 129.4, 127.6, 127.2, 126.9, 126.8, 126.8, 125.8, 125.3, 125.2, 124.9, 92.9, 92.7, 80.5, 80.4, 31.5, 28.9, 28.8, 22.7,

19.7, 14.3. *Note: not all carbon signals are visible in the ^{13}C-NMR spectrum due to fortuitous overlaps of several peaks.* MS (ESI) *m/z*: $[M+H]^+$ calcd for $C_{51}H_{47}N_2OS_2$ 768.1; found: 768.4.

4-(5-(8-(5-Iodothiophen-2-yl)-2,3-*bis*(4-(oct-1-yn-1-yl)phenyl)quinoxalin-5-yl)thiophen-2-yl)benzaldehyde (42)

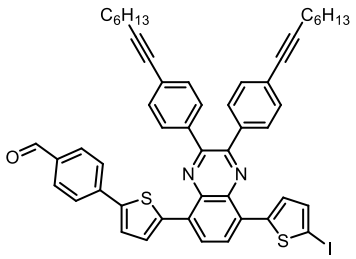

Compound **41** (141 mg, 0.18 mmol, 1.0 eq.) was dissolved in a mixture of CH_3Cl/AcOH 5:1 (6 mL). Then *N*-iodosuccinimide (49 mg, 0.22 mmol, 1.2 eq.) was added at room temperature, and the resulting solution was stirred for 4h. Then, water was added, and the mixture was extracted with DCM (3 × 10 mL). The organic phases were combined and dried over anhydrous Na_2SO_4, filtered and the solvent evaporated under reduced pressure. The crude product was purified by flash column chromatography (SiO_2, gradient from petroleum ether/DCM 85:15 to petroleum ether/ DCM 70:30) to afford compound **42** (138 mg, 0.16 mmol, 84% yield) as an orange solid. ^{1}H NMR (400 MHz, $CDCl_3$) δ 9.94 (s, 1H), 7.76 (d, *J* = 7.9 Hz, 2H), 7.61 – 7.57 (m, 2H), 7.52 (d, *J* = 8.0 Hz, 2H), 7.49 – 7.43 (m, 4H), 7.40 – 7.29 (m, 5H), 7.18 – 7.09 (m, 3H), 2.54 – 2.39 (m, 4H), 1.74 – 1.60 (m, 4H), 1.57 – 1.44 (m, 4H), 1.42 – 1.30 (m, 8H), 1.06 – 0.85 (m, 6H).^{13}C NMR (100 MHz, $CDCl_3$) *δ* 191.5, 150.8, 150.6, 145.1, 143.9, 140.1, 139.3, 137.1, 137.0, 136.5, 136.4, 136.0, 134.9, 131.6, 131.4, 130.5, 130.4, 130.3, 130.2, 126.9, 126.6, 126.0, 125.4, 125.3, 125.3, 124.3, 93.1, 92.9, 80.4, 80.3, 31.5, 28.9, 28.8, 22.8, 19.8, 19.7, 14.3. *Note: not all carbon signals are visible in the ^{13}C-NMR spectrum due to fortuitous overlaps of several peaks.* MS (ESI) *m/z*: $[M+H]^+$ calcd for $C_{51}H_{46}IN_2OS_2$ 894.0; found: 894.2.

4-(5-(2,3-*Bis*(4-(oct-1-yn-1-yl)phenyl)-8-(5-(4-(pyridin-4-ylmethoxy)phenyl)thiophen-2-yl)quinoxalin-5-yl)thiophen-2-yl)benzaldehyde (44)

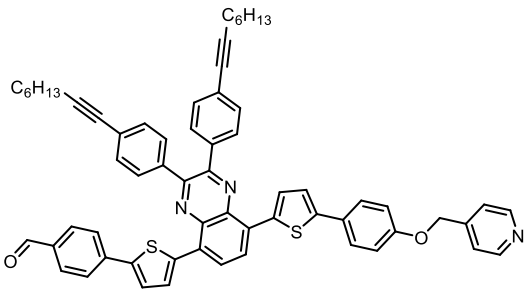

Compound **42** (138 mg, 0.16 mmol, 1.0 eq.) and $Pd(PPh_3)_4$ (9 mg, 0.008 mmol, 5 mol%) were added to a Schlenk tube and put under inert atmosphere by performing three vacuum-nitrogen cycles. The solids were then dissolved in dry THF (10 mL) and 4-hydroxyphenyl boronic acid (**25**, 64 mg, 0.46 mmol, 3.0 eq.) and K_2CO_3 (0.214 g, 1.55 mmol, 10.0 eq.), previously solubilized in a mixture of THF/H_2O 2:1 v/v (3 mL), was subsequently added. The reaction mixture was then vigorously stirred at 90°C for 16 h. The solution was cooled to room temperature, diluted with DCM (20 mL) and washed with water (2 × 20 mL) and brine (20 mL). The organic phase was dried over Na_2SO_4, filtered, and the solvent evaporated under reduced pressure.

Without any further purification, the crude mixture was dissolved in *N,N*-DMF (6 mL). 4-(Bromomethyl)pyridine hydrobromide (**35**, 0.194 g, 0.78 mmol, 5.0 eq.) and K_2CO_3 (0.192 g, 1.39 mmol, 9.0 eq) were then added and the reaction mixture was vigorously stirred at 90°C for 6 h. The solution was cooled to room temperature, diluted with DCM (15 mL), filtered over a pad of Celite®, and washed with water (2 × 20 mL) and brine (20 mL). The organic phase was dried over Na_2SO_4, filtered, and the solvent evaporated under reduced pressure. The crude product was purified by flash column chromatography (SiO_2, gradient from DCM/THF 95:5 to DCM /THF 70:30) to afford compound **44** (45 mg, 0.047 mmol, 31% yield) as a red solid. ^{1}H NMR (400 MHz, CD_2Cl_2/HFIP-d_2 4:1) δ 9.62 (s, 1H), 8.46 – 8.41 (m, 2H), 7.69 (d, *J* = 7.4 Hz, 4H), 7.56 – 7.49 (m, 8H), 7.43 – 7.34 (m, 8H), 7.23 (d, *J* = 4.0 Hz, 1H), 7.08 – 7.00 (m, 1H), 6.88 (d, *J* = 8.3 Hz, 2H), 5.05 (s, 2H), 2.55 – 2.46 (m, 4H), 1.76 – 1.63 (m, 4H), 1.60 – 1.50 (m, 4H), 1.44 – 1.37 (m, 8H), 1.01 – 0.92 (m, 6H). ^{13}C-NMR (100 MHz, CD_2Cl_2/HFIP-d_2 4:1) δ 194.4, 150.3, 149.6, 147.1, 141.2, 139.9, 137.2, 136.4, 133.6, 131.2, 130.9, 130.4, 128.1, 127.2, 126.4, 126.1, 125.6, 125.1, 125.0, 124.7, 122.8, 122.4, 121.6, 120.0, 117.2, 114.9, 110.5, 93.0, 92.8, 80.1, 80.0, 67.5, 31.3, 28.7, 28.6, 22.5, 19.3, 13.5. *Note: not all carbon signals are visible in the ^{13}C-NMR spectrum due to fortuitous overlaps of several peaks.* HRMS (ESI) *m/z*: $[M+H]^+$ calcd for $C_{63}H_{56}N_3O_2S_2$ 950.3814; found 950.3786.

3-(4-(5-(2,3-*Bis*(4-(oct-1-yn-1-yl)phenyl)-8-(5-(4-(pyridin-4-ylmethoxy)phenyl)thiophen-2-yl)quinoxalin-5-yl)thiophen-2-yl)phenyl)-2-cyanoacrylic acid (D1A2)

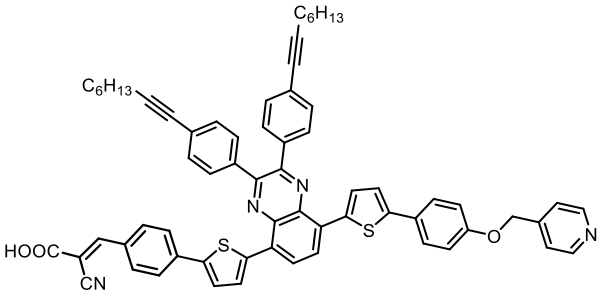

Compound **44** (45 mg, 0.047 mmol, 1.0 eq.) was added to a Schlenk tube, put under inert atmosphere by performing three vacuum-nitrogen cycles and dissolved in dry THF (8 mL). Cyanoacetic acid (**15**, 40 mg, 0.47 mmol, 10.0 eq.) and a few drops of piperidine were then added and the reaction mixture was stirred at 90°C for 16 h. After cooling down to room temperature, HCl (0.01 M) was added (10 mL) and the mixture was extracted with DCM (3 × 10 mL). The combined organic phases were dried over anhydrous Na_2SO_4, filtered, and the solvent evaporated under reduced pressure. The crude mixture was washed several times with cold ethanol to afford compound **D1A2** as a red solid (41 mg, 0.040 mmol, 85 % yield). ^{1}H-NMR (400 MHz, *N.N*-DMF-d_7, 70°C) δ 8.47 – 8.32 (m, 3H), 8.17 (d, *J* = 8.2 Hz, 2H), 8.13 – 8.06 (m, 2H), 7.97 (d, *J* = 8.4 Hz, 2H), 7.91 – 7.72 (m, 8H), 7.70 – 7.58 (m, 4H), 7.59 – 7.45 (m, 4H), 7.26 – 7.14 (m, 2H), 5.31 (s, 2H), 2.52 (t, *J* = 7.0 Hz, 4H), 1.72 – 1.61 (m, 4H), 1.58 – 1.49 (m, 4H), 1.43 – 1.34 (m, 8H), 1.02 – 0.91 (m, 6H).^{13}C NMR (100 MHz, *N,N*-DMF-d_7) δ 158.5, 153.6, 151.6, 149.6, 138.1, 137.0, 132.2, 131.6, 131.1, 128.8, 128.6, 127.1, 125.9, 125.2, 122.8, 122.5, 116.4, 115.9, 92.9, 80.7, 68.3, 31.5, 28.9, 28.8, 22.7, 19.3, 13.9. *Note: not all carbon signals are visible in the ^{13}C-NMR spectrum due to low solubility.* HRMS (ESI) m/z: $[M+H]^+$ calcd for $C_{66}H_{56}N_4O_3S_2$ 1017.3872; found 1017.3877.

[Ru(bda)(pic)(dmso)](45)

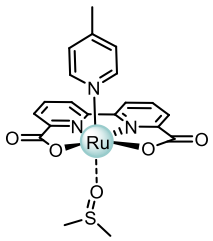

[Ru(bda)(DMSO)$_2$] (241 mg, 0.483 mmol, 1.5 eq.) was placed into a Schlenk tube, put under inert atmosphere by performing three vacuum-nitrogen cycles, and suspended in dry methanol (20 mL). The mixture was degassed by bubbling N_2 for 15 min. Then 4-picoline (30 mg, 0.322 mmol, 1.0 eq.) was added via a gas-tight syringe. The reaction mixture was vigorously stirred at 80°C for 16 h. After cooling down to room temperature, the mixture was filtered to remove the unconverted starting material and the solvent evaporated under reduced pressure. The crude product was purified by flash column chromatography (SiO_2, gradient from DCM/MeOH 95:5 to DCM/MeOH 80:20) to afford compound **[Ru(bda)(pic)dmso)]** (40 mg, 0.078 mmol, 24% yield) as a brown solid. ^{1}H-NMR (400 MHz, CD_3OD) δ 8.61 – 8.55 (m, 2H), 8.12 – 8.08 (m, 4H), 7.75 (d, *J* = 6.1 Hz, 2H), 7.17 (d, *J* = 6.4 Hz, 2H), 2.91 (s, 6H), 2.43 (s, 3H). Spectroscopic data are in agreement with those reported in the literature.[13]

Synthesis of Ru-D1A2

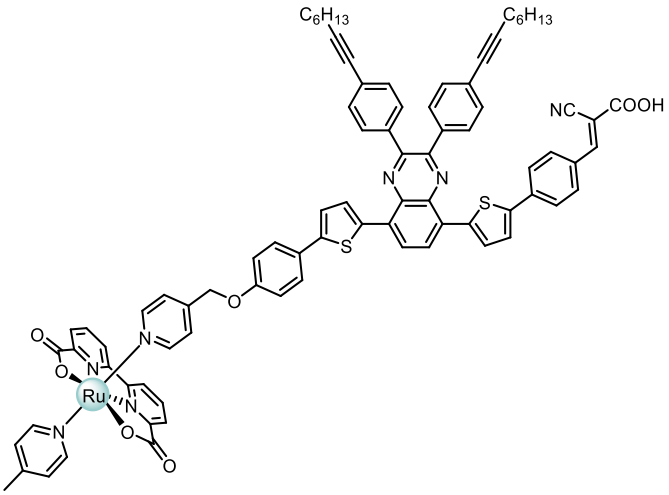

[Ru(bda)(pic)(dmso)] (12 mg, 0.024 mmol, 1.6 eq) was added to a Schlenk tube, put under inert atmosphere by performing three vacuum-nitrogen cycles, and dissolved in dry methanol (10 mL). The mixture was degassed by bubbling N_2 for 15 min and heated at 60°C. Then a solution of dye **D1A2** (15 mg, 0.015 mmol, 1.0 eq) in N,N-DMF (2 mL), previously prepared in another Schlenk tube under inert atmosphere and pre-heated at 60°C, was added via a gas-tight syringe. Then, a couple of drops of triethylamine were added and the reaction mixture was stirred under reflux overnight. After cooling down to room temperature the solvent was evaporated and the resulting crude was washed with several portions of DCM, methanol and Et_2O to afford the desired product **Ru-D1A2** as dark purple solid. HRMS (ESI) m/z: $[M+H]^+$ calcd for $C_{84}H_{70}N_7O_7RuS_2$ 1454.3822; found 1454.3812.

4.5 References

(1) Ashford, D. L.; Gish, M. K.; Vannucci, A. K.; Brennaman, M. K.; Templeton, J. L.; Papanikolas, J. M.; Meyer, T. J. Molecular Chromophore-Catalyst Assemblies for Solar Fuel Applications. *Chem. Rev.* 2015, *115* (23), 13006–13049. https://doi.org/10.1021/ACS.CHEMREV.5B00229/ASSET/IMAGES/MEDIUM/CR-2015-002299_0031.GIF.

(2) Hanson, K.; Torelli, D. A.; Vannucci, A. K.; Kyle Brennaman, M.; Luo, H.; Alibabaei, L.; Song, W.; Ashford, D. L.; Norris, M. R.; K Glasson, C. R.; Concepcion, J. J.; Meyer, T. J.; Hanson, K.; Torelli, D. A.; Vannucci, A. K.; Brennaman, M. K.; Luo, H.; Alibabaei, L.; Song, W.; Ashford, D. L.; Norris, M. R.; K Glasson, C. R.; Concepcion, J. J.; Meyer, T. J. Self-Assembled Bilayer Films of Ruthenium(II)/Polypyridyl Complexes through Layer-by-Layer Deposition on Nanostructured Metal Oxides. *Angew. Chem. Int. Ed.* 2012, *124* (51), 12954–12957. https://doi.org/10.1002/ANGE.201206882.

(3) Decavoli, C.; Boldrini, C. L.; Faroldi, F.; Baldini, L.; Sansone, F.; Ranaudo, A.; Greco, C.; Cosentino, U.; Moro, G.; Manfredi, N.; Abbotto, A. Calix[4]Arene-Based Sensitizers for Host-Guest Supramolecular Dyads for Solar Energy Conversion in Photoelectrochemical Cells. *Eur. J. Org. Chem.* 2022, *2022* (34), e202200649. https://doi.org/10.1002/ejoc.202200649.

(4) Wang, D.; Wang, L.; Brady, M. D.; Dares, C. J.; Meyer, G. J.; Meyer, T. J.; Concepcion, J. J. Self-Assembled Chromophore-Catalyst Bilayer for Water Oxidation in a Dye-Sensitized Photoelectrosynthesis Cell. *J. Phys. Chem. C* 2019, *123* (50), 30039–30045. https://doi.org/https://doi.org/10.1021/ACS.JPCC.9B07125.

(5) Ashford, D. L.; Song, W.; Concepcion, J. J.; Glasson, C. R. K.; Brennaman, M. K.; Norris, M. R.; Fang, Z.; Templeton, J. L.; Meyer, T. J. Photoinduced Electron Transfer in a Chromophore–Catalyst Assembly Anchored to TiO 2. *J. Am. Chem. Soc.* 2012, *134* (46), 19189–19198. https://doi.org/10.1021/ja3084362.

(6) Yamamoto, M.; Wang, L.; Li, F.; Fukushima, T.; Tanaka, K.; Sun, L.; Imahori, H. Visible Light-Driven Water Oxidation Using a Covalently-Linked Molecular Catalyst–Sensitizer Dyad Assembled on a TiO 2 Electrode. *Chem. Sci.* 2016, *7* (2), 1430–1439. https://doi.org/10.1039/C5SC03669K.

(7) Antón-García, D.; Warnan, J.; Reisner, E. A Diketopyrrolopyrrole Dye-Based Dyad on a Porous TiO2 Photoanode for Solar-Driven Water Oxidation. *Chem. Sci.* 2020, *11* (47), 12769–12776. https://doi.org/10.1039/D0SC04509H.

(8) Decavoli, C.; Boldrini, C. L.; Trifiletti, V.; Luong, S.; Fenwick, O.; Manfredi, N.; Abbotto, A. Dye–Catalyst Dyads for Photoelectrochemical Water Oxidation Based on Metal-Free Sensitizers. *RSC Adv.* 2021, *11* (10), 5311–5319. https://doi.org/10.1039/D0RA10971A.

(9) Kolb, H. C.; Finn, M. G.; Sharpless, K. B. Click Chemistry: Diverse Chemical Function from a Few Good Reactions. *Angew. Chem. Int. Ed.* 2001, *40* (11), 2004–2021. https://doi.org/10.1002/1521-3773(20010601)40:11<2004::AID-ANIE2004>3.0.CO;2-5.

(10) Haldón, E.; Nicasio, M. C.; Pérez, P. J. Copper-Catalysed Azide–Alkyne Cycloadditions (CuAAC): An Update. *Org. Biomol. Chem.* 2015, *13* (37), 9528–9550. https://doi.org/10.1039/C5OB01457C.

(11) Tornøe, C. W.; Christensen, C.; Meldal, M. Peptidotriazoles on Solid Phase: [1,2,3]-Triazoles by Regiospecific Copper(I)-Catalyzed 1,3-Dipolar Cycloadditions of Terminal Alkynes to Azides. *J Org Chem* 2002, *67* (9), 3057–3064. https://doi.org/10.1021/jo011148j.

(12) Huisgen, R. 1,3-Dipolar Cycloadditions. Past and Future. *Angew. Chem. Int. Ed. Engl.* 1963, *2* (10), 565–598. https://doi.org/10.1002/anie.196305651.

(13) Gao, Y.; Ding, X.; Liu, J.; Wang, L.; Lu, Z.; Li, L.; Sun, L. Visible Light Driven Water Splitting in a Molecular Device with Unprecedentedly High Photocurrent Density. *J. Am. Chem. Soc.* 2013, *135* (11), 4219–4222. https://doi.org/10.1021/ja400402d.

(14) Aranzaes, J. R.; Daniel, M.-C.; Astruc, D. Metallocenes as References for the Determination of Redox Potentials by Cyclic Voltammetry — Permethylated Iron and Cobalt Sandwich Complexes, Inhibition by Polyamine Dendrimers, and the Role of Hydroxy-Containing Ferrocenes. *Can. J. Chem.* 2006, *84* (2), 288–299. https://doi.org/10.1139/v05-262.

(15) Duan, L.; Bozoglian, F.; Mandal, S.; Stewart, B.; Privalov, T.; Llobet, A.; Sun, L. A Molecular Ruthenium Catalyst with Water-Oxidation Activity Comparable to That of Photosystem II. *Nat. Chem* 2012, *4* (5), 418–423. https://doi.org/10.1038/nchem.1301.

(16) Kavan, L. Electrochemistry and Band Structure of Semiconductors (TiO2, SnO2, ZnO): Avoiding Pitfalls and Textbook Errors. *J. Solid State Chem.* 2024, *28* (3–4), 829–845. https://doi.org/10.1007/s10008-023-05770-w.

Chapter 5

Novel photochemical strategy for functional group migration on aromatic rings

5.1 Introduction

As anticipated in chapter 2, the present chapter of this dissertation describes the research project conducted during a six-month research stay in the laboratories of Prof. Dr. Daniele Leonori at RWTH Aachen University (Germany). The project focused on developing novel synthetic methodologies driven by Ultraviolet (UV) and visible light irradiation. Specifically, the research aimed to establish new photochemical techniques for N-functional group migration on aromatic rings, allowing conversion of arylazides into anilines with a regioisomeric substitution pattern. Before delving into the details of the synthetic work, a brief general introduction to synthetic photochemical approaches is provided below.

5.1.1 Photochemical reactions: a powerful tool in organic synthesis

Since the advent of modern chemistry, scientists have been fascinated by the use of light as an energy source to drive chemical reactions.[1] By absorbing light, molecules reach an electronically excited state. At these states, the distribution of electrons in the molecules is significantly different when compared to the ground state.[2] Their chemical properties, and particularly their reactivity, also change, and the reaction spectrum of various families of compounds is considerably broadened. In many cases, incorporating photochemical steps into synthetic pathways dramatically reduces the complexity and length of the process. This approach often enables the transformation of simple substrates into complex, polycyclic, or highly functionalized structures. Moreover, photochemical reactions allow access to entirely new families of products, often unattainable through ground-state chemistry. These innovations open exciting opportunities for discovering biologically active compounds and developing novel chemical libraries.

Photochemical substrate activation often occurs without additional reagents, which diminishes formation of byproducts. Due to this fact, photochemical reactions appear particularly interesting in the context of green chemistry. Some of these reactions can be carried out with visible light or sunlight as a renewable energy source. These possibilities, as already mentioned in Chapter 1, were considered by Giacomo Ciamician almost a century ago in a limpid article entitled “The photochemistry of the future”.[3] Since then, photochemistry has evolved into a mature research field, with its golden era occurring in the second half of the twentieth century.[4,5] During this period, a deep mechanistic understanding of photochemical processes, mainly driven by UV-light irradiation, emerged. This exploration led to the development of a wide range of remarkable reactions, facilitating the synthesis of intricate three-dimensional (3D) architectures.[6] However, the field was

primarily shaped by a small number of specialized research groups, who often relied on custom-built or modified equipment to carry out their experiments.
For these reasons, synthetic photochemistry entered a period of stagnation at the turn of the new century. It wasn't until about 15 years ago, with the development of visible-light photocatalysis, that the field experienced a remarkable resurgence. This breakthrough has since then transformed photochemistry into one of the most vibrant and rapidly advancing areas of research in chemistry today.[7,8]

5.1.1.1 UV/near-UV-light photochemistry

UV light-mediated photochemistry is often perceived as an old-fashioned approach, because the use of such light source is generally associated with harsh conditions, low selectivity and complex reaction set-ups, including the need for specific glassware (quartz cuvettes), cooling systems and apparatuses such as Xe or Hg lamps.[1] However, today, running a photochemical reaction under UV light can be as easy as setting up a classical organic reaction in standard laboratory conditions.[8] Remarkable technological advancements[9] have enabled the effective replacement of broad-emission light sources with monochromatic, high-intensity light-emitting diodes (LEDs). In particular, energy-efficient UV-A LEDs ($\lambda > 315$ nm) are now widely available on the market. Ongoing efforts to enhance the performance of UV-B ($280 < \lambda < 315$ nm) and UV-C ($100 < \lambda < 280$ nm) LEDs are expected to make these available for photochemical applications in the near future as well.

In the last decade, several reports have demonstrated the impressive potential of UV light in organic synthesis. As an example, the Melchiorre group reported that UV light-driven hydrogen-bonding catalysis as well as covalent iminium-ion catalysis can be efficiently used to perform an enantioselective [4 + 2] cycloaddition (Scheme 5.1) or a Michael addition (Scheme 5.2), respectively.[10,11]
Regarding the first example, as illustrated in the proposed mechanism, the excitation of 2-alkyl benzophenones (**I**) with a 366 nm light source generates transient hydroxy-*o*-quinodimethanes (**II**) (Scheme 5.1). These enols exhibit unique reactivity, acting as dienes in [4+2] cycloaddition reactions with electron-deficient alkenes (**III**), leading to the formation of benzannulated carbocyclic products (**IV**). Although the light-induced generation of hydroxy-*o*-quinodimethanes from 2-alkyl benzophenones was first established in 1961[12], dictating the absolute configuration of the corresponding [4+2] cycloaddition has remained for many years a challenging task. By employing the

chiral organocatalyst **V**, Melchiorre and co-workers could perform controlled activation the dienophile **III** and trap the transient photoenol **II** stereoselectively.

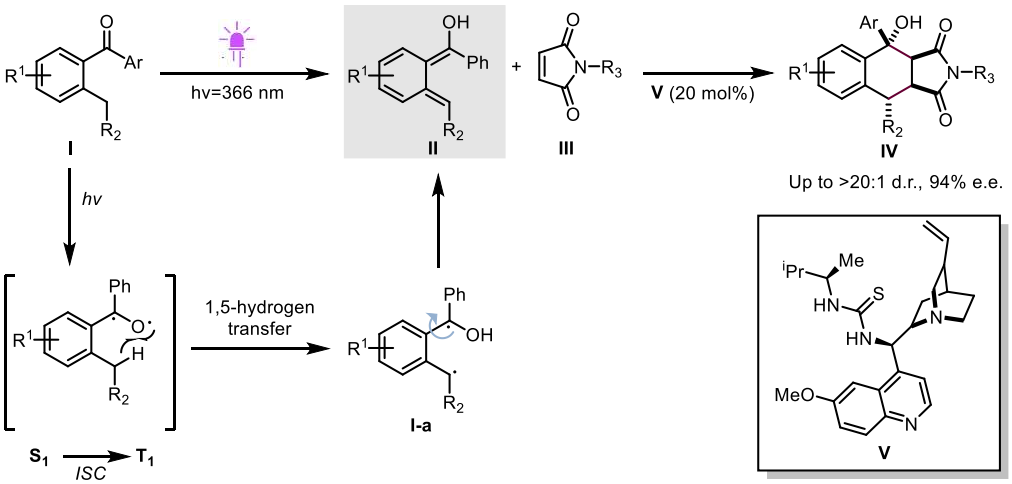

Scheme 5.1 Enantioselective UV-light driven [4+2] cycloaddition.

Later on, the same group documented that the reactivity of photoenol **II** is not restricted to cycloaddition mechanism, but can be extended to conjugate addition reactions. More specifically, they found that a chiral iminium ion intermediate **VI**, formed upon condensation of a secondary amine catalyst **VII** and α,β-unsaturated aldehydes **VIII**, can stereoselectively intercept **II** and lead to the exclusive formation of the Michael addition product **IX**. Also in this case very high stereocontrol was observed (up to >20:1 d.r. and >98% e.e.).

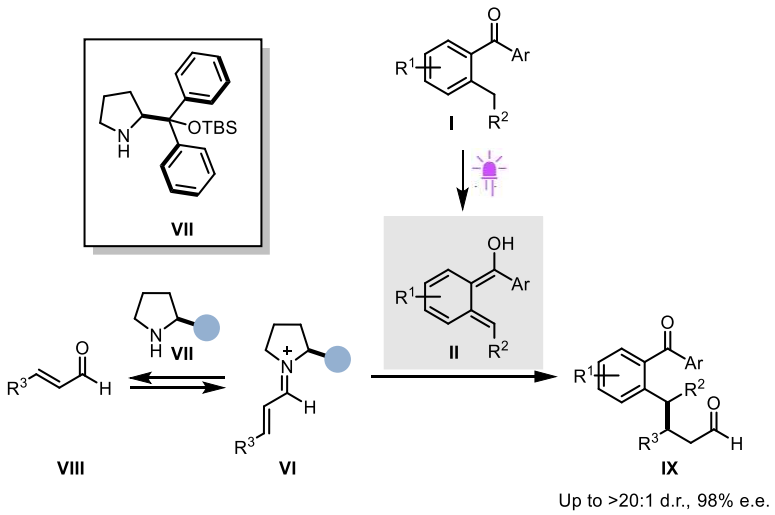

Scheme 5.2 Enantioselective UV-light driven Michael addition.

More recently, the group of Dell'Amico showed that it is also possible to perform these reactions efficiently and with high selectivity under flow conditions.[13,14] In this context, it is important to note that UV-light processes can be easily translated to flow set-ups.[15]

5.1.1.2 Photochemical skeletal editing of heteroaromatics

As mentioned in the previous paragraph, the introduction of monochromatic, highly emissive LEDs has revolutionized the field of photochemistry, providing chemists with the optimal light sources to selectively excite the desired molecules or intermediates, and therefore investigate unexplored reactivities. This breakthrough turned out to be a powerful tool for the development of the so-called 'molecular editing' methodologies.

Molecular editing is defined as the precise insertion, deletion, or exchange of atoms in highly functionalized compounds[16]. This broad definition includes many types of chemical transformations across different regions of chemical space. [17] However, most current molecular editing methods focus on modifying functional groups on peripheral sites of the molecule (*e.g.* C-H functionalization), leaving the core molecular structure largely unchanged. However, the ability to modify the core of a molecule by interconverting between (hetero)aromatic substructures would be potentially extremely valuable due to their ubiquity in biologically active compounds.[18–20] This type of transformations falls within the broader – and only recently defined – field of molecular editing and includes established concepts such as 'transannulation',[21]having been historically referred to as 'heterocycle interconversions'.[22,23] In a 2022 review, Sarpong, Levin, and co-workers introduced another new term by defining 'skeletal editing' as the subset of 'molecular editing' that concerns the precise modification of molecular skeletons, mainly ring systems.[24] Such transformations promise to facilitate the rapid diversification of complex molecular architectures while avoiding cost- and labor-intensive *de novo* synthesis. As such, they have the potential to accelerate both drug discovery and total synthesis.[25]

In the last few years, numerous photo-driven skeletal editing methodologies have been developed by various research groups. Notably, significant contributions to this field have been made by the research teams of Levin and Leonori.

In 2022, Levin and coworkers reported the transformation of quinoline N-oxides **X** and related azaarenes into 3,1-benzoxazepine intermediates (**XI**) that, upon acid hydrolysis, provide the corresponding N-acylindole products **XII** (Scheme 5.3). Such a photochemical carbon-deletion process had already been observed for quinoline N-oxides, but the use of unselective light sources generally provided complex reaction mixtures, with the desired N-acylindoles present only as the minor products. The Levin group recognized that these side products originated mainly from further photoexcitation of the 3,1-benzoxazepine intermediates **XI**. Thus, the use of a 390-nm LED allowed selective irradiation of the quinoline N-oxide, providing access to densely functionalized indole and azaindole scaffolds. The reaction was applied to a number of highly functionalized

molecules, such as the leukotriene receptor antagonist montelukast and was shown to tolerate different heterocyclic substrates including 1,8- naphthyridines and quinoxalines.

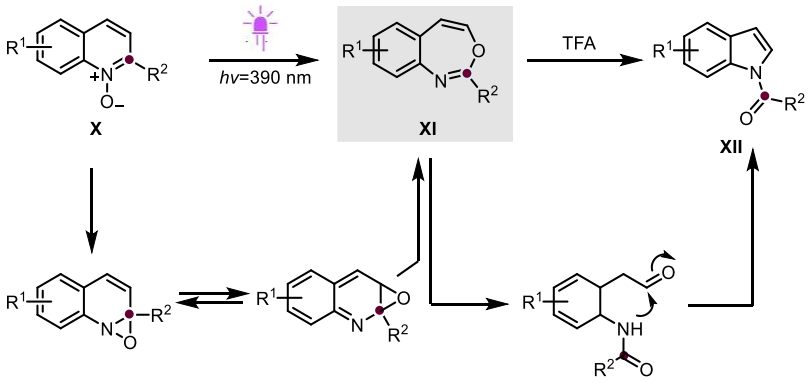

Scheme 5.3 Proposed mechanistic pathway for the conversion of quinoline N-oxides into N-acylindoles via 3,1-benzoxazepine intermediates.

Building on similar chemistry, the group of Levin later reported another skeletal editing methodology, namely the carbon-to-nitrogen single-atom transmutation of quinoline N-oxides **XI** yielding quinazolines **XIV** (Scheme 5.4).[26]

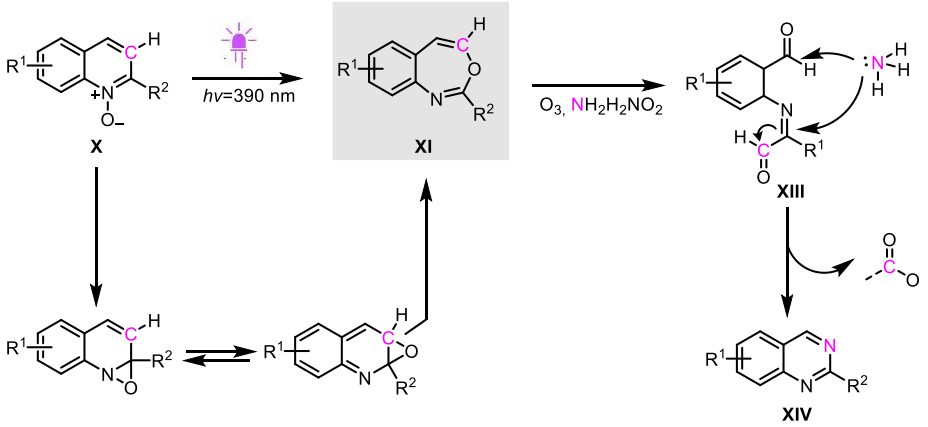

Scheme 5.4 Proposed mechanistic pathway for the conversion of quinoline N-oxides into quinazolines via 3,1-benzoxazepine intermediates.

As can be seen from Scheme 5.4, in this case the photo-generated 3,1-benzoxazepine intermediates (**XI**) undergoes oxidative cleavage *via* ozonolysis yielding intermediate **XIII** bearing two electrophilic carbonyl groups. Upon addition of the ammonia nucleophile (in the form of ammonium carbamate) the carboxylate subunit contained in the imidic function can be displaced as a leaving group, leading to the desired final products.

As anticipated above, other important contributions to light-driven skeletal editing methodologies have been made by the Leonori group, who explored processes relying on singlet nitrene chemistry.[27–31] The photo-decomposition of aryl azides or nitroarenes (**A,** Scheme 5.5) into high-energy singlet nitrenes species (**B,** Scheme 5.5) was first demonstrated by the pioneering studies of Sundberg [32] and Platz[33] with the use of high-energy Hg lamps (λ=250 nm). The blueprint followed

by the group of Leonori for aryl nitrene generation from nitroaromatics was instead based on the use of lower energy (near UV/visible-light) photoexcitation. Specifically purple light (λ=390 nm) was used for aryl azides and blue light (λ=427 nm) for nitroarenes.

As shown in the proposed mechanism reported in Scheme 5.5, the photogenerated nitrene undergoes a dearomative cascade starting with the intramolecular cyclization from the iminyl radical-type resonance to form azirine **C.**[34] Then, a facile 6π-electrocyclic ring opening transforms the all-carbon benzenoid system into the seven-membered ring ketimine **D**.[35] At this point, Leonori and co-workers showed how the strain-amplified electrophilic character of this species enables facile reaction with soft nucleophiles like aryl amines, alcohols or thiophenols, producing 1H-azepine **E**.[36] However, since this species has anti-aromatic character, it is known to immediately isomerize to the thermodynamically stable 3H-azepine **F**.[37]

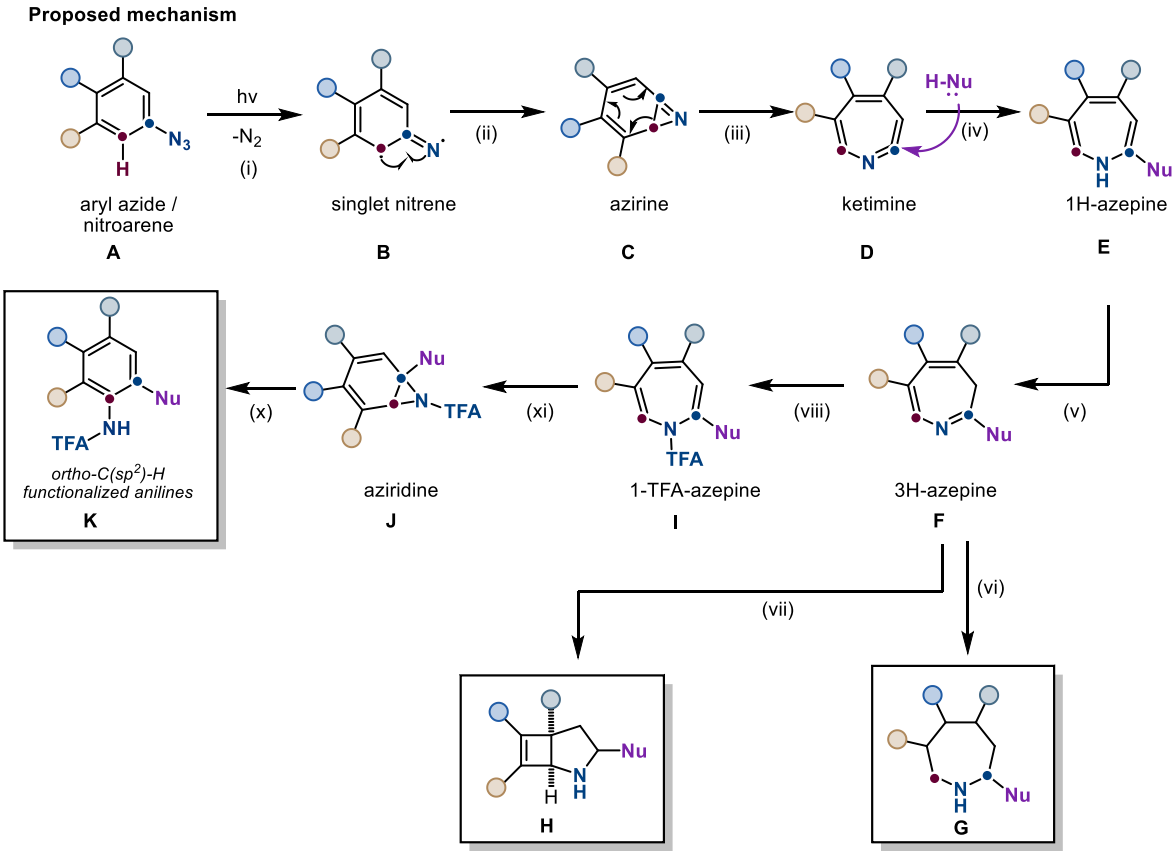

Scheme 5.5 Proposed mechanistic pathway for the conversion of aryl azides into saturated azepanes, bicyclic pyrrolidines, and ortho-anilines via singlet nitrene chemistry.

The 3H-azepine intermediate can be further derivatized to access a number of different final products. Indeed, direct hydrogenation of 3H-azepine leads to the corresponding polysubstituted azepane product **G**.[27] Alternatively, a second low-energy photoexcitation (λ=427 nm) can trigger a

disrotatory 4π electrocyclization producing the bicyclic product **H.**[30] Interestingly, the addition of an electrophilic trapping agent, such as trifluoroacetic anhydride (TFAA), can take place at the azepine N-atom, thus giving, after enolization, the anti-aromatic intermediate **I** that cannot isomerize. This strong thermodynamic perturbation ought to trigger a second 6π electrocyclic reaction, this time in a closing direction, to give the N-TFA aziridine **J**. The push-pull nature of this system results in a facile aromatization to the ortho-aniline **K**, where the newly introduced functionality (Nu in Scheme 5.5) is linked to the initial nitro/azide-bearing carbon, whereas the nitrogen functionality has been shifted to the neighbouring ortho position, reduced, and amidated.[29] Therefore, such photochemical approach allows access to anilines whose heteroatom disposition across the aromatic ring challenges the rules of electrophilic aromatic substitution (S_EAr). Moreover, this example opens the doors to the possible development of new photochemical methodologies aimed at modifying the substitution patterns of benzene rings leading to the corresponding regioisomers, without the need of *de novo* synthesis.

The exploration of some of these new synthetic avenues has been the focus of the research work carried out in Prof. Dr. Daniele Leonori's group at RWTH Aachen University and will be discussed in greater detail in the following sections. First, a brief analysis of the state-of-the-art of functional group migration strategies on aromatic rings is given in the next paragraph.

5.1.2 Functional group migration on aromatic rings: state-of-the-art

Substitution reactions on (hetero) aromatic substrates are some of the most important reactions in organic chemistry.[38] However, some substitution patterns can be more difficult to forge than others based on the different propensity of the positions on the (hetero)arene ring to engage in electrophilic, nucleophilic, or radical-based substitution. In these cases, aromatic rearrangement reactions can help access ring positions that are difficult to functionalize otherwise.

Although there are many well-known aromatic rearrangements such as the Smiles, Claisen, and Bamberger rearrangements, these transformations leave behind a functional group at the carbon atom that was originally substituted in the starting material (Scheme 5.6). A rarer type of aromatic rearrangements involves translocation of a functional group, in which the carbon atom bearing the functional group in the starting material loses the group entirely, and the same group is brought back to another carbon atom on the aromatic ring. One example of this type of aromatic translocations is transalkylation, which is a disproportionation of an alkyl group under Friedel-Crafts alkylation conditions, also known as a carbon-substituent rearrangement (Scheme 5.6).[39–41] This reaction can translocate an alkyl substituent to another position on the same aromatic ring or onto

another aromatic ring, allowing for several compounds, including isomers, to form a single product; therefore, it is used mainly in the petrochemical industry. However, this reaction requires extremely harsh conditions and generates an unpredictable mixture of products.

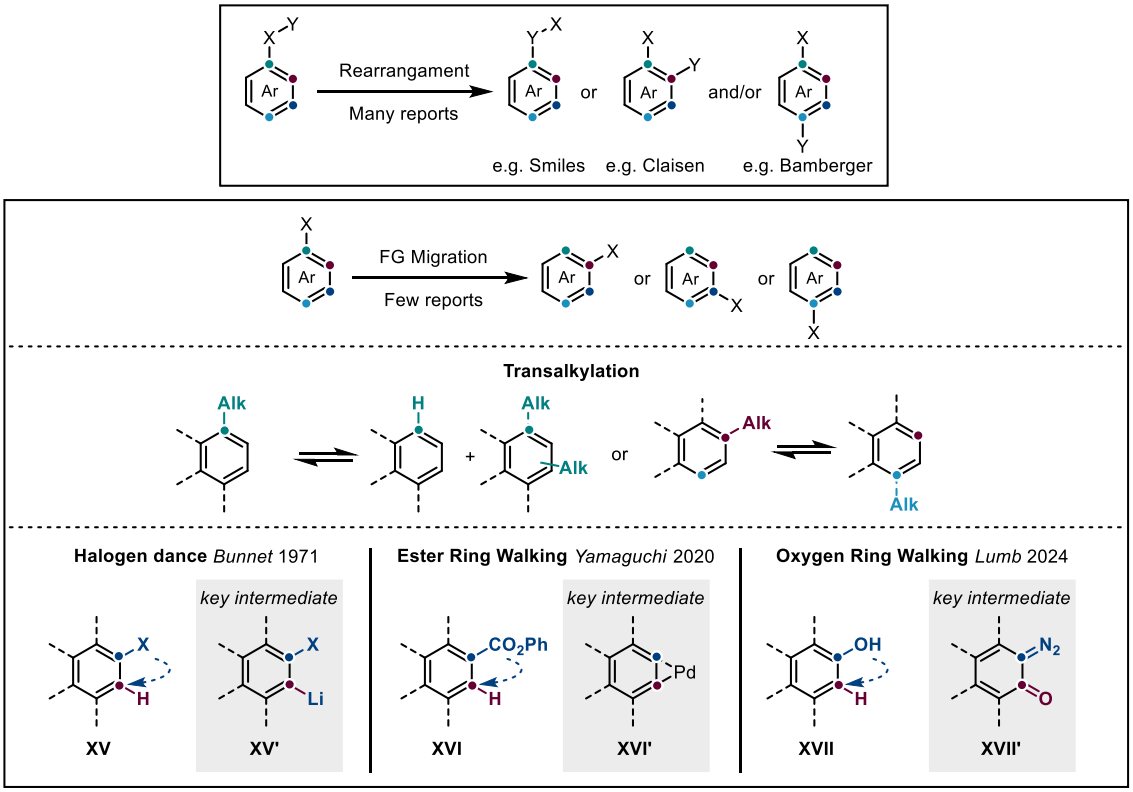

Scheme 5.6 Examples of functional group migration strategies.

An intriguing process, applied in the synthesis of fine chemicals, is the so-called "halogen dance" reaction of haloarenes. This base-catalysed transformation was discovered in 1959 when, upon reaction of sodium amide with polyhalobenzenes in liquid ammonia, 1,2,4-tribromobenzene was converted to its 1,3,5-isomer.[42] Later, the group of Bunnett identified more satisfactory isomerization catalysts, but could not avoid the formation of arynes and dismutation events, leading to a large number of unwanted products.[43,44] In spite of such issues, by showing that the isomerization of available compounds containing heavy halogens into less accessible ones was feasible, this study attracted the interest of chemists. In the developments that have resulted, halogen 'dance' has been related to two essential reactions involving organometallic compounds, namely halogen/lithium exchange[45,46] and deprotonative lithiation.[47,48] Indeed, the lithio intermediate (**XV'**, Scheme 5.6) has to be first generated by base-mediated arene metalation before halogen migration. The method is restricted to compounds bearing heavy halogens (Br, I).

More recent breakthroughs by Yamaguchi and Lumb have demonstrated innovative approaches to achieving directionality in "group ring-walk" strategies. Yamaguchi's Pd-catalyzed *ortho*-isomerization of ester groups exploits the thermodynamic equilibrium of η^2-aryne-palladium complexes **XVI'** (Scheme 5.6) during carbonylation and elimination steps.[49] Meanwhile, Lumb's method for oxygen migration in phenolic systems employs a specially designed sulfonyl hydrazide reagent to selectively generate diazonium intermediates **XVII'**(Scheme 5.6).[50]

5.2 Novel synthetic methodologies for Nitrogen Ring Walking

5.2.1 Aim of the work

Nitrogenated benzene rings represent one of the most prevalent structural motifs in bioactive molecules such as pharmaceuticals, agrochemicals and natural compounds.[51] The nature of substituents and substitution patterns relative to the nitrogen functionality profoundly influences the ring electronic and steric properties. This interplay imparts key physicochemical properties, including variations in reactivity (*e.g.*, inductive and mesomeric effects), acidity (Hammett coefficient), oxidative potential, triplet-state energy, and overall molecular geometry.[52] Collectively, these factors profoundly influence the interactions of bioactive molecules with biological targets.[16]

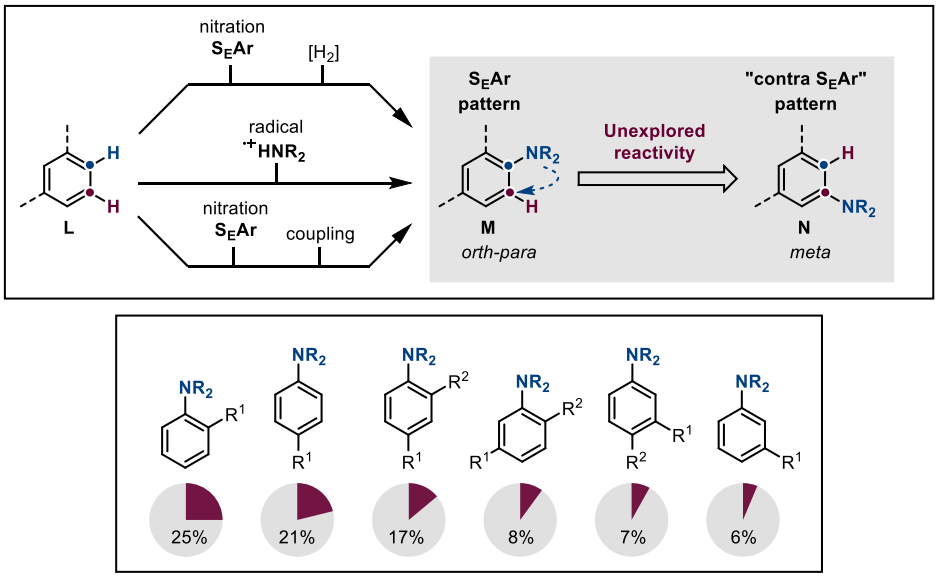

Scheme 5.7 Possible strategies for nitrogen atom ortho insertion (top) and S_EAr substitution pattern for commercially available nitrogen-containing molecules (bottom).

Substitution patterns arising from the chemical manipulation of sp^2 C–H bonds of feedstock arenes, with the exception of a few examples of directed C–H functionalization, are predominantly governed by the intrinsic reactivity of the substrate. Functionalization of feedstock **L** (Scheme 5.7, top) at a large scale predominantly relies on traditional nitration-reduction sequences,[53] while the

fine chemicals sector has increasingly adopted modern methodologies, such as radical C–H amination[54] and cross-coupling reactions involving pre-functionalized substrates.[55]

This trend is evident by an analyzing the substitution patterns of commercially available nitrogenated benzene derivatives, which is predominantly dictated by electrophilic aromatic substitution (S_EAr). Specifically, *ortho*-, *para*-, and *ortho-para*-substituted derivatives account for 65% of the observed chemical space, whereas meta-substituted compounds constitute only 6% (Scheme 5.7, bottom). This disparity highlighted the need for synthetic strategies capable of reconfiguring substitution patterns from S_EAr arrangements **M** (Scheme 5.7) to "contra- S_EAr" substitution patterns **N** (Scheme 5.7).

Thereby, we investigated a new photo-mediated "nitrogen ring-walk" strategy that enables selective late-stage reconfiguration of substitution patterns in benzene derivatives and avoids the need of a *de novo* synthesis. Details about the design, optimization and substrate scope are given below.

5.2.2 Design plan

The "nitrogen ring walk" strategy was designed based on the insights gained from the earliest study conducted in the Leonori group on the synthesis of *ortho*-C(sp^2)-H functionalized anilines (Scheme 5.8, top), briefly anticipated in the previous paragraph.

In that work, UV-light photoexcitation (390 nm) was employed to trigger the decomposition of aryl azides into singlet nitrenes, which can then undergo a dearomative-rearomative sequence. This allows the incorporation of different nucleophiles, such as alcohols, amines, thiols and thiophenols, into a seven-membered ring azepine intermediate via temporary disruption of aromaticity, followed by electrophile-induced rearomatization. As already mentioned, a key event in the mechanistic sequence is the migration of the nitrogen atom across the aromatic framework, with the nucleophile being selectively trapped at the *para*- position of the original aryl azide.

Leveraging this framework, we envisioned the possibility to develop a synthetic strategy that allows the direct transformation of nitrogen-containing benzene derivatives into the corresponding reduced regioisomer. However, to achieve this goal, we first had to overcome the key limitation of the previously described methodology: the nucleophile used in the rearrangement remains bound to the ring in the final product, preventing the formation of a simple nitrogen translocation product. By keeping in mind our goal, we therefore identified two principal criteria for an ideal nucleophile reagent: (1) it must serve as a competent nucleophile during the addition step, and (2) it must enable facile cleavage once the aromatization is complete. Among the possible nucleophiles, thiophenol derivatives align seamlessly with our design, exploiting their dual functionality

as effective nucleophiles in dearomative steps while ensuring high conversions during the re-aromatization step.

A significant challenge in this approach, however, lies in the efficient cleavage of the carbon–sulfur bond. Our strategy, summarized in Scheme 5.8 (bottom), addresses this requirement through the formation of sulfonium derivatives **O**. Indeed, these compounds have been reported in literature[56] to undergo photo-mediated cleavage under UV/visible-light irradiation, yielding the desired rearranged anilines **P**.

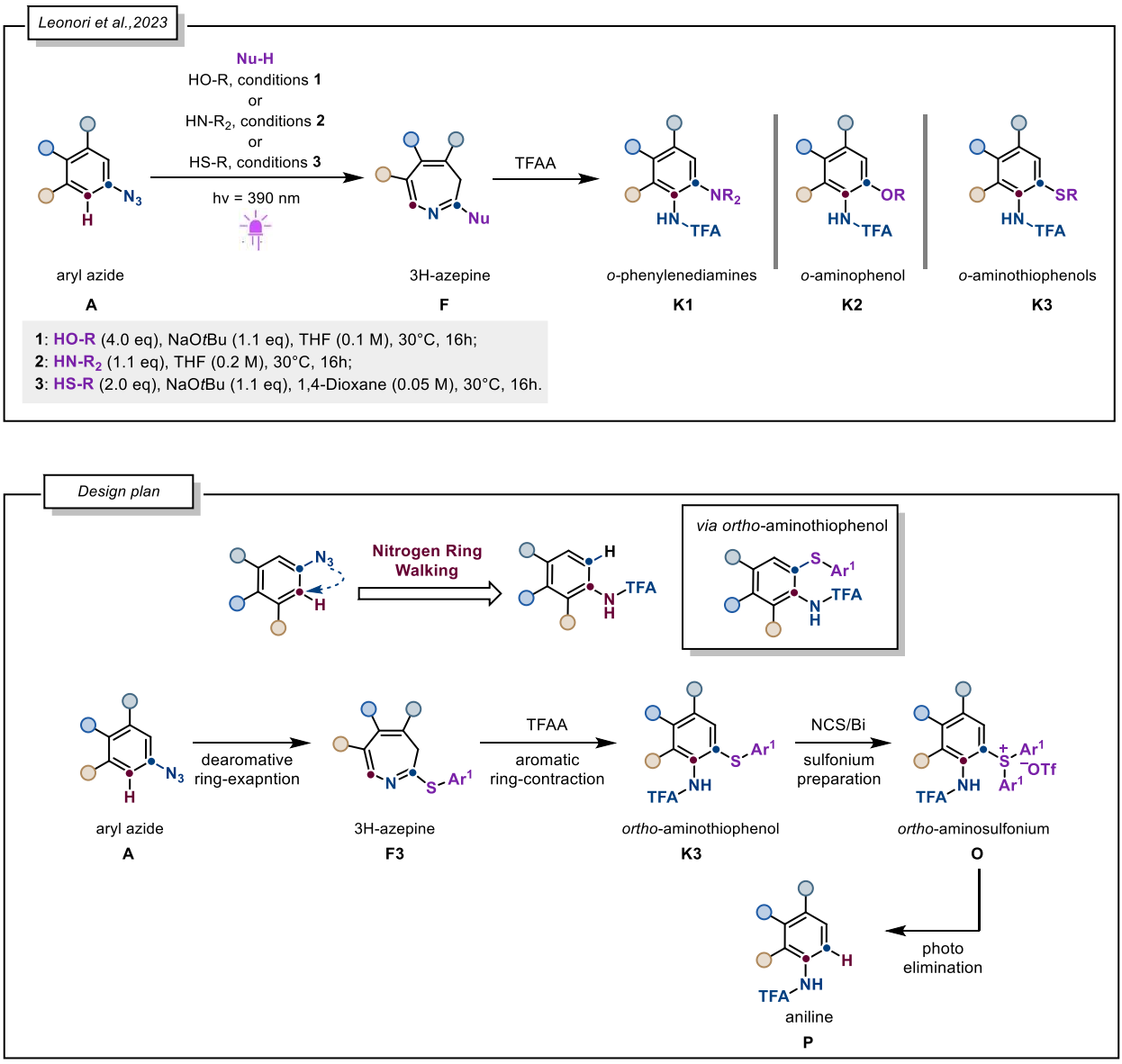

Scheme 5.8 Conversion of aryl azides into regioisomeric anilines via singlet nitrene chemistry (top); Synthetic strategy design for the nitrogen ring walking reaction (bottom).

As anticipated, the success of this synthetic design hinges on the precise structural and electronic features of the thiophenols, which must effectively support three distinct steps: (1) formation of *ortho*-aminothiophenols (**K3**), (2) generation of the sulfonium intermediate (**O**), and (3) efficient

photocleavage to anilines (**P**). In optimizing these steps, both electronic and steric parameters of the thiophenol structure played pivotal roles. Additionally, selecting the appropriate reagent capable of performing efficiently across all three transformations proved critical for the overall success of this strategy.

By keeping in mind the previous discussions, eight potential thiophenol reagents (**46a-h**), shown in Scheme 5.9, were selected and investigated.

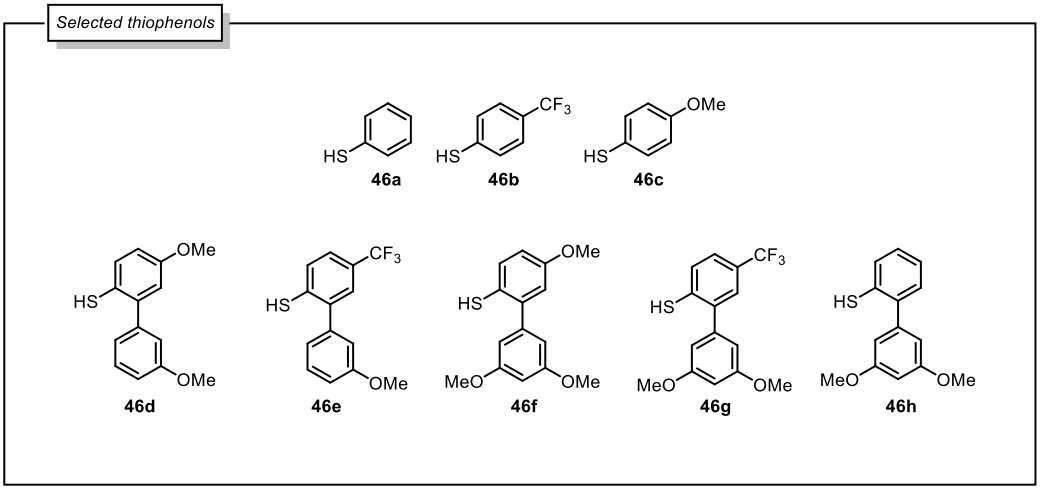

Scheme 5.9 Selected thiophenols.

5.2.3 Reaction development

5.2.3.1 Step 1: Formation of the *ortho*-aminothiophenols 49a-h

The investigation was initiated by screening the various thiophenol reagents for the formation of the *ortho*-aminophenol products. First, however, commercially unavailable thiophenols **46d-h** were prepared following the reported synthetic pathway shown in Scheme 5.10.

Briefly, thiols **46d-h** were obtained in two steps, starting with the Pd-catalyzed coupling of the appropriate substrate **47a-c** with 3-mercaptopropionate **48** to form protected thiols **49a-c** in good yields (68-98%). Subsequent Suzuki-Miyaura coupling of the obtained intermediates with the suitable boronic acids **50a,b**, followed by direct deprotection under basic conditions, provided the desired products **46d-h** with moderate (18-22%) to good yields (70-75%), depending on the specific substrate (see Experimental Section).

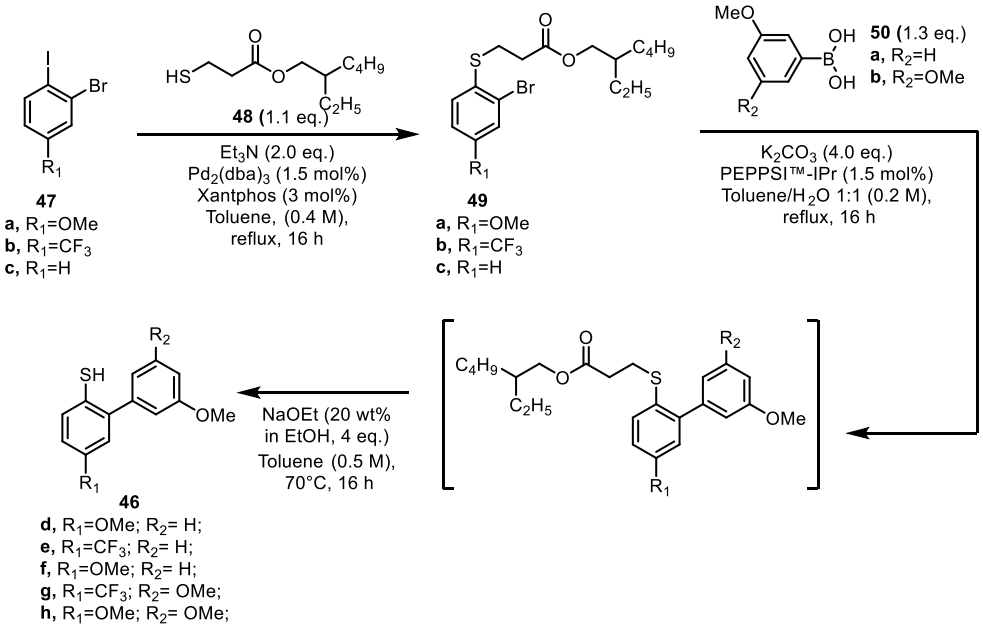

Scheme 5.10 General synthetic pathway for the synthesis of thiophenols ***46d-h.***

With the desired thiophenols in hand, we then attempted the transformation of 4-*tert*-butylazide **51a**, chosen as the model substrate, into the corresponding *ortho*-aminothiophenol derivative, exploiting the same conditions of the previously reported protocol.[29] However, we found that rapid decomposition of thiolate derivatives occurred when the electron-rich biaryl thiophenols **46c,d,f,h** were employed, resulting in a complete lack of conversion during the initial steps.

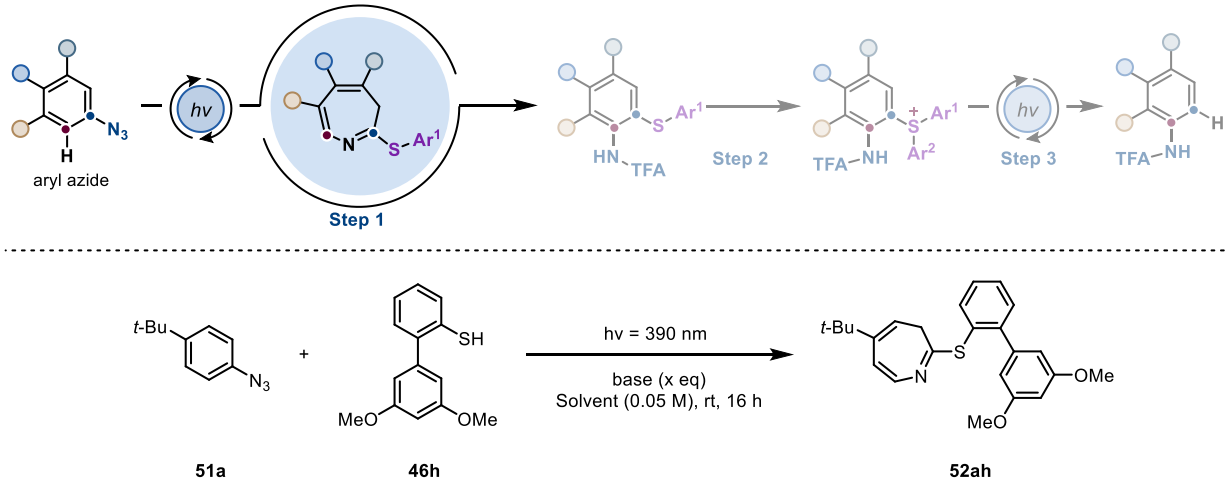

Scheme 5.11 Optimization of azepine ***49ah.***

For this reason, using aryl azide **51a** and thiophenol **46h** as model substrates, a systematic optimization of the reaction parameters was carried out for the formation of the first key intermediate, azepine **52ah** (Scheme 5.11).

*Table 5.1 Optimization of azepine **52ah** formation reaction: screening of different solvents and bases.*

[a]Entry	Solvent	Base	Yield (%)[b]
1	1,4-Dioxane	NaO*t*Bu	0
2	Ethyl Acetate	NaO*t*Bu	0
3	1,2-Dichloroethane	NaO*t*Bu	0
4	Acetonitrile	NaO*t*Bu	0
5	THF	NaO*t*Bu	0
6	1,4-Dioxane	NaOH	0
7	1,4-Dioxane	K_3PO_4	0
8	1,4-Dioxane	DABCO	0
9	1,4-Dioxane	K_2CO_3	0
10	1,4-Dioxane	NaOAc	0
11	**1,4-Dioxane**	**DMAP**	**35**
12	1,4-Dioxane	DBU	0
13	1,4-Dioxane	NEt_3	0
14	1,4-Dioxane	1-methylimidazole	28
15	1,4-Dioxane	DIPEA	0
16	1,4-Dioxane	Pyridine	0
17	1,4-Dioxane	4-methylmorpholine	12

[a] Conditions: **51a** (0.1 mmol, 1.0 equiv.), **46h** (2.2 equiv.) and base (2.0 equiv.) in degassed solvent [0.05 M] were irradiated with purple LED. [b] NMR yields

As can be seen in Table 5.1, when compounds **51a** and **46h** were irradiated in the presence of NaO*t*Bu as base, in 1,4-dioxane (best conditions found in the previously reported protocol[29]) no desired product was detected (entry 1). The same outcome was observed also when different solvents were employed instead of 1,4-dioxane. Therefore, our optimization process continued with the screening of a wide range of inorganic and organic bases. Notably, only the use of DMAP, 1-methylimidazole and 4-methylmorpholine led to the formation of the desired product, with DMAP giving the best result (35% determined by quantitative NMR, entry 11). With the aim of increasing the yield of azepine **52ah**, we then continued our investigation by screening different solvents, stoichiometry ratios and reaction times. The obtained results are summarized in Table 5.2.

*Table 5.2 Optimization of the reaction conditions for the formation of azepine **52ah**: screening of different solvents and stoichiometry ratios.*

Entry	51a:46h ratio	Solvent	DMAP (x eq.)	Yield (%)[a]
1	1:2.2	1,4-Dioxane	2	35
2	1:2.2	1,4-Dioxane	4	35
3	1:2.2	1,4-Dioxane	1	37
4	1:2.2	1,4-Dioxane	0.02	22
5	1:2.2	DMF	1	0
6	1:2.2	DCE	1	10

7	1:2.2	DCM	1	19
8	1:2.2	MeCN	1	5
9	1:2.2	Toluene	1	28
10	1:2.2	Et_2O	1	34
11	1:2.2	THF	1	5
12	1:2.2	EtOAc	1	0
13	1:2.2	$PhCF_3$	1	33
14	1:2.2	MeOH	1	0
15	1:2.2	HFIP	1	0
16	1:2.2	MTBE	1	10
17	1:2.2	DME	1	0
18	1:1.2	Acetone	1	10
19	1:1.2	1,4-Dioxane	1	57
20	1:2.4	1,4-Dioxane	1	38
21	1.2:1	1,4-Dioxane	1	53
22	**2.4:1**	**1,4-Dioxane**	**1**	**70**

[a] NMR yields

The best reaction conditions turned out to be the following: **51a** (2.4 eq.), **46h** (1.0 eq.), DMAP (1.0 eq.) at room temperature in 1,4-Dioxane under 390 nm light irradiation. Under these conditions the desired product **52ah** could be obtained in 70% yield.

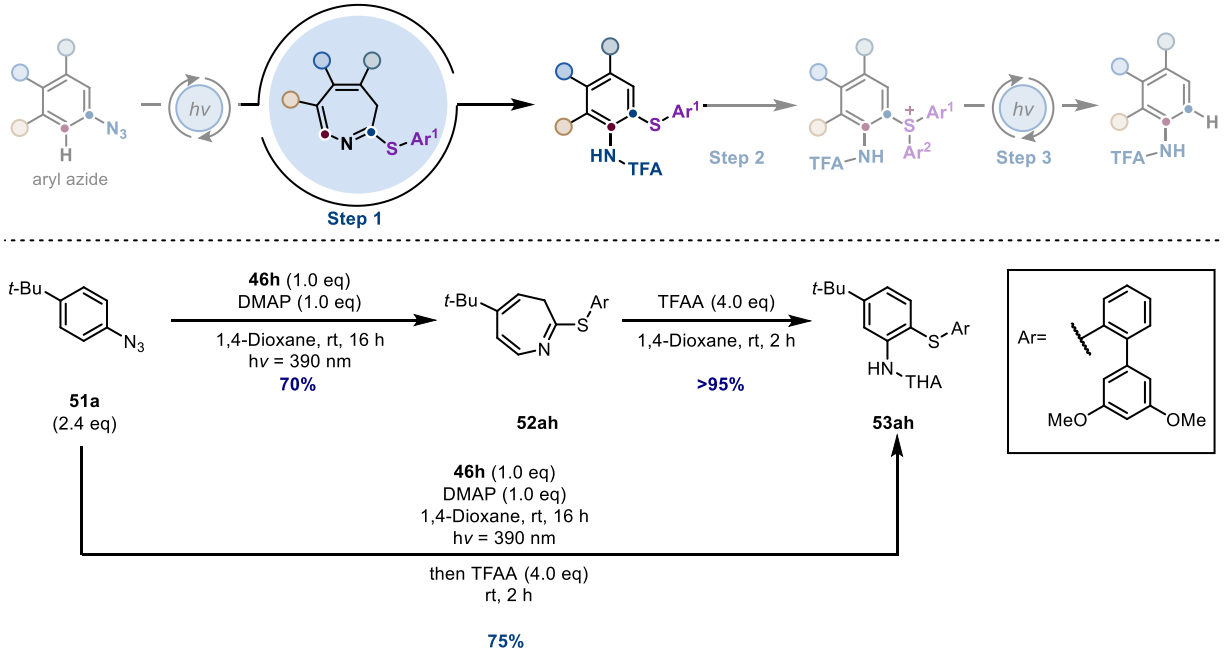

Scheme 5.12 Comparison between step-wise and one-pot telescopic approach for the synthesis of compound **53ah.**

With compound **52ah** in hand, we proceeded to investigate the synthesis of the corresponding *ortho*-aminothiophenol **53ah** (Scheme 5.12). By reacting compound **52ah** with TFAA in 1,4-dioxane at room temperature for 2h, compound **53ah** could indeed be obtained with a quantitative

yield. Encouraged by this result, we pursued the synthesis of compound **53ah** using a one-pot telescopic approach. In this method, TFAA was added directly to the reaction mixture containing intermediate **52ah**, bypassing any prior purification of the intermediate. In this case the desired product could be obtained with 75% yield, in agreement with the results obtained with the step-wise method.

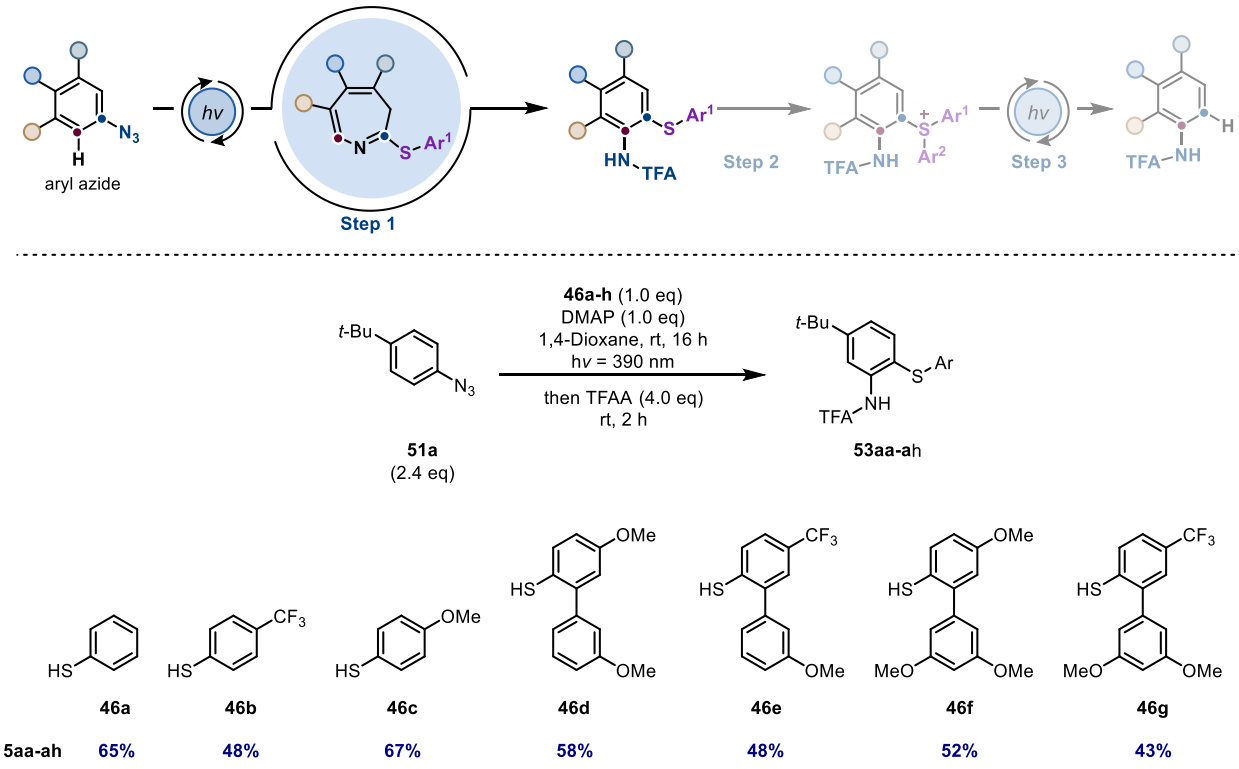

Scheme 5.13 Synthesis of *ortho*-aminothiophenols **53aa-ag**.

With the optimized conditions established, our study continued by comparing the reactivity of azide **51a** with commercially available thiophenols **46a-c** and of the series of synthetized biaryl thiophenols **46d-h** (Scheme 5.13). *Para*-methoxy-substituted thiophenols **46c**, **46d**, and **46f** delivered the corresponding *ortho*-aminothiophenols **53ac**, **53ad** and **53af** with the best yields, mainly due to their higher nucleophilicity arising from the presence of electron-donating methoxy groups. Surprisingly, electron-neutral thiophenol **46a** performed comparably well, yielding the corresponding compound **53aa** with a good yield of 65%**.** On the other hand, using trifluoromethyl-substituted thiophenols **46b**, **46e** and **46g** caused only slight reductions in yield for the formation of *ortho*-aminothiophenols **53ab**, **53ae** and **53ag**. By comparing all data, it can be concluded that, among all tested thiophenols, the best result was yielded by compound **46h**.

5.2.3.2 Synthesis of aniline derivatives : step 2 and 3

Moving to the next step, namely the synthesis of the sulfonium ion derivatives, the two classes of thiophenols mentioned above required different approaches to carry out this reaction. For amino-thiophenols **53aa–ac** a simple methylation using MeOTf was carried out. In contrast, in the case of biaryl aminothiophenols **53ad-ah**, we investigated sulfonium salt formation by means of an intramolecular cyclization pathway, using NCS as chlorinating reagent and $Bi(OTf)_3$ as Lewis acid. The proposed mechanism for such transformation is reported in Scheme 5.14.[57] As can be seen, protonation of NCS triggers electrophilic attack of chlorine on the thioether group to give an intermediate chlorosulfonium salt, which subsequently rearranges through an intramolecular S_EAr reaction to yield the target dibenzothiophene sulfonium salt.

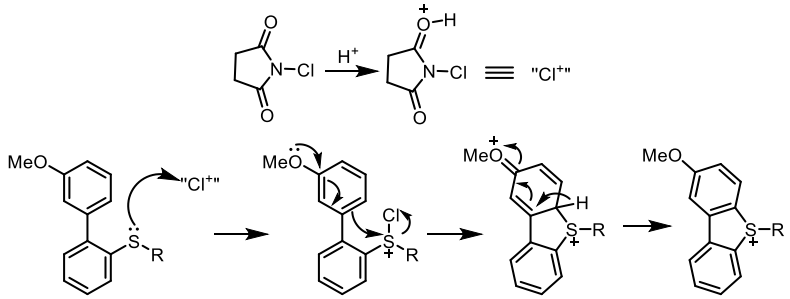

Scheme 5.14 Proposed mechanism for the intramolecular thiophenol cyclization.[57]

When subjected to methylation protocol, compound **53ac** was quantitatively converted to sulfonium derivative **54ac** (Scheme 5.15), while **53aa** and **53ab** did not react at all. Unfortunately, sulfonium salt **54ac** resulted insoluble in most organic solvents, which prevented its use for the remainder of the synthetic sequence. Focusing on biaryl aminothiophenols **53ad-ah**, the substituents present on their structure profoundly influenced both reactivity and stability in the formation of the corresponding sulfonium salts **54ad-ah**. Substituents at the 4-position of aminothiophenols **53ad,ae** had minimal impact on sulfonium yields (68%-69%). Notably, an additional methoxy group at position 11 was deleterious for aminothiophenols **53af,ag**, but enhanced conversion in the case of **53ah**. Under cyclization conditions, *ortho*-aminothiophenols **53ae** and **53ag** underwent competing chlorination, resulting in inseparable mixtures of polyhalogenated compounds.

All desired sulfonium salt products could be isolated by simple precipitation from the reaction mixture and could be employed directly in the subsequent photocleavage step without any further purification.

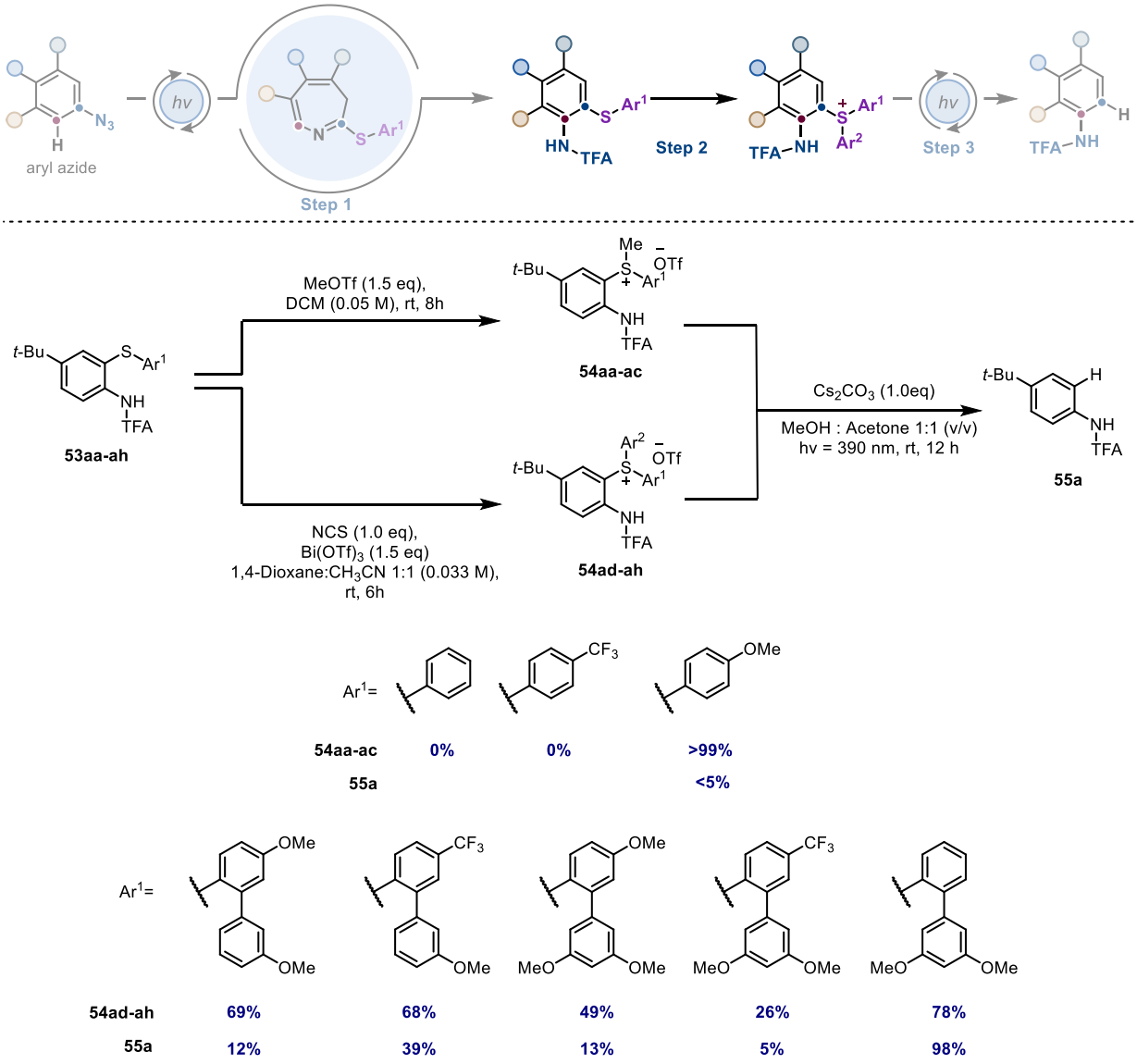

*Scheme 5.15 Synthesis of sulfonium derivatives **54ac-ah** and subsequent homolytic cleavage to aniline **55a.***

Homolytic cleavage of sulfonium derivatives is well-documented in the literature. Notably, in 2022, Zhang and co-workers demonstrated the efficient deuteration of aryl sulfonium substrates.[58] This was achieved in high yield by reacting the substrates with Cs_2CO_3 in a 1:1 (v/v) solvent mixture of CD_3OD and acetone-d_6 under 390 nm LED irradiation for 12 hours. Inspired by this work, we tried to perform the photocleavage of compounds **54ac-ah** by using a similar protocol. The proposed mechanism for this transformation is shown in Scheme 5.16.

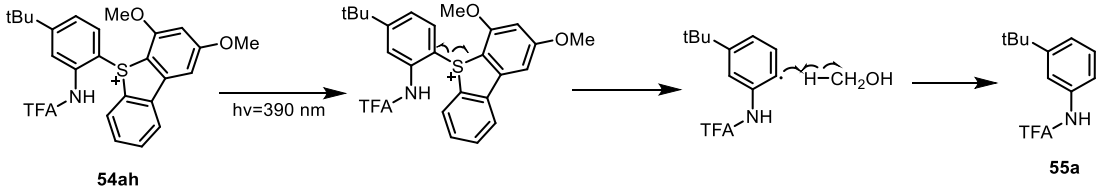

Scheme 5.16 Proposed mechanism for the cleavage of aryl sulfonium salt.

Under the chosen conditions sulfonium derivative **54ac** yielded the desired product **55a** only in traces. 3-Methoxy-substituted sulfonium salts **54ad** and **54af** proved poorly soluble in the chosen solvent mixture, thereby yielding product **55a** in low yields. Similarly, trifluoromethylated compounds **54ae,ag** provided suboptimal yields of the desired product, whereas **54ah** emerged as the optimal candidate, achieving quantitative conversion to the aniline product (Scheme 5.15).
Overall, thiophenol **46h** and its derivatives **52**,**53,54ah** demonstrated superior performances in all steps of the overall synthetic sequence from aryl azide **51a** to aniline **55a**. **48h** was therefore selected as the reagent of choice for the exploration of the full scope of the synthetic route.

5.2.4 Substrate scope

After having established the optimized conditions for the entire synthetic sequence, we moved to the substrate scope evaluation (carried out in collaboration with Giovanni Lenardon) by employing *para*-substituted aryl azides **51b-y**, readily accessible from the corresponding *para*-anilines, to synthesize *meta*-anilines that would be otherwise challenging to prepare. It is important to note that both the overall yield and the yields of individual intermediates (in brackets) are shown in Scheme 5.17. As can be seen para-alkyl substituents are well tolerated, delivering the products **55b-d** in decent yields (33%-41%) over three steps. Even dibenzylic substrate **51e** could be converted to **55e** without additional complications, providing a similar yield of the product. Electron-withdrawing substituents such as the trifluoromethyl group of **51f** are also compatible, as testified by the obtainment of product **55f** in 47% yield, while diverse benzylic functionalities, including cyano, trifluoromethyl, and protected oxygen groups, were tolerated, albeit the corresponding products **55g-i** were formed only in moderate yields (21–29%). Remarkably, substrates presenting free alcohol functions, as aryl azide **51j**, perform well, with no observed side reactions during the initial step, showcasing the protocol's chemoselectivity for thiol nucleophiles. Synthetically sensitive groups, such as Bpin (**51k**) and alkenes (**51l**), which enable potential downstream functionalization, are also tolerated, yielding anilines **55k** and **55l** in 51% and 42% yield, respectively. It is important to highlight that for substrate **51k** we have not been able to isolate the corresponding *ortho*-aminothiophenol derivative **53kh** formed with thiophenol **46h**, due to partial hydrolyzation on column chromatography. Therefore for this substrate we slightly modified our procedure by performing step 2 directly on the crude mixture resulting from step 1. The corresponding sulfonium salt **54kh** was then simply isolated by precipitation from diethyl ether and subjected to the last photocleavage step.
Furthermore, *para*-phenyl substited azide **51m** is also a viable substrate, affording aniline **55m** in 31% yield. Mono-substituted phenyl residues, both with EDG (**51n**) and EWG (**51o,p**) groups, in

4-position were found to enhance reactivity, producing **55n-p** in 47%, 48%, and 57% yield, respectively. Azides bearing symmetrically di*meta*-substituted 4-phenyl substituents **51q** and **51r** provided the corresponding aniline derivatives **55q,r** in 53% and 32% yields, respectively. The introduction of an additional *para*-phenyl substituent in **51s** enables the synthesis of a rare tetrasubstituted aniline **55s**, achieved in 29% yield, which highlights the method capacity to overcome steric constraints often limiting traditional cross-coupling approaches.

For unsymmetrical *meta*-substituted azides **51t-v**, mixtures of *ortho* and *para* products arise due to the incipient nitrene capacity to cyclize at two distinct *ortho* positions (see Scheme 5.17). Strong electron-donating groups, such as methoxy groups in compound **51u**, favor formation of the *ortho* product, providing regioisomeric anilines **55u** and **55u'** in a 1:9 ratio, with a total yield of 59%. In contrast, weaker donors like *tert*-butyl, in compound **51t**, and bicyclic 6-azido-tetrahydronaphthalene **51v** produce nearly equimolar mixtures of isomers, with total yields of 36% and 52%, respectively.

The scope of the methodology was expanded to include azide derivatives of bioactive compounds, enabling late-stage exploration of substitution patterns. Use of Butamben, a local anesthetic, demonstrated ester functionality compatibility, producing *meta*-Butamben **55w** in 42% yield. Similarly, the azide derived from anticancer agent aminoglutethimide underwent efficient *para*-to-*meta* isomerization to form **55x** in 55% yield. Estrone-derived azides yielded both possible *ortho* isomerized products **55y** and **55y'** in excellent 56% yield with a 1:1 regioisomeric ratio; it is worth noting that regioisomer **55y'** had remained synthetically inaccessible to date, which highlights the transformative potential in medicinal chemistry of the developed nitrogen walk protocol.

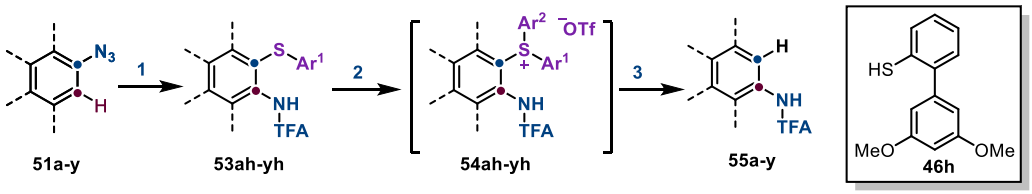

(1) **46h** (1.0 eq), DMAP (1.0 eq), 1,4-Dioxane, rt, 16 h, hν = 390 nm; (2) NCS (1.0 eq), $Bi(OTf)_3$ (1.5 eq), 1,4-Dioxane:CH_3CN 1:1 (0.033 M), rt, 6h; (3) Cs_2CO_3 (1.0eq), hν=390 nm, MeOH:Acetone 1:1 (0.05M), rt. 12h.

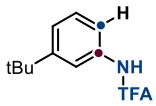

55a 53%
[**(1)** 65%, **(2-3)** 81%]

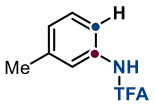

55b 33%
[**(1)** 44%, **(2-3)** 75%]

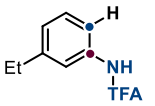

55c 41%
[**(1)** 52%, **(2-3)** 78%]

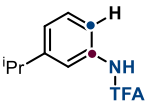

55d 33%
[**(1)** 42%, **(2-3)** 77%]

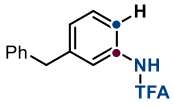

55e 33%
[**(1)** 42%, **(2-3)** 78%]

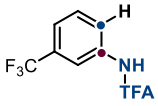

55f 47%
[**(1)** 63%, **(2-3)** 74%]

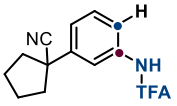

55g 21%
[**(1)** 42%, **(2-3)** 49%]

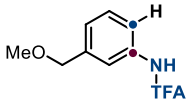

55h 25%
[**(1)** 40%, **(2-3)** 63%]

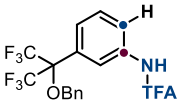

55i 29%
[**(1)** 53%, **(2-3)** 55%]

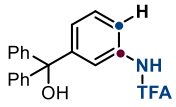

55j 55%
[**(1)** 72%, **(2-3)** 76%]

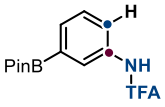

55k 51%
[**(1-2)** 59%, **(3)** 98%]

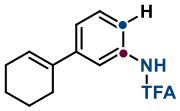

55l 42%
[**(1)** 78%, **(2-3)** 66%]

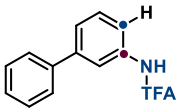

55m 31%
[**(1)** 43%, **(2-3)** 71%]

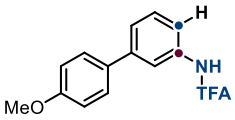

55n 47%
[**(1)** 60%, **(2-3)** 79%]

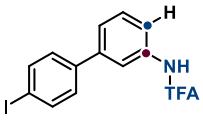

55o 48%
[**(1)** 62%, **(2-3)** 77%]

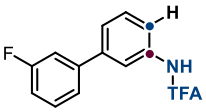

55p 57%
[**(1)** 76%, **(2-3)** 75%]

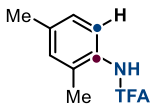

55q 53%
[**(1)** 80%, **(2-3)** 67%]

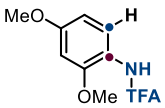

55r 32%
[**(1)** 80%, **(2-3)** 40%]

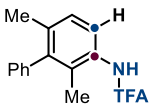

55s 29%
[**(1)** 59%, **(2-3)** 49%]

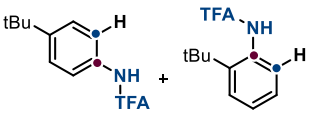

55t : 55t' (1.1:1) 36%
[**(1)** 56%, **(2-3)** 64%]

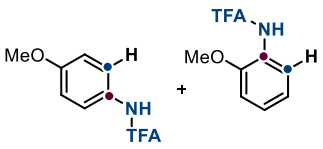

55u : 55u' (1:9) 59%
[**(1)** 79%, **(2-3)** 75%]

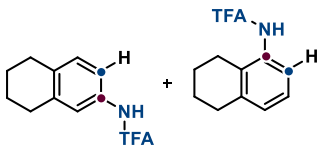

55v : 55v' (1.1:1) 52%
[**(1)** 77%, **(2-3)** 68%]

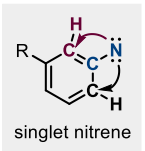

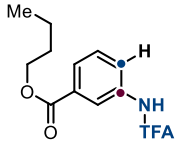

55w 42%
[**(1)** 58%, **(2-3)** 72%]
from Butamben

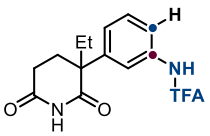

55x 55%
[**(1)** 69%, **(2-3)** 80%]
from Aminoglutethimide

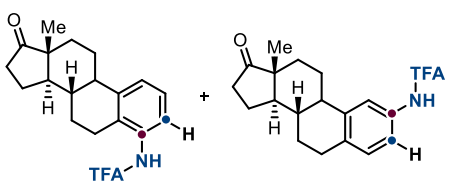

55y : 55y' (1:1) 56%
[**(1)** 67%, **(2-3)** 84%]
from Estrone

Scheme 5.17 Scope of nitrogen ring walk.

5.2.5 Synthesis of *ortho*-sbstituted anilines

Although in the previous paragraph we aimed for the cleavage of the sulfonium salt in order to obtain the desired rearranged anilines, it is important to notice that such intermediates have emerged in the last years as powerful synthetic handles for diverse functionalization processes, including cross-coupling reactions and redox chemistry.[59–61] Traditionally, these structures are either pre-installed on functionalized starting materials or introduced directly via C–H activation with remarkable para-selectivity.[62,63]

With the protocol described above we expand this paradigm by enabling the installation of sulfonium salts with complete regiocontrol at the *ipso* position relative to the nitrogen atom, yielding *ortho*-substituted sulfonium derivatives inaccessible via traditional methods. This strategy allows direct access to a broad array of *ortho*-aniline derivatives, extending the scope of previous methodology. (Scheme 5.18). For example photo-redox-mediated decomposition of **54qh** afforded *ortho*-fluoroaniline **56a** and *ortho*-chloroaniline **56b** in 76% and 69% yield, respectively. Remarkably, the light-mediated protocol unlocked the direct exchange of the sulfonium group for a BPin moiety in 75% yield. This approach delivered **56c**, a organometallic reagent of exceptional utility, serving as a versatile intermediate for cross-coupling reactions. Furthermore, the utility of sulfonium salts in transition-metal catalysis was demonstrated through Suzuki–Miyaura cross-coupling, delivering ortho-arylated aniline **56d** in 69% yield.

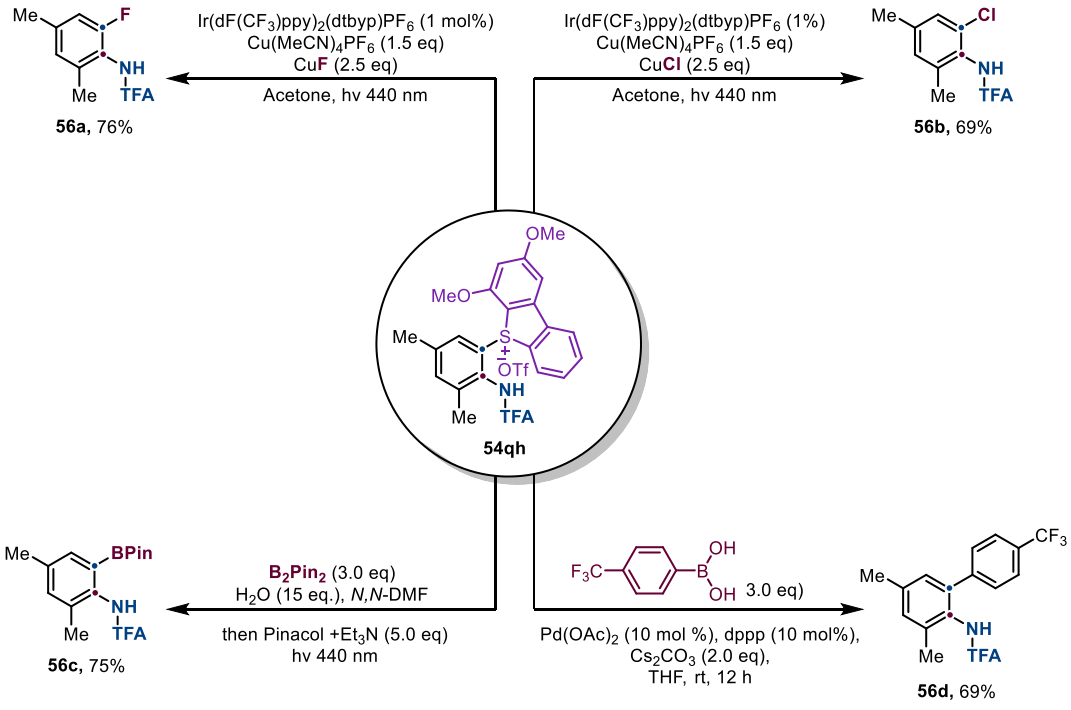

*Scheme 5.18 Possible diversification of substrate **54qh.***

5.3 Conclusions

In conclusion, we have developed a novel synthetic strategy for nitrogen ring migration, enabling the transformation of readily accessible para-aminated building blocks into more challenging meta-aminated derivatives. This approach utilizes well-established singlet nitrene chemistry to capture biaryl thiophenol nucleophiles within seven-membered azepine ring systems. The resulting intermediate can undergo an efficient in situ rearrangement to yield the corresponding ortho-aminothiophenol through a simple treatment with TFAA. Subsequent intramolecular cyclization of the resulting biaryl thioethers afforded functionalized sulfonium salts under mild conditions. Finally, photo-induced cleavage facilitated the formation of the desired ortho-isomerized anilines. This protocol has proven efficient for late-stage reconfiguration of substitution patterns in bioactive molecules, facilitating chemical space exploration without the requirement for *de novo* total synthesis. Additionally, sulfonium intermediates have been harnessed for the synthesis of diverse *ortho*-substituted anilines, overcoming limitations of traditional methods and expanding the scope of accessible molecular architectures.

5.4 Materials and methods

5.4.1 General Synthetic remarks

All required fine chemicals were used directly without purification unless stated otherwise. All air and moisture sensitive reactions were carried out under nitrogen atmosphere using standard Schlenk manifold techniques. All solvents were bought from Acros as 99.8% purity and degassed by N_2 bubbling. ^{1}H, ^{13}C and ^{19}F NMR spectra were recorded on Bruker Avance Neo 600 MHz, Varian VNMRS 600 MHz, Bruker NanoBay Avance III HD NMR 500 MHz or on Varian VNMRS 400 MHz instruments, at various field strengths as indicated and were referenced to the residual peak solvent (for ^{1}H and ^{13}C) or by the instrument internally after locking and shimming to the deuterated solvent (for ^{19}F). ^{1}H NMR coupling constants (J) are reported in Hertz (Hz) and refer to apparent multiplicities and not true coupling constants. Data is reported as follows: chemical shift (δ), integration, multiplicity (s = singlet, br s = broad singlet, d = doublet, t = triplet, q = quartet, qi = quintet, sx = sextet, sp = septet, m = multiplet, dd = doublet of doublets, etc.), proton assignment (determined by 2D NMR experiments: COSY, HSQC and HMBC) where possible. High-resolution mass spectra were obtained using a JEOL JMS-700 spectrometer, a Fissions VG Trio 2000 quadrupole mass spectrometer, Thermo Scientific LTQ Orbitrap XL spectrometer or

Finnigan MAT 95. Spectra were obtained using electron impact ionization (EI) or positive electrospray (ESI) techniques. Analytical TLC: aluminum backed plates pre-coated (0.25 mm) with Merck Silica Gel 60 F254. Compounds were visualized by exposure to UV light or by dipping the plates in ninhydrin or permanganate ($KMnO_4$) stain followed by heating. Flash column chromatography was performed using Merck Silica Gel 60 (40–63 μm). All mixed solvent eluents are reported as v/v solutions. The LEDs used are Kessil PR 160 with irradiation wavelengths of 427 and 390 nm. All the reactions were conducted in CEM 9 mL glass microwave tubes.

5.4.2 Synthetic procedures

5.4.2.1 Synthesis of thiol substrates

General Procedure 1

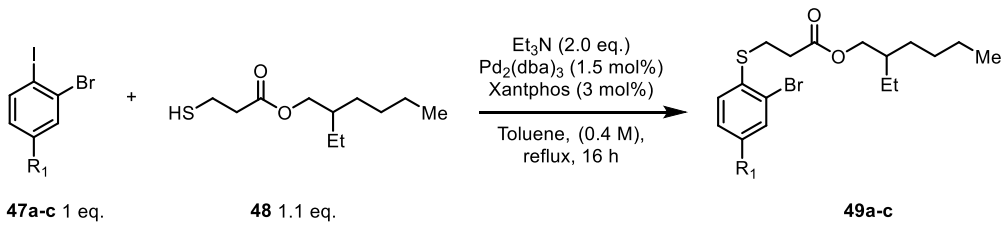

47a-c 1 eq. **48** 1.1 eq. **49a-c**

Under N_2 atmosphere, to a Schlenk tube were added the suitable 2-bromo-1-iodobenzene **47a-c**, 1.0 eq.), $Pd_2(dba)_3$ (1.5 mol%), Xantphos (3.0 mol%) and 2-ethylhexyl 3-mercaptopropanoate (**48**, 1.1 eq.). The vessel was evacuated and backfilled with argon (× 3). Toluene (the required volume to obtain a 0.4 M solution of the substrate) was added, followed by Et_3N (2.0 eq.). The resulting mixture was degassed with argon for 5 min. and then heated to reflux for 16 h. The reaction was then allowed to cool down to room temperature. The mixture was filtered over a pad of Celite® and concentrated *in vacuo*. The resulting yellow oil was purified by flash column chromatography to afford the title compound as a colorless viscous oil.

2-ethylhexyl 3-((2-bromo-4-methoxyphenyl)thio)propanoate (49a)

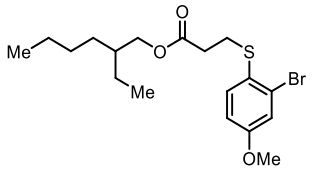

Following **GP1**, 2-bromo-1-iodo-4-methoxybenzene (**49a**, 3.0 g, 9.6 mmol, 1.0 eq.) gave the title compound as colorless viscous oil after flash column chromatography (Pentane/EtOAc 9:1 to 7:3) (2.6 g, 6.5 mmol, 68%).

^{1}H NMR ($CDCl_3$, 600 MHz) δ 7.39 (d, *J*=8.6 Hz,1H), 7.17 (d, *J*=2.8 Hz, 1H), 6.82 (dd, *J*=8.7, 2.8 Hz,1H), 4.04 – 3.96 (m, 2H), 3.79 (s, 3H), 3.10 (t, *J*=7.3 Hz, 2H), 2.58 (t, *J*=7.3 Hz, 2H), 1.60 – 1.50 (m, 1H), 1.40– 1.18 (m, 8H), 0.93 – 0.81 (m, 6H); ^{13}C NMR ($CDCl_3$, 151 MHz) *δ* 172.0, 159.7, 134.5, 128.5, 126.4, 119.0, 114.3, 67.3, 55.8, 38.8, 34.4, 30.5, 30.1, 29.0, 23.9, 23.1, 14.2, 11.1.

2-ethylhexyl 3-((2-bromo-4-(trifluoromethyl)phenyl)thio)propanoate (49b)

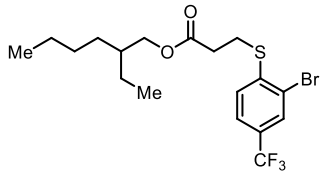

Following **GP1**, 2-bromo-1-iodo-4-methoxybenzene (**49b**, 3.4 g, 9.6 mmol, 1.0 eq.) gave the title compound as colorless viscous oil after flash column chromatography (Pentane/EtOAc 9:1 to 7:3) (4.2 g, 9.5 mmol, 98%).

^{1}H NMR ($CDCl_3$, 600 MHz) δ 7.78 (1H, s), 7.53 (1H, d, *J*=8.3 Hz), 7.29 (1H, d, *J*=8.5 Hz), 4.04 (2H, d, *J*=5.5 Hz), 3.26 (2H, t, *J*=7.4 Hz), 2.73 (2H, t, *J*=7.5 Hz), 1.65 – 1.47 (1H, m), 1.42 – 1.21 (8H, m), 0.89 (6H, t, *J*=7.5 Hz); ^{13}C NMR ($CDCl_3$, 151 MHz) δ 171.5, 143.1, 130.0 (q, *J* = 4.1 Hz), 128.5 (q, *J* = 33.2 Hz), 126.4, 124.7 (q, *J* = 3.9 Hz), 122.5 (q, *J* = 17.3 Hz), 67.7, 38.9, 33.5, 30.5, 29.1, 27.6, 23.9, 23.1, 14.2, 11.1; ^{19}F NMR ($CDCl_3$, 564 MHz) δ -62.51.

2-ethylhexyl 3-((2-bromophenyl)thio)propanoate (49c)

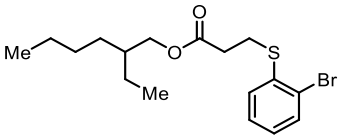

Following **GP1**, 1-bromo-2-iodobenzene (**49c**, 10 g, 35.4 mmol, 1.0 eq) gave the title compound after flash column chromatography (Pentane/EtOAc 9:1 to 7:3) as colorless viscous oil (12.1 g, 32.4 mmol, 92%).

^{1}H NMR ($CDCl_3$, 600 MHz) δ 7.56 – 7.53 (1H, m), 7.31 – 7.23 (2H, m), 7.07 – 7.00 (1H, m), 4.05 – 3.97 (2H, m), 3.19 (2H, t, J = 7.5 Hz), 2.66 (2H, t, J = 7.5 Hz), 1.60 – 1.51 (1H, m), 1.34 (2H, p, J = 7.5 Hz), 1.31 – 1.22 (6H, m), 0.87 (6H, t, J = 7.4 Hz); ^{13}C NMR ($CDCl_3$, 151 MHz) δ 171.6, 136.8, 133.1, 128.7, 127.8, 127.0, 124.2, 67.3, 38.6, 33.8, 30.3, 28.8, 28.0, 23.7, 22.9, 14.0, 10.9..

General Procedure 2

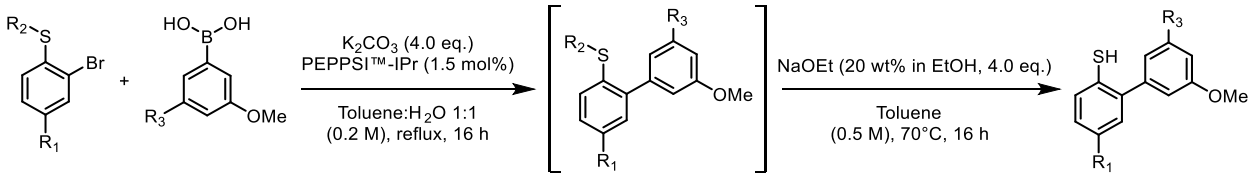

Under N_2 atmosphere, to a Schlenk tube were added **49a-c** (1.0 eq.) and toluene (the required amount to obtain a 0.4 M solution), followed by a solution of potassium carbonate (4.0 eq.) in water (0.4 M) and the suitable boronic acid **50a,b** (1.3 eq.). The reaction vessel was degassed with argon under vigorous stirring. PEPPSI™- IPr catalyst (1.5 mol%) was added and, after additional degassing, the resulting mixture was heated to reflux for 16 h. The reaction was allowed to cool down to room temperature. The mixture was filtered over a pad of Celite®. The organic phase was washed with saturated aq. potassium carbonate (2 × 50 mL), dried over magnesium sulfate and concentrated *in vacuo*. Without any further purification, the crude was solubilized in toluene (0.5 M) and NaOEt (21 wt% in denatured EtOH, 4.0 eq.) was added. The resulting mixture was heated at 70° C for 16 h. After cooling down to room temperature, the reaction mixture was diluted with EtOAc and then acidified to pH 4 using 1 M aq. HCl. After separation, the organic phase was washed with brine, dried over anhydrous magnesium sulfate, filtered and concentrated *in vacuo*. The crude was purified by flash column chromatography to afford the title compound as a colorless viscous oil, which was dried under high vacuum overnight prior to use for further reactions. The final thiophenols can be purified also by acid/base extraction using 2 M aqueous NaOH and Et_2O as the organic phase.

3',5-dimethoxy-[1,1'-biphenyl]-2-thiol (46d)

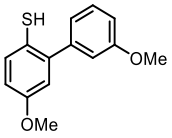

Following **GP2**, 2-ethylhexyl 3-((2-bromo-4-methoxyphenyl)thio)propanoate (**49a**, 1.3 g, 3.2 mmol, 1 eq.) and (3-methoxyphenyl)boronic acid (**50a**, 636 mg, 4.2 mmol, 1.3 eq.) gave the title compound after column chromatography (Pentane to Pentane/EtOAc 8:2) as a colorless viscous oil (660 mg, 2.7 mmol, 83% over two steps).

^{1}H NMR ($CDCl_3$, 600 MHz) δ 7.39 – 7.33 (1H, m), 7.30 (1H, d, *J* = 8.5 Hz), 6.98 (1H, dt, *J* = 7.6, 1.3 Hz), 6.96 – 6.91 (2H, m), 6.84 – 6.83 (1H, m), 6.82 – 6.80 (1H, m), 3.85 (3H, s), 3.80 (3H, s), 3.27 (1H, s); ^{13}C NMR ($CDCl_3$, 151 MHz) δ 159.6, 158.1, 142.5, 142.4, 131.4, 129.6, 121.6, 120.6, 116.0, 114.7, 114.2, 113.5, 55.6, 55.4.

3'-methoxy-5-(trifluoromethyl)-[1,1'-biphenyl]-2-thiol (46e)

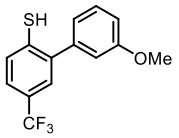

Following **GP2**, 2-ethylhexyl 3-((2-bromo-4-(trifluoromethyl)phenyl)thio)propanoate (**49b**, 2.1 g, 4.8 mmol, 1 eq.) and (3-methoxyphenyl)boronic acid (**50a**, 942 mg, 6.2 mmol, 1.3 eq.) gave the title compound after column chromatography (Pentane to Pentane/EtOAc 8:2) as a colorless viscous oil (260 mg, 1 mmol, 21% over two steps).

^{1}H NMR ($CDCl_3$, 600 MHz) δ 7.48 (1H, s), 7.44 (1H, s), 7.39 (1H, t, *J*=7.9 Hz), 7.00 – 6.96 (2H, m), 6.93 (2H, t, *J*=2.1 Hz), 3.86 (3H, s), 3.62 (1H, s); ^{13}C NMR ($CDCl_3$, 151 MHz) δ 159.9, 140.9, 140.4, 136.7, 130.0, 129.2, 127.7 (q, *J* = 32.7 Hz), 127.1 (q, *J* = 3.8 Hz), 124.6 (q, *J* = 3.7 Hz), 124.2 (q, *J* = 271.8 Hz), 121.4, 114.6, 114.1, 55.5; ^{19}F NMR ($CDCl_3$, 564 MHz) δ -62.4.

3',5,5'-trimethoxy-[1,1'-biphenyl]-2-thiol (46f)

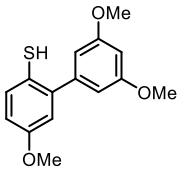

Following **GP2**, 2-ethylhexyl 3-((2-bromo-4-methoxyphenyl)thio)propanoate (**49a**, 1.3 g, 3.2 mmol, 1 eq.) and (3,5-dimethoxyphenyl)boronic acid (**50b**, 762 mg, 4.2 mmol, 1.3 eq.) gave the title compound after column chromatography (Pentane to Pentane/EtOAc 8:2) as a colorless viscous oil (160 mg, 0.6 mmol, 18% over two steps).

^{1}H NMR ($CDCl_3$, 600 MHz) δ 7.46 (1H, d, *J*=8.6 Hz), 6.81 – 6.76 (2H, m), 6.44 (1H, t, *J*=2.2 Hz), 6.41 (2H, d, *J*=2.3 Hz), 3.80 (3H, s), 3.78 (6H, s); ^{13}C NMR ($CDCl_3$, 151 MHz) δ 160.4, 159.2, 144.7, 142.3, 132.9, 126.4, 115.4, 114.3, 107.9, 99.9, 55.6, 55.5.

3',5'-dimethoxy-5-(trifluoromethyl)-[1,1'-biphenyl]-2-thiol (46g)

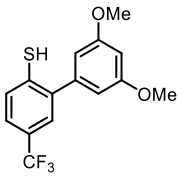

Following **GP2**, 2-ethylhexyl 3-((2-bromo-4-(trifluoromethyl)phenyl)thio)propanoate (**49b**, 2.1 g, 4.8 mmol, 1 eq.) and (3,5-dimethoxyphenyl)boronic acid (**50b**, 1.1 g, 6.2 mmol, 1.3 eq.) gave the title compound after column chromatography (Pentane to Pentane/EtOAc 8:2) as a colorless viscous oil (160 mg, 0.6 mmol, 18% over two steps).

^{1}H NMR ($CDCl_3$, 600 MHz) δ 7.47 (1H, s), 7.43 (1H, s), 6.51 (3H, s), 3.67 (1H, s); ^{13}C NMR ($CDCl_3$, 151 MHz) δ 161.2, 141.4, 140.4, 136.7, 129.2, 127.7 (q, *J* = 32.6 Hz), 127.0 (q, *J* = 4.1 Hz), 124.7 (q, *J* = 3.8 Hz), 124.2 (q, *J* = 273.3 Hz), 107.1, 100.5, 55.6; ^{19}F NMR ($CDCl_3$, 564 MHz) δ -62.40.

3',5'-dimethoxy-[1,1'-biphenyl]-2-thiol (46h)

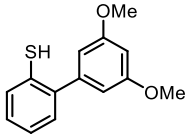

Following **GP2**, 2-ethylhexyl 3-((2-bromo-4-methoxyphenyl)thio)propanoate (**49c**, 12.1 g, 32.4 mmol, 1 eq) and (3,5-dimethoxyphenyl)boronic acid (**50b**, 7.73 g, 15.0 mmol, 1.3 eq) gave the title compound after column chromatography (Pentane to Pentane/EtOAc 8:2) as a colorless viscous oil (3.5 g, 14.1 mmol, 70%).

^{1}H NMR ($CDCl_3$, 600 MHz) δ 7.34 (1H, d, *J* = 6.6 Hz), 7.29 – 7.12 (4H, m), 6.53 (3H, s), 6.49 (1H, s), 3.82 (6H, s), 3.49 (1H, s); ^{13}C NMR ($CDCl_3$, 151 MHz) δ 160.9, 142.9, 140.4, 131.0, 130.3, 129.4, 128.1, 125.5, 107.3, 100.0, 55.5

5.4.2.2 Synthesis of azide substrates

General procedure 3

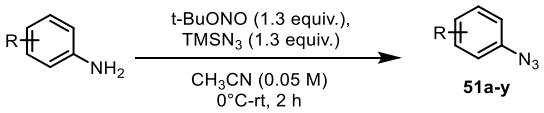

Under N_2 atmosphere, to a Schlenk tube was added the suitable aniline substrate (1.3 eq.), which was dissolved in CH_3CN (0.05 M). After warming up to rt, *t*-BuONO (1.3 equiv.) was added, followed by $TMSN_3$ (1.3 equiv.), added dropwise. The solution was then allowed to warm to r.t. and stirring continued for 2 h. At this point, azide formation was confirmed by TLC analysis. The solvent was removed *in vacuo*, and the crude product was purified by flash column chromatography to afford the desired compound.

1-azido-4-(tert-butyl)benzene (51a)

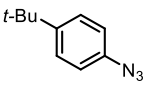

Following **GP3**, 4-(tert-butyl)aniline (2.0 g, 13.4 mmol, 1 eq.) gave **51a** (63%) as an oil. ^{1}H NMR ($CDCl_3$, 600 MHz) δ 7.3 (1H, t, *J*=7.9 Hz), 7.2 (1H, d, *J*=10.7 Hz), 7.0 (1H, t, *J*=2.1 Hz), 6.9 (1H,

d, *J*=11.2 Hz), 1.3 (9H, s); ^{13}C NMR ($CDCl_3$, 151 MHz) δ 153.3, 139.6, 129.4, 122.1, 116.2, 116.0, 34.8, 31.2. Spectroscopic data are in agreement with those reported in the literature.[64]

1-azido-4-methylbenzene (51b)

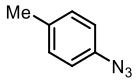

Following **GP3**, p-toluidine (2.0 g, 18.7mmol, 1 eq.) gave **51b** (63%) as an oil. ^{1}H NMR ($CDCl_3$, 600 MHz) δ 7.21 (2H, d, *J*=5.3 Hz), 6.90 (2H, d, *J*=8.1 Hz), 2.35 (3H, s); ^{13}C NMR ($CDCl_3$, 151 MHz) δ 137.2, 134.6, 130.3, 118.8, 20.8. Spectroscopic data are in agreement with those reported in the literature.[65]

1-azido-4-ethylbenzene (51c)

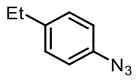

Following **GP3**, 4-ethylaniline (2.0 g, 16.5 mmol, 1 eq.) gave **51c** (63%) as an oil. ^{1}H NMR ($CDCl_3$, 600 MHz) δ 7.22 (2H, d, *J*=8.4 Hz), 7.04 (2H, d, *J*=8.5 Hz), 2.61 (2H, q, *J*=7.6 Hz), 1.24 (4H, t, *J*=7.6 Hz); ^{13}C NMR ($CDCl_3$, 151 MHz) δ 141.1, 137.3, 129.2, 118.9, 28.3, 15.6. Spectroscopic data are in agreement with those reported in the literature.[66]

1-azido-4-isopropylbenzene (51d)

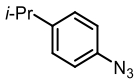

Following **GP3**, 4-isopropylaniline (2.0 g, 14.8 mmol, 1 eq.) gave **51d** (63%) as an oil. ^{1}H NMR ($CDCl_3$, 600 MHz) δ 7.21 (2H, d, *J*=8.4 Hz), 6.96 (2H, d, *J*=8.5 Hz), 2.90 (1H, hept, *J*=6.9 Hz), 1.24 (6H, d, *J*=7.0 Hz); ^{13}C NMR ($CDCl_3$, 151 MHz) δ 145.74, 137.36, 127.74, 118.91, 33.58, 23.99. Spectroscopic data are in agreement with those reported in the literature.[67]

1-azido-4-benzylbenzene (51e)

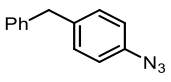

Following **GP3**, 4-benzylaniline (2.0 g, 10.9 mmol, 1 eq.) gave **51e** (63%) as an oil. ^{1}H NMR ($CDCl_3$, 600 MHz) δ 7.30 (2H, t, *J*=7.6 Hz), 7.22 (1H, t, *J*=7.4 Hz), 7.18 (5H, d, *J*=8.0 Hz), 6.96 (2H, d, *J*=8.3 Hz), 3.97 (2H, s); ^{13}C NMR ($CDCl_3$, 151 MHz) δ 140.8, 138.0, 137.9, 130.3, 128.8, 128.6, 126.2, 119.1, 41.3. Spectroscopic data are in agreement with those reported in the literature.[68]

1-azido-4-(trifluoromethyl)benzene (51f)

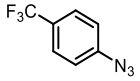

Following **GP3**, 4-(trifluoromethyl)aniline (2.0 g, 12.4 mmol, 1 eq.) gave **51f** (63%) as an oil. ^{1}H NMR ($CDCl_3$, 600 MHz) δ 7.61 (2H, d, *J*=8.4 Hz), 7.11 (2H, d, *J*=8.3 Hz); ^{13}C NMR ($CDCl_3$, 151 MHz) δ δ 143.7, 127.0 (q, *J*=31.7 Hz), 127.0 (q, *J*=3.7 Hz), 123.9 (d, *J*=271.9 Hz), 119.2 Spectroscopic data are in agreement with those reported in the literature. [69]

1-(4-azidophenyl)cyclopentane-1-carbonitrile (51g)

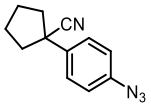

Following **GP3**, 1-(4-aminophenyl)cyclopentane-1-carbonitrile (1.0 g, 5.4 mmol, 1 eq.) gave **51g** (63%) as an oil. ^{1}H NMR ($CDCl_3$, 600 MHz) δ 7.43 (2H, d, *J*=8.6 Hz), 7.03 (2H, d, *J*=8.7 Hz), 2.53 – 2.40 (2H, m), 2.11 – 2.00 (4H, m), 1.98 – 1.86 (2H, m); ^{13}C NMR ($CDCl_3$, 151 MHz) δ 139.7, 136.5, 127.5, 124.1, 119.4, 47.3, 40.4, 24.1. Spectroscopic data are in agreement with those reported in the literature.[70]

1-azido-4-(methoxymethyl)benzene (51h)

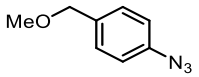

Following **GP3**, 4-(methoxymethyl)aniline (2.0 g, 14.6 mmol, 1 eq.) gave **51h** (63%) as an oil. ^{1}H NMR ($CDCl_3$, 600 MHz) δ 7.32 (2H, d, *J*=8.5 Hz), 7.01 (2H, d, *J*=8.4 Hz), 4.42 (2H, s), 3.38 (3H, s); ^{13}C NMR ($CDCl_3$, 151 MHz) δ 139.5, 135.1, 129.4, 119.1, 74.2, 58.2.

1-azido-4-(2-(benzyloxy)-1,1,1,3,3,3-hexafluoropropan-2-yl)benzene (51i)

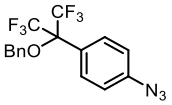

Following **GP3**, 2-(4-azidophenyl)-1,1,1,3,3,3-hexafluoropropan-2-ol (1.0 g, 3.5 mmol, 1 eq.) gave **51i** (63%) as an oil. ^{1}H NMR ($CDCl_3$, 600 MHz) δ 7.61 (2H, d, *J*=8.5 Hz), 7.42 – 7.32 (5H, m), 7.14 – 7.10 (2H, m), 4.63 (2H, s); ^{13}C NMR ($CDCl_3$, 151 MHz) δ 142.6, 136.2, 129.9, 128.8, 128.4, 127.3, 124.6, 122.5 (q, *J*=291.2 Hz), 119.5, 68.2, 64.8; ^{19}F NMR ($CDCl_3$, 564 MHz) δ -70.83. Spectroscopic data are in agreement with those reported in the literature.[70]

(4-azidophenyl)diphenylmethanol (51j)

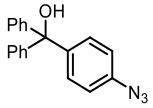

Following **GP3**, (4-bromophenyl)diphenylmethanol (2 g, 5.9 mmol, 1 eq.) gave **51j** (63%) as an oil. ^{1}H NMR ($CDCl_3$, 600 MHz) δ 7.34 – 7.24 (12H, m), 6.97 (2H, d, *J* = 8.6 Hz), 2.78 (1H, s); ^{13}C NMR ($CDCl_3$, 151 MHz) δ 146.7, 143.8, 139.1, 129.6, 128.2, 127.9, 127.6, 118.6, 81.9.

2-(4-azidophenyl)-4,4,5,5-tetramethyl-1,3,2-dioxaborolane (51k)

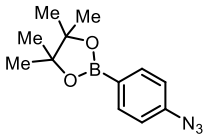

Following **GP3**, 4-(4,4,5,5-tetramethyl-1,3,2-dioxaborolan-2-yl)aniline (2 g, 9.13 mmol, 1 eq.) gave **51k** (63%) as an oil. ^{1}H NMR ($CDCl_3$, 600 MHz) δ 8.89 (1H, s), 8.44 (1H, d, *J*=2.1 Hz), 7.52 (1H, d, *J*=8.2 Hz), 7.41 (2H, d, *J*=8.1 Hz), 7.25 (1H, dd, *J*=8.2, 2.1 Hz), 7.05 (2H, d, *J*=8.0 Hz), 1.30 (9H, s); ^{13}C NMR ($CDCl_3$, 151 MHz) δ 156.2, 154.6 (q, *J*=37.7 Hz), 140.4, 137.3, 136.8, 129.5, 128.7 (q, *J*=32.8 Hz), 126.7, 126.2 (q, *J*=3.8 Hz), 124.0, 123.8 (q, *J*=271.8 Hz), 118.8, 116.7, 115.5 (d, *J*=288.8 Hz), 35.4, 31.1; ^{19}F NMR ($CDCl_3$, 564 MHz) δ -62.7, -76.. Spectroscopic data are in agreement with those reported in the literature.[71]

4'-azido-2,3,4,5-tetrahydro-1,1'-biphenyl (51l)

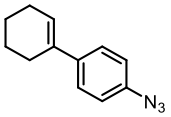

Following **GP3,** 2',3',4',5'-tetrahydro-[1,1'-biphenyl]-4-amine (2.0 g, 11.5 mmol, 1 eq.) gave **51l** (63%) as an oil. ^{1}H NMR ($CDCl_3$, 600 MHz) δ 8.89 (1H, s), 8.44 (1H, d, *J*=2.1 Hz), 7.52 (1H, d, *J*=8.2 Hz), 7.41 (2H, d, *J*=8.1 Hz), 7.25 (1H, dd, *J*=8.2, 2.1 Hz), 7.05 (2H, d, *J*=8.0 Hz), 1.30 (9H, s); ^{13}C NMR ($CDCl_3$, 151 MHz) δ 156.2, 154.6 (q, *J*=37.7 Hz), 140.4, 137.3, 136.8, 129.5, 128.7 (q, *J*=32.8 Hz), 126.7, 126.2 (q, *J*=3.8 Hz), 124.0, 123.8 (q, *J*=271.8 Hz), 118.8, 116.7, 115.5 (d, *J*=288.8 Hz), 35.4, 31.1; ^{19}F NMR ($CDCl_3$, 564 MHz) δ -62.7, -76. Spectroscopic data are in agreement with those reported in the literature.[70]

4-azido-1,1'-biphenyl (51m)

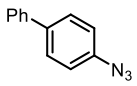

Following **GP3**, [1,1'-biphenyl]-4-amine (2 g, 11.8 mmol, 1 eq.) gave **51m** (63%) as an oil. ^{1}H NMR ($CDCl_3$, 600 MHz) δ .61 – 7.53 (4H, m), 7.45 (2H, t, *J*=7.6 Hz), 7.35 (1H, t, *J*=6.8 Hz), 7.11 (2H, d, *J*=8.0 Hz); ^{13}C NMR ($CDCl_3$, 151 MHz) δ 140.1, 139.1, 138.0, 128.9, 128.4, 127.4, 126.9, 119.4. Spectroscopic data are in agreement with those reported in the literature.[68]

4-azido-4'-methoxy-1,1'-biphenyl (51n)

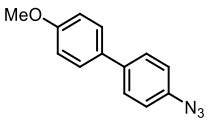

Following **GP3**, 4'-methoxy-[1,1'-biphenyl]-4-amine (2.0 g, 10.0 mmol, 1 eq.) gave **51n** (63%) as an oil. ^{1}H NMR ($CDCl_3$, 600 MHz) δ 7.55 (2H, d, *J*=8.5 Hz), 7.50 (2H, d, *J*=8.7 Hz), 7.10 (2H, d, *J*=8.5 Hz), 7.01 (2H, d, *J*=8.7 Hz), 3.94 (3H, s); ^{13}C NMR ($CDCl_3$, 151 MHz) δ 159.2, 138.5, 137.7, 132.7, 128.0, 127.9, 119.4, 114.3, 55.4; ^{19}F NMR ($CDCl_3$, 564 MHz) δ -62.7, -76. Spectroscopic data are in agreement with those reported in the literature.[72]

4-azido-4'-iodo-1,1'-biphenyl (51o)

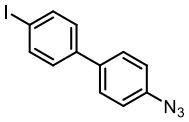

Following **GP3**, 4'-iodo-[1,1'-biphenyl]-4-amine (2.0 mg, 6.8 mmol, 1 eq.) gave **51o** (63%) as an oil. ^{1}H NMR ($CDCl_3$, 600 MHz) δ 7.76 (2H, d, *J*=8.5 Hz), 7.54 (2H, d, *J*=8.6 Hz), 7.29 (2H, d, *J*=8.5 Hz), 7.10 (2H, d, *J*=8.5 Hz); ^{13}C NMR ($CDCl_3$, 151 MHz) δ 139.8, 138.1, 136.9, 128.8, 128.4, 119.7, 93.2.

4'-azido-3-fluoro-1,1'-biphenyl (51p)

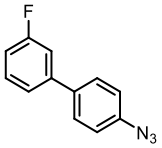

Following **GP3**, 3'-fluoro-[1,1'-biphenyl]-4-amine (2.0 g, 10.7 mmol, 1 eq.) gave **51p** (63%) as an oil. ^{1}H NMR ($CDCl_3$, 600 MHz) δ 7.56 (2H, d, *J*=8.6 Hz), 7.43 – 7.36 (1H, m), 7.35 – 7.31 (1H, m), 7.29 – 7.21 (1H, m), 7.11 (2H, d, *J*=8.5 Hz), 7.04 (1H, td, *J*=8.4, 1.5 Hz); ^{13}C NMR ($CDCl_3$, 151 MHz) δ 163.2 (d, *J*=245.8 Hz), 142.4 (d, *J*=7.5 Hz), 139.8, 136.6 (d, *J*=2.3 Hz), 130.3 (d, *J*=8.5 Hz), 128.4, 122.4 (d, *J*=2.6 Hz), 114.1 (d, *J*=21.0 Hz), 113.7 (d, *J*=22.1 Hz); ^{19}F NMR ($CDCl_3$, 564 MHz) δ -112.98. Spectroscopic data are in agreement with those reported in the literature.[73]

1-azido-3,5-dimethylbenzene (51q)

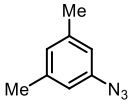

Following **GP3**, 3,5-dimethylaniline (2.0 g, 16.5 mmol, 1 eq.) gave **51q** (63%) as an oil. ^{1}H NMR ($CDCl_3$, 600 MHz) δ 6.78 (1H, s), 6.65 (2H, s), 2.30 (6H, s); ^{13}C NMR ($CDCl_3$, 151 MHz) δ 140.0, 140.0, 127.1, 117.1, 21.6. Spectroscopic data are in agreement with those reported in the literature.[74]

1-azido-3,5-dimethoxybenzene (51r)

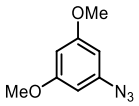

Following **GP3**, 3,5-dimethoxyaniline (2.0 g, 13.1 mmol, 1 eq.) gave **51r** (63%) as an oil. ^{1}H NMR ($CDCl_3$, 600 MHz) δ 7.3 (1H, t, *J*=8.1 Hz), 6.7 (1H, dd, *J*=8.3, 2.4, Hz), 6.6 (1H, ddd, *J*=8.0, 2.1, 0.9 Hz), 6.6 (1H, t, *J*=2.3 Hz), 3.8 (3H, s); ^{13}C NMR ($CDCl_3$, 151 MHz) δ 156.2, 154.6 (q, *J*=37.7 Hz), 140.4, 137.3, 136.8, 129.5, 128.7 (q, *J*=32.8 Hz), 126.7, 126.2 (q, *J*=3.8 Hz), 124.0, 123.8 (q, *J*=271.8 Hz), 118.8, 116.7, 115.5 (d, *J*=288.8 Hz), 35.4, 31.1; ^{19}F NMR ($CDCl_3$, 564 MHz) δ -62.7, -76.. Spectroscopic data are in agreement with those reported in the literature.[74]

4-azido-2,6-dimethyl-1,1'-biphenyl (51s)

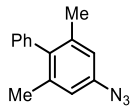

Following **GP3**, 2,6-dimethyl-[1,1'-biphenyl]-4-amine (2.0 g, 10.1 mmol, 1 eq.) gave **51s** (63%) as an oil. ^{1}H NMR ($CDCl_3$, 600 MHz) δ 7.43 (2H, t, *J*=7.5 Hz), 7.35 (1H, t, *J*=7.5 Hz), 7.12 (2H, d, *J*=6.8 Hz), 6.79 (2H, s), 2.02 (6H, s); ^{13}C NMR ($CDCl_3$, 151 MHz) δ 140.2, 138.8, 138.3, 138.0, 129.2, 128.5, 126.8, 117.7, 20.9. Spectroscopic data are in agreement with those reported in the literature.[70]

1-azido-3-(tert-butyl)benzene (51t)

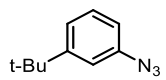

Following **GP3** 3-(tert-butyl)aniline (2.0 g, 13.4 mmol, 1 eq.) gave **51t** (63%) as an oil. ^{1}H NMR ($CDCl_3$, 600 MHz) δ 8.89 (1H, s), 8.44 (1H, d, *J*=2.1 Hz), 7.52 (1H, d, *J*=8.2 Hz), 7.41 (2H, d, *J*=8.1 Hz), 7.25 (1H, dd, *J*=8.2, 2.1 Hz), 7.05 (2H, d, *J*=8.0 Hz), 1.30 (9H, s); ^{13}C NMR ($CDCl_3$, 151 MHz) δ 156.2, 154.6 (q, *J*=37.7 Hz), 140.4, 137.3, 136.8, 129.5, 128.7 (q, *J*=32.8 Hz), 126.7,

126.2 (q, *J*=3.8 Hz), 124.0, 123.8 (q, *J*=271.8 Hz), 118.8, 116.7, 115.5 (d, *J*=288.8 Hz), 35.4, 31.1; ^{19}F NMR ($CDCl_3$, 564 MHz) δ -62.7, -76.. Spectroscopic data are in agreement with those reported in the literature.[75]

1-azido-3-methoxybenzene (51u)

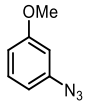

Following **GP3**, 3-methoxyaniline (2.0 , 16.2 mmol, 1 eq.) gave **51u** (63%) as an oil. ^{1}H NMR ($CDCl_3$, 600 MHz) δ 7.25 (1H, t, *J*=8.1 Hz), 6.69 (1H, dd, *J*=8.3, 2.4 Hz), 6.65 (1H, dd, *J*=8.0, 2.1 Hz), 6.55 (1H, t, *J*=2.3 Hz), 3.80 (3H, s); ^{13}C NMR ($CDCl_3$, 151 MHz) δ 160.78, 141.26, 130.43, 111.27, 110.67, 104.91, 55.35. Spectroscopic data are in agreement with those reported in the literature.[74]

6-azido-1,2,3,4-tetrahydronaphthalene (51v)

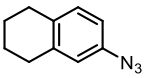

Following **GP3**, 5,6,7,8-tetrahydronaphthalen-2-amine (2.0 g, 13.6 mmol, 1 eq.) gave **51ac** (63%) as an oil. ^{1}H NMR ($CDCl_3$, 600 MHz) δ .04 (1H, d, *J*=8.1 Hz), 6.76 (1H, d, *J*=8.2 Hz), 6.74 (1H, s), 2.82 – 2.65 (4H, m), 1.85 – 1.70 (4H, m); ^{13}C NMR ($CDCl_3$, 151 MHz) δ 138.79, 136.91, 134.01, 130.37, 119.17, 116.31, 29.42, 28.85, 23.12, 22.92. Spectroscopic data are in agreement with those reported in the literature.[70]

Butyl 4-azidobenzoate (51w)

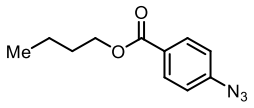

Following **GP3**, butyl 4-aminobenzoate (2.0 g, 10.3 mmol, 1 eq.) gave **51w** (63%) as an oil. ^{1}H NMR ($CDCl_3$, 600 MHz) δ 8.02 (2H, d, *J*=8.7 Hz), 7.05 (2H, d, *J*=8.7 Hz), 4.31 (2H, t, *J*=6.6 Hz), 1.81 – 1.67 (2H, m), 1.53 – 1.39 (2H, m), 0.97 (3H, t, *J*=7.4 Hz); ^{13}C NMR ($CDCl_3$, 151 MHz) δ 165.8, 144.6, 131.3, 127.1, 118.8, 64.9, 30.7, 19.3, 13.7. Spectroscopic data are in agreement with those reported in the literature.[76]

3-(4-azidophenyl)-3-ethylpiperidine-2,6-dione (51x)

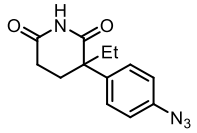

Following **GP3**, 3-(4-aminophenyl)-3-ethylpiperidine-2,6-dione (2.0 g, 8.6 mmol, 1 eq.) gave **51x**(63%) as an oil. ^{1}H NMR ($CDCl_3$, 600 MHz) δ 8.00 (1H, s), 7.28 (2H, d, *J* = 1.1 Hz), 7.03 (2H, d, *J* = 8.8 Hz), 2.62 (1H, dt, *J* = 18.2, 3.7 Hz), 2.46 – 2.31 (2H, m), 2.23 (1H, td, *J* = 14.1, 4.3 Hz), 2.11 – 1.84 (3H, m), 0.86 (3H, t, *J* = 7.4 Hz); ^{13}C NMR ($CDCl_3$, 151 MHz) δ 156.2, 154.6 (q, *J*=37.7 Hz), 140.4, 137.3, 136.8, 129.5, 128.7 (q, *J*=32.8 Hz), 126.7, 126.2 (q, *J*=3.8 Hz), 124.0, 123.8 (q, *J*=271.8 Hz), 118.8, 116.7, 115.5 (d, *J*=288.8 Hz), 35.4, 31.1; ^{19}F NMR ($CDCl_3$, 564 MHz) δ -62.7, -76. Spectroscopic data are in agreement with those reported in the literature.[77]

(8S,9R,13R,14R)-3-azido-13-methyl-6,7,8,9,11,12,13,14,15,16-decahydro-17H-cyclopenta[a]phenanthren-17-one (51y)

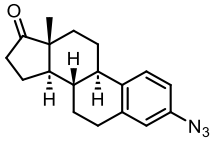

Following **GP3**, (8S,9R,13R,14R)-3-amino-13-methyl-6,7,8,9,11,12,13,14,15,16-decahydro-17H-cyclopenta[a]phenanthren-17-one (2.0 g, 7.4 mmol, 1 eq.) gave **51y** (63%) as an oil. ^{1}H NMR ($CDCl_3$, 600 MHz) δ 8.89 (1H, s), 8.44 (1H, d, *J*=2.1 Hz), 7.52 (1H, d, *J*=8.2 Hz), 7.41 (2H, d, *J*=8.1 Hz), 7.25 (1H, dd, *J*=8.2, 2.1 Hz), 7.05 (2H, d, *J*=8.0 Hz), 1.30 (9H, s); ^{13}C NMR ($CDCl_3$, 151 MHz) δ 156.2, 154.6 (q, *J*=37.7 Hz), 140.4, 137.3, 136.8, 129.5, 128.7 (q, *J*=32.8 Hz), 126.7, 126.2 (q, *J*=3.8 Hz), 124.0, 123.8 (q, *J*=271.8 Hz), 118.8, 116.7, 115.5 (d, *J*=288.8 Hz), 35.4, 31.1; ^{19}F NMR ($CDCl_3$, 564 MHz) δ -62.7, -76.. Spectroscopic data are in agreement with those reported in the literature.[78]

5.4.2.3 Synthesis of *ortho*-thioaminophenols

General Procedure 4

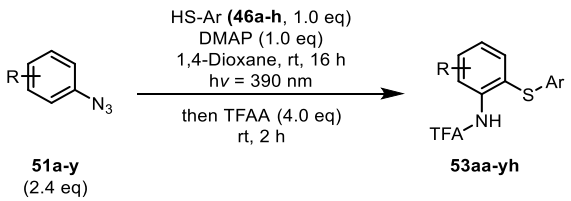

An oven-dried tube equipped with a stirring bar was charged with DMAP (1.0 eq.) and the suitable thiophenol (**46a-h,** 1.0 eq.). Then, the tube was capped under air with a Supelco aluminum crimp seal containing a septum (PTFE/butyl), and anhydrous 1,4-dioxane (0.05 M), and the appropriate aryl azide (2.4 equiv.) were added sequentially *via* syringe. Under vigorous ventilation with a fan, the mixture was stirred (900 rpm) and irradiated with a purple LED (Kessil PR160L-390 nm) for 16 h at room temperature. Then, trifluoroacetic anhydride (4.0 eq.) was added and the mixture was stirred for another 2 h. All volatiles were evaporated *in vacuo*, and the residue was purified by flash column chromatography on silica gel to give the desired product. Note: arylazides in solid form were added into the reaction vessel before sealing.

N-(5-(tert-butyl)-2-((4-(trifluoromethyl)phenyl)thio)phenyl)-2,2,2-trifluoroacetamide (53aa)

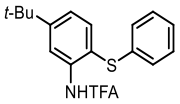

Following **GP4**, 1-azido-4-(tert-butyl)benzene (44.9 mg, 0.24 mmol, 2.4 eq.) gave **53aa** (65%) as an oil.^{1}H NMR (600 MHz, CD_3CN) δ 9.12 (1H, br s), 7.95 (1H, d, J = 2.2 Hz), 7.49 (1H, d, J = 8.3 Hz), 7.39 (1H, dd, J = 8.3, 2.2 Hz), 7.33–7.29 (2H, m), 7.27–7.23 (1H, m), 7.22–7.19 (2H, m), 1.33 (9H, s); ^{13}C NMR (151 MHz, CD_3CN) δ 154.8, 136.6, 136.1, 135.9, 130.5, 130.2, 128.1, 126.0, 125.2, 122.7, 35.6, 31.6, 31.3; ^{19}F NMR (376 MHz, CD_3CN) δ –76.62. Spectroscopic data are in agreement with those reported in the literature. [29]

N-(5-(tert-butyl)-2-((4-(trifluoromethyl)phenyl)thio)phenyl)-2,2,2-trifluoroacetamide (53b)

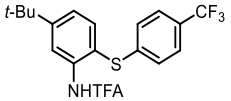

Following **GP4**, 11-azido-4-(tert-butyl)benzene (44.9 mg, 0.24 mmol, 2.4 eq.) gave **53ab** (48%) as an oil. ^{1}H NMR ($CDCl_3$, 600 MHz) δ 8.89 (1H, s), 8.44 (1H, d, J=2.1 Hz), 7.52 (1H, d, J=8.2 Hz), 7.41 (2H, d, J=8.1 Hz), 7.25 (1H, dd, J=8.2, 2.1 Hz), 7.05 (2H, d, J=8.0 Hz), 1.30 (9H, s); ^{13}C NMR ($CDCl_3$, 151 MHz) δ 156.2, 154.6 (q, J=37.7 Hz), 140.4, 137.3, 136.8, 129.5, 128.7 (q, J=32.8 Hz), 126.7, 126.2 (q, J=3.8 Hz), 124.0, 123.8 (q, J=271.8 Hz), 118.8, 116.7, 115.5 (d, J=288.8 Hz), 35.4, 31.1; ^{19}F NMR ($CDCl_3$, 564 MHz) δ -62.7, -76.

N-(5-(tert-butyl)-2-((4-methoxyphenyl)thio)phenyl)-2,2,2-trifluoroacetamide (53aac)

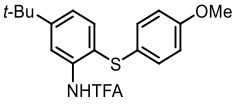

Following **GP4**, 1-azido-4-(tert-butyl)benzene (44.9 mg, 0.24 mmol, 2.4 eq.) gave **53ac** (67%) as an oil. ^{1}H NMR ($CDCl_3$, 600 MHz) δ 9.14 (1H, s), 8.42 (1H, d, *J*=2.1 Hz), 7.54 (1H, d, *J*=8.2 Hz), 7.23 (1H, dd, *J*=8.2, 2.1 Hz), 7.17 (2H, d, *J*=8.8 Hz), 6.82 (2H, d, *J*=8.8 Hz), 3.77 (3H, s), 1.34 (9H, s); ^{13}C NMR ($CDCl_3$, 151 MHz) δ 159.3, 154.5 (q, *J*=39.2 Hz),154.4, 136.3, 135.3, 131.2, 124.9, 123.5, 120.9, 118.4, 115.6 (q, *J*=294.4 Hz), 115.1, 55.4, 35.1, 31.1; ^{19}F NMR ($CDCl_3$, 564 MHz) δ -76.0.

N-(5-(tert-butyl)-2-((3',5-dimethoxy-[1,1'-biphenyl]-2-yl)thio)phenyl)-2,2,2-trifluoroacetamide (53ad)

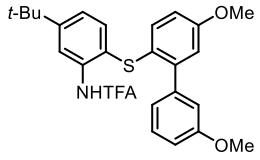

Following **GP4**, 1-azido-4-(tert-butyl)benzene (44.9 mg, 0.24 mmol, 2.4 eq.) gave **53ad** (58%) as an oil. ^{1}H NMR ($CDCl_3$, 600 MHz) δ 8.68 (1H, s), 8.28 (1H, d, *J*=2.1 Hz), 7.30 (1H, t, *J*=7.9 Hz), 7.27 (1H, s), 7.14 (1H, dd, *J*=8.2, 2.1 Hz), 7.10 (1H, d, *J*=8.6 Hz), 6.91 (1H, dd, *J*=8.3, 3.6 Hz), 6.87 (1H, d, *J*=8.9 Hz), 6.85 – 6.78 (2H, m), 6.75 – 6.70 (1H, m), 3.79 (3H, s), 3.78 (3H, s), 1.32 (9H, s); ^{13}C NMR ($CDCl_3$, 151 MHz) δ 159.3, 159.1, 154.4 (q, *J*=37.4 Hz), 153.7, 144.5, 141.5, 135.9, 135.0, 131.9, 129.2, 123.9, 123.4, 121.3, 121.3, 118.1, 116.4, 115.5 (q, *J*)286.9 Hz), 114.6, 114.1, 113.2, 55.4, 55.2, 35.0, 31.1; ^{19}F NMR ($CDCl_3$, 564 MHz) δ -75.91.

N-(5-(tert-butyl)-2-((3'-methoxy-5-(trifluoromethyl)-[1,1'-biphenyl]-2-yl)thio)phenyl)-2,2,2-trifluoroacetamide(53ae)

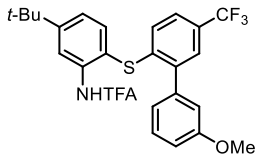

Following **GP4**, 1-azido-4-(tert-butyl)benzene (44.9 mg, 0.24 mmol, 2.4 eq.) gave **53ae** (49%) as an oil. ^{1}H NMR ($CDCl_3$, 600 MHz) δ 8.76 (1H, s), 8.46 (1H, s), 7.52 (1H, s), 7.50 (1H, d, *J*=8.2 Hz), 7.41 (2H, t, *J*=8.2 Hz), 7.30 (1H, dd, *J*=8.2, 1.1 Hz), 7.00 (2H, t, *J*=8.0 Hz), 6.92 (1H, s), 6.83 (1H, d, *J*=8.4 Hz), 3.87 (3H, s), 1.37 (9H, s); ^{13}C NMR ($CDCl_3$, 151 MHz) δ 159.8, 156.0. 154.6 (q, *J*=37.6 Hz), 141.2, 140.0, 139.3, 137.2, 136.9, 129.9, 128.6 (q, *J*=32.8 Hz), 127.2 (q, *J*=3.5 Hz), 126.8, 125.1 (q, *J*=3.3 Hz), 124.1, 123.8 (q, *J*=271.8 Hz), 121.4, 118.9, 117.5, 115.4 (q, *J*=288.4 Hz), 114.7, 114.2, 55.4, 35.5, 31.12; ^{19}F NMR ($CDCl_3$, 564 MHz) δ -62.55, -76.11.

N-(5-(tert-butyl)-2-((3',5,5'-trimethoxy-[1,1'-biphenyl]-2-yl)thio)phenyl)-2,2,2-trifluoroacetamide(53af)

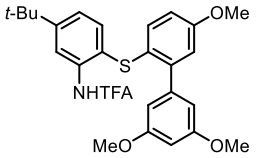

Following **GP4**, 1-azido-4-(tert-butyl)benzene (44.9 mg, 0.24 mmol, 2.4 eq.) gave **53af** (52%) as an oil. ^{1}H NMR ($CDCl_3$, 600 MHz) δ 8.70 (1H, s), 8.28 (1H, d, *J*=2.1 Hz), 7.28 (1H, d, *J*=8.2 Hz), 7.14 (1H, dd, *J*=8.2, 2.1 Hz), 7.08 (1H, d, *J*=8.6 Hz), 6.83 (1H, d, *J* = 2.8 Hz), 6.80 (1H, dd, *J* = 8.6, 2.9 Hz), 6.46 (1H, t, *J*=2.3 Hz), 6.36 (2H, d, *J*=2.3 Hz), 3.79 (3H, s), 3.77 (6H, s), 1.31 (9H, s); ^{13}C NMR ($CDCl_3$, 151 MHz) δ 160.6, 159.2, 154.6 (q, *J*=37.3 Hz), 153.8, 144.6, 142.2, 136.1, 135.2, 131.9, 123.9, 123.5, 121.4, 118.3, 116.4, 115.5 (q, *J*=289.9 Hz), 114.3, 107.2, 99.8, 55.6, 55.4, 31.2, 29.9. ^{19}F NMR ($CDCl_3$, 564 MHz) δ -75.99.

N-(5-(tert-butyl)-2-((3',5'-dimethoxy-5-(trifluoromethyl)-[1,1'-biphenyl]-2-yl)thio)phenyl)-2,2,2-trifluoroacetamide (53ag)

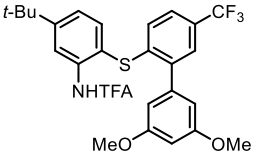

Following **GP4**, 1-azido-4-(tert-butyl)benzene (44.9 mg, 0.24 mmol, 2.4 eq.) gave **53ag** (43%) as an oil. ^{1}H NMR ($CDCl_3$, 600 MHz) δ 8.77 (1H, s), 8.45 (1H, d, *J*=2.1 Hz), 7.52 (1H, s), 7.50 (1H, d, *J* = 8.1 Hz), 7.41 (1H, dd, *J*=8.5, 2.1 Hz), 7.29 (1H, dd, *J*=8.2, 2.1 Hz), 6.82 (1H, d, *J*=8.4 Hz), 6.55 (1H, t, *J*=2.3 Hz), 6.51 (2H, d, *J*=2.3 Hz), 3.84 (6H, s), 1.37 (9H, s); ^{13}C NMR ($CDCl_3$, 151 MHz) δ 161.0, 156.0, 154.6 (q, *J* = 37.4 Hz), 141.4, 140.5, 139.2, 137.1, 136.9, 128.6 (q, *J* = 33.0 Hz), 127.0 (q, *J* = 3.4 Hz), 126.8, 125.2 (q, *J* = 3.4 Hz), 124.1, 123.9 (q, *J*=271.8 Hz), 118.9, 117.5, 115.5 (q, *J*=289.1 Hz), 107.2, 100.6, 55.6, 35.5, 31.2; ^{19}F NMR ($CDCl_3$, 564 MHz) δ -62.55, -76.11.

N-(5-(tert-butyl)-2-((3',5'-dimethoxy-[1,1'-biphenyl]-2-yl)thio)phenyl)-2,2,2-trifluoroacetamide (53ah)

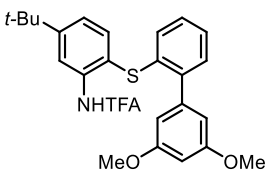

Following **GP4**, 1-azido-4-(tert-butyl)benzene (42 mg, 0.24 mmol, 2.4 eq.) gave **53ah** (75%) as an oil. ^{1}H NMR ($CDCl_3$, 600 MHz) δ 8.82 (1H, s), 8.42 (1H, s), 7.47 (1H, d, *J* = 8.1 Hz), 7.29 (1H,

t, *J* = 7.8 Hz), 7.26 (2H, t, *J* = 7.7 Hz), 7.22 (1H, t, *J* = 7.6 Hz), 6.89 (1H, d, *J* = 9.0 Hz), 6.53 (1H, s), 6.51 (2H, s), 3.84 (6H, s), 1.38 (9H, s); ^{13}C NMR ($CDCl_3$, 151 MHz) δ 160.7, 154.9, 154.6 (q, *J* = 37.4 Hz), 142.0, 141.8, 136.8, 136.4, 133.7, 130.5, 128.5, 127.7, 126.7, 123.7, 119.3, 118.5, 115.7 (q, *J* = 289.0 Hz), 107.3, 100.0, 55.5, 35.3, 31.2; ^{19}F NMR ($CDCl_3$, 564 MHz) δ -76.08.

N-(2-((3',5'-dimethoxy-[1,1'-biphenyl]-2-yl)thio)-5-methylphenyl)-2,2,2-trifluoroacetamide (53bh)

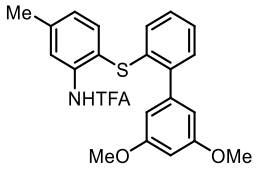

Following **GP4**, 1-azido-4-methylbenzene (31.9 mg, 0.24 mmol, 2.4 eq.) gave **53bh** (44%) as an oil. ^{1}H NMR ($CDCl_3$, 600 MHz) δ 8.80 (1H, s), 8.16 (1H, s), 7.42 (1H, d, *J*=7.9 Hz), 7.27 (1H, dd, *J*=7.5, 1.7 Hz), 7.23 (1H, t, *J*=7.5 Hz), 7.17 (1H, td, *J*=7.6, 1.7 Hz), 7.03 (1H, d, *J*=7.8 Hz), 6.82 (1H, dd, *J*=7.9, 1.2 Hz), 6.51 (1H, t, *J*=2.3 Hz), 6.48 (2H, d, *J*=2.2 Hz), 3.82 (6H, s), 2.41 (3H, s); ^{13}C NMR ($CDCl_3$, 151 MHz) δ 160.6, 154.4 (q, *J*=37.3 Hz), 141.8, 141.6, 141.5, 136.8, 136.6, 133.8, 130.3, 128.4, 127.3, 127.2, 126.5, 121.7, 119.1, 115.5 (q, *J*=289.2 Hz), 107.2, 99.9, 55.3, 21.7; ^{19}F NMR ($CDCl_3$, 564 MHz) δ -76.0.

N-(2-((3',5'-dimethoxy-[1,1'-biphenyl]-2-yl)thio)-5-ethylphenyl)-2,2,2-trifluoroacetamide (53ch)

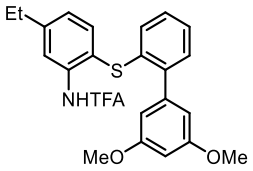

Following **GP4**, 1-azido-4-ethylbenzene (35 mg, 0.24 mmol, 2.4 eq.) gave **53ch** (52%) as an oil. ^{1}H NMR ($CDCl_3$, 600 MHz) δ 8.84 (1H, s), 8.22 (1H, s), 7.47 (1H, d, *J* = 7.9 Hz), 7.32 – 7.23 (2H, m), 7.21 (1H, td, *J* = 7.5, 1.9 Hz), 7.09 (1H, d, *J* = 7.9 Hz), 6.87 (1H, d, *J* = 7.7 Hz), 6.56 – 6.51 (1H, m), 6.51 (2H, s), 3.85 (6H, s), 2.73 (2H, q, *J* = 7.6 Hz), 1.30 (3H, t, *J* = 7.5 Hz); ^{13}C NMR ($CDCl_3$, 151 MHz) δ 160.8, 154.6 (d, *J* = 37.4 Hz), 148.0, 142.0, 141.7, 137.0, 136.8, 133.9, 130.5, 128.5, 127.5, 126.7, 126.2, 120.7, 119.4, 115.7 (d, *J* = 289.0 Hz), 107.4, 100.0, 55.5, 29.1, 15.3; ^{19}F NMR ($CDCl_3$, 564 MHz) δ -76.05.

N-(2-((3',5'-dimethoxy-[1,1'-biphenyl]-2-yl)thio)-5-ethylphenyl)-2,2,2-trifluoroacetamide (53dh)

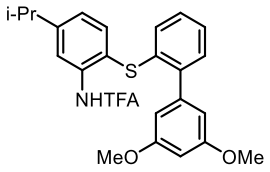

Following **GP4**, 1-azido-4-isopropylbenzene (39 mg, 0.24 mmol, 2.4 eq.) gave **53dh** (42%) as an oil. ^{1}H NMR ($CDCl_3$, 600 MHz) δ 8.81 (1H, s), 8.22 (1H, s), 7.44 (1H, d, *J* = 7.9 Hz), 7.30 – 7.21 (2H, m), 7.18 (1H, td, *J* = 7.5, 1.9 Hz), 7.07 (1H, dd, *J* = 8.0, 1.9 Hz), 6.87 – 6.83 (1H, m), 6.50 (1H, d, *J* = 2.1 Hz), 6.48 (2H, d, *J* = 2.2 Hz), 3.81 (6H, s), 2.95 (1H, p, *J* = 6.9 Hz), 1.28 (6H, d, *J* = 6.9 Hz); ^{13}C NMR ($CDCl_3$, 151 MHz) δ 160.8, 154.5 (q, *J* = 37.4 Hz), 152.6, 142.0, 141.7, 137.0, 136.8, 133.8, 130.5, 128.5, 127.6, 126.7, 124.7, 115.7 (q, *J* = 289.0 Hz), 107.3, 100.0, 55.5, 34.4, 23.8; ^{19}F NMR ($CDCl_3$, 564 MHz) δ -76.07.

N-(5-benzyl-2-((3',5'-dimethoxy-[1,1'-biphenyl]-2-yl)thio)phenyl)-2,2,2-trifluoroacetamide (53eh)

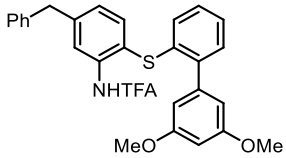

Following **GP4**, 1-azido-4-benzylbenzene (50 mg, 0.24 mmol, 2.4 eq.) gave **53eh**(48%) as an oil. ^{1}H NMR ($CDCl_3$, 600 MHz) δ 8.78 (1H, s), 8.23 (1H, s), 7.42 (1H, d, *J* = 8.0 Hz), 7.32 (2H, t, *J* = 7.6 Hz), 7.28 – 7.24 (2H, m), 7.22 (3H, t, *J* = 6.6 Hz), 7.18 (1H, td, *J* = 7.6, 1.7 Hz), 7.00 (1H, dd, *J* = 8.0, 1.9 Hz), 6.85 (1H, dd, *J* = 7.9, 1.3 Hz), 6.50 (1H, t, *J* = 2.3 Hz), 6.46 (2H, d, *J* = 2.3 Hz), 4.01 (2H, s), 3.80 (6H, s); ^{13}C NMR ($CDCl_3$, 151 MHz) δ 160.8, 154.6 (q, *J* = 37.4 Hz), 144.8, 142.0, 141.9, 140.0, 137.1, 136.9, 133.6, 130.5, 129.1, 128.8, 128.6, 127.8, 127.0, 126.8, 126.7, 121.6, 120.2, 115.6 (q, *J* = 289.0 Hz), 107.3, 100.0, 55.5, 42.1; ^{19}F NMR ($CDCl_3$, 564 MHz) δ -76.05.

N-(2-((3',5'-dimethoxy-[1,1'-biphenyl]-2-yl)thio)-5-(trifluoromethyl)phenyl)-2,2,2 trifluoro-acetamide (53fh)

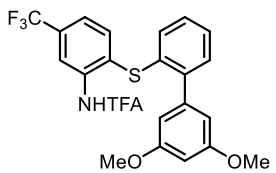

Following **GP4**, 1-azido-4-(trifluoromethyl)benzene (44.9 mg, 0.24 mmol, 2.4 eq.) gave **53fh** (63%) as an oil. ^{1}H NMR ($CDCl_3$, 600 MHz) δ 8.69 (1H, s), 8.50 (1H, d, *J*=1.9 Hz), 7.48 (1H, d, *J*=8.1), 7.39 – 7.32 (2H, m), 7.31 – 7.27 (2H, m), 7.19 (1H, dd, *J*=7.9, 1.3 Hz), 6.44 (1H, t, *J*=2.3 Hz), 6.31 (2H, d, *J*=2.3 Hz), 3.75 (6H, s); ^{13}C NMR ($CDCl_3$, 151 MHz) δ 160.8, 154.7 (q, *J*=37.9 Hz), 143.5, 141.9, 136.6, 135.8, 132.0 (q, *J*=37.7 Hz), 131.9, 131.1, 130.6, 128.8, 128.4, 125.5, 123.4 (q, *J*=273.0 Hz), 122.7 (q, *J*=3.7 Hz), 117.9 (q, *J*=4.0 Hz), 115.4 (q, *J*=289.0 Hz), 107.2, 99.6, 55.4; ^{19}F NMR ($CDCl_3$, 564 MHz) δ -63.03, -76.01.

N-(5-(1-cyanocyclopentyl)-2-((3',5'-dimethoxy-[1,1'-biphenyl]-2-yl)thio)phenyl)-2,2,2-trifluoroacetamide (53gh)

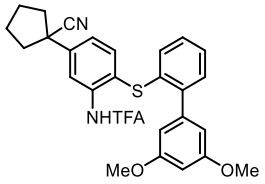

Following **GP4**, 1-(4-azidophenyl)cyclopentane-1-carbonitrile (50.9 mg, 0.24 mmol, 2.4 eq.) gave **53gh** (42%) as an solid. ^{1}H NMR ($CDCl_3$, 600 MHz) δ 8.75 (1H, s), 8.35 (1H, d, *J*=2.1 Hz), 7.47 (1H, d, *J*=8.1 Hz), 7.35 (1H, dd, *J*=8.2, 2.1 Hz), 7.29 – 7.27 (2H, d), 7.25 – 7.21 (1H, m), 6.99 (1H, d, *J*=7.8 Hfz), 6.47 (1H, t, *J*=2.2 Hz), 6.40 (2H, d, *J*=2.2 Hz), 3.79 (6H, s), 2.50 (2H, m), 2.13 – 2.01 (4H, m), 1.97 (2H, m); ^{13}C NMR ($CDCl_3$, 151 MHz) δ 160.8, 154.8 (q, *J*=37.6 Hz), 142.9, 142.5, 141.9, 137.2, 136.6, 132.8, 130.8, 128.9, 128.7, 127.5, 124.6, 123.8, 123.0, 118.2, 115.5 (q, *J*=288.6 Hz), 107.3, 99.8, 55.5, 47.9, 40.7, 24.4 . ^{19}F NMR ($CDCl_3$, 564 MHz) δ -76.1.

N-(2-((3',5'-dimethoxy-[1,1'-biphenyl]-2-yl)thio)-5-(methoxymethyl)phenyl)-2,2,2-trifluoroacetamide (53hh)

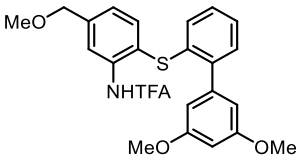

Following **GP4**, 1-azido-4-(methoxymethyl)benzene (39.2 mg, 0.24 mmol, 2.4 eq.) gave **53hh** (40%) as an oil. ^{1}H NMR ($CDCl_3$, 600 MHz) δ 8.79 (1H, s), 8.28 (1H, d, *J*=1.9 Hz), 7.56 – 6.81 (6H, m), 6.48 (3H, dd, *J*=18.2, 2.3 Hz), 4.48 (2H, s), 3.81 (6H, s), 3.44 (3H, s); ^{13}C NMR ($CDCl_3$, 151 MHz) δ 160.8, 154.6 (q, *J*=37.6 Hz), 141.9, 141.9, 141.9, 137.0, 136.8, 133.5, 130.5, 128.6, 127.9, 126.9, 125.3, 121.8, 120.1, 115.6 (q, *J*=288.9 Hz), 107.3, 100.0, 74.0, 58.7, 55.5. ^{19}F NMR ($CDCl_3$, 564 MHz) δ -76.04.

N-(5-(2-(benzyloxy)-1,1,1,3,3,3-hexafluoropropan-2-yl)-2-((3',5'-dimethoxy-[1,1'-biphenyl]-2-yl)thio)phenyl)-2,2,2-trifluoroacetamide (53ih)

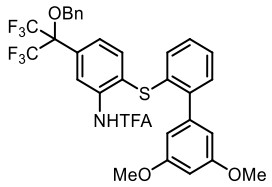

Following **GP4**, 1-azido-4-(2-(benzyloxy)-1,1,1,3,3,3-hexafluoropropan-2-yl)benzene (90 mg, 0.24 mmol, 2.4 eq.) gave **53ih** (53%) as an oil. ^{1}H NMR ($CDCl_3$, 600 MHz) δ 8.59 (1H, s), 8.54 (1H, s), 7.44 (2H, m), 7.42 – 7.39 (3H, mf), 7.38 – 7.33 (3H, m), 7.32 – 7.27 (3H, m), 6.37 (1H, t, *J*=2.3 Hz), 6.34 (2H, d, *J*=2.3 Hz), 4.65 (2H, s), 3.71 (6H, s); ^{13}C NMR ($CDCl_3$, 151 MHz) δ 160.6, 154.6 (q, *J*=37.6 Hz), 142.7, 142.3, 141.8, 137.1, 136.5, 132.7, 130.6, 128.8, 128.5, 127.3, 124.4, 123.7, 122.9, 118.1, 115.4 (q, *J*=288.6 Hz), 107.1, 104.9, 99.6, 82.8. 55.3, 47.7, 40.6, 24.3. ^{19}F NMR ($CDCl_3$, 564 MHz) δ -70.52, -75.97.

N-(2-((3',5'-dimethoxy-[1,1'-biphenyl]-2-yl)thio)-5-(hydroxydiphenylmethyl)phenyl)-2,2,2-trifluoroacetamide (53jh)

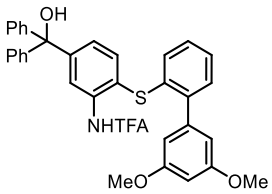

Following **GP4**, (4-azidophenyl)diphenylmethanol (72 mg, 0.24 mmol, 2.4 eq.) gave (**53jh)** (72%) as an oil. ^{1}H NMR ($CDCl_3$, 600 MHz) δ 8.67 (1H, s), 8.27 (1H, d, *J* = 2.0 Hz), 7.38 (1H, d, *J* = 8.2 Hz), 7.36 – 7.32 (4H, m), 7.31 – 7.26 (8H, m), 7.25 – 7.21 (1H, m), 7.11 (1H, dd, *J* = 8.2, 2.0 Hz), 7.04 (1H, d, *J* = 7.7 Hz), 6.47 (1H, t, *J* = 2.3 Hz), 6.42 (2H, d, *J* = 2.3 Hz), 3.79 (6H, s), 2.97 (1H, s); ^{13}C NMR ($CDCl_3$, 151 MHz) δ 160.7, 154.5 (q, *J* = 37.1 Hz), 149.8, 146.2, 142.5, 142.0, 136.3, 135.6, 133.1, 130.7, 129.1, 128.6, 128.3, 127.9, 127.8, 127.4, 126.1, 122.4, 120.8, 115.6 (q, *J* = 289.1 Hz), 107.4, 99.8, 81.8, 55.5; ^{19}F NMR ($CDCl_3$, 564 MHz) δ -76.02.

N-(4-((3',5'-dimethoxy-[1,1'-biphenyl]-2-yl)thio)-2',3',4',5'-tetrahydro-[1,1'-biphenyl]-3-yl)-2,2,2-trifluoroacetamide (53lh)

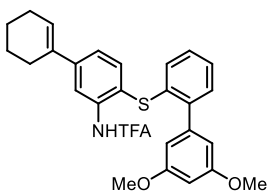

Following **GP4**, 4'-azido-2,3,4,5-tetrahydro-1,1'-biphenyl (47.8 mg, 0.24 mmol, 2.4 eq.) gave **53lh** (65%) as an oil. ^{1}H NMR ($CDCl_3$, 600 MHz) δ 8.76 (1H, s), 8.35 (1H, d, *J*=1.9 Hz), 7.43 (1H, d, *J*=8.3 Hz), 7.28 – 7.20 (3H, m), 7.17 (1H, td, *J*=7.6, 1.7 Hz), 6.86 (1H, dd, *J*=7.9, 1.3 Hz), 6.49 (1H, t, *J*=2.3 Hz), 6.46 (2H, d, *J*=2.2 Hz), 6.26 (1H, dt, *J*=4.1, 2.4 Hz), 3.80 (6H, d, *J*=1.3 Hz), 2.41 (2H, td, *J*=6.2, 3.8 Hz), 2.30 – 2.19 (2H, m), 1.84 – 1.73 (2H, m), 1.72 – 1.62 (2H, m); ^{13}C NMR ($CDCl_3$, 151 MHz) δ 160.61, 154.31, 145.37, 141.84, 141.63, 136.80, 136.38, 135.34, 133.71, 130.32, 128.38, 127.55, 127.33, 126.59, 122.78, 120.06, 117.50, 107.17, 99.86, 55.33, 27.10, 25.93, 22.86, 21.94; ^{19}F NMR ($CDCl_3$, 564 MHz) δ -76.08.

N-(4-((3',5'-dimethoxy-[1,1'-biphenyl]-2-yl)thio)-[1,1'-biphenyl]-3-yl)-2,2,2-trifluoroacetamide (53mh)

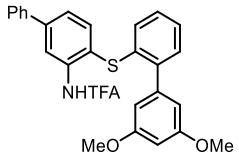

Following **GP4**, 4-azido-2,6-dimethyl-1,1'-biphenyl (46.8 mg, 0.24 mmol, 2.4 eq.) gave **53mh** (43%) as an oil. ^{1}H NMR ($CDCl_3$, 600 MHz) δ 8.81 (1H, s), 8.56 (1H, d, *J*=2.0 Hz), 7.63 (2H, d, *J*=7.2), 7.55 (1H, d, *J*=8.1 Hz), 7.49 – 7.44 (2H, m), 7.44 – 7.35 (2H, m), 7.30 – 7.26 (2H, m), 7.23 (1H, ddd, *J*=7.8, 6.9, 2.0 Hz), 7.00 (1H, dd, *J*=7.9, 1.2 Hz), 6.50 (1H, t, *J*=2.3 Hz), 6.45 (2H, d, *J*=2.3 Hz), 3.79 (6H, s); ^{13}C NMR ($CDCl_3$, 151 MHz) δ 160.8, 154.7 (q, *J* = 37.5 Hz), 143.8, 142.2, 142.0, 139.5, 137.3, 136.9, 133.5, 130.6, 129.1, 128.6, 128.4, 128.4, 127.3, 127.1, 125.0, 121.8, 119.7, 115.7 (q, *J* = 288.9 Hz), 107.3, 99.9, 55.5; ^{19}F NMR ($CDCl_3$, 564 MHz) δ -76.01.

N-(4-((3',5'-dimethoxy-[1,1'-biphenyl]-2-yl)thio)-4'-methoxy-[1,1'-biphenyl]-3-yl)-2,2,2-trifluoroacetamide (53nh)

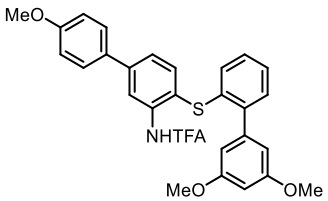

Following **GP4**, 4-azido-4'-methoxy-1,1'-biphenyl (54 mg, 0.24 mmol, 2.4 eq.) gave **53nh** (60%) as an oil. ^{1}H NMR ($CDCl_3$, 600 MHz) δ 8.81 (1H, s), 8.53 (1H, d, *J* = 2.0 Hz), 7.57 (2H, d, *J* = 8.7 Hz), 7.53 (1H, d, *J* = 8.1 Hz), 7.38 (1H, dd, *J* = 8.1, 2.0 Hz), 7.28 (1H, dd, *J* = 7.5, 1.9 Hz), 7.27 – 7.24 (1H, m), 7.21 (1H, td, *J* = 7.5, 1.9 Hz), 7.00 – 6.93 (3H, m), 6.50 (1H, t, *J* = 2.3 Hz), 6.46 (2H, d, *J* = 2.3 Hz), 3.86 (3H, s), 3.79 (6H, s); ^{13}C NMR ($CDCl_3$, 151 MHz) δ 160.8, 160.0, 154.7 (q, *J* = 37.5 Hz), 143.5, 142.0, 142.0, 137.3, 137.0, 133.7, 131.9, 130.6, 128.6, 128.4, 128.1, 127.0,

124.5, 120.8, 119.1, 115.7 (q, *J* = 288.8 Hz), 114.5, 107.3, 100.0, 55.5, 55.5; ^{19}F NMR ($CDCl_3$, 564 MHz) δ -76.02.

N-(4-((3',5'-dimethoxy-[1,1'-biphenyl]-2-yl)thio)-4'-iodo-[1,1'-biphenyl]-3-yl)-2,2,2-trifluoroacetamide (53oh)

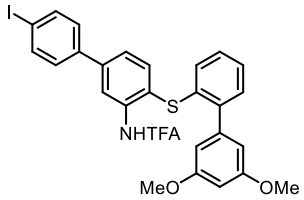

Following **GP4**, 4'-azido-3-fluoro-1,1'-biphenyl (77.4 mg, 0.24 mmol, 2.4 eq.) gave **53oh** (79%) as an oil. ^{1}H NMR ($CDCl_3$, 600 MHz) δ 8.78 (1H, s), 8.50 (1H, d, *J*=2.0 Hz), 7.78 (2H, d, *J*=8.5 Hz), 7.53 (1H, d, *J*=8.1 Hz), 7.38 – 7.32 (3H, m), 7.27 (3H, d, *J*=16.0 Hz), 7.23 (1H, ddd, *J*=7.9, 6.3, 2.7 Hz), 7.04 – 6.98 (1H, m), 6.48 (1H, t, *J*=2.3 Hz), 6.43 (2H, d, *J*=2.3 Hz), 3.77 (6H, s); ^{13}C NMR ($CDCl_3$, 151 MHz) δ 160.8, 142.5, 142.3, 142.0, 139.0, 138.2, 138.2, 137.3, 136.9, 133.3, 130.7, 129.1, 128.6, 127.3, 124.7, 122.6, 119.4, 107.3, 99.9, 94.4, 55.5; ^{19}F NMR ($CDCl_3$, 564 MHz) δ -76.02.

N-(4-((3',5'-dimethoxy-[1,1'-biphenyl]-2-yl)thio)-3'-fluoro-[1,1'-biphenyl]-3-yl)-2,2,2-trifluoroacetamide (53ph)

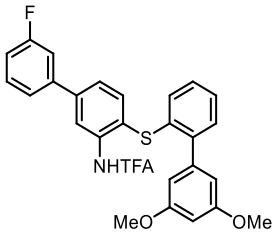

Following **GP4**, 4'-azido-3-fluoro-1,1'-biphenyl (51.1 mg, 0.24 mmol, 2.4 eq.) gave **53ph** (76%) as an oil. ^{1}H NMR ($CDCl_3$, 600 MHz) δ 8.79 (1H, s), 8.53 (1H, d, *J*=2.0 Hz), 7.54 (1H, d, *J*=8.1 Hz), 7.46 – 7.36 (3H, m), 7.34 – 7.18 (4H, m), 7.08 (1H, ddt, *J*=9.0, 6.8, 2.3 Hz), 7.03 (1H, d, *J*=7.8 Hz), 6.49 (1H, t, *J*=2.3 Hz), 6.43 (2H, d, *J*=2.3 Hz), 3.78 (6H, s); ^{13}C NMR ($CDCl_3$, 151 MHz) δ 160.8, 142.4 (q, *J* = 54.4 Hz), 142.0, 141.8 (d, *J* = 7.8 Hz), 137.3, 136.8, 133.3, 130.7, 130.6 (d, *J* = 8.5 Hz), 128.7, 128.6, 127.3, 124.9, 123.0, 123.0, 122.8, 119.7, 115.2 (d, *J* = 21.2 Hz), 114.3 (d, *J* = 22.4 Hz), 107.3, 99.9, 55.5; ^{19}F NMR ($CDCl_3$, 564 MHz) δ -73.61, -112.60.

N-(2-((3',5'-dimethoxy-[1,1'-biphenyl]-2-yl)thio)-4,6-dimethylphenyl)-2,2,2-trifluoroacetamide (53qh)

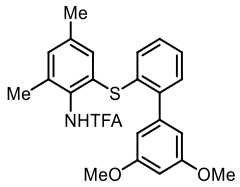

Following **GP4**, 1-azido-3,5-dimethylbenzene (35.9 mg, 0.24 mmol, 2.4 eq.) gave **53qh** (80%) as an oil. ^{1}H NMR ($CDCl_3$, 600 MHz) δ 7.51 (1H, s), 7.29 – 7.24 (2H, m), 7.23 – 7.19 (1H, m), 7.11 (1H, dd, *J*=7.7, 1.0 Hz), 7.07 (1H, d, *J*=1.9 Hz), 7.03 (1H, d, *J*=2.0 Hz), 6.46 (1H, t, *J*=2.3 Hz), 6.39 (2H, d, *J*=2.3 Hz), 3.77 (6H, s), 2.26 (3H, s), 2.15 (3H, s); ^{13}C NMR ($CDCl_3$, 151 MHz) δ 160.4, 154.8 (q, *J*=37.0 Hz), 142.5, 142.4, 138.5, 136.0, 133.7, 133.3, 132.3, 130.8, 130.5, 130.4, 129.7, 128.4, 127.1, 115.7 (q, *J*=288.9 Hz), 107.1, 99.7, 55.3, 20.8, 18.5; ^{19}F NMR ($CDCl_3$, 564 MHz) δ -75.50.

N-(2-((3',5'-dimethoxy-[1,1'-biphenyl]-2-yl)thio)-4,6-dimethoxyphenyl)-2,2,2-trifluoroacetamide (53rh)

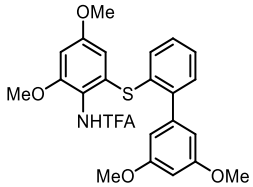

Following **GP4**, 1-azido-3,5-dimethoxybenzene (43 mg, 0.24 mmol, 2.4 eq.) gave **53rh** (80%) as an oil. ^{1}H NMR ($CDCl_3$, 600 MHz) δ 7.36 – 7.27 (5H, m), 7.17 (1H, s), 6.42 (1H, s), 6.39 (2H, s), 3.79 (3H, s), 3.76 (6H, s), 3.69 (3H, s); ^{13}C NMR ($CDCl_3$, 151 MHz) δ 160.4, 160.2, 155.8, 155.3 (q, *J*=36.2 Hz), 143.6, 142.5, 135.3, 133.4, 131.8, 130.6, 128.5, 127.8, 116.3, 116.0 (q, *J*=288.9 Hz), 109.4, 107.3, 99.8, 99.2, 56.2, 55.7, 55.4; ^{19}F NMR ($CDCl_3$, 564 MHz) δ -75.38.

N-(4-((3',5'-dimethoxy-[1,1'-biphenyl]-2-yl)thio)-2,6-dimethyl-[1,1'-biphenyl]-3-yl)-2,2,2-trifluoroacetamide (53sh)

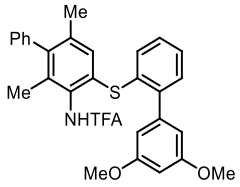

Following **GP4**, 4-azido-2,6-dimethyl-1,1'-biphenyl (53.5 mg, 0.24 mmol, 2.4 eq.) gave **53sh** (59%) as an oil. ^{1}H NMR ($CDCl_3$, 600 MHz) δ 7.58 (1H, s), 7.44 (2H, t, *J*=7.6 Hz), 7.36 (1H, t, *J*=7.3 Hz), 7.32 – 7.25 (4H, m), 7.13 (1H, d, *J*=7.3 Hz), 7.12 (2H, s), 6.44 (1H, d, *J*=2.3 Hz), 6.42

(2H, d, *J*=2.3 Hz), 3.78 (6H, sf), 1.93 (3H, s), 1.80 (3H, s); ^{13}C NMR ($CDCl_3$, 151 MHz) δ 160.5, 155.2 (q, *J* = 37.1 Hz), 143.6, 142.8, 142.7, 140.0, 137.1, 134.6, 133.9, 133.6, 131.2, 130.7, 130.5, 129.9, 129.0, 128.8, 128.5, 127.4, 127.3, 116.0 (q, *J* = 288.8 Hz), 107.4, 99.5, 55.5, 20.9, 16.8; ^{19}F NMR ($CDCl_3$, 564 MHz) δ -75.46.

N-(4-(tert-butyl)-2-((3',5'-dimethoxy-[1,1'-biphenyl]-2-yl)thio)phenyl)-2,2,2-trifluoroacetamide (53th)

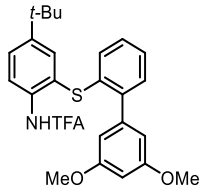

Following **GP4**, 1-azido-3-(tert-butyl)benzene (42 mg, 0.24 mmol, 2.4 eq.) gave **53th** (29%) as an oil. ^{1}H NMR ($CDCl_3$, 600 MHz) δ 8.70 (1H, s), 8.21 (1H, d, *J* = 8.7 Hz), 7.55 (1H, d, *J* = 2.3 Hz), 7.48 (1H, dd, *J* = 8.6, 2.3 Hz), 7.29 (1H, dd, *J* = 7.5, 1.6 Hz), 7.24 (1H, td, *J* = 7.4, 1.3 Hz), 7.19 (1H, td, *J* = 7.6, 1.7 Hz), 6.82 (1H, dd, *J* = 7.9, 1.3 Hz), 6.50 (3H, s), 3.82 (6H, s), 1.30 (9H, s); ^{13}C NMR ($CDCl_3$, 151 MHz) δ 160.8, 154.5 (q, *J* = 37.4 Hz), 149.9, 142.0, 141.6, 134.4, 133.7, 133.7, 130.5, 128.6, 128.0, 127.4, 126.7, 122.2, 121.0, 115.7 (q, *J* = 289.0 Hz), 107.3, 100.1, 55.5, 34.8, 31.3; ^{19}F NMR ($CDCl_3$, 564 MHz) δ.

N-(2-(tert-butyl)-6-((3',5'-dimethoxy-[1,1'-biphenyl]-2-yl)thio)phenyl)-2,2,2-trifluoroacetamide (53th')

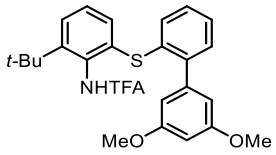

Following **GP4**, 1-azido-3-(tert-butyl)benzene (42 mg, 0.24 mmol, 2.4 eq.) gave **53th'** (27%) as an oil. ^{1}H NMR ($CDCl_3$, 600 MHz) δ 7.54 (1H, dd, *J* = 7.6, 1.5 Hz), 7.36 (1H, td, *J* = 7.5, 1.6 Hz), 7.32 (1H, td, *J* = 7.5, 1.7 Hz), 7.22 (3H, s), 7.12 (1H, t, *J* = 7.9 Hz), 7.06 (1H, dd, *J* = 7.8, 1.4 Hz), 6.37 (1H, t, *J* = 2.3 Hz), 6.29 (2H, d, *J* = 2.2 Hz), 3.70 (6H, s), 1.31 (9H, s); ^{13}C NMR ($CDCl_3$, 151 MHz) δ 160.0, 156.6 (q, *J* = 36.9 Hz), 148.3, 144.8, 143.0, 138.7, 134.1, 133.9, 131.4, 131.4, 130.9, 129.1, 128.4 (q, *J* = 5.1 Hz), 126.1, 116.1 (d, *J* = 289.1 Hz), 107.3, 99.8, 55.4, 35.6, 30.9, 29.9; ^{19}F NMR ($CDCl_3$, 564 MHz) δ -75.64.

N-(2-((3',5'-dimethoxy-[1,1'-biphenyl]-2-yl)thio)-6-methoxyphenyl)-2,2,2-trifluoroacetamide (53uh)

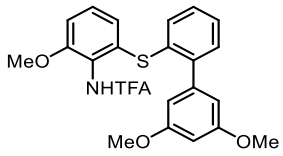

Following **GP4**, 1-azido-3-methoxybenzene (36 mg, 0.24 mmol, 2.4 eq.) gave **53uh** (53%) as an oil. ^{1}H NMR ($CDCl_3$, 600 MHz) δ; ^{13}C NMR ($CDCl_3$, 151 MHz) δ 8.52 (1H, s), 8.16 (1H, d, *J* = 9.0 Hz), 7.29 (1H, dd, *J* = 7.5, 1.9 Hz), 7.28 – 7.25 (1H, m), 7.21 (1H, td, *J* = 7.5, 1.9 Hz), 7.03 (1H, d, *J* = 2.9 Hz), 6.99 – 6.94 (2H, m), 6.49 (1H, t, *J* = 2.3 Hz), 6.45 (2H, d, *J* = 2.2 Hz), 3.81 (6H, s), 3.78 (3H, s); ^{19}F NMR ($CDCl_3$, 564 MHz) δ 160.7, 157.4, 154.3 (q, *J* = 37.2 Hz), 142.2, 142.0, 133.2, 130.6, 129.9, 128.6, 128.4, 127.1, 124.8, 122.7, 121.3, 115.9, 115.8 (q, *J* = 288.9 Hz), 107.3, 100.0, 55.7, 55.5.

N-(3-((3',5'-dimethoxy-[1,1'-biphenyl]-2-yl)thio)-5,6,7,8-tetrahydronaphthalen-2-yl)-2,2,2-trifluoroacetamide (53vh)

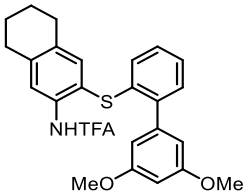

Following **GP4**, 5-azido-1,2,3,4-tetrahydronaphthalene (41.5 mg, 0.24 mmol, 2.4 eq.) gave **53wh** (37%) as an oil. ^{1}H NMR ($CDCl_3$, 600 MHz) δ 8.73 (1H, s), 8.03 (1H, s), 7.40 – 7.14 (4H, m), 6.87 (1H, dd, *J*=7.7, 1.5 Hz), 6.52 (1H, d, *J*=2.1 Hz), 6.51 (2H, d, *J*=2.2 Hz), 3.84 (6H, s), 2.83 (2H, t, *J*=3.5 Hz), 2.72 (2H, d, *J*=5.2 Hz), 1.82 (4H, p, *J*=3.2 Hz); ^{13}C NMR ($CDCl_3$, 151 MHz) δ 160.7, 154.4 (q, *J* = 37.2 Hz), 142.0, 141.6, 140.8, 137.4, 135.9, 134.3, 130.4, 128.5, 128.2, 127.9, 126.6, 121.7, 119.0, 115.7 (q, *J* = 289.1 Hz), 107.3, 100.1, 55.5, 29.7, 28.9, 22.9, 22.9; ^{19}F NMR ($CDCl_3$, 564 MHz) δ -75.50.

N-(2-((3',5'-dimethoxy-[1,1'-biphenyl]-2-yl)thio)-5,6,7,8-tetrahydronaphthalen-1-yl)-2,2,2-trifluoroacetamide (53vh')

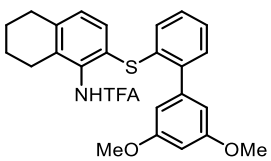

Following **GP4**, 6-azido-1,2,3,4-tetrahydronaphthalene (41.5 mg, 0.24 mmol, 2.4 eq.) gave **53wc'** (40%) as an oil. ^{1}H NMR ($CDCl_3$, 600 MHz) δ 7.40 (1H, s), 7.24 – 7.10 (3H, m), 7.07 (2H, d, *J*=7.0 Hz), 6.93 (1H, d, *J*=8.0 Hz), 6.36 (1H, d, *J*=2.3 Hz), 6.29 (2H, d, *J*=2.3 Hz), 3.68 (6H, s),

2.70 (2H, t, *J*=6.1 Hz), 2.42 (2H, t, *J*=6.0 Hz), 1.69 (4H, q, *J*=7.2 Hz); ^{13}C NMR ($CDCl_3$, 151 MHz) δ 160.5, 155.1 (q, *J* = 37.0 Hz), 142.7, 142.7, 139.7, 135.8, 134.4, 133.4, 132.1, 130.5, 130.0, 129.9, 128.4, 128.2, 127.1, 115.9 (q, *J* = 288.9 Hz), 107.2, 99.7, 55.4, 29.7, 25.5, 22.5, 22.4; ^{19}F NMR ($CDCl_3$, 564 MHz) δ -75.97.

Butyl-4-((3',5'-dimethoxy-[1,1'-biphenyl]-2-yl)thio)-3-(2,2,2-trifluoroacetamido)benzoate (53wh)

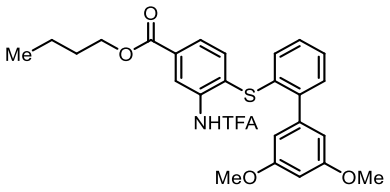

Following **GP4**, butyl 4-azidobenzoate (52.6 mg, 0.24 mmol, 2.4 eq.) gave **53wh** (58%) as an oil. ^{1}H NMR ($CDCl_3$, 600 MHz) δ 8.79 (1H, d, *J*=1.8 Hz), 8.58 (1H, s), 7.81 (1H, dd, *J*=8.1, 1.8 Hz), 7.46 (1H, d, *J*=8.1 Hz), 7.37 – 7.28 (2H, m), 7.28 – 7.21 (2H, m), 7.11 (1H, dd, *J*=7.8, 1.2 Hz), 6.45 (1H, t, *J*=2.3 Hz), 6.35 (2H, d, *J*=2.3 Hz), 4.34 (2H, t, *J*=6.7 Hz), 3.76 (6H, s), 3.70 (2H, s), 1.83 – 1.63 (2H, m), 1.54 – 1.44 (2H, m), 0.98 (3H, t, *J*=7.4 Hz); ^{13}C NMR ($CDCl_3$, 151 MHz) δ 165.5, 160.7, 154.7 (q, *J* = 37.8 Hz), 143.2, 141.9, 136.1, 135.3, 132.2, 130.9, 130.2, 130.0, 128.7, 128.0, 127.2, 122.1, 115.6 (q, *J* = 289.0 Hz), 107.3, 99.7, 67.2, 65.5, 55.4, 30.8, 19.3, 13.9; ^{19}F NMR ($CDCl_3$, 564 MHz) δ -75.97.

N-(2-((3',5'-dimethoxy-[1,1'-biphenyl]-2-yl)thio)-5-(3-ethyl-2,6-dioxopiperidin-3-yl)phenyl)-2,2,2-trifluoroacetamide(53x)

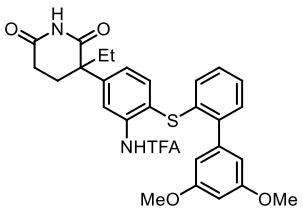

Following **GP4**, 3-(4-azidophenyl)-3-ethylpiperidine-2,6-dione (62 mg, 0.24 mmol, 2.4 eq.) gave **49af** (69%) as an oil. ^{1}H NMR ($CDCl_3$, 600 MHz) δ 8.73 (1H, s), 8.30 (1H, d, *J*=2.2 Hz), 7.84 (1H, s), 7.43 (1H, d, *J*=8.2 Hz), 7.32 – 7.26 (2H, m), 7.26 – 7.21 (1H, m), 7.09 (1H, dd, *J*=8.2, 2.1 Hz), 7.01 (1H, d, *J*=8.7 Hz), 6.46 (1H, t, *J*=2.3 Hz), 6.39 (2H, d, *J*=2.2 Hz), 3.79 (6H, s), 2.71 – 2.62 (1H, m), 2.49 – 2.41 (1H, m), 2.40 – 2.33 (1H, m), 2.26 (1H, td, *J*=14.0, 4.4 Hz), 2.13 – 2.04 (1H, m), 1.98 – 1.88 (1H, m), 0.89 (3H, t, *J*=7.4 Hz); ^{13}C NMR ($CDCl_3$, 151 MHz) δ 174.5, 172.0, 160.8, 154.9 (q, *J*=37.8 Hz), 142.7, 142.0, 141.9, 137.2, 136.6, 132.6, 130.8, 129.3, 128.7, 127.9, 127.6, 124.7, 123.1, 115.5 (q, *J*=37.8 Hz), 107.4, 99.7, 55.5, 51.4, 32.9, 29.3, 27.1, 9.2; ^{19}F NMR ($CDCl_3$, 564 MHz) δ -76.05.

N-((8R,9S,13S,14S)-3-((3',5'-dimethoxy-[1,1'-biphenyl]-2-yl)thio)-13-methyl-17-oxo-7,8,9,11,12,13,14,15,16,17-decahydro-6H-cyclopenta[a]phenanthren-2-yl)-2,2,2-trifluoroacetamide (53yh')

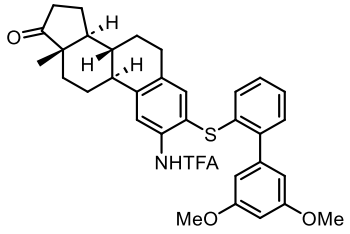

Following **GP4**, (8R,9S,13S,14S)-3-azido-13-methyl-6,7,8,9,11,12,13,14,15,16-decahydro-17H-cyclopenta[a]phenanthren-17-one (71 mg, 0.24 mmol, 2.4 eq.) gave **53wh'** (28%) as an oil. ^{1}H NMR ($CDCl_3$, 600 MHz) δ 8.68 (1H, s), 8.25 (1H, s), 7.29 – 7.23 (1H, m), 7.23 (1H, d, *J*=5.7 Hz), 7.18 (1H, t, *J*=7.1 Hz), 6.87 (1H, d, *J*=7.9 Hz), 6.49 (1H, s), 6.47 (2H, s), 3.82 (6H, s), 2.86 (2H, d, *J*=7.5 Hz), 2.52 (1H, dd, *J*=19.0, 8.8 Hz), 2.44 (1H, dd, *J*=13.5, 3.6 Hz), 2.32 (1H, td, *J*=11.8, 11.2, 3.9 Hz), 2.22 – 2.11 (1H, m), 2.10 – 2.01 (2H, m), 1.99 (1H, d, *J*=12.9 Hz), 1.69 – 1.40 (7H, m), 0.93 (3H, s); ^{13}C NMR ($CDCl_3$, 151 MHz) δ 220.6, 160.7, 143.2, 142.0, 141.7, 137.0, 135.3, 134.7, 133.8, 130.5, 128.5, 127.6, 126.7, 119.7, 118.5, 107.3, 100.0, 55.5, 50.6, 48.1, 44.8, 37.9, 36.0, 31.6, 28.9, 26.3, 25.7, 21.7, 14.0; ^{19}F NMR ($CDCl_3$, 564 MHz) δ -76.06.

5.4.2.4 Synthesis of sulfonium salts

2,4-dimethoxy-5-(4-(4,4,5,5-tetramethyl-1,3,2-dioxaborolan-2-yl)-2-(2,2,2trifluoroacetamido)phenyl) -5H-dibenzo[b,d]thiophen-5-ium trifluoromethanesulfonate (54kh)

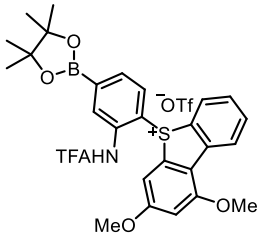

An oven-dried tube equipped with a stirring bar was charged with 2-(4-azidophenyl)-4,4,5,5-tetramethyl-1,3,2-dioxaborolane (59 mg, 0.24 mmol, 2.4 eq.) DMAP (12 mg, 0.10 mmol, 1.0 eq.) and thiophenol **46h** (25 mg, 0.10 mmol, 1.0 eq.). After the tube was capped under air with a Supelco aluminum crimp seal containing a septum (PTFE/butyl), anhydrous 1,4-dioxane (0.05 M) was added *via* syringe. Under vigorous ventilation with a fan, the mixture was stirred (900 rpm) and irradiated with a purple LED (Kessil PR160L-390 nm) for 16 h at room temperature. Then, trifluoroacetic anhydride (85 mg, 0.40 mmol, 4.0 eq.) was added and the mixture was stirred for another 2 h. All volatiles were evaporated in vacuo and the obtained crude was used without any further purification

Subsequently, an oven-dried tube equipped with a stirring bar was charged with NCS (13 mg, 0.10 mmol, 1.0 eq.) and $Bi(OTf)_3$ (98 mg, 0.15 mmol, 1.5 eq.). The tube was then capped under air with a Supelco aluminum crimp seal with septum (PTFE/butyl), evacuated and backfilled with argon three times. After the addition of anhydrous MeCN (0.066 M), the mixture was vigorously stirred while a solution of the previously obtained crude in dry 1,4-dioxane (0.066 M) was added via syringe. The reaction was then stirred at 1300 rpm for 6h at room temperature. Upon consumption of the starting material (TLC analysis), the solvent was evaporated and the residue redissolved in $MeOH/CHCl_3$. The suspension was filtered through Celite® and the filtrate evaporated under vacuum. The residue was dissolved in the minimum amount of $CHCl_3$, and the product was precipitated by addition of Et_2O as an off-white solid. The solid was recollected by filtration and further washed with Et_2O affording compound **54kh** (59%) as white solid ^{1}H NMR ($CDCl_3$, 600 MHz) δ 11.41 (1H, s), 8.53 (1H, d, *J* = 8.1 Hz), 8.18 (1H, d, *J* = 7.8 Hz), 8.08 (1H, s), 7.88 (1H, t, *J* = 7.7 Hz), 7.66 (1H, t, *J* = 8.0 Hz), 7.59 (1H, d, *J* = 8.2 Hz), 7.24 (1H, s), 6.53 – 6.45 (2H, m), 3.99 (3H, s), 3.84 (3H, s), 1.28 (12H, s); ^{13}C NMR ($CDCl_3$, 151 MHz) δ 167.7, 158.5, 158.1 (q, *J* = 39.2 Hz), 141.3, 139.9, 137.5, 135.8, 135.7, 134.5, 132.2, 131.3, 129.8, 126.1, 125.2, 124.3, 120.5 (q, *J* = 319.7 Hz), 115.9 (q, *J* = 287.4 Hz), 108.2, 101.2, 100.1, 84.9, 57.1, 56.6, 29.7, 24.8; ^{19}F NMR ($CDCl_3$, 564 MHz) δ -72.71, -76.18.

5.4.2.5 Synthesis of aniline derivatives

General Procedure 5

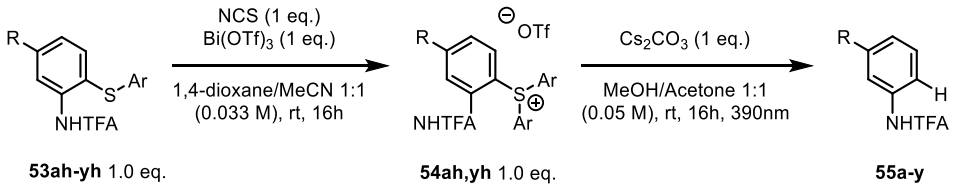

a. An oven-dried tube equipped with a stirring bar was charged with NCS (1.0 eq.) and $Bi(OTf)_3$ (1.0 eq.). The tube was then capped under air with a Supelco aluminum crimp seal with septum (PTFE/butyl), evacuated and backfilled with argon three times. After the addition of anhydrous MeCN (0.066 M), the mixture was vigorously stirred while a solution of **53ah-yh** in dry 1,4-dioxane (0.066 M) was added via syringe. The reaction was then stirred at 1300 rpm for 6 h at room temperature. Upon consumption of the starting material (TLC analysis), the solvent was evaporated and the residue redissolved in $MeOH/CHCl_3$. The suspension was filtered through Celite® and the filtrate evaporated under vacuum. The residue was dissolved in the minimum amount of $CHCl_3$, and the product was precipitated

by addition of Et_2O as an off-white solid. The solid was recollected by filtration and further washed with Et_2O.

b. **54ah-yh** (1.0 eq.) was weighed in an oven-dried tube equipped with a stirring bar. Cs_2CO_3 (1.0 eq.) was added and the tube was then capped under air with a Supelco aluminum crimp seal with septum (PTFE/butyl), evacuated and backfilled with argon three times. Anhydrous MeOH (0.1 M) and anhydrous acetone (0.1 M) were added via syringe. The mixture was then purged with Argon for 5 min. Subsequently, it was stirred (600 rpm) and irradiated with purple LEDs (Kessil PR160L-390 nm) for 12 h at room temperature (fan ventilation). Ethylene carbonate (250 µL, 0.1 M in $CDCl_3$) was added and the solution stirred for 1 min., then 0.3 mL of the solution was placed in an NMR tube, diluted with $CDCl_3$ (0.4 mL) and analyzed by ^1H NMR spectroscopy to determine the NMR yield.

5-(3,5-dimethyl-2-(2,2,2-trifluoroacetamido)phenyl)-1,3-dimethoxy-5H-dibenzo[b,d]thiophen-5-ium trifluoromethanesulfonate (54qh)

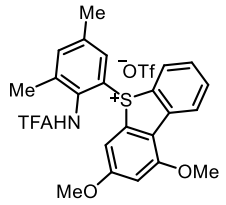

Following **GP5a** N-(2-((4,6-dimethoxy-[1,1'-biphenyl]-2-yl)thio)-4,6-dimethylphenyl)-2,2,2-trifluoroacetamide (50.0 mg, 0.11 mmol, 1.0 eq.) gave **54qh** (81%) as an oil. ^1H NMR ($CDCl_3$, 600 MHz) δ 8.43 (1H, d, *J*=7.4 Hz), 8.22 (1H, s), 7.96 (1H, t, *J*=7.6 Hz), 7.60 (1H, d, *J*=2.0 Hz), 7.54 (1H, s), 6.85 (1H, d, J=2.0 Hz), 6.47 (1H,s), 4.04 (3H, s), 3.91 (3H, s), 2.39 (3H, s), 2.15 (3H, s). ^{13}C NMR ($CDCl_3$, 151 MHz) δ 169.5, 159.9,143.8, 143.5, 141.1, 139.6, 135.4, 134.7, 132.9, 128.7, 126.3, 122.8, 120.5, 118.5, 116.5, 103..1, 101.7, 57.7, 57.3, 20.8, 17.9; ^{19}F NMR ($CDCl_3$, 564 MHz) δ -76.49, -80.14.

N-(3-(tert-butyl)phenyl)-2,2,2-trifluoroacetamide (55a)

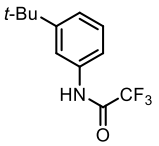

Following **GP5** N-(5-(tert-butyl)-2-((3',5'-dimethoxy-[1,1'-biphenyl]-2-yl)thio)phenyl)-2,2,2-trifluoroacetamide (47.8 mg, 0.24 mmol, 2.4 eq.) gave **55a** (81%) as an oil. ^1H NMR ($CDCl_3$, 600 MHz) δ 7.96 (1H, s), 7.52 (1H, t, *J*=2.0 Hz), 7.45 (1H, d, *J*=7.9 Hz), 7.32 (1H, t, *J*=7.9 Hz), 7.28 (1H, s), 1.32 (9H, s); ^{13}C NMR ($CDCl_3$, 151 MHz) δ 154.8 (q, *J*=37.1 Hz), 153.0, 135.0, 129.2, 123.6, 117.9, 117.8, 115.8 (q, *J*=288.7 Hz), 35.0, 31.3; ^{19}F NMR ($CDCl_3$, 564 MHz) δ -75.77.

2,2,2-trifluoro-N-(m-tolyl)acetamide (55b)

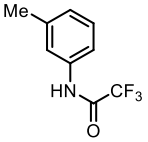

Following **GP5**, N-(2-((3',5'-dimethoxy-[1,1'-biphenyl]-2-yl)thio)-5-methylphenyl)-2,2,2-trifluoroacetamide (47.8 mg, 0.24 mmol, 2.4 eq.) gave **55b** (78%) as n oil. ^{1}H NMR ($CDCl_3$, 600 MHz) δ 7.80 (1H, s), 7.40 (1H, s), 7.35 (1H, d, *J*=8.2 Hz), 7.28 (1H, t, *J*=7.8 Hz), 7.06 (1H, d, *J*=7.5), 2.37 (3H, s); ^{13}C NMR ($CDCl_3$, 151 MHz) δ 154.8 (q, *J*=37.4 Hz), 139.7, 135.1, 129.4, 127.3, 121.2, 117.7, 115.9 (q, *J*=288.9 Hz), 21.6; ^{19}F NMR ($CDCl_3$, 564 MHz) δ -75.65.

N-(3-ethylphenyl)-2,2,2-trifluoroacetamide (55c)

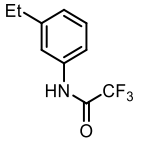

Following **GP5** N-(2-((3',5'-dimethoxy-[1,1'-biphenyl]-2-yl)thio)-5-ethylphenyl)-2,2,2-trifluoroacetamide (47.8 mg, 0.24 mmol, 2.4 eq.) gave **55c** (78%) as an oil. ^{1}H NMR ($CDCl_3$, 600 MHz) δ 8.03 (1H, s), 7.41 (1H, s), 7.39 (1H, d, *J*=8.03 Hz), 7.30 (1H, t, *J*=7.8 Hz), 7.09 (1H, d, *J*=7.6), 2.65 (2H, q, *J*=7.6), 1.24 (3H, t, *J*=7.6 Hz); ^{13}C NMR ($CDCl_3$, 151 MHz) δ 155.0 (q, *J*=37.1 Hz), 146.0, 135.2, 129.4, 126.1, 120.2, 118.0, 115.9 (q, *J*=288.8 Hz), 28.9, 15.5; ^{19}F NMR ($CDCl_3$, 564 MHz) δ -75.78.

2,2,2-trifluoro-N-(3-isopropylphenyl)acetamide (55d)

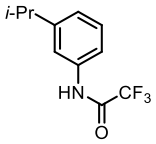

Following **GP5**, N-(2-((3',5'-dimethoxy-[1,1'-biphenyl]-2-yl)thio)-5-isopropylphenyl)-2,2,2-trifluoroacetamide (47.8 mg, 0.24 mmol, 2.4 eq.) gave **55d** (77%) as an oil. ^{1}H NMR ($CDCl_3$, 600 MHz) δ 8.00 (1H, s), 7.43 – 7.39 (2H, m), 7.31 (1H, t, *J*=8.2 Hz), 7.12 (1H, d, *J*=7.8 Hz), 2.91 (1H, hept, *J*=6.9 Hz), 1.25 (6H, d, *J*=7.0 Hz); ^{13}C NMR ($CDCl_3$, 151 MHz) δ 154.9 (q, *J*=37.3 Hz), 150.6, 135.2, 129.4, 124.7, 118.8, 118.2, 115.9 (q, *J*=288.7 Hz), 34.2, 23.9; ^{19}F NMR ($CDCl_3$, 564 MHz) δ -75.69.

N-(3-benzylphenyl)-2,2,2-trifluoroacetamide(55e)

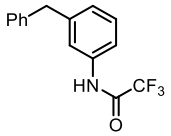

Following **GP5**, N-(5-benzyl-2-((3',5'-dimethoxy-[1,1'-biphenyl]-2-yl)thio)phenyl)-2,2,2-trifluoroacetamide (47.8 mg, 0.24 mmol, 2.4 eq.) gave **55e** (78%) as an oil. ^{1}H NMR ($CDCl_3$, 600 MHz) δ 7.76 (1H, s), 7.47 (1H, d, *J*=6.8 Hz), 7.35 – 7.27 (4H, m), 7.23 (1H, d, *J*=7.5 Hz), 7.19 (2H, d, *J*=7.0 Hz), 7.09 (1H, d, *J*=7.7 Hz), 3.99 (2H, s); ^{13}C NMR ($CDCl_3$, 151 MHz) δ 154.8 (q, *J*=37.8 Hz), 143.0, 140.4, 135.4, 129.7, 129.1, 128.8, 127.1, 126.5, 120.9, 118.4, 115.8 (q, *J*=288.2 Hz), 41.9; ^{19}F NMR ($CDCl_3$, 564 MHz) δ -70.8.

2,2,2-trifluoro-N-(3-(trifluoromethyl)phenyl)acetamide (55f)

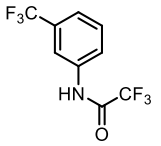

Following **GP5**, N-(2-((3',5'-dimethoxy-[1,1'-biphenyl]-2-yl)thio)-5-(trifluoromethyl)phenyl)-2,2,2 trifluoroacetamide (47.8 mg, 0.24 mmol, 2.4 eq.) gave **55f** (74%) as an oil. ^{1}H NMR ($CDCl_3$, 600 MHz) δ 7.98 (1H, s), 7.87 (1H, s), 7.80 (1H, dt, *J*=7.9, 1.8 Hz), 7.57 – 7.51 (2H, m); ^{13}C NMR ($CDCl_3$, 151 MHz) δ 155.1 (q, *J*=37.8 Hz), 132.1 (q, *J*=33.2 Hz), 130.3, 123.7, 123.4 (q, *J*=273.3 Hz), 123.2 (q, *J*=4.5 Hz), 117.5 (q, *J*=4.5 Hz), 115.6 (q, *J*=288.4 Hz); ^{19}F NMR ($CDCl_3$, 564 MHz) δ -62.95, -75.84.

N-(3-(1-cyanocyclopentyl)phenyl)-2,2,2-trifluoroacetamide (55g)

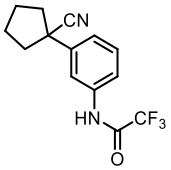

Following **GP5**, N-(5-(1-cyanocyclopentyl)-2-((3',5'-dimethoxy-[1,1'-biphenyl]-2-yl)thio)phenyl)-2,2,2-trifluoroacetamide (47.8 mg, 0.24 mmol, 2.4 eq.) gave **55g** (49%) as an oil. ^{1}H NMR ($CDCl_3$, 600 MHz) δ 8.05 (1H, s), 7.67 (1H, t, *J*=2.0 Hz), 7.59 (1H, d, *J*=8.1 Hz), 7.42 (1H, t, *J*=8.0 Hz), 7.34 (1H, d, *J*=4.9 Hz), 2.52 – 2.46 (2H, m), 2.12 – 2.01 (4H, m), 1.99 – 1.93 (2H, m); ^{13}C NMR ($CDCl_3$, 151 MHz) δ 154.9 (q, *J*=37.7 Hz), 141.6, 135.9, 130.1, 124.1, 124.0, 120.0, 118.3, 115.8 (q, *J*=288.9 Hz), 47.9, 40.7, 24.4; ^{19}F NMR ($CDCl_3$, 564 MHz) δ -75.71.

2,2,2-trifluoro-N-(3-(methoxymethyl)phenyl)acetamide (55h)

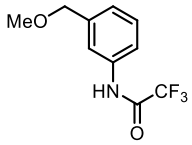

Following **GP5**, N-(2-((3',5'-dimethoxy-[1,1'-biphenyl]-2-yl)thio)-5-(methoxymethyl)phenyl)-2,2,2-trifluoroacetamide (47.8 mg, 0.24 mmol, 2.4 eq.) gave **55h** (63%) as an oil. ^{1}H NMR ($CDCl_3$, 600 MHz) δ 8.45 (1H, s), 7.53 – 7.48 (2H, m), 7.33 (1H, t, *J*=7.8 Hz), 7.18 (1H, d, *J*=7.6 Hz), 4.45 (2H, s), 3.41 (3H, s); ^{13}C NMR ($CDCl_3$, 151 MHz) δ 155.1 (q, *J*=37.4 Hz), 139.4, 135.5, 129.4, 125.6, 120.2, 120.0, 115.9 (q, *J*=288.5 Hz), 74.2, 58.3; ^{19}F NMR ($CDCl_3$, 564 MHz) -75.80 δ.

N-(3-(2-(benzyloxy)-1,1,1,3,3,3-hexafluoropropan-2-yl)phenyl)-2,2,2-trifluoroacetamide (55i)

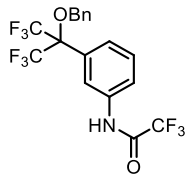

Following **GP5**, N-(5-(2-(benzyloxy)-1,1,1,3,3,3-hexafluoropropan-2-yl)-2-((3',5'-dimethoxy-[1,1'-biphenyl]-2-yl)thio)phenyl)-2,2,2-trifluoroacetamide (47.8 mg, 0.24 mmol, 2.4 eq.) gave **55i** (65%) as an oil. ^{1}H NMR ($CDCl_3$, 600 MHz) δ 7.91 (1H, s), 7.88 – 7.80 (1H, m), 7.73 (1H, s), 7.53 (2H, d, *J*=5.1 Hz), 7.45 – 7.33 (5H, m), 4.68 (2H, s); ^{13}C NMR ($CDCl_3$, 151 MHz) δ 136.1, 135.8, 130.2, 130.0, 128.8, 128.5, 127.6, 126.2, 122.7, 122.4 (q, *J*=286.9 Hz), 120.5, 68.6; ^{19}F NMR ($CDCl_3$, 564 MHz) δ -70.57, -75.69.

2,2,2-trifluoro-N-(3-(hydroxydiphenylmethyl)phenyl)acetamide (55j)

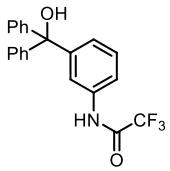

Following **GP5**, N-(2-((3',5'-dimethoxy-[1,1'-biphenyl]-2-yl)thio)-5-(hydroxydiphenylmethyl)phenyl)-2,2,2-trifluoroacetamide (47.8 mg, 0.24 mmol, 2.4 eq.) gave **55j** (76%) as an oil. ^{1}H NMR ($CDCl_3$, 600 MHz) δ 7.84 (1H, s), 7.66 (1H, d, *J*=5.9 Hz), 7.36 – 7.18 (12H, m), 7.10 (1H, d, *J*=7.9 Hz); ^{13}C NMR ($CDCl_3$, 151 MHz) δ 154.9 (q, *J*=37.4 Hz), 148.5, 146.4, 135.0, 129.1, 128.3, 128.0, 127.7, 126.1, 119.9, 119.6, 115.8 (q, *J*=288.8 Hz), 81.9; ^{19}F NMR ($CDCl_3$, 564 MHz) δ -75.77.

2,2,2-trifluoro-N-(3-(4,4,5,5-tetramethyl-1,3,2-dioxaborolan-2-yl)phenyl)acetamide (55k)

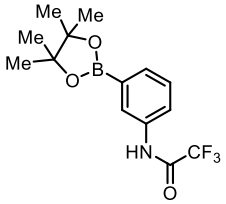

Following **GP5**, 2,4-dimethoxy-5-(4-(4,4,5,5-tetramethyl-1,3,2-dioxaborolan-2-yl)-2-(2,2,2trifluoroacetamido)phenyl)-5H-dibenzo[b,d]thiophen-5-ium trifluoromethanesulfonate (47.8 mg, 0.24 mmol, 2.4 eq.) gave **55k** (98%) as an oil. ^{1}H NMR ($CDCl_3$, 600 MHz) δ 7.90 (1H, d, *J*=10.8 Hz), 7.73 (1H, s), 7.67 (1H, d, *J*=7.3 Hz), 7.42 (1H, t, *J*=7.7 Hz), 1.35 (12H, s); ^{13}C NMR ($CDCl_3$, 151 MHz) δ 154.9 (q, *J*=37.2 Hz), 134.7, 132.7, 129.1, 126.5, 123.5, 115.9 (q, *J*=289.2 Hz), 84.4, 25.0; ^{19}F NMR ($CDCl_3$, 564 MHz) δ -75.87. *Note: Quaternary carbon not visible for quadrupolar effect of boron*

2,2,2-trifluoro-N-(2',3',4',5'-tetrahydro-[1,1'-biphenyl]-3-yl)acetamide (55l)

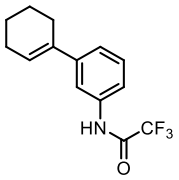

Following **GP5**, N-(4-((3',5'-dimethoxy-[1,1'-biphenyl]-2-yl)thio)-2',3',4',5'-tetrahydro-[1,1'-biphenyl]-3-yl)-2,2,2-trifluoroacetamide (47.8 mg, 0.24 mmol, 2.4 eq.) gave **55l** (66%) as an oil. ^{1}H NMR ($CDCl_3$, 600 MHz) δ 7.91 (1H, s), 7.55 (1H, s), 7.43 (1H, d, *J*=8.1 Hz), 7.32 (1H, t, *J*=7.9 Hz), 7.26 (1H, d, *J*=8.0 Hz), 6.18 – 6.13 (1H, m), 2.41 – 2.34 (4H, m), 2.25 – 2.17 (4H, m), 1.83 – 1.75 (2H, m), 1.69 – 1.60 (3H, m); ^{13}C NMR ($CDCl_3$, 151 MHz) δ 154.9 (q, *J*=37.4 Hz), 144.3, 135.8, 135.1, 129.3, 126.3, 123.2, 118.7, 117.3, 115.9 (q, *J*=288.9 Hz), 27.5, 26.0, 23.1, 22.1; ^{19}F NMR ($CDCl_3$, 564 MHz) δ -75.78.

N-([1,1'-biphenyl]-3-yl)-2,2,2-trifluoroacetamide (55m)

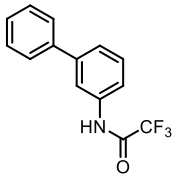

Following **GP5**, N-(4-((3',5'-dimethoxy-[1,1'-biphenyl]-2-yl)thio)-[1,1'-biphenyl]-3-yl)-2,2,2-trifluoroacetamide (47.8 mg, 0.24 mmol, 2.4 eq.) gave **55m** (65%) as an oil. ^{1}H NMR ($CDCl_3$, 600 MHz) δ 7.95 (1H, s), 7.80 (1H, s), 7.59 (2H, d, *J*=8.1 Hz), 7.58 – 7.54 (1H, m), 7.50 – 7.43 (4H, m), 7.38 (1H, t, *J*=6.9 Hz); ^{13}C NMR ($CDCl_3$, 151 MHz) δ 154.7 (q, *J*=37.6 Hz), 142.8, 140.1,

135.7, 129.9, 1289.0, 128.0, 127.3, 125.3, 119.3, 118.0 (q, *J*=362.4 Hz) ; ^{19}F NMR ($CDCl_3$, 564 MHz) δ -75.71.

2,2,2-trifluoro-N-(4'-methoxy-[1,1'-biphenyl]-3-yl)acetamide (55n)

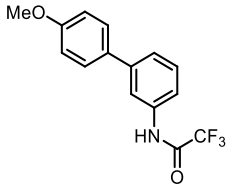

Following **GP5**, N-(4-((3',5'-dimethoxy-[1,1'-biphenyl]-2-yl)thio)-4'-methoxy-[1,1'-biphenyl]-3-yl)-2,2,2-trifluoroacetamide (47.8 mg, 0.24 mmol, 2.4 eq.) gave **55o** (79%) as an oil. ^{1}H NMR ($CDCl_3$, 600 MHz) δ 7.94 (1H, s), 7.76 (1H, s), 7.52 (2H, d, *J*=8.7 Hz), 7.51 – 7.48 (1H, m), 7.46 – 7.41 (2H, m), 6.98 (2H, d, *J*=8.7 Hz), 3.86 (3H, s); ^{13}C NMR ($CDCl_3$, 151 MHz) δ 159.7, 154.9 (q, *J*=37.3 Hz), 142.4, 135.6, 132.6, 129.9, 128.4, 124.9, 118.9, 118.7, 115.9 (q, *J*=288.5 Hz), 114.5, 55.5; ^{19}F NMR ($CDCl_3$, 564 MHz) δ -76.1.

2,2,2-trifluoro-N-(4'-iodo-[1,1'-biphenyl]-3-yl)acetamide (55o)

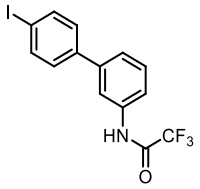

Following **GP5**, N-(4-((3',5'-dimethoxy-[1,1'-biphenyl]-2-yl)thio)-4'-iodo-[1,1'-biphenyl]-3-yl)-2,2,2-trifluoroacetamide (47.8 mg, 0.24 mmol, 2.4 eq.) gave **55o** (77%) as an oil. ^{1}H NMR ($CDCl_3$, 600 MHz) δ 8.00 (1H, s), 7.80 (1H, s), 7.58 (2H, d, *J*=7.1 Hz), 7.56 (1H, dt, *J*=6.8, 2.2 Hz), 7.49 – 7.43 (3H, m), 7.38 (1H, t, *J*=7.4 Hz); ^{13}C NMR ($CDCl_3$, 151 MHz) δ 155.0 (q, *J*=37.3 Hz), 142.8, 140.1, 135.7, 129.9, 129.0, 128.0, 127.3, 125.3, 120.9, 119.4, 119.4, 115.9 (q, *J*=288.7 Hz); ^{19}F NMR ($CDCl_3$, 564 MHz) δ -75.71.

2,2,2-trifluoro-N-(3'-fluoro-[1,1'-biphenyl]-3-yl)acetamide (55p)

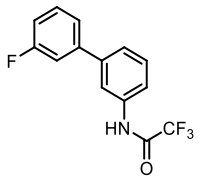

Following **GP5,** N-(4-((3',5'-dimethoxy-[1,1'-biphenyl]-2-yl)thio)-3'-fluoro-[1,1'-biphenyl]-3-yl)-2,2,2-trifluoroacetamide (47.8 mg, 0.24 mmol, 2.4 eq.) gave **55p** (75%) as an oil. ^{1}H NMR ($CDCl_3$, 600 MHz) δ 7.94 (1H, s), 7.79 (1H, s), 7.57 – 7.49 (3H, m), 7.46 (1H, t, *J*=7.8 Hz), 7.42 (1H, d,

J=7.6 Hz), 7.14 (2H, t, *J*=8.6 Hz); ^{13}C NMR ($CDCl_3$, 151 MHz) δ 162.9 (d, *J*=247.5 Hz), 155.0 (q, *J*=37.4 Hz), 141.9, 136.3, 135.7, 130.0, 129.0, 128.9, 125.2, 119.3, 119.2, 116.0, 115.9, 115.6 (q, *J*=289.9 Hz); ^{19}F NMR ($CDCl_3$, 564 MHz) δ -75.72, -114.71.

N-(2,4-dimethylphenyl)-2,2,2-trifluoroacetamide (55q)

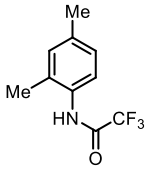

Following **GP5**, N-(2-((3',5'-dimethoxy-[1,1'-biphenyl]-2-yl)thio)-4,6-dimethylphenyl)-2,2,2-trifluoroacetamide (47.8 mg, 0.24 mmol, 2.4 eq.) gave **55q** (67%) as an oil. ^{1}H NMR ($CDCl_3$, 600 MHz) δ 7.63 (1H, s), 7.60 (1H, d, *J*=6.0 Hz), 7.07 (1H, d, *J*=6.5 Hz), 7.06 (1H, s), 2.32 (3H, s), 2.25 (1H, s); ^{13}C NMR ($CDCl_3$, 151 MHz) δ 137.2, 131.7, 130.3, 130.2, 127.8, 123.5, 116.0 (q, *J*=286.9), 21.1, 17.5; ^{19}F NMR ($CDCl_3$, 564 MHz) δ -75.63.

N-(2,4-dimethoxyphenyl)-2,2,2-trifluoroacetamide (55r)

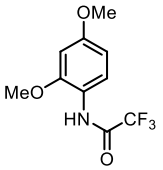

Following **GP5**, N-(2-((3',5'-dimethoxy-[1,1'-biphenyl]-2-yl)thio)-4,6-dimethoxyphenyl)-2,2,2-trifluoroacetamide (47.8 mg, 0.24 mmol, 2.4 eq.) gave **55r** (40%) as an oil. ^{1}H NMR ($CDCl_3$, 600 MHz) δ 8.37 (1H, s), 8.19 (1H, d, *J*=9.2 Hz), 6.51 – 6.49 (2H, m), 3.89 (3H, s), 3.81 (3H, s); ^{13}C NMR ($CDCl_3$, 151 MHz) δ 158.1, 154.1 (q, *J*=37.0 Hz), 149.8, 121.2, 118.6, 116.0 (q, *J*=288.2 Hz), 104.1, 98.8, 56.0, 55.7; ^{19}F NMR ($CDCl_3$, 564 MHz) δ -75.75.

N-(2,6-dimethyl-[1,1'-biphenyl]-3-yl)-2,2,2-trifluoroacetamide (55s)

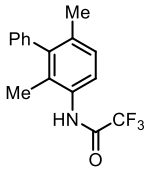

Following **GP5**, N-(4-((3',5'-dimethoxy-[1,1'-biphenyl]-2-yl)thio)-2,6-dimethyl-[1,1'-biphenyl]-3-yl)-2,2,2-trifluoroacetamide (47.8 mg, 0.24 mmol, 2.4 eq.) gave **55s** (49%) as an oil. ^{1}H NMR ($CDCl_3$, 600 MHz) δ 7.73 (1H, s), 7.60 (1H, d, *J*=8.2 Hz), 7.45 (1H, t, *J*=7.4 Hz), 7.37 (1H, t, *J*=7.5 Hz), 7.18 (1H, d, *J*=8.3 Hz), 7.11 (1H, d, *J*=6.8 Hz), 2.02 (3H, s), 1.94 (3H, s); ^{13}C NMR

($CDCl_3$, 151 MHz) δ 155.4 (q, *J*=36.9 Hz), 143.2, 140.4, 135.8, 130.6, 129.1, 128.8, 128.1, 127.3, 122.9, 116.2 (q, *J*=289.0 Hz), 21.1, 15.3; ^{19}F NMR ($CDCl_3$, 564 MHz) δ -75.60.

N-(4-(tert-butyl)phenyl)-2,2,2-trifluoroacetamide (55t)

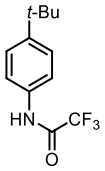

Following **GP5**, N-(4-(tert-butyl)-2-((3',5'-dimethoxy-[1,1'-biphenyl]-2-yl)thio)phenyl)-2,2,2-trifluoroacetamide (47.8 mg, 0.24 mmol, 2.4 eq.) gave **55t** (34%) as an oil. ^1H NMR ($CDCl_3$, 600 MHz) δ 8.02 (1H, s), 7.49 (2H, d, *J*=7.2 Hz), 7.40 (2H, d, *J*=7.4 Hz), 1.32 (9H, s); ^{13}C NMR ($CDCl_3$, 151 MHz) δ 155.0 (q, *J*=37.1 Hz), 149.7, 132.6, 126.3, 120.5, 115.9 (q, *J*=288.6 Hz), 34.7, 31.4; ^{19}F NMR ($CDCl_3$, 564 MHz) δ -75.73.

N-(2-(tert-butyl)phenyl)-2,2,2-trifluoroacetamide(55t')

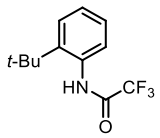

Following **GP5**, N-(2-(tert-butyl)-6-((3',5'-dimethoxy-[1,1'-biphenyl]-2-yl)thio)phenyl)-2,2,2-trifluoroacetamide (47.8 mg, 0.24 mmol, 2.4 eq.) gave **55t'** (31%) as an oil. ^1H NMR ($CDCl_3$, 600 MHz) δ 8.01 (1H, s), 7.67 (1H, d, *J*=7.7 Hz), 7.50 – 7.41 (1H, m), 7.29 (1H, td, *J*=7.6, 1.8 Hz), 7.29 – 7.23 (1H, m), 1.43 (9H, s); ^{13}C NMR ($CDCl_3$, 151 MHz) δ 155.2 (q, *J*=39.2) 142.8, 132.5, 127.8, 127.4, 127.2, 126.8, 116.3 (q, *J*=289.9) 34.6, 30.8; ^{19}F NMR ($CDCl_3$, 564 MHz) δ -75.95.

2,2,2-trifluoro-N-(2-methoxyphenyl)acetamide (55u')

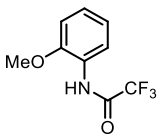

Following **GP5**, N-(2-((3',5'-dimethoxy-[1,1'-biphenyl]-2-yl)thio)-6-methoxyphenyl)-2,2,2-trifluoroacetamide (47.8 mg, 0.24 mmol, 2.4 eq.) gave **55u'** (68%) as an oil. ^1H NMR ($CDCl_3$, 600 MHz) δ 8.57 (1H, s), 8.32 (1H, dd, *J*=8.0, 1.6 Hz), 7.17 (1H, td, *J*=7.9, 1.6 Hz), 7.01 (1H, td, *J*=7.8, 1.3 Hz), 6.94 (1H, dd, *J*=8.3, 1.3 Hz), 3.93 (3H, s); ^{13}C NMR ($CDCl_3$, 151 MHz) δ 154.5 (q, *J*=37.2 Hz), 148.4, 126.1, 125.2, 121.4, 120.3, 115.9 (q, *J*=288.6 Hz), 110.4, 56.0; ^{19}F NMR ($CDCl_3$, 564 MHz) δ -75.84.

2,2,2-trifluoro-N-(5,6,7,8-tetrahydronaphthalen-2-yl)acetamide (55v)

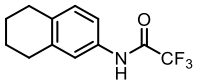

Following **GP5**, N-(3-((3',5'-dimethoxy-[1,1'-biphenyl]-2-yl)thio)-5,6,7,8-tetrahydronaphthalen-2-yl)-2,2,2-trifluoroacetamide (47.8 mg, 0.24 mmol, 2.4 eq.) gave **55v** (27%) as an oil. ^{1}H NMR ($CDCl_3$, 600 MHz) δ 7.85 (1H, s), 7.28 (1H, s), 7.24 (1H, dd, *J*=8.2, 2.4 Hz), 7.06 (1H, d, *J*=8.2 Hz), 2.77 – 2.71 (4H, m), 1.88 – 1.73 (4H, m); ^{13}C NMR ($CDCl_3$, 151 MHz) δ 154.8 (q, *J*=37.0 Hz), 138.5, 135.8, 132.4, 130.0, 121.2, 118.0, 115.9 (q, *J*=288.7 Hz), 29.6, 29.1, 23.1, 23.0; ^{19}F NMR ($CDCl_3$, 564 MHz) δ -75.75.

2,2,2-trifluoro-N-(5,6,7,8-tetrahydronaphthalen-1-yl)acetamide (55v')

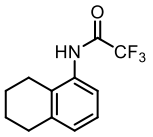

Following **GP5**, N-(2-((3',5'-dimethoxy-[1,1'-biphenyl]-2-yl)thio)-5,6,7,8-tetrahydronaphthalen-1-yl)-2,2,2-trifluoroacetamide (47.8 mg, 0.24 mmol, 2.4 eq.) gave **55v'** (25%) as an oil. ^{1}H NMR ($CDCl_3$, 600 MHz) δ 7.77 (1H, s), 7.56 (1H, d, *J*=7.9 Hz), 7.15 (1H, t, *J*=7.8 Hz), 7.03 (1H, d, *J*=7.7 Hz), 2.80 (2H, t, *J*=6.3 Hz), 2.60 (2H, t, *J*=6.4 Hz), 1.90 – 1.83 (2H, m), 1.82 – 1.72 (2H, m); ^{13}C NMR ($CDCl_3$, 151 MHz) δ 155.2 (q, *J*=36.9 Hz), 138.8, 132.6, 129.3, 128.3, 126.2, 120.9, 116.1 (q, *J*=289.0 Hz), 29.8, 24.3, 22.7, 22.5; ^{19}F NMR ($CDCl_3$, 564 MHz) δ -75.66. HRMS (ESI):.

Butyl 3-(2,2,2-trifluoroacetamido)benzoate (55w)

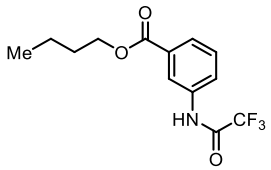

Following **GP5**, Butyl 4-((3',5'-dimethoxy-[1,1'-biphenyl]-2-yl)thio)-3-(2,2,2-trifluoroacetamido)benzoate (47.8 mg, 0.24 mmol, 2.4 eq.) gave **55w** (72%) as an oil. ^{1}H NMR ($CDCl_3$, 600 MHz) δ 8.53 (1H, s), 8.14 (1H, s), 8.00 (1H, d, *J*=8.1 Hz), 7.90 (1H, d, *J*=7.8 Hz), 7.48 (1H, t, *J*=8.0 Hz), 4.32 (2H, t, *J*=6.6 Hz), 1.74 (2H, qi, *J*=6.8 Hz), 1.46 (2H, sx, *J*=7.4 Hz), 0.97 (3H, t, *J*=7.4 Hz); ^{13}C NMR ($CDCl_3$, 151 MHz) δ 166.2, 155.3 (q, *J*=37.7 Hz), 135.7, 131.7, 129.7, 127.3, 125.1, 121.7, 115.8 (q, *J*=288.7 Hz), 65.5, 30.8, 19.3, 13.8; ^{19}F NMR ($CDCl_3$, 564 MHz) δ -75.65.

N-(3-(3-ethyl-2,6-dioxopiperidin-3-yl)phenyl)-2,2,2-trifluoroacetamide (55x)

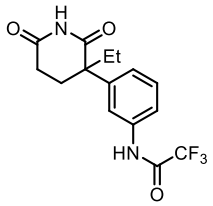

Following **GP5**, N-(2-((3',5'-dimethoxy-[1,1'-biphenyl]-2-yl)thio)-5-(3-ethyl-2,6-dioxopiperidin-3-yl)phenyl)-2,2,2-trifluoroacetamide (47.8 mg, 0.24 mmol, 2.4 eq.) gave **55x** (80%) as an oil. ^{1}H NMR ($CDCl_3$, 600 MHz) δ 8.57 (s, 1H), 8.08 (s, 1H), 7.60 – 7.52 (m, 3H), 7.33 (t, *J* = 7.6 Hz, 1H), 7.19 (m, 1H), 2.71 – 2.62 (1H, m), 2.49 – 2.41 (1H, m), 2.40 – 2.33 (1H, m), 2.26 (1H, td, *J*=14.0, 4.4 Hz), 2.13 – 2.04 (1H, m), 1.98 – 1.88 (1H, m), 0.89 (3H, t, *J*=7.4 Hz); ^{13}C NMR ($CDCl_3$, 151 MHz) δ 172.14 (d, *J* = 1.2 Hz), 154.61 (q, *J* = 37.4 Hz), 139.91, 138.19 (q, *J* = 3.1 Hz), 129.19, 121.75, 121.19, 117.70, 115.45 (q, *J* = 284.5 Hz), 50.3, 31.6, 30.5, 29.2, 9.2. ^{19}F NMR ($CDCl_3$, 564 MHz) δ -75.45.

2,2,2-trifluoro-N-((8R,9S,13S,14S)-13-methyl-17-oxo-7,8,9,11,12,13,14,15,16,17-decahydro-6H-cyclopenta[a]phenanthren-2-yl)acetamide (55y')

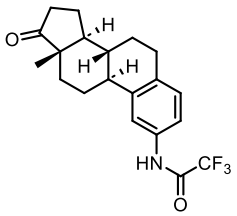

Following **GP5**, N-((8R,9S,13S,14S)-3-((3',5'-dimethoxy-[1,1'-biphenyl]-2-yl)thio)-13-methyl-17-oxo-7,8,9,11,12,13,14,15,16,17-decahydro-6H-cyclopenta[a]phenanthren-2-yl)-2,2,2-trifluoroacetamide (47.8 mg, 0.24 mmol, 2.4 eq.) gave **51af'** (28%) as an oil. ^{1}H NMR ($CDCl_3$, 600 MHz) δ 7.76 (1H, s), 7.48 (1H, s), 7.32 (1H, d, *J*=8.3 Hz), 7.12 (1H, d, *J*=8.2 Hz), 2.99 – 2.85 (2H, m), 2.51 (1H, dd, *J*=19.1, 8.8 Hz), 2.44 – 2.37 (1H, m), 2.31 (1H, t, *J*=11.3 Hz), 2.19 – 2.11 (1H, m), 2.08 – 2.01 (2H, m), 1.98 (1H, d, *J*=12.5 Hz), 1.71 – 1.56 (3H, m), 1.53 – 1.40 (3H, m), 0.88 (3H, t, *J*=7.2 Hz); ^{13}C NMR ($CDCl_3$, 151 MHz) δ 220.8, 141.2, 135.1, 132.9, 130.0, 118.4, (q, *J*=332.2 Hz), 50.6, 46.1, 44.5, 38.0, 36.0, 31.6, 29.0, 26.5, 25.9, 21.7, 14.0; ^{19}F NMR ($CDCl_3$, 564 MHz) δ -75.74.

5.5 References

(1) Roth, H. D. The Beginnings of Organic Photochemistry. *Angew. Chem. Int. Ed.* 1989, *28* (9), 1193–1207. https://doi.org/10.1002/anie.198911931.

(2) Turro, N. J. Geometric and Topological Thinking in Organic Chemistry. *Angew. Chem., Int. Ed. Engl* 1986, *25* (10), 882–901. https://doi.org/10.1002/anie.198608821.

(3) Ciamician, G. The Photochemistry of the Future. *Science (1979)* 1912, *36* (926), 385–394. https://doi.org/10.1126/science.36.926.385.

(4) Hoffmann, N. Photochemical Reactions as Key Steps in Organic Synthesis. *Chem. Rev.* 2008, *108* (3), 1052–1103. https://doi.org/10.1021/cr0680336.

(5) Turro, N. J.; Schuster, G. Photochemical Reactions as a Tool in Organic Syntheses. *Science (1979)* 1975, *187* (4174), 303–312. https://doi.org/10.1126/science.187.4174.303.

(6) N. J. Turro; V. Ramamurthy; J. C. Scaiano. *Modern Molecular Photochemistry of Organic Molecules.* ; 2011; Vol. 12. https://doi.org/10.1002/cphc.201000976.

(7) Nicewicz, D. A.; MacMillan, D. W. C. Merging Photoredox Catalysis with Organocatalysis: The Direct Asymmetric Alkylation of Aldehydes. *Science (1979)* 2008, *322* (5898), 77–80. https://doi.org/10.1126/science.1161976.

(8) Schultz, D. M.; Yoon, T. P. Solar Synthesis: Prospects in Visible Light Photocatalysis. *Science (1979)* 2014, *343* (6174). https://doi.org/10.1126/science.1239176.

(9) Buglioni, L.; Raymenants, F.; Slattery, A.; Zondag, S. D. A.; Noël, T. Technological Innovations in Photochemistry for Organic Synthesis: Flow Chemistry, High-Throughput Experimentation, Scale-up, and Photoelectrochemistry. *Chem. Rev.* 2022, *122* (2), 2752–2906. https://doi.org/10.1021/acs.chemrev.1c00332.

(10) Dell'Amico, L.; Vega-Peñaloza, A.; Cuadros, S.; Melchiorre, P. Enantioselective Organocatalytic Diels–Alder Trapping of Photochemically Generated Hydroxy- *o* -Quinodimethanes. *Angew. Chem. Int. Ed* 2016, *55* (10), 3313–3317. https://doi.org/10.1002/anie.201509472.

(11) Dell'Amico, L.; Fernández-Alvarez, V. M.; Maseras, F.; Melchiorre, P. Light-Driven Enantioselective Organocatalytic B-Benzylation of Enals. *Angewandte Chemie* 2017, *129* (12), 3352–3356. https://doi.org/10.1002/ange.201612159.

(12) Yang, N. C.; Rivas, C. A NEW PHOTOCHEMICAL PRIMARY PROCESS, THE PHOTOCHEMICAL ENOLIZATION OF o-SUBSTITUTED BENZOPHENONES. *J Am Chem Soc* 1961, *83* (9), 2213–2213. https://doi.org/10.1021/ja01470a053.

(13) Mateos, J.; Cherubini-Celli, A.; Carofiglio, T.; Bonchio, M.; Marino, N.; Companyó, X.; Dell'Amico, L. A Microfluidic Photoreactor Enables 2-Methylbenzophenone Light-Driven Reactions with Superior Performance. *Chem Comm* 2018, *54* (50), 6820–6823. https://doi.org/10.1039/C8CC01373J.

(14) Mateos, J.; Rigodanza, F.; Vega-Peñaloza, A.; Sartorel, A.; Natali, M.; Bortolato, T.; Pelosi, G.; Companyó, X.; Bonchio, M.; Dell'Amico, L. Naphthochromenones: Organic Bimodal Photocatalysts Engaging in Both Oxidative and Reductive Quenching Processes. *Angewandte Chemie International Edition* 2020, *59* (3), 1302–1312. https://doi.org/10.1002/anie.201912455.

(15) Plutschack, M. B.; Pieber, B.; Gilmore, K.; Seeberger, P. H. The Hitchhiker's Guide to Flow Chemistry. *Chem. Rev.* 2017, *117* (18), 11796–11893. https://doi.org/10.1021/acs.chemrev.7b00183.

(16) Blakemore, D. C.; Castro, L.; Churcher, I.; Rees, D. C.; Thomas, A. W.; Wilson, D. M.; Wood, A. Organic Synthesis Provides Opportunities to Transform Drug Discovery. *Nat Chem* 2018, *10* (4), 383–394. https://doi.org/10.1038/s41557-018-0021-z.

(17) Campos, K. R.; Coleman, P. J.; Alvarez, J. C.; Dreher, S. D.; Garbaccio, R. M.; Terrett, N. K.; Tillyer, R. D.; Truppo, M. D.; Parmee, E. R. The Importance of Synthetic Chemistry in the Pharmaceutical Industry. *Science (1979)* 2019, *363* (6424). https://doi.org/10.1126/science.aat0805.

(18) Taylor, R. D.; MacCoss, M.; Lawson, A. D. G. Rings in Drugs. *J Med Chem* 2014, *57* (14), 5845–5859. https://doi.org/10.1021/jm4017625.

(19) Pitt, W. R.; Parry, D. M.; Perry, B. G.; Groom, C. R. Heteroaromatic Rings of the Future. *J Med Chem* 2009, *52* (9), 2952–2963. https://doi.org/10.1021/jm801513z.

(20) Horton, D. A.; Bourne, G. T.; Smythe, M. L. The Combinatorial Synthesis of Bicyclic Privileged Structures or Privileged Substructures. *Chem Rev* 2003, *103* (3), 893–930. https://doi.org/10.1021/cr020033s.

(21) Chattopadhyay, B.; Gevorgyan, V. Transition-Metal-Catalyzed Denitrogenative Transannulation: Converting Triazoles into Other Heterocyclic Systems. *Angewandte Chemie International Edition* 2012, *51* (4), 862–872. https://doi.org/10.1002/anie.201104807.

(22) Moderhack, D. Ring Transformations in Tetrazole Chemistry. *Journal for Praktische Chemie/Chemiker-Zeitung* 1998, *340* (8), 687–709. https://doi.org/10.1002/prac.19983400802.

(23) H. C. van der Plas. Pyrimidine–Pyridine Ring Interconversion. In *Advances in Heterocyclic Chemistry*; Katritzky, Academic Press, 2003; Vol. 84, pp 31–70.

(24) Jurczyk, J.; Woo, J.; Kim, S. F.; Dherange, B. D.; Sarpong, R.; Levin, M. D. Single-Atom Logic for Heterocycle Editing. *Nature Synthesis* 2022, *1* (5), 352–364. https://doi.org/10.1038/s44160-022-00052-1.

(25) Hui, C.; Wang, Z.; Wang, S.; Xu, C. Molecular Editing in Natural Product Synthesis. *Organic Chemistry Frontiers* 2022, *9* (5), 1451–1457. https://doi.org/10.1039/D2QO00043A.

(26) Woo, J.; Stein, C.; Christian, A. H.; Levin, M. D. Carbon-to-Nitrogen Single-Atom Transmutation of Azaarenes. *Nature* 2023, *623* (7985), 77–82. https://doi.org/10.1038/s41586-023-06613-4.

(27) Mykura, R.; Sánchez-Bento, R.; Matador, E.; Duong, V. K.; Varela, A.; Angelini, L.; Carbajo, R. J.; Llaveria, J.; Ruffoni, A.; Leonori, D. Synthesis of Polysubstituted Azepanes by Dearomative Ring Expansion of Nitroarenes. *Nat Chem* 2024, *16* (5), 771–779. https://doi.org/10.1038/s41557-023-01429-1.

(28) Sánchez-Bento, R.; Bui, L.; Duong, V. K.; Ruffoni, A.; Leonori, D. A Photochemical Strategy for the Synthesis of Caprolactams via Dearomative Ring Expansion of Nitroarenes. *Synthesis (Stuttg)* 2024, *56* (15), 2385–2391. https://doi.org/10.1055/a-2288-6944.

(29) Li, B.; Ruffoni, A.; Leonori, D. A Photochemical Strategy for *Ortho* -Aminophenol Synthesis via Dearomative-Rearomative Coupling Between Aryl Azides and Alcohols. *Angewandte Chemie International Edition* 2023, *62* (52). https://doi.org/10.1002/anie.202310540.

(30) Matador, E.; Tilby, M. J.; Saridakis, I.; Pedrón, M.; Tomczak, D.; Llaveria, J.; Atodiresei, I.; Merino, P.; Ruffoni, A.; Leonori, D. A Photochemical Strategy for the Conversion of Nitroarenes into Rigidified Pyrrolidine Analogues. *J Am Chem Soc* 2023, *145* (50), 27810–27820. https://doi.org/10.1021/jacs.3c10863.

(31) Sánchez-Bento, R.; Roure, B.; Llaveria, J.; Ruffoni, A.; Leonori, D. A Strategy for Ortho-Phenylenediamine Synthesis via Dearomative-Rearomative Coupling of Nitrobenzenes and Amines. *Chem* 2023, *9* (12), 3685–3695. https://doi.org/10.1016/j.chempr.2023.10.008.

(32) Sundberg, R. J.; Das, B. P.; Smith, R. H. Photochemical Deoxygenation of Aromatic Nitro Compounds in Triethyl Phosphite. Substituent Effects and Evidence for the Involvement Aryl Nitrenes. *J Am Chem Soc* 1969, *91* (3), 658–668. https://doi.org/10.1021/ja01031a024.

(33) Gritsan, N. P.; Yuzawa, T.; Platz, M. S. Direct Observation of Singlet Phenylnitrene and Measurement of Its Rate of Rearrangement. *J Am Chem Soc* 1997, *119* (21), 5059–5060. https://doi.org/10.1021/ja963753n.

(34) Marcinek, A.; Platz, M. S.; Chan, S. Y.; Floresca, R.; Rajagopalan, K.; Golinski, M.; Watt, D. Unusually Long Lifetimes of the Singlet Nitrenes Derived from 4-Azido-2,3,5,6-Tetrafluorobenzamides. *J Phys Chem* 1994, *98* (2), 412–419. https://doi.org/10.1021/j100053a012.

(35) DeGraff, B. A.; Gillespie, D. W.; Sundberg, R. J. Phenyl Nitrene. Flash Photolytic Investigation of the Reaction with Secondary Amines. *J Am Chem Soc* 1974, *96* (24), 7491–7496. https://doi.org/10.1021/ja00831a017.

(36) Chapman, O. L.; Le Roux, J. P. 1-Aza-1,2,4,6-Cycloheptatetraene. *J Am Chem Soc* 1978, *100* (1), 282–285. https://doi.org/10.1021/ja00469a049.

(37) Satake, K.; Okuda, R.; Hashimoto, M.; Fujiwara, Y.; Watadani, I.; Okamoto, H.; Kimura, M.; Morosawa, S. Synthesis and Characterization of 2H-, 3H- and 4H-Azepine: The First Observation of the Thermal Distribution Equilibrium of Azepines. *J Chem Soc Chem Commun* 1991, No. 17, 1154. https://doi.org/10.1039/c39910001154.

(38) J. Mortier. *Arene Chemistry: Reaction Mechanisms and Methods for Aromatic Compounds* , Wiley & Sons Inc.; 2015.

(39) Voronin, I. O.; Nesterova, T. N.; Strelchik, B. S.; Zhuravskii, E. A. Efficiency of Sulfonic Cation-Exchange Resins Used in Para-Tert-Butylphenol Production: A Comparison Based on the Kinetics of Transalkylation in the Phenol-Tert-Butylphenols System. *Kinetics and Catalysis* 2014, *55* (6), 705–711. https://doi.org/10.1134/S0023158414060147.

(40) Tsai, T. Disproportionation and Transalkylation of Alkylbenzenes over Zeolite Catalysts. *Appl Catal A Gen* 1999, *181* (2), 355–398. https://doi.org/10.1016/S0926-860X(98)00396-2.

(41) G. Bellussi; J. Scholtz; K. Sundmacher; R. Ulber; U. Wietelmann. *Ullmann's Encyclopedia of Industrial Chemistry*; 2011.

(42) WOTIZ, J. H.; HUBA, F. Low Temperature Amination of Aromatic Polyhalides 1. *J Org Chem* 1959, *24* (5), 595–598. https://doi.org/10.1021/jo01087a005.

(43) Bunnett, J. F.; Moyer, C. E. Isomerization and Disproportionation of Trihalobenzenes Catalyzed by Potassium Anilide in Liquid Ammonia. *J Am Chem Soc* 1971, *93* (5), 1183–1190. https://doi.org/10.1021/ja00734a026.

(44) Bunnett, J. F. Base-Catalyzed Halogen Dance, and Other Reactions of Aryl Halides. *Acc Chem Res* 1972, *5* (4), 139–147. https://doi.org/10.1021/ar50052a004.

(45) Nájera, C.; Sansano, J. M.; Yus, M. Recent Synthetic Uses of Functionalised Aromatic and Heteroaromatic Organolithium Reagents Prepared by Non-Deprotonating Methods. *Tetrahedron* 2003, *59* (47), 9255–9303. https://doi.org/10.1016/j.tet.2003.09.065.

(46) Tilly, D.; Chevallier, F.; Mongin, F.; Gros, P. C. Bimetallic Combinations for Dehalogenative Metalation Involving Organic Compounds. *Chem Rev* 2014, *114* (2), 1207–1257. https://doi.org/10.1021/cr400367p.

(47) Gschwend, H. W.; Rodriguez, H. R. Heteroatom-Facilitated Lithiations. In *Organic Reactions*; Wiley, 1979; pp 1–360. https://doi.org/10.1002/0471264180.or026.01.

(48) Beak, P.; Snieckus, V. Directed Lithiation of Aromatic Tertiary Amides: An Evolving Synthetic Methodology for Polysubstituted Aromatics. *Acc Chem Res* 1982, *15* (10), 306–312. https://doi.org/10.1021/ar00082a002.

(49) Matsushita, K.; Takise, R.; Muto, K.; Yamaguchi, J. Ester Dance Reaction on the Aromatic Ring. *Sci Adv* 2020, *6* (28). https://doi.org/10.1126/sciadv.aba7614.

(50) Edelmann, S.; Lumb, J.-P. A Para- to Meta-Isomerization of Phenols. *Nat Chem* 2024, *16* (7), 1193–1199. https://doi.org/10.1038/s41557-024-01512-1.

(51) Vitaku, E.; Smith, D. T.; Njardarson, J. T. Analysis of the Structural Diversity, Substitution Patterns, and Frequency of Nitrogen Heterocycles among U.S. FDA Approved Pharmaceuticals. *J Med Chem* 2014, *57* (24), 10257–10274. https://doi.org/10.1021/jm501100b.

(52) *Arene Chemistry:Reaction Mechanisms and Methods for Aromatic Compounds*; Wiley, 2015. https://doi.org/10.1002/9781118754887.

(53) Patra, S.; Mosiagin, I.; Giri, R.; Katayev, D. Organic Nitrating Reagents. *Synthesis (Stuttg)* 2022, *54* (15), 3432–3472. https://doi.org/10.1055/s-0040-1719905.

(54) Xiong, T.; Zhang, Q. New Amination Strategies Based on Nitrogen-Centered Radical Chemistry. *Chem Soc Rev* 2016, *45* (11), 3069–3087. https://doi.org/10.1039/C5CS00852B.

(55) Park, Y.; Kim, Y.; Chang, S. Transition Metal-Catalyzed C–H Amination: Scope, Mechanism, and Applications. *Chem Rev* 2017, *117* (13), 9247–9301. https://doi.org/10.1021/acs.chemrev.6b00644.

(56) Timmann, S.; Feng, Z.; Alcarazo, M. Recent Applications of Sulfonium Salts in Synthesis and Catalysis. *Chemistry – A European Journal* 2024, *30* (70). https://doi.org/10.1002/chem.202402768.

(57) Gendron, T.; Sander, K.; Cybulska, K.; Benhamou, L.; Sin, P. K. B.; Khan, A.; Wood, M.; Porter, M. J.; Årstad, E. Ring-Closing Synthesis of Dibenzothiophene Sulfonium Salts and Their Use as Leaving Groups for Aromatic 18 F-Fluorination. *J Am Chem Soc* 2018, *140* (35), 11125–11132. https://doi.org/10.1021/jacs.8b06730.

(58) Lin, Z.-H.; Yao, Y.-F.; Zhang, C.-P. Deuteration of Arylthianthren-5-Ium Salts in CD 3 OD. *Org Lett* 2022, *24* (45), 8417–8422. https://doi.org/10.1021/acs.orglett.2c03541.

(59) Péter, Á.; Perry, G. J. P.; Procter, D. J. Radical C−C Bond Formation Using Sulfonium Salts and Light. *Adv Synth Catal* 2020, *362* (11), 2135–2142. https://doi.org/10.1002/adsc.202000220.

(60) Xu, H.; Zhang, J.; Zuo, J.; Wang, F.; Lü, J.; Hun, X.; Yang, D. Recent Advances in Visible-Light-Catalyzed C—C Bonds and C—Heteroatom Bonds Formation Using Sulfonium Salts. *Chinese Journal of Organic Chemistry* 2022, *42* (12), 4037. https://doi.org/10.6023/cjoc202209004.

(61) Li, J.; Chen, J.; Sang, R.; Ham, W.-S.; Plutschack, M. B.; Berger, F.; Chabbra, S.; Schnegg, A.; Genicot, C.; Ritter, T. Photoredox Catalysis with Aryl Sulfonium Salts Enables Site-Selective Late-Stage Fluorination. *Nat Chem* 2020, *12* (1), 56–62. https://doi.org/10.1038/s41557-019-0353-3.

(62) Engl, P. S.; Häring, A. P.; Berger, F.; Berger, G.; Pérez-Bitrián, A.; Ritter, T. C–N Cross-Couplings for Site-Selective Late-Stage Diversification via Aryl Sulfonium Salts. *J Am Chem Soc* 2019, *141* (34), 13346–13351. https://doi.org/10.1021/jacs.9b07323.

(63) Ye, F.; Berger, F.; Jia, H.; Ford, J.; Wortman, A.; Börgel, J.; Genicot, C.; Ritter, T. Aryl Sulfonium Salts for Site-Selective Late-Stage Trifluoromethylation. *Angewandte Chemie International Edition* 2019, *58* (41), 14615–14619. https://doi.org/10.1002/anie.201906672.

(64) Lee, W.-T.; Dickie, D. A.; Metta-Magaña, A. J.; Smith, J. M. A Tripodal Ligand Constructed from Mesoionic Carbene Donors. *Inorg Chem* 2013, *52* (21), 12842–12846. https://doi.org/10.1021/ic402311c.

(65) Markiewicz, J. T.; Wiest, O.; Helquist, P. Synthesis of Primary Aryl Amines Through a Copper-Assisted Aromatic Substitution Reaction with Sodium Azide. *J Org Chem* 2010, *75* (14), 4887–4890. https://doi.org/10.1021/jo101002p.

(66) Cummings, S. P.; Le, T.-N.; Fernandez, G. E.; Quiambao, L. G.; Stokes, B. J. Tetrahydroxydiboron-Mediated Palladium-Catalyzed Transfer Hydrogenation and Deuteriation of Alkenes and Alkynes Using Water as the Stoichiometric H or D Atom Donor. *J Am Chem Soc* 2016, *138* (19), 6107–6110. https://doi.org/10.1021/jacs.6b02132.

(67) Xu, S.; Zhuang, X.; Pan, X.; Zhang, Z.; Duan, L.; Liu, Y.; Zhang, L.; Ren, X.; Ding, K. 1-Phenyl-4-Benzoyl-1 *H* -1,2,3-Triazoles as Orally Bioavailable Transcriptional Function Suppressors of Estrogen-Related Receptor α. *J Med Chem* 2013, *56* (11), 4631–4640. https://doi.org/10.1021/jm4003928.

(68) Teregulova, A. N.; Yarullin, A. R.; Chainikova, E. M.; Lobov, A. N.; Safiullin, R. L.; Khursan, S. L. Transformations of 4-R-6-Oxohexa-2,4-Diene Nitrile Oxides – Intermediates of Photooxidation of Para-R-C6H4N3, R = Ph, CH2Ph, OPh. *Tetrahedron* 2024, *153*, 133849. https://doi.org/10.1016/j.tet.2024.133849.

(69) Yang, Z.; Du, F.-H.; Zhang, C.; Du, Y. Accessing Aryl Azides *via* Copper Powder-Catalyzed Cross-Coupling of Arylboronic Acids with the Hypervalent Azido-Iodine Reagent ABZ(I). *Organic Chemistry Frontiers* 2023, *10* (16), 4131–4138. https://doi.org/10.1039/D3QO00732D.

(70) Pearson, T. J.; Shimazumi, R.; Driscoll, J. L.; Dherange, B. D.; Park, D.-I.; Levin, M. D. Aromatic Nitrogen Scanning by *Ipso* -Selective Nitrene Internalization. *Science (1979)* 2023, *381* (6665), 1474–1479. https://doi.org/10.1126/science.adj5331.

(71) Zhou, F.; Driver, T. G. Efficient Synthesis of 3 *H* -Indoles Enabled by the Lead-Mediated α-Arylation of β-Ketoesters or γ-Lactams Using Aryl Azides. *Org Lett* 2014, *16* (11), 2916–2919. https://doi.org/10.1021/ol5010615.

(72) Cho, Y. A.; Kim, D.-S.; Ahn, H. R.; Canturk, B.; Molander, G. A.; Ham, J. Preparation of Potassium Azidoaryltrifluoroborates and Their Cross-Coupling with Aryl Halides. *Org Lett* 2009, *11* (19), 4330–4333. https://doi.org/10.1021/ol901669k.

(73) Zuo, Z.; Liu, X.; Qian, X.; Zeng, T.; Sang, N.; Liu, H.; Zhou, Y.; Tao, L.; Zhou, X.; Su, N.; Yu, Y.; Chen, Q.; Luo, Y.; Zhao, Y. Bifunctional Naphtho[2,3- *d*][1,2,3]Triazole-4,9-Dione Compounds Exhibit Antitumor Effects In Vitro and In Vivo by Inhibiting Dihydroorotate Dehydrogenase and Inducing Reactive Oxygen Species Production. *J Med Chem* 2020, *63* (14), 7633–7652. https://doi.org/10.1021/acs.jmedchem.0c00512.

(74) Zhu, W.; Ma, D. Synthesis of Aryl Azides and Vinyl Azides via Proline-Promoted CuI-Catalyzed Coupling ReactionsElectronic Supplementary Information (ESI) Available: Experimental Procedures. See Http://Www.Rsc.Org/Suppdata/Cc/B4/B400878b/. *Chemical Communications* 2004, No. 7, 888. https://doi.org/10.1039/b400878b.

(75) Bertrand, H. C.; Schaap, M.; Baird, L.; Georgakopoulos, N. D.; Fowkes, A.; Thiollier, C.; Kachi, H.; Dinkova-Kostova, A. T.; Wells, G. Design, Synthesis, and Evaluation of Triazole Derivatives That Induce Nrf2 Dependent Gene Products and Inhibit the Keap1–Nrf2 Protein–Protein Interaction. *J Med Chem* 2015, *58* (18), 7186–7194. https://doi.org/10.1021/acs.jmedchem.5b00602.

(76) Bończak, B.; Lisowski, W.; Kamińska, A.; Hołdyński, M.; Fiałkowski, M. Gold Nanoparticles Functionalized with Fully Conjugated Fullerene C 60 Derivatives as a Material with Exceptional Capability of Absorbing Electrons. *The Journal of Physical Chemistry C* 2019, *123* (10), 6229–6240. https://doi.org/10.1021/acs.jpcc.8b10842.

(77) Meng, G.; Guo, T.; Ma, T.; Zhang, J.; Shen, Y.; Sharpless, K. B.; Dong, J. Modular Click Chemistry Libraries for Functional Screens Using a Diazotizing Reagent. *Nature* 2019, *574* (7776), 86–89. https://doi.org/10.1038/s41586-019-1589-1.

(78) Powers, I. G.; Andjaba, J. M.; Luo, X.; Mei, J.; Uyeda, C. Catalytic Azoarene Synthesis from Aryl Azides Enabled by a Dinuclear Ni Complex. *J Am Chem Soc* 2018, *140* (11), 4110–4118. https://doi.org/10.1021/jacs.8b00503.

List of Abbreviations

ABPE	Applied Bias Photon to Current Efficiency
AP	Artificial Photosynthesis
a-Si	Amorphous silicon
BIPV	Building integrated photovoltaics
BTD	Benzothiadiazole
CA	Chronoamperometry
CB	Conduction band
CBZ	Carbazole
CSP	Concentrated solar power
CV	Cyclic Voltammetry
dba	Dibenzylideneacetone
DCM	Dichloromethane
DCM	Dichloromethane.
DFT	Density functional theory
DFT	Density Functional Theory
DMSO	Dimethylsulfoxide
DPP	Diketopyrrolopyrrole
dppf	1,1'-bis(diphenylphosphino)ferrocene
DSPEC	Dye-Sensitized Photoelectrochemical Cell
DSSC	Dye-Sensitized Solar Cells
DSSC	Dye-sensitized solar cells
D-π-A	Donor-π-Acceptor
$\mathbf{E^*_{ox}}$	Excited-state oxidation potential
EADS	Evolution Associated Difference Spectrum
EIS	Electrochemical impedance spectroscopy
$\mathbf{E_{ox}}$	Oxidation potential
ESI-MS	Electrospray ionization-mass spectrometry
$\mathbf{Et_2O}$	Diethyl ether
EtOH	Ethanol
FE	Faradaic Efficiency
FMOs	Frontier molecular orbitals
FQY	Fluorescence Quantum Yield.
FTO	Fluorine-Tin oxide

HEC	Hydrogen Evolution Catalyst
HER	Hydrogen Evolution Reaction
HFIP	1,1,1,3,3,3-hexafluoro-2-propanol
HOMO	Highest Occupied Molecular Orbital
HRMS	High-resolution mass spectrometry
ICT	Intramolecular charge transfer
IoT	Internet of Things
IPCE	Incident photon-to-current conversion efficiency
IR	Infrared
ITO	Indium-Tin oxide
LED	Light Emitting Diode
LSV	Linear Sweep Voltammetry
LUMO	Lowest unoccupied molecular orbital
MeCN	Acetonitrile
MeOH	Methanol
MLCT	Metal-to-Ligand Charge Transfer
MW	Microwave
***N,N*-DMF**	N,N-dimethylformamide
NBS	N-bromosuccinimide
NHE	Normal hydrogen electrode
NIR	Near infrared
NIS	N-iodosuccinimide
OEC	Oxygen Evolving Complex
PA	Photoanode
PC	Photocatalytic
PCM	Polarizable Continuum Model
PDI	Perylene Diimides
PE	Petroleum ether
PEC	Photoelectrochemical Cell
PMI	Perylene Monoimides
POZ	Phenoxazine
PS	Photosensitizer
PSC	Perovskite solar cells
PTZ	Phenothiazine

PV	Photovoltaic
PV-EC	Photovoltaic-Electrochemical
QE	Quantum Efficiency
RM	Redox mediator
SC	Semiconductor
SCE	Saturated Calomel Electrode
SET	Single-electron transfer
STH	Solar-to-Hydrogen Efficiency
TAS	Transient Absorption Spectroscopy
TCD-GC	Thermal Conductivity Detector-Gas Chromatography
TD-DFT	Time-Dependent Density Functional Theory
THF	Tetrahydrofuran
TOF	Turnover Frequency
TON	Turnover Number
UV	Ultraviolet
VB	Valence band
WOC	Water Oxidation Catalyst